Fundamental effective temperature measurements for eclipsing binary stars

Nicola Jane Miller

Doctor of Philosophy

Department of Physics, Keele University

December 2022

Abstract

Modern high-precision spectroscopy and photometry has made it possible to directly measure masses and radii for stars in detached eclipsing binaries (DEBs) to 0.5% or better. These stars, due to their wide orbits, are suitable for testing models of single stars. However, effective temperature (T_{eff}) estimates for FGK-type stars are lagging behind, with Jofré et al. (2019) noting that most T_{eff} estimates are no more accurate than 50 K.This is an important issue to address, as inaccurate T_{eff} estimates limit the calibration of stellar models using DEBs. A consistent T_{eff} scale for stars with a range of masses and ages is essential to avoid spurious trends in population studies for exoplanet host stars and Galactic archaeology.

This thesis aims to address this problem by developing a new method to measure the fundamental, i.e. direct, effective temperatures for stars in DEBs. The new method is based on the Stefan-Boltzmann law. We use a Bayesian approach to obtain the integrated bolometric fluxes for the two stars from observed magnitudes, colours, and flux ratios. Angular diameters are obtained from measurements of the stellar radii using *TESS* light curves and radial velocities measured from high-resolution spectroscopy, and parallax from the *Gaia* satellite. Fundamental effective temperatures have been measured for five FGK-type stars in three DEBs: the F7 V+K0 V binary AI Phoenicis, the F5 V+F6 V binary CPD-54 810, and the primary component of the F+M binary with a low-mass component EBLM J0113+31. The results significantly improve on the accuracies of existing T_{eff} estimates: better than $\pm0.4\%$ for AI Phoenicis and $\pm0.7\%$ for CPD-54 810 and EBLM J0113+31 A. The choice of model SED has no impact on the derived effective temperatures.

This work provides the basis for building a large sample of well-studied FGK-type stars with very accurate and precise T_{eff} measurements. Such a sample has a wide applicability in the rest of astrophysics, as it can be used for testing and calibrating stellar models and large-scale spectroscopic surveys.

Acknowledgements

Contents

List of Figures

List of Tables

1 Introduction

There are ways of approach to unknown territory which lead surprisingly far, and repay their followers richly. There is probably no better example of this than eclipses of heavenly bodies.

Henry Norris Russell (1948)

1.1 Stars

Stars are celestial objects that are bound by self-gravity, and radiate energy produced by an internal source. Stars therefore tend to be spherical, due to the spherical symmetry of gravitational fields, but may be spheroidal if there are axisymmetric forces at play, such as rotation or tidal interactions with another object. The internal source of energy for stars is typically nuclear fusion, but at certain points during their evolution, gravitational potential energy is released by contraction or collapse of the star. Stars tend to exist in hydrostatic equilibrium, where the gravitational pressure inwards is balanced by radiation pressure outwards.

1.1.1 Fundamental properties of stars

Knowledge of the fundamental parameters of stars, such as the mass, radius, temperature, chemical composition, and age, is critical to the core foundations of astrophysics. These properties allow us to better understand the past and future of our local stellar neighbourhood, our Galaxy and beyond.

The observational information we can gather about stars comes solely from the radiation they emit. The spectrum of a star can give information about the chemical composition, temperature, surface gravity and rotation, while shifts in the wavelength of spectral lines for a spectroscopic binary star can give information on the mass of the two components. Monitoring the position of a star on the sky (astrometry) may give

information on the trigonometric parallax and hence distance to the star, and stellar masses in resoled binary star systems. Photometry gives information about the flux of a star, which when measured across the optical wavelength range can be used to obtain measurements of bolometric flux, luminosity and temperature. Time-series photometry reveals variation in the brightness of stars, which may be due to e.g. activity, rotation, interaction with another object, flares, accretion, exoplanet transits or eclipses of a binary star component. For binary stars with their orbital plane aligned with the Solar System (eclipsing binaries; EBs), the shape, duration and separation of their eclipses can give information on the stellar radius. The radius may also be determined using interferometric observations of the stellar disc.

Stars are typically divided into groups based on their spectral characteristics. The Morgan–Keenan (MK) system, built on the Harvard system constructed by Cannon & Pickering (1901), gives stars a 'spectral type' letter classification and a 'luminosity type' roman numeral classification. The spectral type is based on the strength of prominent absorption lines such as the hydrogen Balmer lines, and is a proxy for the temperature. Stars are typically placed into one of the main categories: O, B, A, F, G, K, M. These may be sub-divided with an additional number 0-9, e.g. a star halfway between F and G would be a F5-type star. The luminosity type is broken into I-V, where I – supergiants, II – bright giants, III – giants, IV – sub-giant stars, V – dwarfs, i.e. main-sequence stars. For example, a main-sequence star with an effective temperature of 6500 K would have a classification of F5 V (Pecaut & Mamajek, 2013).

1.1.2 FGK-type stars

Most stars observed by the *Gaia* satellite are small, cool main-sequence stars. While M-dwarfs outnumber other stars in a volume-limited sample (e.g. Gaia Collaboration et al. 2021b), observational bias causes the overall distribution of the temperatures of stars in Figure 1.1 to shift to predominantly F, G and K spectral classes[1]. Not only are

---

[1] https://gea.esac.esa.int/archive/visualization/
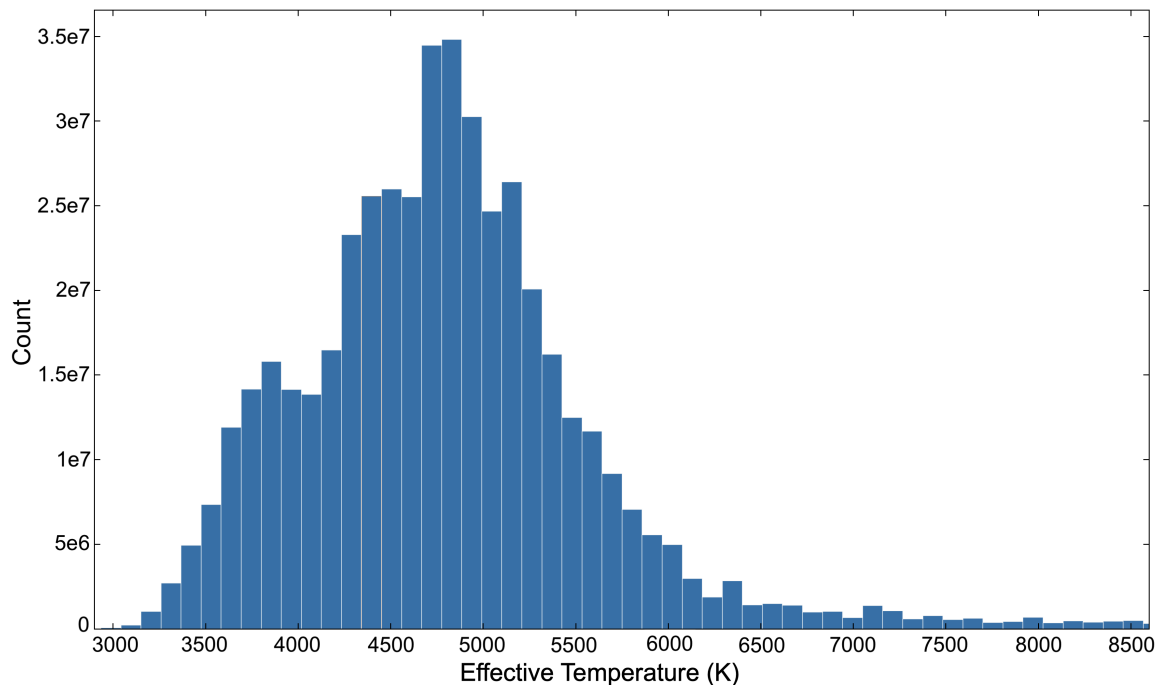
Figure 1.1: Histogram of the temperatures of stars from *Gaia* DR3 spectro-photometry.

FGK-type stars numerous, they are important tracers for the chemical evolution of the Galaxy. Their lifetimes are sufficiently long and convective regions sufficiently shallow such that the chemical composition of the gas from which they formed remains in their spectra (Jofré et al., 2019). Having a good understanding of the physical properties of FGK-type dwarfs, particularly the effective temperature, is therefore important for measuring accurate chemical abundances from spectra.

The discovery of thousands of exoplanets in recent years has motivated efforts to characterise their properties and environments, both which are heavily influenced by the host star. Without a robust understanding of the fundamental properties of the host star, the derived parameters for the planet will remain uncertain. The majority of exoplanets discovered to date have been found orbiting FGK-type stars (and M-dwarfs): Figure 1.2 shows the distribution of temperature estimates for the host stars
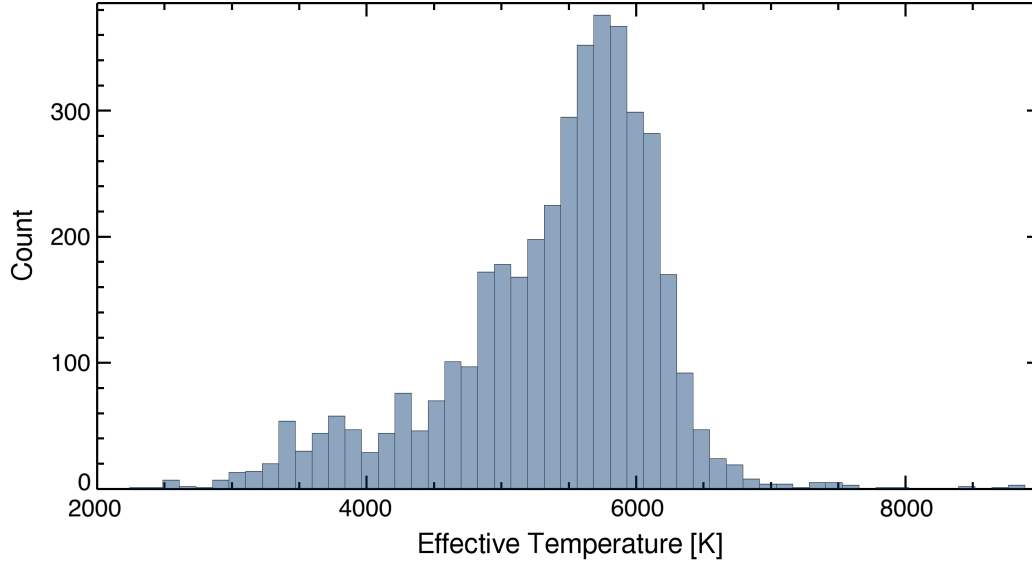
Figure 1.2: Histogram of temperature estimates for host stars of confirmed exoplanets.

of all confirmed exoplanets (as of 18 June 2022) from the NASA Exoplanet Archive[2]. Therefore, it is important to the advancement of exoplanet science that the detailed characterisation of FGK-type stars does not get overlooked.

The upcoming European Space Agency (ESA) PLAnetary Transits and Oscillations (*PLATO*) mission aims to find Earth-like planets orbiting Sun-like stars, and plans to be able to measure the properties of the host stars to high precision. For example, the current specifications demand that the stellar ages from asteroseismology of stars observed by *PLATO* should be accurate to 10% (after corrections for bias and systematics, for a reference star at $V = 10$; Goupil 2017). To reach this target, some improvement on the current generation of stellar models is required. To this end, the work package 'WP125500 Benchmark Stars' was formed to address these needs[3], and some of the work I present in this thesis will feed into these benchmarking efforts.

---

[2]https://exoplanetarchive.ipac.caltech.edu/index.html
[3]https://warwick.ac.uk/fac/sci/physics/research/astro/plato-science/research/researchareas/stellar/wp125500/

1.1.3 Stellar models

Stellar models are useful for predicting the properties of stars based on observable quantities. Stellar evolution models typically take an initial mass and chemical composition as inputs and predict the physical properties of the star(s) at any age. These codes produce evolution tracks and isochrones, for example PARSEC (Bressan et al., 2012), GARSTEC (Weiss & Schlattl, 2008) and MESA (Dotter, 2016). Evolution tracks are useful tools for studying stellar evolution, and produce an output of stellar parameters over a grid of time-steps for a single given mass. Isochrones are derived from a set of evolution tracks across a range of masses, making time the independent variable rather than mass. Isochrones are particularly useful for studying stellar populations.

Stellar evolution models are constructed using a combination of micro-physics (e.g. equations of state, opacities, nuclear reaction rates) and macro-physics (e.g. mixing length theory, convective core overshooting, boundary conditions, diffusion and gravitational settling), along with numerical considerations (Paxton et al., 2011). Variations in these parameters can result in very different conclusions being drawn about the evolutionary path of a star. For example, the convective core overshooting parameter, which describes the additional mixing of convective layers with the outer layers of the core, and can increase the lifetime of stars by causing more fuel to be available in the core. Eclipsing binaries have been used to observationally constrain the mass-dependence of this parameter e.g. Claret (2007); Claret & Torres (2016, 2018), though the conclusions drawn by this work has been debated (Constantino & Baraffe, 2018; Claret & Torres, 2019). Notably, Constantino & Baraffe (2018) comment that "In many examples, the allowed range of the overshooting parameters could be reduced with more precise determinations of effective temperature and metallicity". Viani & Basu (2020) find that the amount of overshoot required to correctly model stars with asteroseismological parameters increases with mass, supporting the findings with eclipsing binaries.

In contrast, stellar atmosphere models strive to produce accurate models of the spectral properties of stars. These models usually take the observed properties of stars,

such as the effective temperature, surface gravity and metallicity, and generate detailed model spectra based on physical parameterisations of stars and state-of-the-art atomic and molecular line lists. Oftentimes, these models are computed in one dimension, i.e. spherically symmetric or plane-parallel, and assume local thermal equilibrium (LTE). 3-dimensional hydrodynamical models, or those which consider non-LTE effects, tend to be much more computationally expensive. Models atmospheres are typically computed over a grid of stellar properties. Prominent examples of stellar atmosphere models include ATLAS (1D, LTE; Kurucz 1970), MARCS (1D, LTE; Gustafsson et al. 2008), PHOENIX (1D and 3D, LTE and non-LTE; Husser et al. 2013), and STAGGER (3D, LTE; Magic et al. 2013). Stellar atmosphere models are used to generate synthetic spectra, which can be used as a 'template' to fit observed spectroscopy.

1.1.3.1 Calibration of models

Theoretical stellar models must be grounded in observation, and this is where calibration stars come in. A set of 'benchmark' stars with well-measured, ideally model-independent parameters is used to tune the parameters in stellar models, such as the convective core overshooting parameter, in order to force the model to match the observations more closely. Benchmark stars may also be used in testing models, i.e. comparing the output of some pipeline or model prediction with observations.

One recent example of theoretical models being shaped by observational constraints is the 'Solar abundance problem', a disagreement between predictions by state-of-the-art, 3D, non-LTE stellar models for the Sun, and observed data from helioseismology (Antia & Basu, 2005; Asplund et al., 2009). The conflict was eventually resolved by improving the models with new atomic and molecular data, new non-LTE model atoms and a careful treatment of the 3D model atmospheres and abundances (Magg et al., 2022). This highlights the value that precise observational constraints can have in improving predictions from stellar models.

There is still plenty of work to be done on both theoretical and observational fronts. Current samples of benchmark stars, for example the *Gaia* sample (Jofré et al.,

2014), are often limited by observational constraints and this results in sparse coverage of certain regions of parameter space, e.g. metallicity (Hawkins et al., 2016). A lack of reliable calibration stars undermines efforts in constraining several fundamental aspects of astrophysics, e.g. the estimation of stellar ages, which are needed to constrain models for planet (Valle et al., 2016, 2018) and galaxy formation (VandenBerg et al., 2014).

1.2 Effective temperatures

1.2.1 How do we define stellar temperature?

The effective temperature (T_{eff}) of a star is defined as the temperature of a blackbody which emits the same amount of total, or bolometric, flux ($\mathcal{F}_{\text{Bol}}$) as the star as defined by the Stefan-Boltzmann law,

$$\mathcal{F}_{\text{Bol}} = \sigma_{\text{SB}} T_{\text{eff}}^4, \tag{1.1}$$

where σ_{SB} is the Stefan-Boltzmann constant, which is approximately $5.67 \times 10^{-8}\,\text{W m}^{-2}\,\text{K}^{-4}$. It follows that the bolometric luminosity of a star is given by

$$\mathcal{L}_{\text{Bol}} = 4\pi R^2 \sigma_{\text{SB}} T_{\text{eff}}^4, \tag{1.2}$$

where R is the radius of the star, specifically defined as the radius at which the Rosseland optical depth is equal to one (Baschek et al., 1991). As measurements of stellar radii reach better than 1% accuracy, the effect of centre-to-limb darkening of the star becomes non-negligible and a correction from the seismic, interferometric or photometric radius should be made, such as that made for the Sun by Haberreiter et al. (2009).

1.2.2 Common methods to estimate T_{eff}

Most effective temperature estimates in the literature are made using indirect methods, such as photometric or spectroscopic temperature indicators. Here I will give a brief overview of the principles of each of these techniques, and their limitations.

1.2.2.1 Spectroscopic temperature estimates

In general, spectroscopic determinations of effective temperature can give precise values with typical uncertainties of 50 K (Jofré et al., 2019), but these depend considerably on stellar atmosphere models. One of the most popular approaches for estimating temperature with spectroscopy involves measuring the equivalent widths (see Section 2.2.1 for a detailed definition) of metal lines, such as Fe I and Fe II. The T_{eff} can then be determined using the excitation potential, which requires abundances from the same element to agree for all excitation potentials, or the ionisation balance, which requires the abundances from different ionisation stages of the same element (e.g. Fe I and Fe II) to agree (Smalley, 2014). Neutral hydrogen lines are numerous in high-resolution spectra of cool stars, so it is possible to make precise measurements, but many of these lines experience non-LTE effects and so carry an additional error that is not usually accounted for (Bensby et al., 2014). Another spectroscopic method involves fitting the profiles of the Balmer H I lines, which for stars cooler than approximately 8000 K have very little dependence on the surface gravity (Heiter et al., 2002). This method is challenging on two fronts. Firstly, due to the width of the Balmer lines, the continuum of the spectrum must be determined carefully: single-order, medium-resolution spectra are more suitable than échelle spectra (Smalley, 2014). Secondly, a detailed approach to modelling convection is required to reproduce the observed line profiles, making it important to use 3-D models. Finally, global spectroscopic fitting can be performed on spectra (including low-resolution spectra) with least-squares fits or machine learning methods (Valenti & Piskunov, 1996; Wang et al., 2020). This approach can be automated, making it ideal for large surveys such as LAMOST (Xiang

et al., 2015). However, as with all spectroscopic techniques, the quality of the derived spectroscopic parameters relies on the quality of the model atmospheres used to fit them. While it is common to obtain fairly precise estimates of T_{eff} using modern, high-resolution spectroscopy, it is necessary to calibrate and test the results of these techniques using benchmark stars. As we show in Chapter 5, spectroscopic methods can severely under- or over-estimate the fundamental or photometric T_{eff}, even when a conservative uncertainty is given.

1.2.2.2   Infrared flux method

As an alternative to using high quality spectroscopy, effective temperatures are often determined using colour-temperature relations based on the infrared flux method (IRFM; Casagrande et al. 2010). The IRFM, first introduced by Blackwell & Shallis (1977), uses widely available photometry to obtain a relatively accurate T_{eff} by capitalising on the idea that the ratio of the flux in the infrared region to the total flux $F_{\text{IR}}/F_{\text{total}}$ is largely insensitive to the details of models. However, results from this method suffer from uncertainties in interstellar extinction, flux calibrations and stars with anomalous abundances — the variation in T_{eff} values for the same star with different photometry, extinction law or colour-temperature relation is typically $100\,\text{K}$ (Casagrande et al., 2011; Jofré et al., 2019). A recent large-scale characterisation of 186,301 stars in the *Gaia-Kepler* catalog (Berger et al., 2020) found, along with a median catalog uncertainty of $112\,\text{K}$, systematic trends in the temperatures derived for FGK and M stars when compared to results from interferometric direct temperatures. This makes it clear that while photometric temperatures are useful for large samples of single stars with standard photometry, they must be checked and calibrated against direct measurements of T_{eff} to avoid unwanted systematic trends.

1.2.2.3   Direct measurements

The most accurate, model-independent determinations of effective temperature come from a fundamental approach based on the Stefan-Boltzmann law. Rewriting Equation 1.2 in terms of observable quantities, we note that this approach requires measurements of the angular diameter θ and absolute flux as observed at the top of the Earth's atmosphere, $f_{0,b}$:

$$f_{0,b} = \frac{\sigma_{SB}}{4}\theta^2 T_{eff}^4.$$

(1.3)

However, there are few stars for which the necessary data exist and are accurate. Heiter et al. (2015) used interferometric angular diameters along with bolometric fluxes from integrated observed spectral energy distributions to calculate T_{eff} values for a sample of FGK stars to a precision of 1.5% or better. The accuracy of their values of θ and F_{bol} were up to 3% and 5% respectively, corresponding to errors in T_{eff} of 1.5% and 1%, i.e. approximately $100\,\mathrm{K}$ for a solar-type star. This approach is only possible for nearby stars with suitably large angular diameters. Angular diameter can also be inferred from radius measured in an eclipsing binary (EB), along with a parallax. This technique has not been applied much to date because good parallax measurements have not been available for many EBs. For example, Ribas et al. (1998) used a sample of well-studied detached EBs and *Hipparcos* parallax measurements to determine T_{eff} to $1 - 10\%$. The results from this study suffered from uncertainties dominated by *Hipparcos* parallax and bolometric corrections, which were used along with visual apparent magnitudes to obtain bolometric flux.

1.2.3   The effect of T_{eff} uncertainties on derived parameters

Substantial work has already been invested in calibrating the effective temperature scale for FGK-type main-sequence and subgiant stars. The testing and calibration of effective temperature estimates for these stars currently relies on measurements of angular diameter (θ) for nearby stars using interferometry, and estimates of the bolo-

metric flux (F_{bol}). For example, the *Gaia* FGK benchmark sample consists of 35 stars with T_{eff} estimates derived using this approach (Heiter et al., 2015), and is used widely by the community. These stars are very bright, with *V*-band magnitude typically in the range 1-6 (Jofré et al., 2014), which is significantly brighter than the magnitude limits for typical spectroscopic surveys. Since interferometric angular diameter measurements are limited to nearby stars with sufficiently large resolved discs, the sample of stars for which it is feasible to obtain a direct T_{eff} estimate remains quite restricted. Consequently, there are gaps in the parameter space of T_{eff} benchmark samples: cool dwarfs and metal-poor stars are missing. An additional problem comes from the uncertainties present in angular diameter measurements, with repeated measurements of the same star showing variation larger than the quoted errors, often up to $5\,\%$. For the *Gaia* benchmark sample, θ and F_{bol} are measured to $3\,\%$ and $5\,\%$ respectively, corresponding to uncertainties in T_{eff} of $1.5\,\%$ and $1\,\%$, i.e. approximately $100\,\mathrm{K}$ for a solar-type star. Tayar et al. (2022) suggest that this uncertainty is even higher, with current θ and F_{bol} measurements carrying a systematic uncertainty floor in T_{eff} of $2\,\%$, corresponding to $120\,\mathrm{K}$ for a solar-type star. It is therefore important to pursue other ways to determine angular diameters to obtain robust T_{eff} measurements to a higher accuracy and for a more representative sample of stars.

1.3 Eclipsing binary stars

Detached (non-interacting) eclipsing binary stars, DEBs, are extremely powerful tools for observational astrophysics. Besides the Sun and some nearby stars, DEBs are the only way to directly and accurately measure the radii and masses of normal stars without relying on models. These masses and radii can be accurate to better than 0.5%, and provide rigorous observational tests for improving stellar models. DEBs that are also double-lined spectroscopic binaries (SB2s) are the most useful, because we can combine precise photometric and spectroscopic information for both stars. From these measurements, we can deduce other properties of the system, such as distances,

effective temperatures and metallicites, using models and calibrations. These values are often far more accurate than those obtained using single stars. DEBs provide us with a clearer understanding of stellar properties and can provide results, such as a more precise effective temperature scale for solar-type stars. This will be very useful for large–scale spectroscopic studies such as 4MOST, Galah and *Gaia*–ESO.

For a totally-eclipsing DEB, the fractional radii $r = R/a$ of the stars can be derived using the geometry of the light curve alone. Here, R is the radius of the star and a is the orbital semi-major axis. First, we define the quantities δ_1, δ_2 and ϵ shown in Figure 1.3 in terms of features we can measure from the light curve:

$$\delta_1 = \pi(t_4 - t_1)/P \tag{1.4}$$

$$\delta_2 = \pi(t_3 - t_2)/P \tag{1.5}$$

$$\epsilon = \Delta_{tr}/(I - \Delta_{ecl}) \tag{1.6}$$

t_1, t_2 etc. are the contact points of the eclipse and P is the orbital period of the system. Now, the fractional radii $r_1 = R_1/a$ and $r_2 = R_2/a$ are simply expressions of these quantities (Maxted, 2010).

$$r_1 = \frac{1}{2\sqrt[4]{\epsilon}}\sqrt{\sin^2(\delta_1) - \sin^2(\delta_2)} \tag{1.7}$$

$$r_2 = \frac{\sqrt[4]{\epsilon}}{2}\sqrt{\sin^2(\delta_1) - \sin^2(\delta_2)} \tag{1.8}$$

In practice, r_1 and r_2 are measured by fitting models to the observational data, but we know the results are robust as there is a direct relation between these parameters and measurable features of the light curve. Therefore, we have a method for measuring very precise and model–independent radii of DEBs with total eclipses. Other information we can infer from the light curve includes the flux ratio of the two stars, the contribution to the flux from sources external to the binary ("third light"), and the eccentricity and orbital inclination. The curvature in the transit is caused by limb darkening. If a system is not totally eclipsing, the same information can be obtained by fitting a model to the light curve.
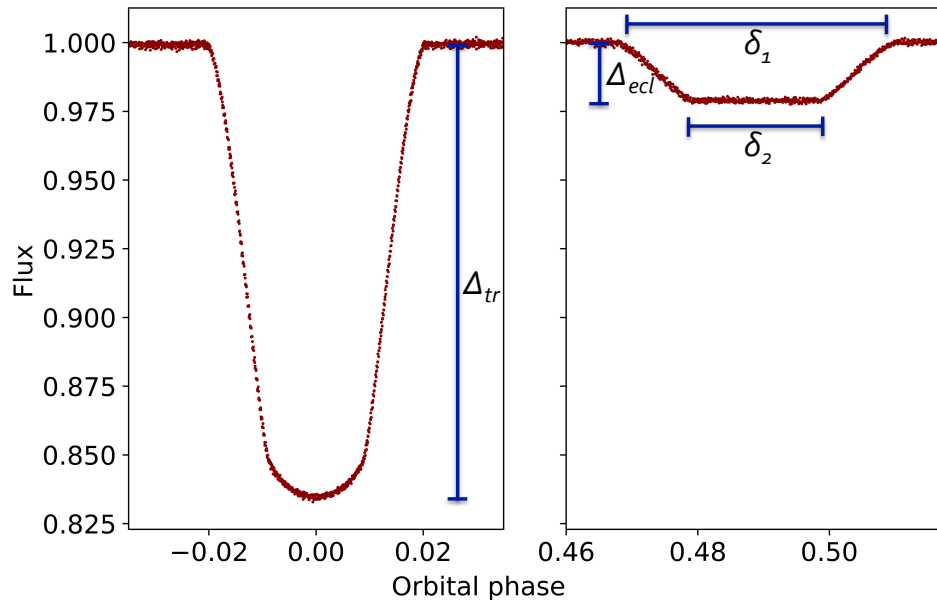
Figure 1.3: *TESS* light curve of HD 50876 centered around primary and total secondary eclipses. Eclipse depth Δ_{ecl}, transit depth Δ_{tr} and quantities δ_1, δ_2 are labelled.

Masses of double–lined (SB2) DEBs are retrieved by measuring the radial velocity of each star from high resolution spectra at multiple orbital phases, and fitting a Keplerian orbit to these measurements. Quantities derived from photometry are often used to constrain results from spectroscopy, and vice versa, to ensure consistency. For SB2 DEBs observed with spectrographs such as HARPS, the value of a can be measured from the spectroscopic orbit to much better than 1%.

The effective temperatures of the stars are usually determined from photometry in multiple band passes, from spectroscopy (maximising the correlation between observed spectra and template spectra) or from disentangled spectra (where the observed spectrum split into two spectra based on the light ratio and stellar lines from each component), though this is less common. Literature effective temperature estimates for DEBs are rather heterogeneous, based on a variety of different photometric systems and calibrations (Torres et al., 2010).

1.3.1   'Detached' eclipsing binaries

Detached eclipsing binaries are of particular importance since they can be used as tests for stellar models for single stars. The definition of a 'detached' binary was first given by Kopal (1955), "The volumes of both components are smaller than those of the largest closed equipotential capable of containing the masses of the two stars (hereafter called the Roche limit) for a given value of their mass-ratio". Consequently, this rules out stars undergoing Roche lobe overflow and mass transfer, and most evolved stars. Along with detached binaries, Kopal (1955) described two other categories: semi-detached, where one component fills its Roche lobe, and contact, where both stars are in contact via the inner Lagrangian point and mass transfer is usually occurring. Typical light curves for detached, semi-detached and contact binaries are shown in Figure 1.4. For the rest of this thesis, I will only consider detached binary systems.

However, if we want to earnestly compare the measured properties of detached eclipsing binary stars to models for single stars, we must impose additional, stricter constraints on the state of the binary. One such constraint is tidal interaction, as we would not expect most single stars to be tidally influenced.

The orbits of binary stars are both predicted and observed to become more circular over their lifetime. This evolution can be split into tidal synchronisation, where the stellar and orbital periods align and the stars become tidally locked, and tidal circularisation, where eccentric orbits become more circular over time due to tidal interaction. Orbital perturbations from exchanges and loss of mass and angular momentum are considered to be dominant factors in the synchronisation and circularisation of binary star orbits, but it is not yet possible to fully predict the timescales from scratch using tidal theory (Ogilvie, 2014). Zahn (1977) sets out the theoretical basis for the timescales over which typical stars with large convective envelopes (such as the Sun) are expected to synchronise and circularise. Their work predicts that for normal stars, there should be a cut-off period for tidal circularisation of about $\sim$8 days (Hilditch, 2001). The steep scaling of $(R/a)^8$ in Equation 4.13 of Zahn (1977) implies that small changes in the primary star radius results in significant changes to the circularisation time. For
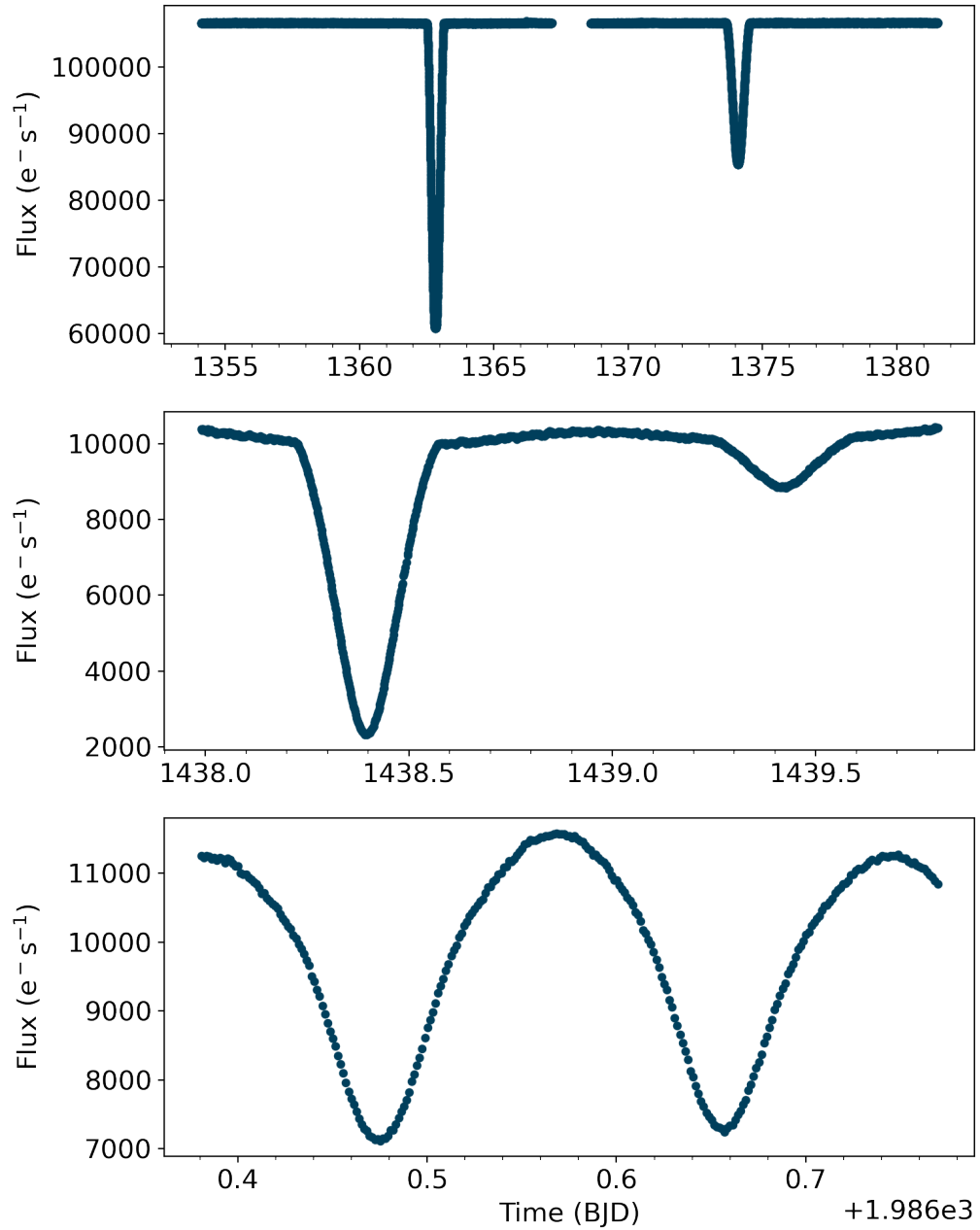
Figure 1.4: *TESS* light curves for examples of detached (AI Phoenicis, upper), semi-detached (TIC 262412046, middle) and contact (TIC 298498697, lower) eclipsing binaries.

binary stars with $P > 10$ days we expect the orbit to circularise rapidly when the primary starts evolving. Assuming the circularisation timescale is short compared to the evolution timescale along the subgiant and giant branches, the circularisation period for a sample of stars correlates with the radius or evolutionary state of the primary components.

Observational studies of eclipsing binary stars have given insight into the relationship between orbital period and eccentricity. An early study was performed by Mayor & Mermilliod (1984), who noted an significant transition from circular orbits for main-sequence stars at an orbital period of 5.7 days. Torres et al. (2010) find no eccentric systems with an orbital period less than 1.5 days. Studies of large-scale samples of eclipsing binary stars observed with modern instrumentation, e.g. *Kepler* (Kjurkchieva et al., 2017), APOGEE (Price-Whelan & Goodman, 2018) and *TESS* (Justesen & Albrecht, 2021) show similar trends. Figure 1.5 shows binaries from Torres et al. (2010), Kjurkchieva et al. (2017), and Justesen & Albrecht (2021).

While the circularisation trends depend on several variables such as age and effective temperature, a general rule-of-thumb that main-sequence binary systems with orbital periods greater than 10 days are suitable for use as calibration stars for single-star models.

1.3.2 EBs as benchmark stars

The seminal papers by Popper (1980), Andersen (1991) and Torres et al. (2010) established the potential of detached eclipsing binary stars as powerful astrophysical tools. Some applications explored include testing stellar evolution models using the constraint that a single model should be able to fit both stars in a binary with a single age, distance and composition; calibrating stellar model parameters such as the convective core overshooting parameter and mixing length parameter; and investigating effects such as tidal interaction and apsidal motion in binaries. Stars in binaries which can be considered sufficiently detached are particularly valuable tests for stellar models, as the mass and radius are known to a level of accuracy not usually possible for single
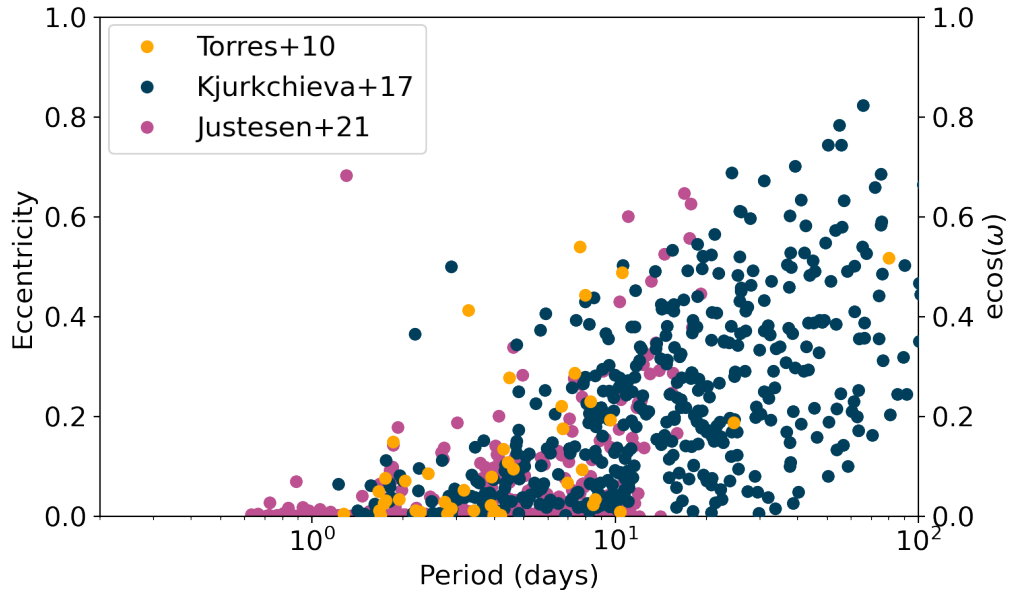
Figure 1.5: Orbital period versus eccentricity (Torres et al. 2010 and Kjurkchieva et al. 2017) and $e \cos \omega$ (for Justesen & Albrecht 2021) for eclipsing binary stars.

stars. Unfortunately, the accuracy of the effective temperature estimates for such stars is falling behind, so work is required to improve measurements of T_{eff} to make DEBs even more valuable benchmarks. In Section 10 of their paper, Torres et al. (2010) makes the motivation for focusing efforts on improving the estimates of T_{eff} for stars in binaries clear:

> "T_{eff} is a key parameter in all discussions of stellar and Galactic evolution, directly affecting the location of a star in the HR diagram and the use of a star to determine distances to other galaxies or age scales of galactic populations. Given the current disagreement between several spectroscopic and photometric temperature scales (see, e.g., Holmberg et al. 2007 for a detailed discussion), improvement of the T_{eff} scale via additional accurate angular diameter and flux measurements is the most urgent priority. In the process, the interstellar reddening must be carefully determined for both programme stars and calibrators."

In addition to stellar models, stellar spectroscopy, either performed by large surveys (e.g., RAVE (Steinmetz et al., 2020), SDSS (Abdurro'uf et al., 2022), LAMOST

(Deng et al., 2012), Gaia-ESO (Gilmore et al., 2012), APOGEE (Majewski et al., 2017), GALAH (Buder et al., 2018), the upcoming WEAVE and 4MOST) or on an individual basis, needs a reliable $T_{\rm eff}$ scale with which to calibrate stellar parameters. In these large surveys, data-driven approaches and machine learning methods are increasingly being used for the analysis. These are trained and calibrated on data with classical determinations of parameters. There is no physics in these data-driven methods so they must use benchmark calibration stars to establish how features in the data relate to astrophysical quantities, such as $T_{\rm eff}$. There is therefore an urgent need for improved measurements of effective temperature for a large, representative sample of stars.

1.4   Goals of the thesis

The work I have carried out during my PhD has been to serve the following three goals: (1) To develop a new method to measure fundamental effective temperature for FGK-type stars in detached eclipsing binary systems; (2) to begin work towards creating a homogeneous sample of stars with very accurate and precise measured stellar properties; (3) to develop a custom scheduler code to support the Xamidimura project, which also aims to improve the characterisation of eclipsing binary stars by observing systems in multiple optical bands during eclipse.

In Chapter 2 I describe the methods I used in my thesis work to develop the temperature method, along with other methods used throughout the thesis, for example for characterising the eclipsing binary system CPD-54 810 using photometry and radial velocities. In Chapter 3 I present my work on developing the scheduler program for the Xamidimura instrument, from selecting a suitable approach to implementing and optimising the algorithm to maximise the number of completed light curves. In Chapter 4 I present the application of the temperature method to our first system, the well-studied F7 V + K0 IV binary AI Phoenicis, for which we were able to obtain very accurate measurements for effective temperature that are an order of magnitude better than previous measurements. In Chapter 5 I present the second application of

the temperature method to a much less well-studied binary CPD-54 810, for which I also performed a re-analysis of the light curve and radial velocities to obtain robust results for all physical properties. For CPD-54 810, despite much fewer data, we still achieve a significant improvement in effective temperature for both stars. In Chapter 6 I present the third system we applied the temperature method to, EBLM J0113+31. This publication was led by Dr Pierre Maxted so I outline my contributions to the work in Chapter 6. Finally in Chapter 7 I summarise the current status of the temperature method and present a selection of eclipsing binary systems that would be suitable next targets for my work.

2 Methods

Standing on a remote mountain with the earth stretching out into the distance and slowly spinning away from our nearest star, it's a wonderful quiet moment to enjoy the vastness and stillness and colors as the night begins. On any given evening, I can promise you that scattered across the planet are a few small groups of astronomers, standing on dome catwalks or dining hall patios or even just a stretch of hard-packed earth and pausing in their work for a few moments to admire the simple beauty of the sky.

Emily Levesque, *The Last Stargazers: The Enduring Story of Astronomy's Vanishing Explorers* (2020)

2.1 Photometry

Photometry is a technique used to measure the flux arriving from a star or other astronomical object in a well-defined passband at the top of the Earth's atmosphere, either in absolute units are in a relative sense. Images of a star in optical light (i.e. ultraviolet, visible and infrared) can be obtained using a charge-coupled device (CCD) attached to a telescope. Images are often taken through a filter, which restricts the photons measured by the CCD to a specific wavelength range. Before any measurements are taken, effects from the instrumentation that might affect the results are accounted for by taking and applying calibration images. 'Dark' frames are taken with the same settings as the 'light' frames but with the camera shutter closed, and highlight any thermal gradients or hot pixels present in the images. 'Bias' frames are taken with the shortest possible exposure time and the camera shutter closed, and highlight electronic (readout) noise. 'Flat' frames are images of a uniformly lit surface, e.g. the sky at twilight, and highlight parts of the frame that are not uniformly lit, such as stray light or dust on the optics. Dark and bias frames may be taken in separate images or together, and are subtracted from the light frame, while the light frame is divided by the flat frame (or average of several flat frames).

The brightness of a star may be measured from the raw image using a technique called synthetic aperture photometry. Here, an aperture is defined around the star (usually a circle), and the number of photons within the aperture is measured. The intensity of the image background must also be accounted for. This is often done by defining an annulus around the aperture or a region on the image without stars, measuring the count rate of this region. This can be difficult for crowded fields, as contamination of the background aperture by stars can lead to an underestimation of the corrected counts for the star. For crowded fields, fitting a point spread function (PSF) to the star is an alternative to aperture photometry. The target signal, corrected for background, is converted to an instrumental magnitude using the formula

$$m_{\mathrm{inst}} = -2.5 \log_{10}(N/t_{\mathrm{exp}}),$$

where t_{exp} is the exposure time of the image.

To bring an instrumental magnitude onto a standard scale such that measurements from different times, telescopes and sites can be compared, the observed instrumental magnitude should be converted to its value as if it were measured above the Earth's atmosphere. This is done by applying a correction for the atmospheric extinction using a coefficient k that is specific to a site and passband, and a function of airmass $X(Z)$:

$$m_0 = m_{\mathrm{inst}} - kX(Z).$$

A zero-point correction m_{zp} specific to the instrument is then applied:

$$m = m_0 - m_{\mathrm{zp}}.$$

Unfortunately, the equipment used by any two astronomers will produce a different photometric response, and most likely different to the one used to establish the standard system. Therefore, if precise photometric measurements (1% or better) are required, observations of the colours of standard stars can be used to introduce an additional corrective term (Padmanabhan et al., 2007). Space-based observatories avoid the complications of the Earth's atmosphere and so can produce photometry that is more precise and accurate than is possible from the ground.

In contrast to absolute photometry, differential or relative photometry can be used when monitoring changes in brightness are prioritised over measuring a precise absolute flux. Here, the counts from the target are compared to non-variable stars within the field. Since images of the target and comparison stars are taken under the same conditions, the effects of atmospheric extinction on the relative magnitude can be ignored.

2.1.1 AB magnitudes

The AB magnitude system introduced by Oke (1965); Oke & Gunn (1983) defines its relative absolute magnitude as

$$AB_\nu = -2.5 \log f_\nu + 48.60, \tag{2.1}$$

where f_ν is the monochromatic flux in measured in frequency units, i.e. erg cm^{-2} s^{-1} Hz^{-1}. f_ν may be converted to f_λ in wavelength units (erg cm^{-2} s^{-1} Å^{-1}) via

$$f_\nu = f_\lambda \frac{\lambda^2}{c}, \tag{2.2}$$

where c is the speed of light in cgs units. The system is calibrated to the absolute flux of Vega at 5480 Å, and the uncertainty of this measurement should be accounted for as a systematic uncertainty in the observations and derived quantities using AB magnitudes. The AB magnitude system is particularly useful for performing synthetic photometry, which is the process of measuring magnitudes or colours in a specific photometric band using an observed or model spectrum. The mean flux in a photometric band is

$$\langle f_\lambda \rangle = \frac{\int f(\lambda) S(\lambda) \lambda d\lambda}{\int S(\lambda) \lambda d\lambda}. \tag{2.3}$$

Here, $S(\lambda) = R(\lambda)\eta(\lambda)$ is the system response function, combining the filter response profile $R(\lambda)$ with the quantum efficiency of the detector $\eta(\lambda)$ (Bessell & Murphy, 2012). A useful quantity is the pivot wavelength λ_p, which allows direct conversion between the mean fluxes $\langle f_\nu \rangle$ and $\langle f_\lambda \rangle$ in any particular band (Bessell & Murphy, 2012):

$$\langle f_\nu \rangle = \langle f_\lambda \rangle \frac{\lambda_p^2}{c}, \tag{2.4}$$

where

$$\lambda_p = \sqrt{\frac{\int S(\lambda)\lambda d\lambda}{\int S(\lambda)/\lambda d\lambda}}. \tag{2.5}$$

A major part of my thesis work involves using model spectra to generate synthetic magnitudes in various photometric bands. Therefore, all magnitudes and colours I use, from catalogues or observed as part of the project, needed to be converted to the AB magnitude system.

2.1.2 Photometric systems

I have used magnitudes, colours and time-series photometry that were measured in a variety of photometric systems in my work in Chapters 4, 5 and 6. A photometric system defines a set of standard bands and standard stars, and is usually selected or created to achieve a specific set of scientific goals. Each band in a photometric system has a response function, which defines the amount of light that is measured across the wavelength range, and a pivot or effective wavelength λ_{eff}. A wide range of photometric systems have been devised over the years: see Bessell (2005) for a detailed review. Broad-band systems typically employ photometric passbands that are wider than approximately 300 Å, intermediate-band systems tend to be 100-300 Å wide and are placed to maximise information on stellar properties, and narrow-band systems are typically a few tens of Å wide and placed to measure specific spectral features. Some of the systems used in my work are described here and the corresponding filter response profiles (transmission as a function of wavelength) are shown in Figure 2.1.

2.1.2.1 Ground-based photometry

The Johnson-Morgan *UBV* system was originally designed to cover the wavelength range between the atmospheric cutoff in the ultraviolet, and the red limit of the photoelectric detector used to develop the system (Johnson & Morgan, 1953). More photometric bands were added to the system over time, including R and I bands. The

precise photometry of standard stars by Cousins (1976) in the R_C and I_C bands eventually led to the standard practice of Johnson R and I being replaced by Cousins R_C and I_C, and hence the widely-used Johnson-Cousins $UBVRI$ system.

The Strömgren $uvby\beta$ system (Strömgren, 1951, 1966; Crawford, 1958) is an intermediate-band system that is optimised to measure several spectral features of A, F and G-type stars, but was later expanded to other spectral types. Four indices are commonly derived from Strömgren photometry: $(b-y)$ is sensitive to T_{eff} and measures the Paschen continuum, $m_1 = (v-b) - (b-y)$ measures the depth of the depression caused by metal lines around $4100\,\text{Å}$, $c_1 = (u-v) - (v-b)$, which measures the Balmer jump, and $\beta = \beta_w - \beta_n$ which uses a wide ($\Delta\lambda = 150\,\text{Å}$) and narrow ($\Delta\lambda = 30\,\text{Å}$) band centered around the Hβ line to measure its strength.

The SkyMapper $uvgriz$ system is a hybrid broad/intermediate-band system, modified from the broad-band SDSS $ugriz$ system. The SDSS bands were designed for measuring photometric redshift of galaxies, rather than stellar features, but the SkyMapper system (Bessell et al., 2011) redefines the u and g bands to maximise information on stellar properties, and inserts an additional band, v. The u band is sensitive to effective temperature (for hot stars) and surface gravity (for A, F, G stars), and the v band is sensitive to metallicity.

The 2MASS JHK_s system is the photometric system used by the Two-Micron All Sky Survey (2MASS; Cohen et al. 2003; Skrutskie et al. 2006). It is similar to the Mauna Kea Observatory system introduced by Tokunaga et al. (2002), which improved upon the original infrared Johnson-Glass system (e.g. Johnson 1966; Glass 1973). The photometry from the Johnson-Glass system suffered from variability in atmospheric H_2O absorption at the edges of the original JHK bands (Simons & Tokunaga, 2002).

Some instruments are optimised for time-series photometry, such as the Wide-Angle Search for Planets (WASP) instrument (Pollacco et al., 2006) and *TESS* mission (Ricker et al., 2014b), and use very wide photometric bands in order to capture the maximimum signal from the source of interest. These systems are less suitable for absolute photometry than the systems discussed above, so in my work I use WASP and *TESS* data primarily for measuring the timings of eclipses and flux ratios ℓ.
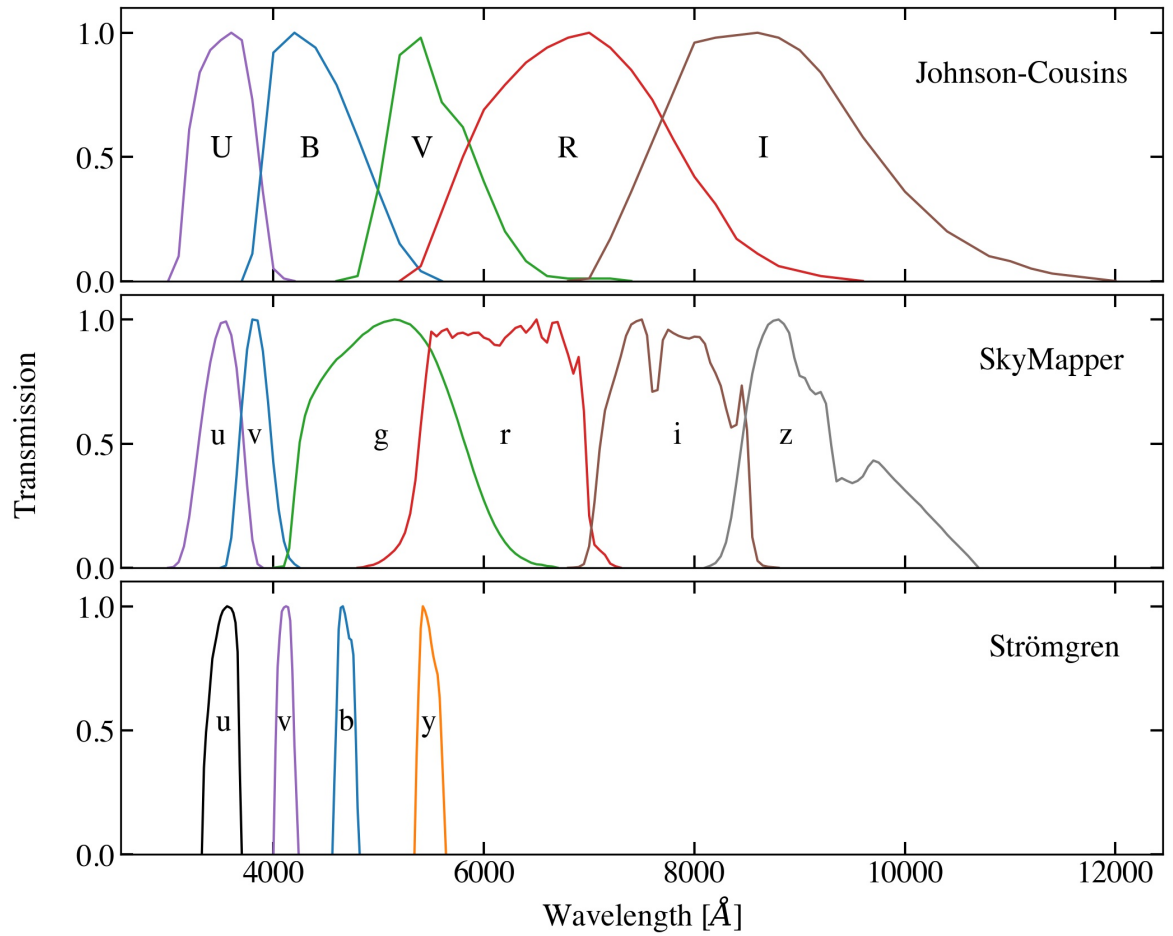
Figure 2.1: Normalised filter response profiles for different photometric systems in visible and near-infrared wavelengths.

2.1.2.2   Space-based photometry

The *Gaia* system consists of three broad photometric bands, with BP in the blue, RP in the red, and the G band encompassing both of these (Gaia Collaboration et al., 2018, 2021a). $BP - RP$ is frequently used as a colour index and temperature indicator, while G can be used in combination with the distance moduli to construct a Herzsprung-Russell diagram for the entire *Gaia* catalogue. The goals of *Gaia* required a system that allows classification of a wide range of stars, so encompassing a wide wavelength range was necessary to achieve these goals.

      The *GALEX* system comprises of a far-infrared FUV band and a near-infrared NUV band, selected to study the evolution of star formation in galaxies via an all-sky survey (Martin et al., 2005). The calibration of the *GALEX* photometry is tied to the *Hubble Space Telescope* system, which is based on the reference spectroscopy of the CALSPEC standard stars (Bohlin et al., 2001).

      The *WISE* system was designed for the Wide-field Infrared Survey Explorer (*WISE*; Wright et al. 2010), which carried out an all-sky survey in the mid-infrared range. The bands were chosen to achieve the mission goals of finding cool brown dwarfs, ultra-luminous infrared galaxies, characterising red active galactic nuclei, finding asteroids in the Solar System and more.

2.1.2.3   Response functions for the PEST Observatory

As part of my work on CPD-54 810 in Chapter 5, I was required to construct a response function for the photometric bands used in our time-series observations with the Perth Exoplanet Survey Telescope[1]. The response function is required by the `teb` code to transform magnitudes to a common system (see Section 2.6). PEST uses an SBIG ST-8XME camera and Astrodon B, V, Rc, Ic filters so I retrieved information on the quantum efficiency (QE) of the camera and transmission efficiency of the filters from the manufacturers. The response function for the overall system is then constructed

---

[1]http://pestobservatory.com/
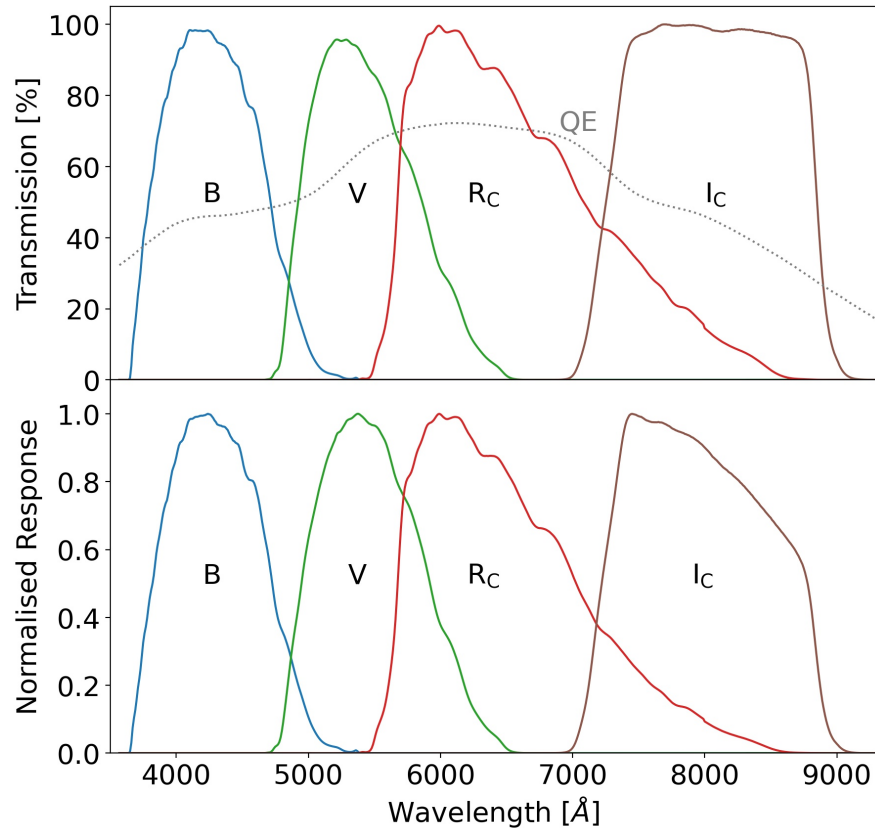
Figure 2.2: Filter response and detector quantum efficiency for PEST (upper panel), and normalised system response functions (lower panel).

by multiplying the QE and filter response, then normalising. The resulting response functions for PEST are shown in Figure 2.2.

2.1.2.4   Zero-point corrections

The calculation of the zero-point for some photometric systems is not perfect, and can lead to an offset between the observed magnitudes of standard stars and synthetic magnitudes generated from calibration spectra such as those from the CALSPEC database (Bohlin et al., 2014). Therefore it is beneficial to check both the literature and the data itself for possible zero-point offsets, especially when the magnitude of the target

is not in the optimised range for the instrument.

GALEX photometry. Calibrations for *GALEX* magnitudes are based on white dwarfs, which have a very different spectrum to FGK-type stars, therefore it is not clear if these calibrations are representative of the typical errors on *GALEX* flux. For our DEBs, a significant portion of the total flux falls in the near-ultraviolet region, so if we use observations in the *GALEX NUV* band it is important to get the zero-point correct. Camarota & Holberg (2014) evaluated the absolute calibration of *GALEX* fluxes using white dwarfs and found there to be a moderate departure from predicted magnitudes, particularly for brighter stars. They proposed that this can be addressed with empirical quadratic corrections. Similarly, Wall et al. (2019) used 1837 DA WDs to verify the *GALEX* absolute flux calibrations and found a more significant offset for brighter stars than fainter stars. They proposed a linear correction to be applied to stars with *NUV* magnitudes greater than 16.95. For AI Phe we found a sample of FGK dwarf stars with both *GALEX* magnitudes and CALSPEC (Bohlin et al., 2014) spectra and compared these observed *NUV* magnitudes with those calculated from CALSPEC. However, the scatter of these few points around the observed magnitude of AI Phe was too large to make a confident assessment of the reliability of the zero-point. We chose not to include the *GALEX NUV* magnitude in our analysis of AI Phe because we had access to alternative UV observations from the *IUE* satellite. However, for CPD-54 810 we had no choice but to find a way to include the *GALEX NUV* photometry, so we inspected the white dwarf calibrators with observed and synthetic (from *IUE* spectra) magnitudes in Table 4 of Camarota & Holberg (2014) and calculated the mean $O - C$ offset of the WDs within $1\,\mathrm{mag}$ of the target observed magnitude in both *NUV* and *FUV*: see Figure 2.3. This offset and the mean absolute deviation of the points about this mean were added in quadrature to the *GALEX* AB magnitude zero-points.

SkyMapper *uv* photometry. Due to the lack of photometry available for CPD-54 810, we chose to include some additional magnitudes from the SkyMapper DR2 catalogue (Onken et al., 2019) to populate the wavelength region between the *GALEX NUV* band and *Gaia BP* band. We chose to inspect the zero-points for these data as there is a known issue causing 5% and 10% *rms* in the u and v bands
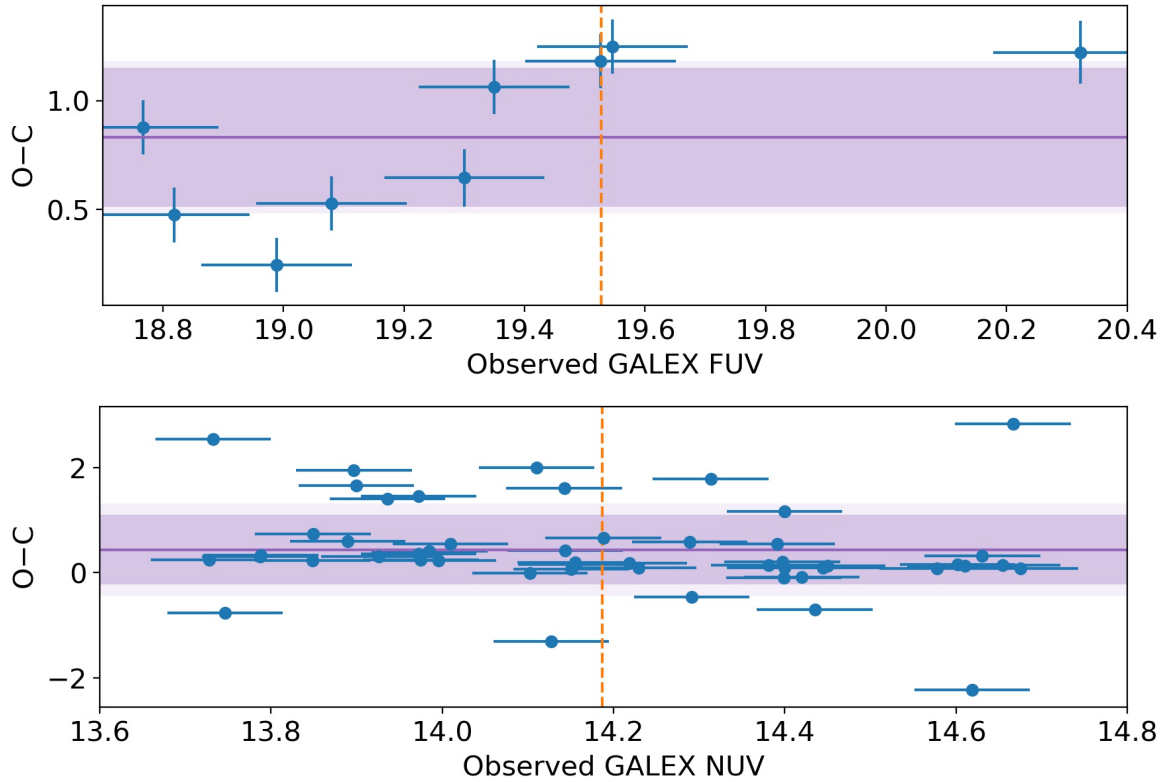
Figure 2.3: Offset between a sample of observed and synthetic *IUE* magnitudes for white dwarf calibration stars in *GALEX FUV* (upper panel) and *NUV* (lower panel) bands. The observed *GALEX* magnitude of CPD-54 810 is shown as the vertical dashed line, the mean offset as a horizontal line and the mean absolute deviation (dark shading) and standard deviation (light shading) about the mean. Data taken from Table 4 of Camarota & Holberg (2014).
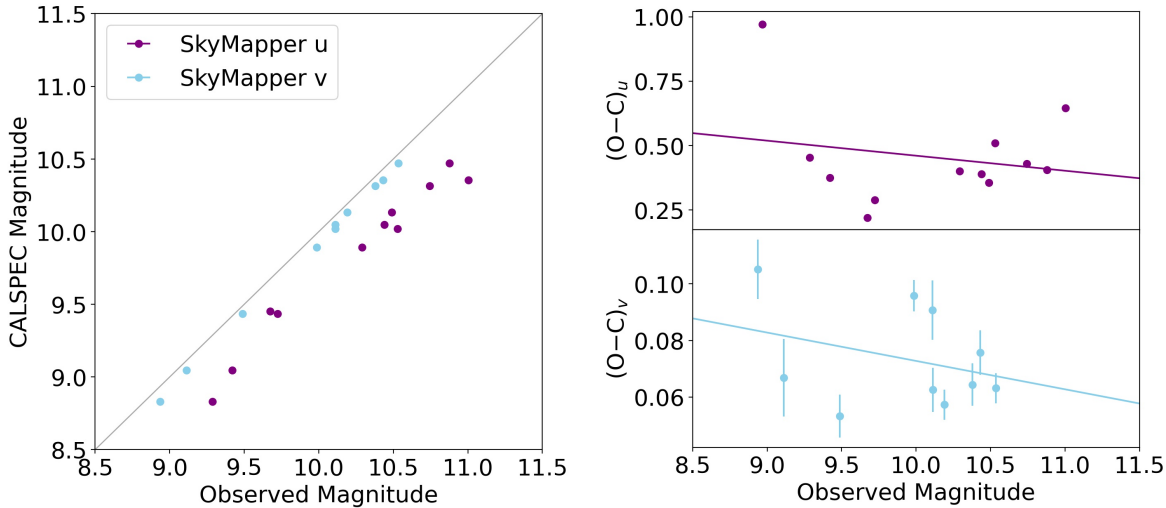
Figure 2.4: Comparison of observed SkyMapper and synthetic uv magnitudes obtained from CALSPEC reference spectra.

respectively, along with a red leak in the u band[2]. The SkyMapper magnitudes are on the AB magnitude system, so by definition have a standard zero-point of -48.6 mag. SkyMapper photometry experiences an approximately 0.1 mag nightly scatter, so I account for this in the uncertainty of the zero-points. I cross-matched the SkyMapper DR2 catalogue with the CALSPEC database, excluding white dwarfs, O-type and M-type stars and stars with large rotational variability to compile a sample of stars with SkyMapper uv photometry and CALSPEC reference spectra. Using these spectra, I calculated the synthetic magnitude in each band for each star, and the comparison of observed to synthetic magnitudes for the sample can be seen in Figure 2.4. Since there is a magnitude-dependence on the offset from zero, I generated a linear fit to the difference between observed and CALSPEC magnitudes for each band. The specific zero-point correction is then derived from an interpolation or extrapolation to these linear fits to the observed magnitude of the target.

Strömgren photometry. For our analysis of AI Phe in Chapter 4, we needed

---

[2]`https://skymapper.anu.edu.au/known-issues/5/`

to create zero-points for the colour indices from Reipurth (1978) and Holmberg et al. (2009) in order to be able to calculate synthetic colours as part of our T_{eff} analysis. For this we found stars with CALSPEC reference spectra that also have Strömgren photometry from the Geneva-Copenhagen Catalog III (Holmberg et al., 2009) to construct synthetic $(b - y)$, m_1, c_1 indices and compare them to the observed indices. The mean and standard deviation of the $O - C$ offset were then used as the zero-point and error.

2.2 Spectroscopy

Spectroscopy is a powerful tool in astrophysics for analysing the light emitted by stars. Analysing the strengths, shapes, velocities, and splitting of atomic and molecular lines can reveal a vast amount of information about the properties and environments of stars.

The spectral class of a star is determined by the features of its spectrum, such as the strength of the hydrogen Balmer lines. The wavelength shift of a spectral line from its rest wavelength gives information on its radial velocity, which can be used to infer spectroscopic orbits of binary stars, discover planets around stars, and measure the redshift of distant stars. Observed spectra can be compared to synthetic spectra generated using theoretical stellar atmosphere models and atomic line lists, to provide information on their physical properties such as effective temperature and surface gravity, along with stellar rotation from line profiles and the presence and strength of magnetic fields from the splitting of lines. The presence of certain absorption lines associated with interstellar dust and gas in stellar spectra can be used to estimate the amount of reddening between the star and the observer.

Spectral classification and estimates of a stars effective temperature can be done using spectra of moderate resolution, but detailed measurements require high resolution spectra. The resolving power $R = \lambda/\Delta\lambda$ used for these purposes is typically $R = 40,000$ and higher. The higher the resolution, the longer it takes to achieve a useful signal-to-noise ratio, so there are some trade-offs involved in selecting the most suitable

instrument and mode.

The work on spectroscopy I carried out for this thesis involved using the high-resolution ($R \sim 48,000$) FEROS échelle spectrograph (Kaufer et al., 1999). In this section I will describe the methods I used in analysing these spectra in more detail than in Chapter 5.

2.2.1 Interstellar reddening from equivalent widths

Space is not truly a vacuum, so when observing stars other than the Sun, we must account for the effect of the interstellar medium in our observations. This is particularly important for photometric studies such as in this thesis: interstellar dust and gas absorbs and scatters radiation, predominantly affecting bluer light. Absorption and scattering of light by the interstellar medium causes the observed light from the star to appear more red – hence the term "reddening". Reddening is often characterised as extinction as a function of a photometric colour, usually $E(B-V)$.

The interstellar extinction can be estimated for any star using either dust maps (e.g. Schlafly & Finkbeiner 2011, Schlegel et al. 1998, Lallement et al. 2014) as a function of position on the sky and distance, or by using observations and some theoretical or empirical law relating the observed characteristic and $E(B-V)$. The stars we study in this thesis are quite nearby, so it feasible to use either method. However, dust maps carry a relatively large uncertainty, and for our stars we prefer to place an upper limit on (or estimate) the $E(B-V)$ given the notable lack of spectroscopic absorption features in the high resolution spectra of these systems.

Munari & Zwitter (1997) described a method to estimate the amount of interstellar reddening experienced by a particular star by measuring the equivalent width of the sodium D I line ($\text{EW}_{\text{D I}}$), which is an absorption feature associated with the interstellar medium. The approach has been used by subsequent works, such as Poznanski et al. (2012), who use an empirical method to relate $\text{EW}_{\text{D I}}$ with $E(B-V)$. In our studies of AI Phoenicis, CPD-54 810 and EBLM J0113+31 we chose to use the relation from Munari & Zwitter (1997) but note that the number of systems included in their work

with low reddening is quite small and future studies to update their sample would be valuable for our work going forward.

The equivalent width is a measure of the quantity of light cut out from the continuum of a star by an absorption line. Geometrically, the equivalent width is the area of the absorption line under a normalised continuum. It is mathematically defined as,

$$W = \int_{\lambda_1}^{\lambda_2} \frac{F_c - F_\lambda}{F_c} d\lambda. \tag{2.6}$$

When measuring the equivalent width of Na I D_1, I modelled the profile of the line as a Gaussian, and fitted the Na I D_1 line with Gaussians across a grid of rest wavelengths across a range corresponding to the $25\,\mathrm{km/s}$ mean velocity of local clouds from Frisch et al. (2011). The mean and standard deviation of these fits was then used in the relation from Munari & Zwitter (1997):

$$W = \alpha \sum_{n=1}^{\infty} (-1)^{n-1} \frac{(\beta E(B-V))^n}{n! \sqrt{n}}. \tag{2.7}$$

I used a Bayesian model to find the posterior probability distribution of $E(B-V)$ letting α and β be free parameters with prior probabilities of $\alpha = 0.354 \pm 0.01, \beta = 11.0 \pm 1.0$ informed by the calibrations of these parameters by the authors.

2.2.2   Spectral synthesis

In order to compare an observed spectrum to a template, we must first generate the template. Except in the case of a spectrum being taken during a total eclipse, the spectra of binary stars contain light from both components. Therefore, for CPD-54 810 we needed to generate two synthetic spectra, shift each in velocity space to match the observed lines, and co-add them. `iSpec`[3] (Blanco-Cuaresma et al., 2014b; Blanco-Cuaresma, 2019) provides useful functions to do this in `Python`. A comparison of the synthetic and observed spectrum for CPD-54 810 is shown in Section 5.6.

---

[3]`https://www.blancocuaresma.com/s/iSpec`

2.2.3   Metallicity from line depths

The metallicity, specifically the ratio [Fe/H], of a star is often measured using the strength of the iron lines. In the high-resolution spectroscopy of FGK-type stars, Fe I and Fe II lines are far more numerous than other elements and hence by using iron lines, the precision of the derived [Fe/H] is as high as it can be. [Fe I/H] is typically more precise than [Fe II/H] since there are typically more Fe I lines present in the spectrum. The accuracy of the measurements depend on line selection, atomic line lists, spectrum normalisation, and calibration of the temperature and surface gravity for the template spectrum used to make the measurement. Results may also vary depending on the technique used to measure the line strength: comparison to a synthetic spectrum, or fitting the equivalent widths.

For CPD-54 810, we decided it was important to re-measure the metallicity as part of the work on measuring the T_{eff} for both components, to ensure we had results that were self-consistent. We chose to use a list of "good", i.e. moderately strong lines without blending, from Doyle et al. (2017), as our reference [Fe/H] lines to measure. With the high-resolution combined spectrum we had of the system, we chose to generate a grid of synethetic spectra with different metallicities to compare the line depths with. Some example lines with synthetic spectra with are shown in Figure 2.5. The results obtained for [Fe/H] using this method are described in Chapter 5.

2.3   Parallax

The relation between trigonometric parallax angle ϖ in arcseconds and distance from the Sun d in parsecs is defined by $d = 1/\varpi$. In my work on measuring T_{eff} in Chapters 4, 5 and 6, I use parallax to calculate the angular diameters of the stars: $\theta = 2R\varpi$. Parallax is typically measured using astrometry, the motion of stars on the sky, using the baseline of the Earth's orbit. In recent years, the *Gaia* satellite has revolutionised astrophysics, measuring the positions and brightnesses of over a billion stars in the
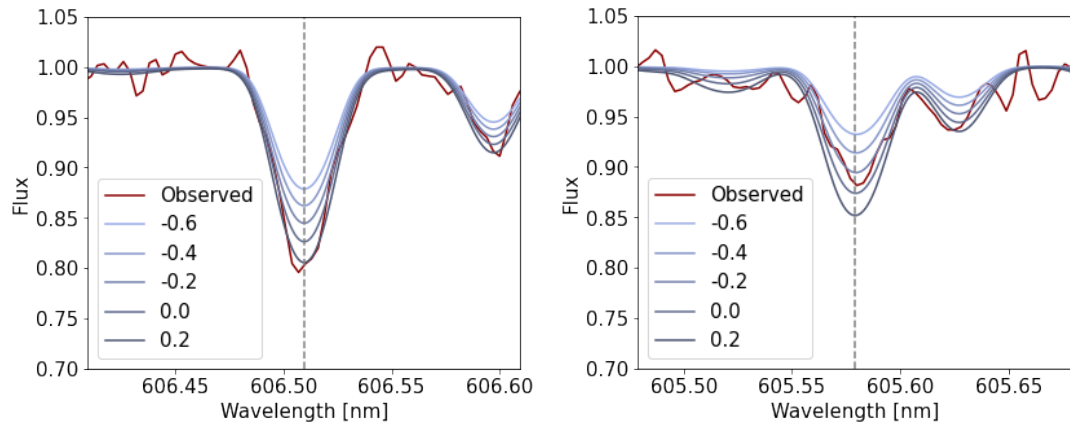
Figure 2.5: Two examples of the synthetic spectrum grids used to estimate [Fe/H] for CPD-54 810. The rest wavelength for each Fe line is shown as a dotted vertical line.

Galaxy to a high precision (Gaia Collaboration et al., 2018, 2021a).

2.3.1 *Gaia* DR2

For AI Phe, the most recent source of a parallax measurement, at the time I did this study, was *Gaia* DR2. A number of studies have independently verified the parallaxes measured by *Gaia* to test for any systematic offsets in the zero-point of the catalogue. For example: eclipsing binaries via surface brightness–colour relations (Graczyk et al., 2019) and bolometric luminosity estimates (Stassun & Torres, 2018), Cepheid variables (Riess et al., 2018) and very long baseline interferometry (Xu et al., 2019). In our analysis of AI Phe we chose to use the zero-point offset measured by Graczyk et al. (2019), which agrees with the DR2 astrometric solution (Lindegren et al., 2018).

A potential concern with using parallaxes from *Gaia* pre-DR3 for binary systems is that the photocenter motion, i.e. the motion of the combined light of the binary system throughout its orbital period, will impact the measured parallax value as it is not explicitly accounted for in DR2. Graczyk et al. (2019) calculated the photocenter motion for their sample of 81 eclipsing binaries and compared these to the errors in ϖ from *Gaia* DR2. They find that the photocenter motion is much smaller than errors in

parallax for the overwhelming majority of these systems, and comment that the *Gaia* DR2 parallaxes are "practically unaffected by binarity". For AI Phe, the independent parallax measurement by Gallenne et al. (2019), using interferometry to measure the apparent separation of the stars and the actual separation from the spectroscopic orbit, agrees with the *Gaia* value.

2.3.2 *Gaia* EDR3

For CPD-54 810 and EBLM J0113+31 we used parallax measurements from *Gaia* EDR3. Like with DR2, a number of studies tested the systematics of the catalogue using a variety of techniques. Lindegren et al. (2021b) propose a corrective function based on observations of extragalactic objects such as quasars and active galactic nuclei, although this may not be a suitable calibration for brighter, nearby stars. Flynn et al. (2022) uses bright ($G < 12$) stars in open and globular clusters to establish an additional correction to the parallax based on $BP - RP$ colour. This proposed correction is supported by measurements of Cepheids (Riess et al., 2021), and red giant branch stars (Zinn, 2021). Therefore we use this correction to the parallax zero-point for CPD-54 810 and EBLM J0113+31.

2.4 Bayesian methods

Bayesian statistics view the probability as the degree of belief in an outcome, given prior knowledge. Review papers giving a detailed description of Bayesian methods in astrophysics already exist, such as those by Sharma (2017) and Parviainen (2018), so I will only give an brief overview of the subject here. Suppose we want to evaluate the best parameters for a model that is describing some data. We frame this problem in terms of a set of model parameters, M, and the data, D, so that the posterior probability distribution (PPD) is

$$P(M|D) \propto P(D|M)P(M), \tag{2.8}$$

where $P(M)$ is the prior probability distribution for M and $P(D|M)$ is the likelihood function $\mathcal{L}$. Priors are particularly important components of the Bayesian approach. They allow us to constrain the 'allowed' region of parameter space to a much smaller range than allowed by $\mathcal{L}$ alone by considering our current knowledge of the parameters. The likelihood $P(D|M)$ is calculated for the case of independent Gaussian random variables. It is often useful to express the likelihood in logarithms, as this makes it easier to combine different aspects of the data into a single likelihood.

Monte-Carlo (MC) methods are a complementary technique to Bayesian statistics, used to sample the PPD. Often, correlations between model parameters will not be uniform Gaussian distributions, or even well-behaved analytical functions, so it is necessary to use sampling to generate a large sample of points drawn from the PPD. Markov chain Monte Carlo (MCMC) is an algorithm designed to efficiently sample PPDs in multiple dimensions. MCMC draws a set of random values (samples) for each model parameter in such a way that only depends on the current values (creating a 'chain'). MCMC algorithms typically use a Metropolis-Hastings algorithm (Metropolis et al., 1953; Hastings, 1970) for sampling. At each step of the chain, a proposed new value θ' is selected from a distribution (often a multi-variate Gaussian; see Sharma 2017). The ratio between the probabilities of the new value $P(M(\theta')|D)$ to the current value $P(M(\theta)|D)$ is compared to a random number between 0 and 1. The proposed new step is accepted if the ratio is greater than the random number, otherwise the new step is rejected and $\theta' = \theta$. This approach means that the chain will tend to converge towards parameter values that have higher probabilities.

In my thesis, I use emcee (Foreman-Mackey et al., 2013), a Python implementation of an affine-invariant MCMC ensemble sampler, to calculate the PPD of the model parameters. In affine-invariant MCMC, the parameter space is reshaped to reduce the time taken by the algorithm to traverse the parameter space. This is particularly useful for skewed distributions. Instead of a single chain, emcee uses an ensemble of 'walkers' that allow multiple locations in the parameter space to be sampled simultaneously, increasing the convergence speed. The chains will usually take some time before their sampling converges on the highest probability parameter space. This 'burn-in' phase

can be visually identified in a diagnostic plot and is discarded before the construction of the PPD.

2.5   Mass and radius measurements

2.5.1   Ephemeris measurements

The ephemeris is a set of parameters that describes the periodicity of binary systems. Three parameters make up the ephemeris: the reference time T_0, often set to the time of superior conjunction (primary minimum) and given in either heliocentric or barycentric Julian days; the orbital period P_0, which is given in days and if the period is not constant, P_0 is specifically the period at T_0; and the rate of period change $\dot{P}_0 = dP/dt$ in days day^{-1}. The full ephemeris defined at the time of mid-primary eclipse for an eclipsing binary is therefore written as

$$T_{\mathrm{mid}} = T_0 + P_0 \times \mathrm{E} + \dot{P}_0 \times \frac{1}{2}\mathrm{E}^2. \tag{2.9}$$

If a set of times of mid-eclipse are measured and a linear ephemeris provides a sufficient fit to these times, the higher-order period term can be set to zero. Even in the case where a linear ephemeris appears sufficient, a higher-order ephemeris fit (e.g. quadratic) can be performed on the measured times of eclipse to place an upper limit on $\dot{P}_0$. CPD-54 810, the system analysed in Chapter 5, is an example of a system that is well-fitted by a linear ephemeris: see Figure 2.6 for a plot of the difference between the observed times of minimum and those calculated using a linear ephemeris. Having a long time-baseline, in this case provided by the WASP observations, is useful for monitoring long-term changes in the orbit of a system, e.g. due to a third body in the system. Therefore, it is beneficial to consider older observations in the calculation of the ephemeris, even though they may not be as precise as those from e.g. *TESS*.
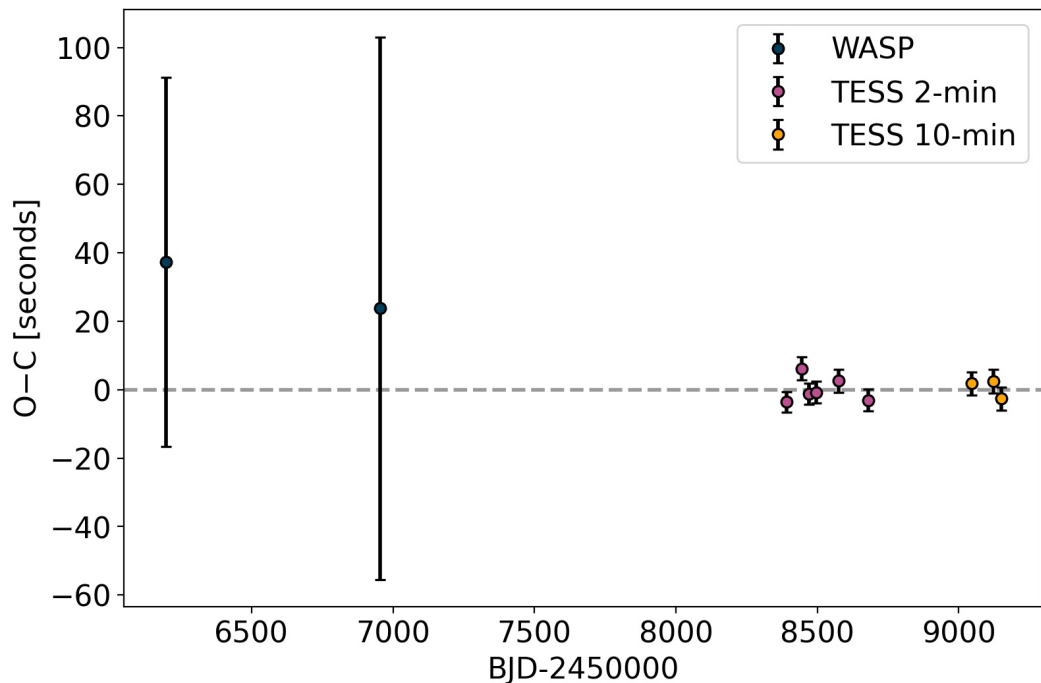
Figure 2.6: Observed versus calculated times of primary minimum for CPD-54 810.

2.5.2 Spectroscopic orbits

If two sets of sharp spectral lines can be identified in the spectra of an eclipsing binary, the system may be referred to as an 'SB2', a double-lined spectroscopic binary. The radial velocity v_r of a line is described as

$$v_r = \frac{c\left(\lambda_{\mathrm{obs}} - \lambda_{\mathrm{rest}}\right)}{\lambda_{\mathrm{rest}}}. \tag{2.10}$$

Radial velocities may be measured in a number of ways, for example cross-correlation (Blanco-Cuaresma et al., 2014b) or using broadening functions (Pilecki et al., 2017). The radial velocities I use in my work on CPD-54 810 in Chapter 5 were already extracted by Ratajczak et al. (2021) using two-dimensional cross-correlation (Zucker & Mazeh, 1994) so I did not extract any radial velocities as part of my thesis work.

The spectroscopic orbit of an SB2 can be described using Keplerian geometry. A

measurement of v_r can be expressed as

$$v_r = K[\cos(\theta + \omega) + e\cos\omega] + \gamma_{\text{sys}}, \tag{2.11}$$

where θ is the true anomaly when the measurement was taken, e is the orbital eccentricity, ω is the longitude of periastron, γ_{sys} is the systemic velocity, and K is the semi-amplitude of the velocity curve, which is defined as

$$K = \frac{2\pi\, a\sin i}{P\sqrt{1 - e^2}}. \tag{2.12}$$

Here, P is the orbital period, a is the semi-major axis and i is the orbital inclination. The values of K, γ, etc. can be measured from the radial velocity curve by fitting this model to the data using a least-squares fit or MCMC approach. The rv module of ellc (Maxted, 2016) provides the functionality to do this.

To obtain stellar masses from these parameters, we can rearrange Equation 2.12:

$$a_{1,2}\sin i = \frac{\sqrt{1 - e^2}}{2\pi}PK_{1,2}$$

Substituting the semi-major axis for mass using Kepler's third law, and noting $M_1\,a_1 = M_2\,a_2$, and $a\sin i$ is a linear combination of $a_1\sin i$ and $a_2\sin i$, we obtain a formula for the mass of each component (Hilditch, 2001):

$$M_{1,2}\sin^3 i = \frac{1}{2\pi G}(1 - e^2)^{3/2}(K_1 + K_2)^2 K_{2,1}P \tag{2.13}$$

For eclipsing binaries, the orbital inclination will be close to $90°$ and can be determined by a careful analysis of the light curve. The orbital eccentricity and period may also be measured from the light curves.

2.5.3   Light curve fitting

There are a number of light curve fitting codes that are suitable for measuring the orbital parameters of eclipsing binary stars. I will give a brief overview of some of the most commonly-used light curve fitting codes and justify my choice of code for my analysis of the light curve of CPD-54 810.

The Wilson-Devinney (WD) code (Wilson & Devinney, 1971) uses full Roche geometry to model the light curves of eclipsing binaries by placing a grid of points across the equipotential surfaces of the stars. This is particularly relevant for components which have distorted surfaces, or systems that are semi-detached or contact. However, light curve fits for eccentric systems can become computationally expensive due to the need to re-calculate the positions for the entire grid for each step in orbital period. For the purposes of analysing CPD-54 810, I chose not to use the WD code because it is a detached (no requirement for Roche geometry), eccentric (computationally expensive) system.

JKTEBOP (Southworth, 2013) is built on the Eclipsing Binary Orbit Program (Nelson & Davis, 1972; Popper & Etzel, 1981), which models the stars as two discs. JKTEBOP is fast, even for eccentric systems, and has very low numerical noise. It uses Levenberg-Marquardt minimisation (Press et al., 1992) to optimise the light curve solution for a number of free parameters. JKTEBOP also provides several methods for estimating the uncertainties. The flexibility and speed of JKTEBOP were cause for selecting it as the main light curve fitting tool I used in my work.

ellc (Maxted, 2016) is a flexible light curve code written in Python that approximates the shape of the stars in a binary system using ellipsoids. It has functionality to handle star spots, Doppler boosting and a variety of limb darkening laws. ellc is easily integrated with other Python packages such as emcee to perform robust optimisation and uncertainty estimation. ellc is a similarly suitable choice of light curve fitting code for my work on CPD-54 810, however since the system is simple and detached, JKTEBOP is more than adequate and wins out on speed.

2.6   Effective temperature measurements

Our method is based on the definition of the effective temperature for a star of radius R and luminosity L (see Section 1.2.1 for a full description),

$$L = 4\pi R^2 \sigma_{\mathrm{SB}} T_{\mathrm{eff}}^4,$$

where $\sigma_{\rm SB}$ is the Stefan-Boltzmann constant. For a binary star at distance d, i.e. with parallax $\varpi = 1/d$, the flux corrected for extinction observed at the top of Earth's atmosphere is

$$f_{0,b} = f_{0,1} + f_{0,2} = \frac{\sigma_{\rm SB}}{4} \left[\theta_1^2 T_{\rm eff,1}^4 + \theta_2^2 T_{\rm eff,2}^4 \right],$$

where $\theta_1 = 2R_1\varpi$ is the angular diameter of star 1, and similarly for star 2. The radius here refers to the the Rosseland radius, which is not necessarily identical to the radius obtained from the analysis of the light curve. Any difference between these definitions of the radius will be on the order of the atmospheric scale height, so will only be a significant difference for stars with very precise radii.

We use observed apparent magnitudes in a number of ultraviolet, optical and infrared photometric systems to measure the integrated (bolometric) flux $f_{0,b}$. The method outlined below tries to find a balance between the contributions from the data and the physics: bolometric luminosity (over the whole spectrum) is only obtainable from band-limited photometric measurements if the spectral energy distribution (SED) is known, which requires knowledge of $T_{\rm eff}$. To break this circular argument we use Legendre polynomials to distort the model SED for each star and produce the functions that are integrated to predict observed magnitudes, flux ratios, etc. We use Legendre polynomials as the basis functions for this distortion because they are smooth functions that are easy to compute and that can be normalised over the wavelength range of interest. The resulting integrating function will therefore have realistic small-scale features (absorption lines, absorption edges and molecular bands) determined by the model atmosphere, but the broad shape of the function determined by the data. By using good models SEDs and sufficient data to constrain the shape of the flux distribution, the integrating functions should be very close to the true SED of each star. This approach is in part motivated by Heiter et al. (2015), in which the authors note a 4% difference in $F_{\rm bol}$ obtained from integrating observed and model spectra for K and M dwarfs.

The integration is done using the following function to represent the shape of the

underlying SED for each star:

$$\tilde{f}_{\lambda,i} = f_{\lambda,i}^m \times \Delta_i(x) = f_{\lambda,i}^m \times \left(d_{0,i} + \sum_{j=1}^{N_\Delta} d_{j,i} P_j(x) \right). \tag{2.14}$$

Here, $f_{\lambda,i}^m$ is the SED from a stellar model atmosphere defined over the range $(\lambda_{\min}, \lambda_{\max})$ for star i, P_j is the jth Legendre polynomial and

$$x = 2(\lambda - \lambda_{\min})/(\lambda_{\max} - \lambda_{\min}) - 1.$$

$\Delta_i(x)$ is the distortion function that is applies to the model SED for star i to obtain the integrating function, $\tilde{f}_{\lambda,i}$. This distortion function is a linear combination of Legendre polynomials with coefficients $d_{j,i}$. These distortion coefficients are determined by finding the best fit to the available data with additional constraints, if necessary, to ensure the integrating functions are realistic. N_Δ is the number of distortion coefficients, which we assume here is the same for both stars. Choosing the best value of N_Δ is a matter of trial-and-error — this is discussed further below. The constant $d_{0,i}$ is calculated such that $\Delta_i(x) = 1$ at $\lambda = 5556\,\text{Å}$. The tilde symbol here denotes that this function is normalised, i.e.

$$\int_{\lambda_{\min}}^{\lambda_{\max}} \tilde{f}_\lambda d\lambda = 1.$$

The limits $\lambda_{\min} = 1000\,\text{Å}$ and $\lambda_{\max} = 30\,\mu\text{m}$ are chosen so that at least 99.8% of the flux from the model SED is included within these limits. The "distortion coefficients" $d_{j,i}$ are included so that the overall shape of the SED for each star is determined by the data, not the model.

Before normalisation, the wavelength-dependent extinction due to interstellar dust (A_λ) is applied to the model SED. We use the extinction law from Cardelli et al. (1989) for diffuse dust with $R(V) = A(V)/E(B-V) = 3.1$. In other words, the observed photometric data are not de-reddened to fit the model SEDs; the models are adjusted by A_λ to account for reddening.

Then, since $\tilde{f}_{\lambda,i}$ is normalised we can use the following function to represent the observed flux at the top of Earth's atmosphere from star i:

$$f_{\lambda,i} = \frac{\sigma_{\text{SB}}}{4} \theta_i^2 \text{T}_{\text{eff},i}^4 \tilde{f}_{\lambda,i}.$$

These are the functions that are integrated over the appropriate response functions to calculate flux ratios, photometric colours and apparent magnitudes in each photometric system.

We use a Bayesian approach to find the posterior distributions for $T_{\mathrm{eff},1}$ and $T_{\mathrm{eff},2}$. The likelihood $P(D|M)$ can be divided into four parts according to the type of the data being used:

$$P(D|M) \propto \mathcal{L}_\theta \, \mathcal{L}_m \, \mathcal{L}_x \, \mathcal{L}_\ell,$$

where the terms on the right hand side correspond to the contributions of the angular diameters ($\mathcal{L}_\theta$), magnitudes ($\mathcal{L}_m$), colours ($\mathcal{L}_x$), and flux ratios ($\mathcal{L}_\ell$) to the overall likelihood. Since we are only interested in relative values of the overall likelihood we omit any constant normalisation factors when we calculate these individual contributions to the likelihoods.

The angular diameters $\theta_1 \pm \sigma_{\theta,1}$ and $\theta_2 \pm \sigma_{\theta,2}$ are not independent because they are both calculated using a single value of the parallax and, in general, R_1 and R_2 will also be correlated, i.e., the joint probability distribution $P(\theta_1, \theta_2)$ has a non-zero correlation coefficient, ρ. For a model where the angular diameters of the stars are θ'_1 and θ'_2, we account for this correlation by using the following expression to calculate the log-likelihood $\mathcal{L}_\theta$:

$$\log_e \mathcal{L}_\theta = -\frac{z}{2(1 - \rho^2)},$$

where

$$z = \frac{(\theta'_1 - \theta_1)^2}{\sigma_{\theta,1}^2} - \frac{2\rho(\theta'_1 - \theta_1)(\theta'_2 - \theta_2)}{\sigma_{\theta,1}\sigma_{\theta,2}} + \frac{(\theta'_2 - \theta_2)^2}{\sigma_{\theta,2}^2}.$$

For each observed apparent magnitude $m_k \pm \sigma_{m,k}$ we predict a synthetic magnitude m'_k by numerical integration of the binary SED, $f_{\lambda,b} = f_{\lambda,1} + f_{\lambda,2}$, weighted by the response function, $R_m(\lambda)$. The details of how this synthetic photometry is calculated vary between different photometric systems, but always requires a zero-point magnitude which has some uncertainty, i.e. a standard error $\sigma_{\mathrm{zp},k}$. In addition to this zero-point error, there will be additional sources of error that are difficult to characterise, e.g. intrinsic stellar variability, errors in the response function, errors in the stellar models, etc. We quantify this additional noise with a single parameter $\sigma_{\mathrm{ext},m}$.

The likelihood $\mathcal{L}_m$ is then given by

$$\log_e \mathcal{L}_m = -0.5 \times \sum_k \left(w_{k,m}(m'_k - m_k)^2 - \log_e(w_{k,m}) \right),$$

where $w_{k,m} = 1/(\sigma_{m,k}^2 + \sigma_{\mathrm{zp},k}^2 + \sigma_{\mathrm{ext},m}^2)$.

For eclipsing binary star systems with independent observations of the photometric colour index, such as AI Phoenicis in the Strömgren system (Holmberg et al., 2009; Reipurth, 1978), we outlined the framework to include these extra data in the temperature method in order to provide additional observational constraints. Hence, for an observed photometric colour index $x_k \pm \sigma_{x,k}$ and a model that predicts an index value x'_k, the likelihood is calculated using

$$\log_e \mathcal{L}_x = -0.5 \times \sum_k \left(w_{k,x} \left(x'_k - x_k \right)^2 - \log_e(w_{k,x}) \right),$$

where $w_k = 1/(\sigma_{x,k}^2 + \sigma_{\mathrm{ext},c}^2)$, and $\sigma_{\mathrm{ext},c}$ is a parameter that quantifies external error sources in photometric colour indices.

It is essential to have measurements of the flux ratio at a number of different wavelengths in order to calculate accurate effective temperatures for both stars independently. We assume that these flux ratios, $\ell_k \pm \sigma_{\ell,k}$, are also affected by an additional noise source with standard deviation $\sigma_{\mathrm{ext},\ell}$, partly because of the reasons listed above for apparent magnitudes, but also because the errors in these ratios derived from the light curve analysis may be underestimated. With this assumption, the contribution to the likelihood for a model that predicts flux ratios ℓ'_k is

$$\log_e \mathcal{L}_\ell = -0.5 \times \sum_k \left(w_{k,\ell}(\ell'_k - \ell_k)^2 - \log_e(w_{k,\ell}) \right),$$

where $w_{k,\ell} = 1/(\sigma_{\ell,k}^2 + \sigma_{\mathrm{ext},\ell}^2)$.

The first eight free parameters in our model, M, are $\mathrm{T}_{\mathrm{eff},1}$, $\mathrm{T}_{\mathrm{eff},2}$, θ'_1, θ'_2, $\mathrm{E(B-V)}$, $\sigma_{\mathrm{ext},m}$, $\sigma_{\mathrm{ext},\ell}$ and $\sigma_{\mathrm{ext},c}$. We find that these parameters are all well-constrained by the data so we use an improper uniform prior that requires these quantities to be positive-definite, but that has no upper bound. For the distortion coefficients we set a uniform prior over the range $[-1, 1]$. We use emcee to calculate the posterior probability distribution of these model parameters.

3 A dispatch scheduler for the Xamidimura instrument

Would you stare forever at the sun, never watch the moon rising?
Would you walk forever in the light, to never learn the secret of the quiet night?

Change, Big Thief (2021)

3.1 Introduction

The Xamidimura instrument consists of two 0.4-m telescopes mounted in place of the SuperWASP instrument at the South African Astronomical Observatory (SAAO). The primary purpose of the new instrument is to obtain light curves of detached eclipsing binary stars in multiple filters. This will allow us to monitor variations in brightness through the eclipse via photometry in several wavelength ranges, and hence colour – a proxy for stellar effective temperature. The instrument will be operated remotely and autonomously, which means that it requires robust software to select targets and filters, track and image the target at a sufficiently high quality, monitor the weather conditions, and control the mount and enclosure.

Target selection is not a trivial task, as it requires the handling of a number of factors that impact the observability of a target at a given time, along with deciding how to prioritise and select a single target over a set of similar targets. As part of the Xamidimura project, I have designed, written and optimised a scheduler that selects the best eclipsing binary target from a preliminary database of targets to observe at any given time.

3.2   Scheduling astronomical observations

3.2.1   Introduction to the scheduling problem

The purpose of a scheduler is to maximise scientific return and optimise use of a telescope or system. There is a wide range of algorithms and approaches currently used by different astronomical observatories, since no single solution is a perfect fit for all of the unique scientific and technical factors required by each system. For a detailed overview to the scheduling problem, see the works by Fraser (2012) and Colome et al. (2012).

Schedulers may operate over three distinct time scales:

- **Short-term**: A short-term scheduler makes scheduling decisions in real time, adapting to dynamical conditions such as changes to the weather at the observatory, to account for new targets e.g. transient objects, or changes to the system itself. Short-term schedulers must be computationally efficient to achieve these objectives.

- **Mid-term**: A mid-term scheduler operates on the timescale of a single observing period or night. It usually performs a pre-selection of targets based on factors such as seasonal weather variations, which reduces the number of targets the short-term scheduler needs to consider for that observing period.

- **Long-term**: A long-term scheduler makes plans on a seasonal scale (usually months) to optimise the overall performance of the system. It can also be used to support the evaluation and allocation of time for observing proposals.

The majority of observatories require a short-term scheduler, but this can be combined with mid- or long-term scheduler to further optimise the efficiency of the system.

Schedulers consider both hard constraints (feasibility) and soft constraints (priority) in their decision-making. These constraints are evaluated using heuristics (merit functions, or feasibility/priority score), which are pre-defined rules that are used in

the prioritisation of targets. Examples of heuristics include location-based constraints (visibility, zenith distance or airmass, distance from the Moon), time-based constraints (specific event such as a planetary transit, or a specific observing window), maximum number of observations required, prioritisation of monitoring tasks that have been initiated, system status constraints (slew time or other overheads), and environmental conditions. Many of these heuristics can be used in mid- to long-term schedulers, but the dynamic conditions such as system status and environmental conditions can only be managed by a short-term scheduler.

Algorithms used in scheduling astronomical observations are suitable for different objectives, and can often be used in conjunction with other algorithms for a complementary solution to the scheduling problem for a specific system. Some commonly used algorithms include:

The dispatch scheduler. This is a simple real-time scheduler which calculates the current merit or score of each task and simply selects the one with the highest value. It has the benefit of running much faster than other methods, but as a short-term scheduler it does not optimise the overall allocation of time and resources as well as other solutions. The dispatcher model is used by the Liverpool Telescope (Fraser & Steele, 2004), Telescopi Joan Oró at the Observatori Astronòmic del Montsec (Colomé et al., 2010), the Antarctic Survey Telescopes (Liu et al., 2018) and others.

The Spike planning and scheduling software. The Spike system was developed for the Hubble Space Telescope (HST, Johnston & Miller 1994) and can function as both a short-term scheduler handling the detailed assignment of activities and as a mid- to long-term optimiser, assigning activities over a timescale of approximately a week. The scheduler takes into account both hard and soft constraints via a set of 'suitability functions' and uses a neural network to implement an iterative method: trial assignment → repair → de-conflict → repeat. The computation cost scales linearly with the number of time slots and quadratically with the number of targets, therefore is not always ideal for short-term dynamic scheduling. In addition to HST, Spike has been used by the Very Large Telescope (VLT, Johnston 1988) and the Subaru Telescope (Sasaki et al., 2004).

Multi-Objective Evolutionary Algorithms (MOEA). MOEAs are ideal for mid- and long-term scheduling and can be combined with other constraint-based methods such as SPIKE to optimise multiple objectives. MOEAs are used in the scheduling framework of the Calar Alto high-Resolution search for M-dwarfs with Exo-earths with Near-infrared and optical Échelle Spectrographs (CARMENES, Garcia-Piquer et al. 2017).

Squeaky Wheel Optimisation (SWO). SWO uses a construct → analyse → prioritise cycle that repeats until a certain condition is met. The 'constructor' generates a scheduling solution out of a set of tasks which may or may not violate hard constraints. The 'analyser' then assigns a 'blame' factor to the tasks that contribute to flaws in the solution, and the 'prioritiser' uses this information to modify the solution (see Joslin & Clements 1999 for more details). SWO is often combined with other algorithms, and is currently used in the Stratospheric Observatory for Infrared Astronomy (SOFIA, Frank & Kürklü 2005) and the Mars 2020 Perseverance Rover (Chi et al., 2021).

3.2.2 Selecting an approach for Xamidimura

The majority of targets observed by Xamidimura will be long-period eclipsing binaries, often with eclipse durations exceeding the length of a single night. The observing conditions at SAAO can be highly variable, so observations will likely be interrupted and re-scheduled for a later time. Therefore, Xamidimura will most likely operate by constructing light curves of eclipsing binary targets through a number of unique visits, and the scheduler must be capable of making rapid decisions due to the dynamic conditions at the site. Unlike many other observatories, 100% of the targets will be from a single target database maintained by the Xamidimura project, so competing time allocations do not need to be considered in the design of the scheduler. For the early stages of the Xamidimura project, only a short-term scheduler is required. We would prefer to maximise the quality of the observation by choosing the best target at any given time, since the volatile weather conditions will easily undermine any careful long-term planning.

The review of scheduling methods by Colome et al. (2012) recommends either a dispatch scheduler, or SPIKE, for short-term scheduling. Due to the requirement that the scheduler reacts quickly to changing weather conditions, and the abundance of time-based constraints on all of the eclipsing binary targets, we chose to create a custom dispatch scheduler. The Xamidimura scheduler evaluates hard (feasibility) and soft (priority) constraints for each target in the database and selects the highest-scoring target at the current time. In Section 3.3 I describe the heuristics employed in the Xamidimura scheduler model. I explain how I implemented each of these into the scheduler software in Section 3.4, and in Section 3.6 I give details of some simulations I performed on the scheduler model using historical weather data, which we used to optimise the heuristic weightings. The scheduler has been deployed into the Xamidimura Telescope Control System (TCS) and was used to select a target for remote observation during the early commissioning phase of the hardware. A light curve from this observation is shown in Section 3.7, and possible future improvements to the scheduler are discussed in Section 3.8.

3.3   Scheduler model

Although all targets in the database are suitable for being observed by the Xamidimura instrument, a number of factors determine whether they are suitable to be observed at any particular time. In addition, if multiple targets are suitable, we need a method to select the most important target to select at any given time.

The Xamidimura dispatch scheduler consists of three models: the feasibility execution model, the scoring model, and the selection model.

Feasibility execution: This model is used to determine if a target is observable, based on predetermined constraints. The basic observability factors taken into consideration are:

- **Solar elevation:** It is not feasible to observe targets if the elevation of the

Sun is too high. We restrict observations to when the Sun is lower than $-12°$ altitude. During civil twilight, i.e. when the Sun has set but is still too high for eclipse observations, the telescope will be used to obtain flat fields.

- **Lunar contrast:** All objects should be a minimum distance on the sky from the Moon for the duration of the proposed observation, with brighter objects permitted to be slightly closer than fainter objects.

- **Limiting air mass:** Below a certain altitude, image distortion due to atmospheric turbulence, extinction, scintillation, and dispersion becomes too significant for high quality observations. Therefore, we restrict targets to high enough altitudes (low enough air masses) for this not to be an issue.

- **Eclipsing status:** There is little or no information about the eclipsing binary in the data between eclipses, particularly for long period binaries. Therefore, if a target is eclipsing, it should be observed before any other target that is not in eclipse.

Scoring: This model combines a number of factors that are desirable in a target, and a user-specified urgency. The scheduler uses the following attributes to calculate a score:

- **Air mass:** How low the current air mass of the target is compared to its lowest possible air mass, i.e. the air mass when the target is at its maximum elevation, $90° - |\lambda - \delta|$, where λ is latitude and δ is declination.

- **Phase:** In order to prioritise obtaining complete light curves, i.e. with full phase coverage, the duration of each eclipsing binary target in phase units is divided into equally sized bins. Each bin has a predetermined number of observations required to be considered complete, and is updated each time a successful observation has been logged.

- *PLATO* **fields:** Targets inside, or near, a nominal *PLATO* long pointing field are prioritised. The exact location of the fields will not be decided until 2 years

before launch, so the score reflects an approximate likelihood that a given target will be inside a field.

- **Urgency:** A user-defined integer from 0 (low priority) to 4 (high priority), which allows the user to force the scheduler to be more likely to choose a specific target.

Selection: Given a set of raw metrics or weighted scores, the selection model decides which object to observe in the next instance. For the Xamidimura scheduler, we will simply select the best feasible target available at the time. If the current target still meets the feasibility criteria when the scheduler is called, it will choose to continue observing the current target.

3.4   Scheduler implementation

3.4.1   Sky brightness due to moonlight

The most significant contributor to the sky background brightness in visible wavelengths is scattered moonlight (Noll et al., 2012; Jones et al., 2013, 2019). An empirical model to describe the effect of moonlight on sky brightness at Mauna Kea was derived by Krisciunas & Schaefer (1991), which considers Rayleigh and Mie scattering and is accurate to between 8% and 23% depending on lunar phase. Other studies have since adapted this model for other sites, producing full spectra of the sky background rather than a single magnitude, and adding in other effects such as molecular absorption (Noll et al., 2012) and 3-D descriptions of single and multiple scattering (Jones et al., 2013). These works are usually motivated by improving the accuracy of exposure time calculators for large telescopes. Despite the more complicated treatment of scattering, the uncertainty in these more advanced models is still in the region of 20%.

For Xamidimura, we require an estimate for the sky brightness due to moonlight in order to determine whether it is feasible to observe a given target. We use this to calculate a contrast between the sky and target, instead of simply using proximity to

the Moon – at the same value of lunar contrast, brighter stars will be closer to the Moon than fainter stars. For these purposes, we only require a single visual magnitude estimate of the sky brightness, and thus we use the empirical model from Krisciunas & Schaefer (1991).

There are four contributions to sky brightness that are considered by this model. The first is the inherent dark sky zenith brightness at the observing site, V_{zen}, which is a fixed sky background which is subtracted from the sky brightness caused by moonlight. For SAAO, there is no exact value available, so we take the value for the Mauna Kea site at $2800\,\text{m}$ used by the authors. V_{zen} in magnitudes is converted into B_{zen} in nanoLamberts (nL) using the conversion

$$B = 34.08 \exp(20.7233 - 0.92104V) \tag{3.1}$$

The dark sky brightness B_0 for any point on the sky with a zenith distance $Z = 90° - altitude$, is calculated from the equation

$$B_0(Z) = B_{zen}10^{-0.4k(X(Z)-1)}X(Z), \tag{3.2}$$

where k is the zenith atmospheric extinction coefficient for the site and $X(Z)$ is a measure of optical path length, p, in air masses:

$$X(Z) = (1 - 0.96(\sin(Z))^{-0.5} \tag{3.3}$$

Now we can consider the second contribution to the sky brightness: the Moon. The illuminance of the Moon outside the atmosphere, I^*, is related to the illuminance of the Moon inside the atmosphere I by

$$I = I^*10^{-0.4kX(Z_m)}, \tag{3.4}$$

where Z_m is the zenith distance of the Moon. I^* is related to the V-band magnitude of the Moon, which in turn is dependent on the lunar phase angle α. Empirically, I^*, is given by the equation

$$I^* = 10^{-0.4(3.84+0.026|\alpha|+4\times10^{-9}\alpha^4)}. \tag{3.5}$$

Next, we include the Rayleigh scattering of light from astronomical objects by air molecules. For any Moon-sky separation, ρ, the Rayleigh scattering $f_R(\rho)$ is calculated using this equation taken from Rozenberg (1966):

$$f_R(\rho) = C_R[1.06 + \cos^2(\rho)] \tag{3.6}$$

Here, the constant of proportionality C_R was derived by the authors by fitting observations of the scattering function for the Mauna Kea site.

The final contribution to the sky brightness we consider is the Mie scattering $f_M(\rho)$, a highly forward directional scatter due to atmospheric aerosols. This is characterised by an empirical relation valid for Moon-sky separations greater than 10 degrees:

$$f_M(\rho) = 10^{6.15-\rho/40} \tag{3.7}$$

For smaller separations, we chose to return a strongly negative result since we would rather avoid pointing the telescopes so close to the Moon. The Rayleigh and Mie contributions to the overall scattering function $f(\rho)$ are combined linearly:

$$f(\rho) = f_R(\rho) + f_M(\rho) \tag{3.8}$$

The sky brightness due to moonlight is hence

$$B_m = f(\rho)I^* 10^{-0.4kX(Z_m)}[1 - 10 - 0.4kX(Z)], \tag{3.9}$$

Converting the derived B_m into magnitudes per square arcsecond, the change in sky brightness due to moonlight ΔV is hence

$$\Delta V = -2.5 \log_{10}[(B_m + B_0(Z))/B_0(Z)]. \tag{3.10}$$

This equation neglects several minor effects, for example the asymmetric albedo of the Moon which causes the scattered moonlight to be slightly brighter before a full Moon than after, the lunar opposition effect for $|\alpha| < 7°$ which causes the Moon to be 35% brighter than calculated during full Moon, the effects of atmospheric refraction causing the apparent position of the Moon to shift by up to 0.5° when at the horizon,
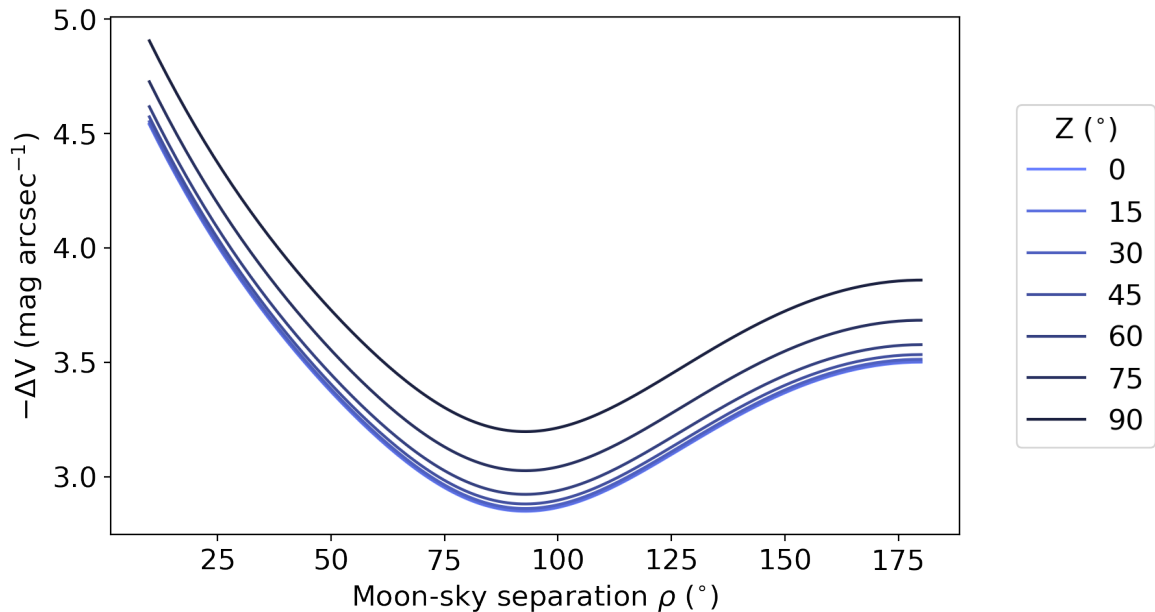
Figure 3.1: Change in sky brightness $-\Delta V$ for increasing angular separation ρ between the Moon at $\alpha = 0°$ and target for several values of target zenith angle Z.

and the 11.6% change in apparent diameter of the Moon between apogee and perigee. The distribution, composition and concentration of aerosols is also highly variable and is not considered in this model. Corrections for these issues can be, and often are, included in more advanced models, but this simple model still reproduces observations to a similar accuracy and is sufficient for our applications.

The effects of Moon-sky separation ρ on the predicted sky brightness due to moonlight ΔV for a range of zenith distances is shown in Figure 3.1. The effect of the Moon on the sky brightness is most significant at small ρ, and we see a smaller peak in ΔV at $\rho = 180°$. As the equation for ΔV is empirically derived, it is not continuous over $360°$.

The effect of the lunar phase angle on the sky brightness due to moonlight for a target at $60°$ separation from the Moon is shown in Figure 3.2. The results for several zenith angles are given, highlighting the increased effect of the scattering function on the sky brightness at low altitudes.
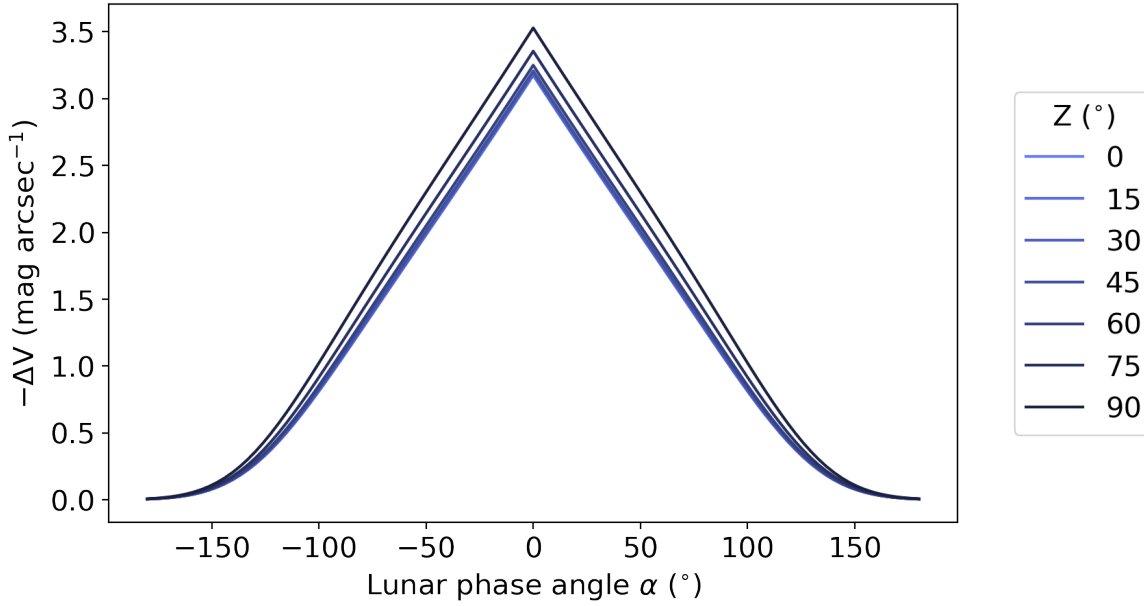
Figure 3.2: Change in sky brightness for $-\Delta V$ throughout a lunar cycle for several values of target zenith angle Z. Phase angle $\alpha = 0°$ corresponds to a full Moon.

The sky brightness due to moonlight is hence incorporated into the scheduler via the 'sky contrast' feasibility test. The scheduler calculates the sky brightness due to moonlight at the location of the target in the sky, subtracts the magnitude of the target and tests whether the result is within a user-defined tolerance level. For our initial tests of the scheduler, we set this tolerance to 5 magnitudes. Other contributions to the sky brightness such as zodiacal light, airglow and background stars are considered negligible.

3.4.2   Air mass

The optical path length or air mass that light from a star travels through to reach an observer affects seeing and apparent brightness, due to increased scattering and absorption as the light from the stars passes through more air. Therefore, if the scheduler is choosing between two otherwise identical targets with different altitudes in the sky,

it should choose the one with the lowest air mass. Since the effect of the atmosphere on the air mass and hence observation quality is not linear, simply using the elevation as the heuristic is not sufficient. I will discuss several equations used to approximate the air mass in the literature, and how we selected the most appropriate choice for the Xamidimura scheduler.

The simplest approximation for air mass treats the atmosphere as a uniform plane-parallel slab, i.e. a flat Earth. For any target with a zenith distance Z, the optical path length in air masses $X(Z)$ for these assumptions is

$$X(Z) = \sec(Z). \tag{3.11}$$

This equation works well for zenith distances smaller than approximately $60°$ to $80°$, however begins to break down when approaching the horizon, where $X(Z \to 90°) \to \infty$. This deviation from the other laws to increasingly overestimated values of air mass can be seen in Figure 3.3.

Many widely used descriptions of air mass are derived from tabulated air masses, either from observations or atmospheric models. One example of this comes from Rozenberg (1966), who derives a simple empirical equation that is used in several models of sky brightness, e.g. Krisciunas & Schaefer (1991) and Noll et al. (2012) for the atmospheric model used at Cerro Paranal:

$$X(Z) = (\cos(Z) + 0.025e^{-11\cos(Z)})^{-1}. \tag{3.12}$$

Another widely cited paper which derives an air mass formula is Garstang (1986). The authors provide an equation, based on work by Snell & Heiser (1968), which reproduces observed air masses for $Z < 85°$ to better than 0.1 air masses. For higher values of Z they use air mass measurements tabulated in Allen (1973), but these values are not included in Figure 3.3. The Garstang (1986) equation is as follows:

$$X(Z) = \sec(Z) - 0.010[\sec(Z) - 1]^2. \tag{3.13}$$

The final approximation I will discuss is from Kasten & Young (1989), who use the Standard Atmosphere model from the International Organization for Standardization

(1972) to calibrate their earlier equation (Kasten, 1965) with improved results: the maximum difference between this formula and observed air masses is $< 0.5\%$. This equation is given in terms of elevation $h = 90° - Z$ and agrees very closely with the equation from Rozenberg (1966):

$$X(h) = \frac{1}{\sin(h) + 0.50572\,(h + 6.07995°)^{-1.6364}}. \tag{3.14}$$

For Xamidimura, we require only a simple formula for the air mass, which gives reasonable values for $X(Z)$ for large Z. This is important because, in the example of Garstang (1986), a zenith angle of 89 to 90 degrees would result in a small air mass and hence wrongly improve the score of the air mass heuristic.

Noting that each variant of $X(Z)$ is specifically calculated to a certain site, and that the differences close to $Z = 90°$ will not be important for the scheduler because targets will be penalised strongly for $Z > 60°$, we choose to use the simple plane-parallel formula $X(Z) = \sec(Z)$ for use in the air mass feasibility calculation in the scheduler. While the function is more approximate than others, it is well-behaved and this helps avoid numerical issues.

3.4.3   Eclipsing status and observational completeness

The orbital phase ϕ of an eclipsing binary at any given time t can be calculated using the orbital period P and time of primary minimum T_0: $\phi = (t - T_0)/P \mod 1$. The phase range in which the primary and secondary eclipses occur can be calculated using knowledge of the phase of the primary eclipse (usually assumed to be 0) and secondary eclipse (either from a pre-existing light curve fit or visual inspection), along with an estimate of the eclipse width (or duration) in phase units, usually taken from a visual inspection of the light curve. The current orbital phase can then be compared to the eclipse phase ranges to determine whether any given system is currently in eclipse. For the Xamidimura scheduler, we are interested in observing systems just before and after eclipses to determine the out-of-eclipse flux level. Therefore, when calculating whether a system is currently in eclipse, we include an additional tolerance of 10% of the eclipse
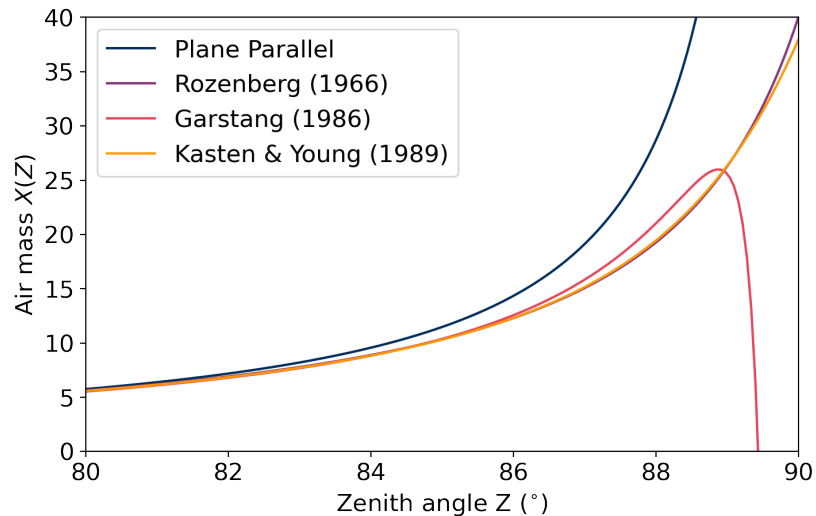
Figure 3.3: Relative air mass $X(Z)$ against zenith angle Z as calculated using approximate formulae from Rozenberg (1966), Garstang (1986) and Kasten & Young (1989).

width. Testing whether a system is currently in eclipse yields a simple feasibility score:

$$\text{Eclipsing status score} \; = \; \begin{cases} 1, & \text{if phase in any eclipse range } \pm \; 10\% \\ 0, & \text{otherwise.} \end{cases}$$

We require as full a phase coverage of each eclipse in each system as possible. Therefore, each primary and secondary eclipse is divided into a number of phase bins and we require each bin to be observed a certain number of times to be considered complete. When designing the scoring system, we decided that the scheduler should prioritise eclipses that are nearly complete and discourage additional visits once an eclipse has been completed. Therefore, we start all bins that have no existing observations, i.e. $N_{\text{obs}} = 0$, with a phase completeness score of 0.5, which increases as more observations are taken, and drops to zero after the observation goal N_{goal} has been exceeded. When calculating the score for a system, only the completeness of the current phase bin is

considered.

$$
\text{Phase completeness score} \ = \begin{cases} 0.5, & \text{if } N_{\text{obs}} = 0 \text{ or } N_{\text{obs}} = N_{\text{goal}} \\ 1.0, & \text{if } N_{\text{obs}} = N_{\text{goal}} - 1 \\ 0.0, & \text{if } N_{\text{obs}} > N_{\text{goal}} \\ \frac{N_{\text{obs}}}{2(N_{\text{goal}}-1)} + 0.5 & \text{otherwise.} \end{cases}
$$

3.4.4   Location relative to *PLATO* long-pointing fields

Targets that fall within the long-pointing fields of the upcoming *PLATO* mission are of particular interest, as ground-based follow-up and characterisation of detached eclipsing binaries observed by *PLATO* could be used as benchmark stars to verify stellar parameters derived by the mission, e.g. by the SAPP pipeline (Gent et al., 2022). As the exact location of the *PLATO* nominal long-pointing fields are yet to be confirmed, we use the approximate locations as shown in Figure 3.4, reproduced from Figure 2 of Magrin et al. (2018). Using this image, we mapped the field boundaries onto a Hammer–Aitoff projection in Galactic coordinates. From this, we can calculate which field each target is closest to (North or South), whether it lies inside that field, and if not, how far it lies from the field boundary, α. This information is used to generate a "*PLATO* score", which prioritises targets in or near the proposed *PLATO* fields:

$$
\textit{PLATO} \text{ score} \ = \begin{cases} 1.0, & \text{if inside } \textit{PLATO} \text{ field, and } \alpha \geq 10° \\ 0.9, & \text{if inside } \textit{PLATO} \text{ field, and } 5° \leq \alpha < 10° \\ 0.7, & \text{if inside } \textit{PLATO} \text{ field, and } 0° \leq \alpha < 5° \\ 0.5, & \text{if outside } \textit{PLATO} \text{ field, and } 0° < \alpha \leq 5° \\ 0.3, & \text{if outside } \textit{PLATO} \text{ field, and } 5° < \alpha \leq 10° \\ 0.1, & \text{otherwise.} \end{cases}
$$

Many targets in the preliminary database will have a low "*PLATO* score", since they originate from *K2* eclipsing binary catalogues. We expect to add more targets with greater proximity to the provisional *PLATO* long-pointing fields from *TESS* in the future.
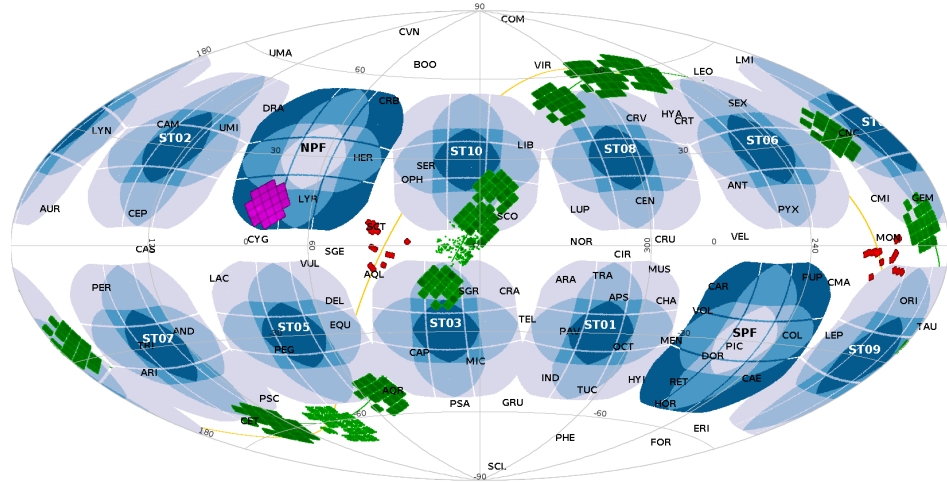
Figure 3.4: Location of the preliminary *PLATO* fields (blue) with the North and South long-pointing fields labelled NPF and SPF, reproduced from Magrin et al. (2018). Regions of the sky studied by other successful exoplanet missions are shown for reference: *Kepler* in pink, *K2* in green and *CoRoT* in red.

3.5   Target database

In order to test the capabilities of the scheduler, it was necessary to compile a realistic, provisional database of eclipsing binary targets for Xamidimura. The list of targets used in the scheduler target information table is a concatenation of several catalogues of eclipsing binary stars from *K2* and WASP, alongside a few other targets of special interest. I collected data on *Kepler* eclipsing binaries from Kirk et al. (2016), *K2* eclipsing binaries from Maxted & Hutcheon (2018) and subsequent work (Hutcheon, R, priv. comm.), WASP eclipsing binaries identified by P. Maxted, and additional binaries from DEBCat (Southworth (2015b)). We are only interested in following up detached eclipsing binary stars that are feasibly observable with the Xamidimura instrument. Many of the binaries initially collected are not suitable for this purpose, therefore I refined the data based on the following criteria:

Magnitude: In the interest of obtaining good quality photometry, I restricted the stars to be brighter than 13th visual magnitude and fainter than 6th. These limits take factors such as the aperture size of the Xamidimura telescopes and atmospheric seeing into account, and remove bright stars which would encounter problems such as a lack of good comparison stars, and detector saturation.

Eclipse width: Eclipse width is a useful proxy for a constraint on how detached systems are. Binaries with long eclipses that cover most of the total phase are likely to fall in the semi-detached or even contact category of binary star, and are therefore not suitable as benchmark stars for *PLATO*. Selecting only stars with narrow eclipses means we avoid RS CVn-type binaries, where tidal forces spin up the stars, leading to significant magnetic activity (e.g. star spots, X-ray emission, mass loss; Schrijver & Zwaan (1991)). Torres et al. (2010) discuss the circularisation and synchronisation of binary stars, noting that all orbits are circular for relative radii (measured from eclipse shape) above 0.25. We restricted the sample to targets with eclipse widths shorter than 5% of the total phase.

Orbital period: Orbital period is another way to prevent non-detached binaries from entering the sample, since binary orbits tend to circularise for orbital periods less than $\sim 5-6$ days (Torres et al., 2010), and hence become tidally locked. The orbital period was therefore restricted to greater than 5 and less than 100 days, such that the targets have a chance of being observed more than once by the instrument during its operational lifetime.

Eclipse depth: Shallow eclipses tend to be partial and contain little information about the geometry of the binary system, particularly for eccentric orbits. Therefore, I chose to restrict the sample to systems with sufficiently deep eclipses — 10% decrease in brightness for primary eclipses, 5% for secondary eclipses — in order to maximise the number of systems that have total eclipses.

Declination: From preliminary runs of the scheduler, I decided to limit the declination of targets to less than +30 degrees. Since Xamidimura is based in the southern hemisphere, with latitude -32 degrees, targets with high declinations simply will not be observed. In the future, once the mechanical limits of the Xamidimura instrument

are better characterised, we may further restrict the targets by declination.

Following these restrictions, the target information table contains 108 suitable targets. Figures 3.5a and 3.5b show the period and magnitude distribution of the targets. There is a clear trend towards fainter targets: this is due to many of the targets having been discovered by *K2*, which primarily observed faint stars (Borucki et al., 2010). There are also significantly more short period targets than long period targets, since they are easier to detect and confirm.

In the future, we intend to add more targets to the database from the recently launched *TESS* mission, an all–sky survey for transiting exoplanets (Ricker et al., 2014a). The results from the scheduler on this initial target list will be useful in deciding which targets to include in an updated list.

3.6   Weather log simulations

3.6.1   Introduction

In order to test the scheduler over a longer period of time, we retrieved a sample of historical weather logs from the WASP–South instrument. Every hour with good weather over a 5 year period was collected, and each of these 6732 hours was shifted into the future. This allows us to investigate how many targets we should be able to observe in a realistic 5 year period. I have run the scheduler at the start of each of these hours, so each "observation" corresponds to one hour on-target.

3.6.2   Feasibility report

With the current target database, the scheduler can be in operation, with at least one feasible target available, for up to 83.44% of the available times (Figure 3.7). When there are no feasible targets, or there are only targets with priority scores of zero (i.e. they have been completed), the scheduler sits idle. When the telescope

(a) Periods of targets in database

(b) Magnitudes of targets in database

(c) Declinations of targets in database
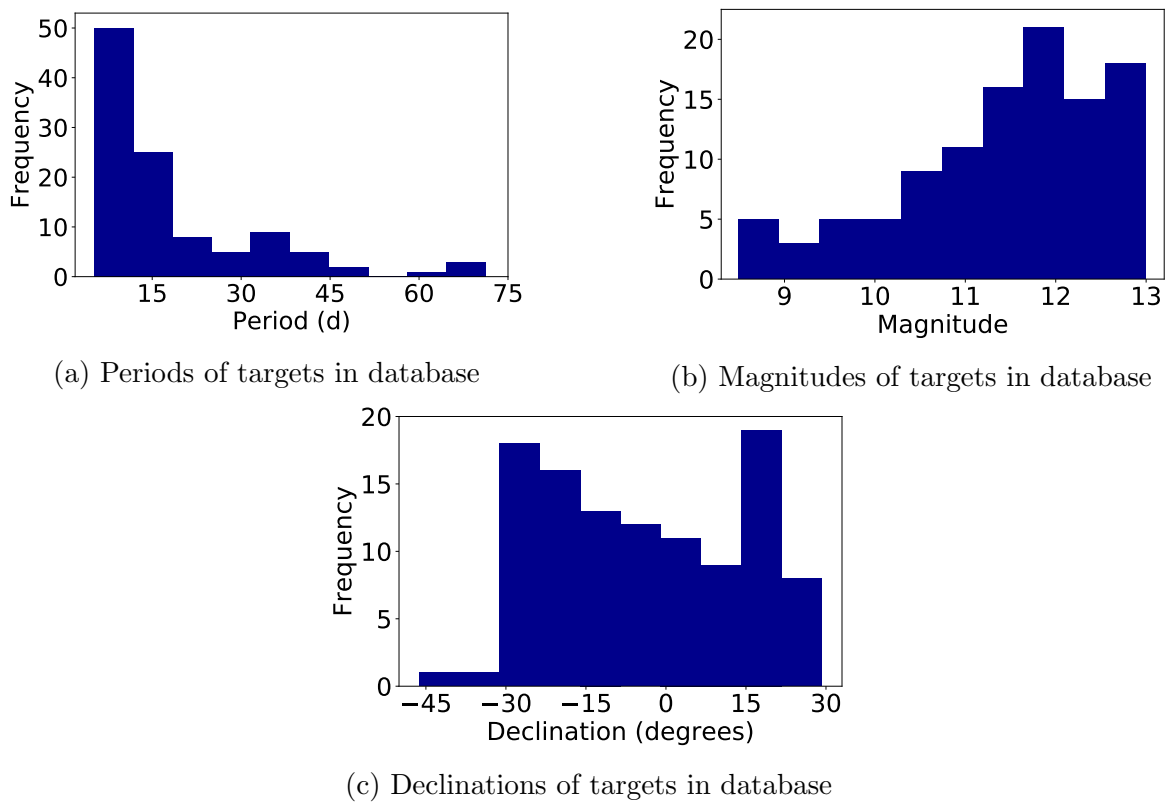
Figure 3.5: Histograms of the period, magnitude and declination distributions of the eclipsing binary target database.
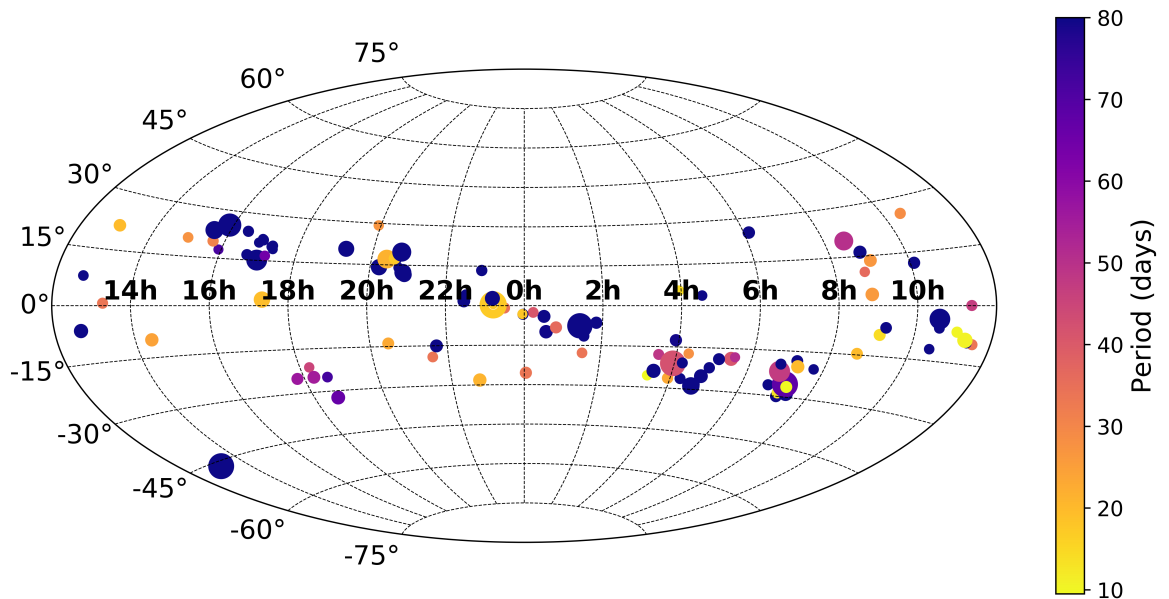
Figure 3.6: Location of targets in Xamidimura database on the sky, colour-coded by orbital period. The size of the symbols represents magnitude, with larger symbols corresponding to brighter objects.

is fully operational, we expect this time to be filled with either additional eclipsing binary targets from *TESS*, other targets requested by the group or collaborators, or photometric standard stars for calibration.

I ran the scheduler with the following scoring model, which combines each priority score p_i with a corresponding weighting w_i:

$$score = \prod_{i=1}^{N} p_i w_i \tag{3.15}$$

The scores for air mass, *PLATO* field proximity and phase completeness were calculated as described previously, with the weights as free parameters which can be adjusted to maximise the number of complete targets.

I set 12 simulations running with a series of different weight combinations, and calculated how many targets were complete or nearly complete, with 9 or 10 bins observed. Only the results for the best four sets of weightings (i.e. those that completed
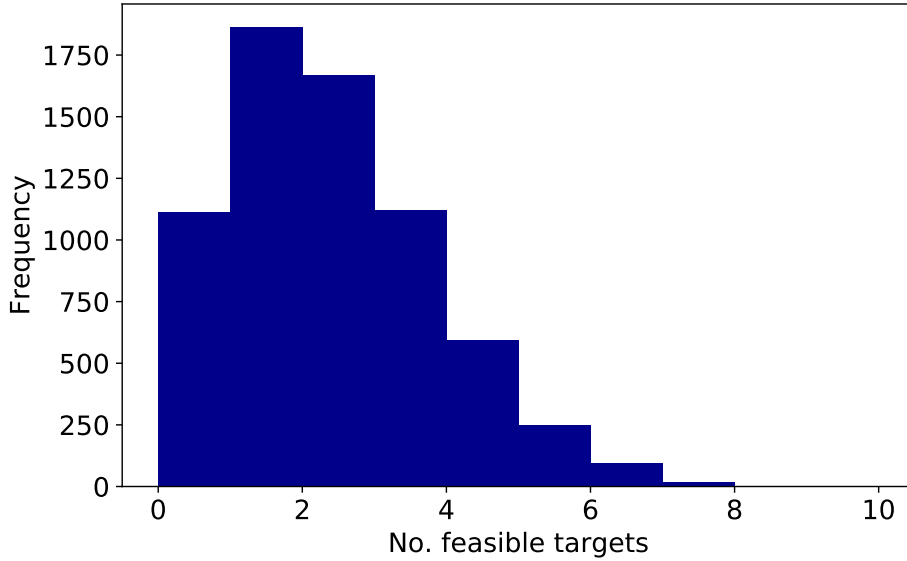
Figure 3.7: Histogram of the number of feasible targets at each time in the simulation run.

Simulation	w_X	w_P	w_ϕ	η	$N_{100\%}$	$N_{>90\%}$	$\bar{n}_{obs}$	$\tilde{n}_{obs}$
A	1	0.8	1.2	56.2%	45	55	35.0	40
B	1	1	1	56.1%	46	55	35.0	39
C	1	0.5	2	55.8%	46	56	34.8	39.5
D	0.5	0.5	1	56.0%	45	59	34.9	39

Table 3.1: Score weightings and results from four selected simulations. The columns w_X, w_P and w_ϕ show the weightings applied to the air mass, $PLATO$ and orbital phase scores respectively. η is the time the telescope spent on target, $N_{100\%}$ and $N_{>90\%}$ are the numbers of targets with 100% and over 90% of requested observations completed, and $\bar{n}_{obs}$ and $\tilde{n}_{obs}$ are the mean and median number of observations made per target.

the most targets) are shown here for clarity.

We can see in Figure 3.8 that some combinations of score weightings result in much wider distributions of target scores than others. In addition, some display a periodic structure with several peaks. This is most likely due to the discrete nature of the $PLATO$ score, as the other two scores are continuous.

(a) Simulation A

(b) Simulation B

(c) Simulation C
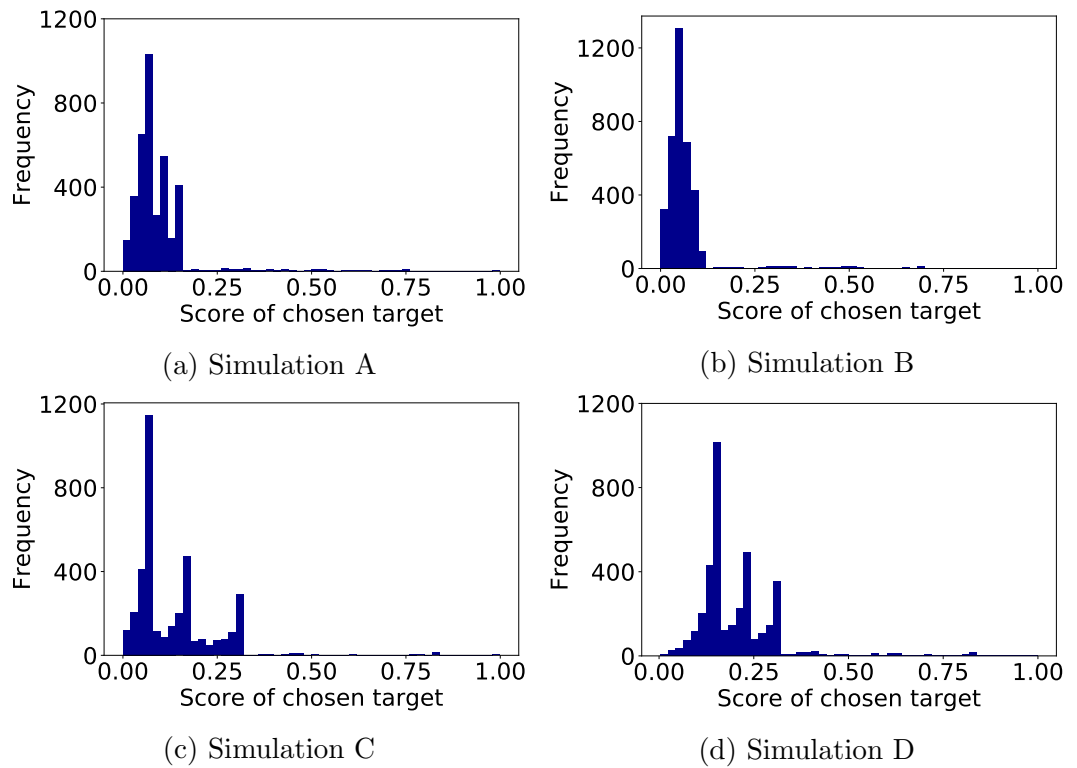
(d) Simulation D

Figure 3.8: Score distribution excluding scores of zero over entire 5 year run of each simulation.

(a) Simulation A

(b) Simulation B

(c) Simulation C
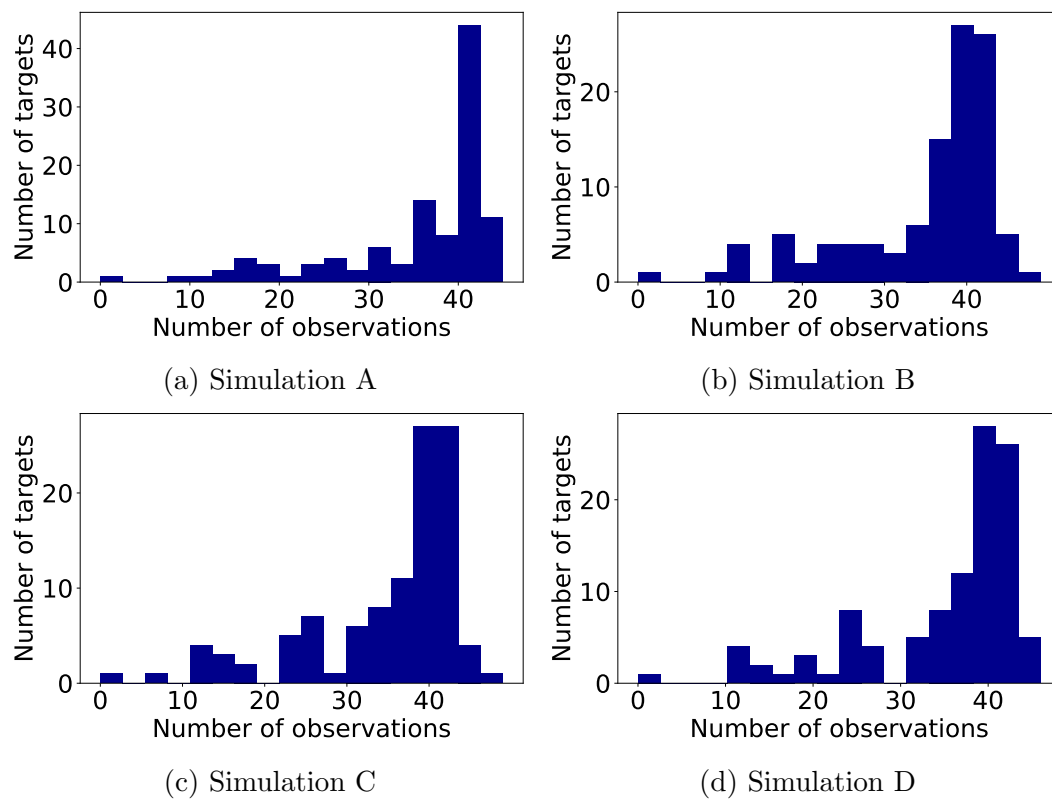
(d) Simulation D

Figure 3.9: Histogram of number of observations per target at the end of the simulation runs.

(a) Period

(b) Magnitude
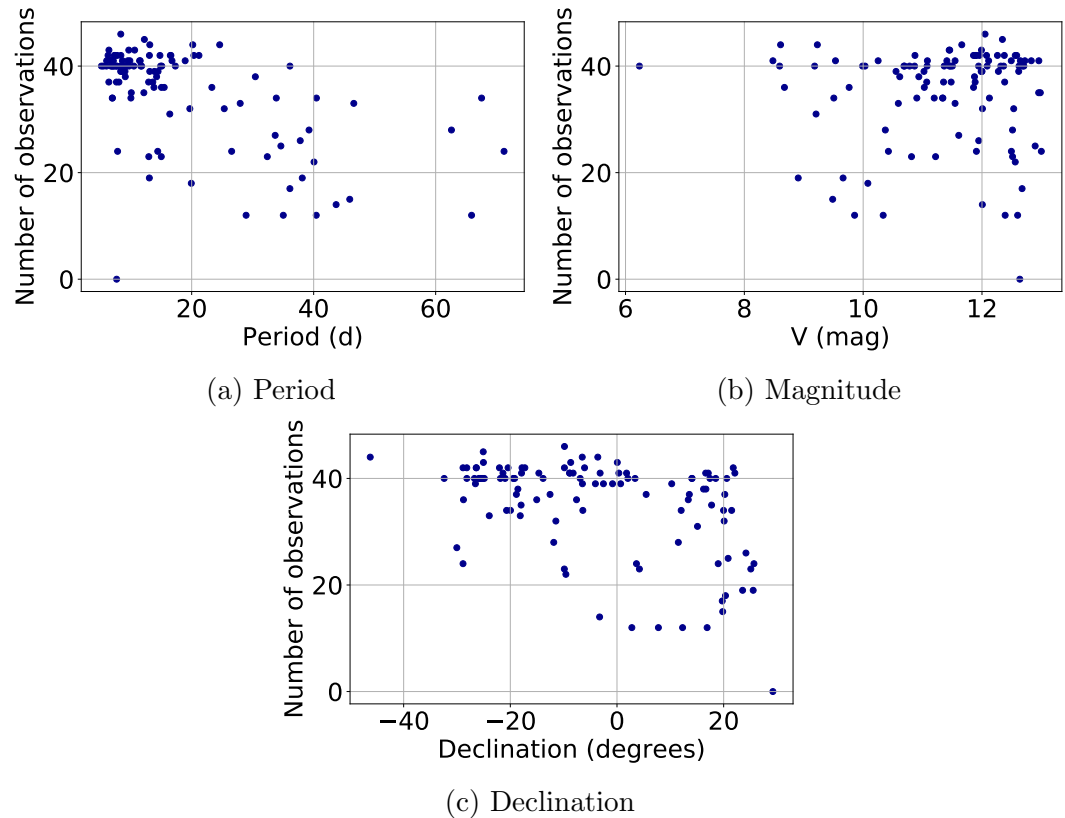
(c) Declination

Figure 3.10: Scatter plots showing how the distribution of observations per target depends on orbital period, magnitude and declination, for simulation D.

In Figure 3.9, we expect the distribution of observations per target to peak at 40, the minimum number of observations required to finish a target (10 bins with 4 observations). Some targets receive more observations than needed since the phase completeness score allows for an extra observation per bin before returning a score of zero.

I investigated the effects of period (Figure 3.10a), magnitude (Figure 3.10b) and declination (Figure 3.10c) on the number of observations each target received at the end of each simulation. The results from simulation D only are shown for clarity.

As seen in Figure 3.5a, the target database contains a bias towards systems with short orbital periods. Nevertheless, we still see a slight trend towards a short period

bias from the scheduler since the scheduler has a larger number of chances of selecting these targets than those which eclipse less frequently. This was not accounted for in the scoring model, so is not unexpected.

There is a higher frequency of faint targets in the database, however this hasn't resulted in a particularly strong observation preference to either faint or bright targets.

Targets with a declination close to the latitude of the observing site will spend more time directly overhead (and hence have a better average air mass) than targets with declinations far from the latitude. This was accounted for in the air mass score by making the score relative to the target's maximum possible air mass, however there is still bias towards southern hemisphere targets. The only target not observed by the scheduler is the target with the most northern declination, which justifies our decision to trim the target database at +30 degrees declination.

3.7 Examples of usage of the scheduler

In September 2019, Dr. Pierre Maxted used the scheduler to select and remotely observe two eclipsing binaries from the preliminary target catalog: LY Peg, a K-type giant orbiting a main sequence star, and SW2040-14. The multi-band light curves for LY Peg and SW2040-14, as taken by Xamidimura, are shown in Figures 3.11 and 3.12 respectively.

3.8 Discussion

The scheduler I have written for the Xamidimura instrument is working well and has been successfully implemented into the observing system. Running simulations based on historical weather logs has produced useful results which have already informed our decisions on which targets to include in the database, and which score weightings to use. Further improvement on the scheduler will require information from how the
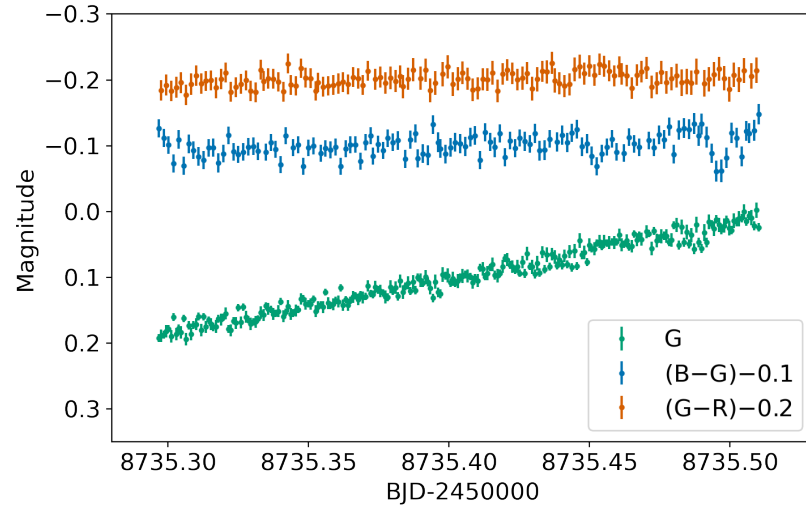
Figure 3.11: Light curve of eclipsing binary LY Peg selected by the scheduler and observed by Xamidimura in three optical bands (B,G,R) in 2019.
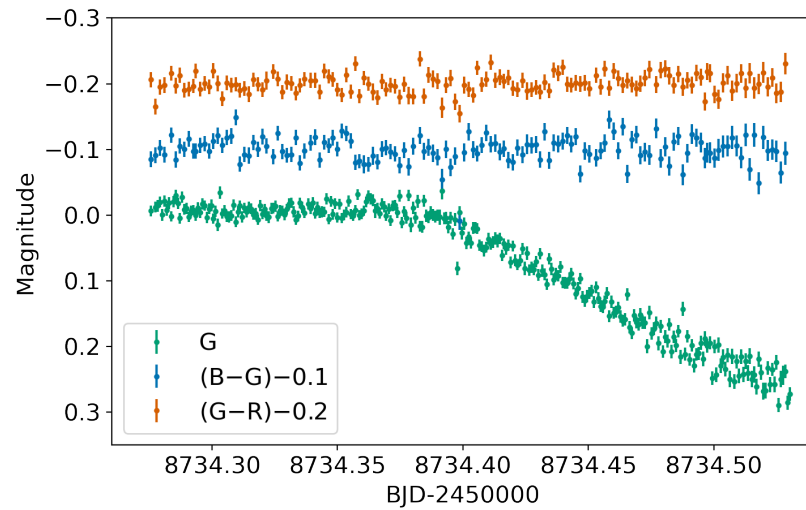
Figure 3.12: Light curve of eclipsing binary SW2040-14 selected by the scheduler and observed by Xamidimura in three optical bands (B,G,R) in 2019.

(a) WASP 0639-32   (b) SW0716+20
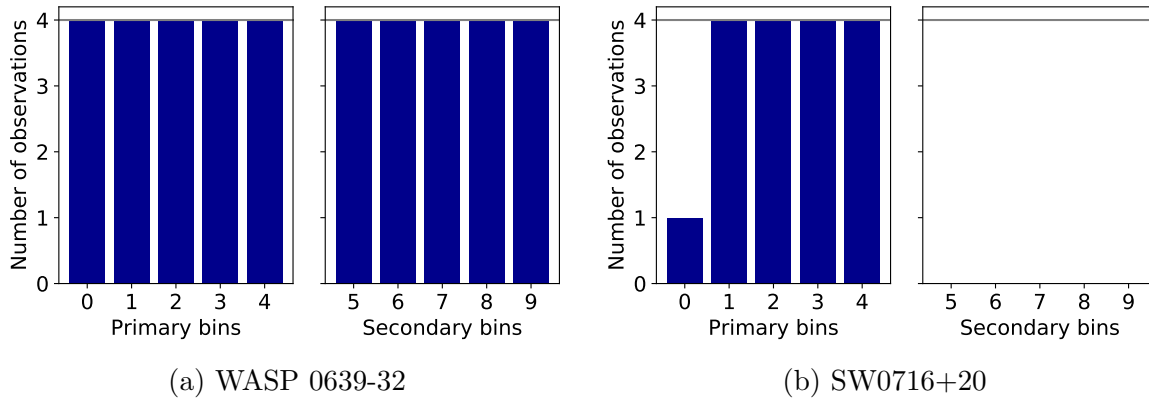
Figure 3.13: Observed phase bins for two targets in the Xamidimura database after running weather log simulations

telescopes behave in practice, particularly regarding slew speed, mechanical and wind–shake limits.

Since the Xamidimura telescopes are much more susceptible to wind shake than the WASP instrument was, in reality we may end up with less observing time than predicted. In the simulations, I also assume that each observation is successful, which may not be the case in reality, as images can be subject to technical, instrumental or observational problems that would render them unsuccessful.

Looking ahead to including *TESS* targets in the database, it will be beneficial to run a series of weather simulations on potential targets to ensure that both eclipses are feasible within the next 5 years of operation. We noticed that while some targets had both eclipses observed sufficiently, e.g. Figure 3.13a, others had orbital phases which meant only one eclipse was visible at night from SAAO for the duration of the simulations, e.g. Figure 3.13b.

Based on the results from the weather log simulations, we have noticed that the scheduler is idle for a significant proportion of the available observing time. While we intend much of this time to be taken up with new targets from TESS, we may need to include other targets such as photometric standard stars.

4 Fundamental effective temperatures measurements for AI Phoenicis

Things are only impossible until they're not.

Captain Jean-Luc Picard, *Star Trek: The Next Generation* (1988)

Note: The following chapter is heavily based on the paper "Fundamental effective temperature measurements for eclipsing binary stars - I. Development of the method and application to AI Phoenicis" (Miller et al. 2020; accepted in MNRAS, July 2020). The analysis and text were contributed by the author. The original idea and proof-of-concept for the effective temperature method, and the near-infrared flux ratio priors section were contributed by P. Maxted.

4.1 Introduction

We selected AI Phe as the first eclipsing binary to analyse with our method because this is a very well studied eclipsing binary that is moderately bright (V=8.6) for which good-quality light curves in several photometric bands are available from the near-ultraviolet (NUV) to the I-band, including a very high quality light curve from the *TESS* mission. Maxted et al. (2020) analysed the *TESS* light curve of AI Phe using several different methods and, in combination with spectroscopic orbits from 3 independent sources, were able to measure the masses and radii of both stars to an accuracy of better than 0.2%. This very high accuracy in the stellar radii is possible because AI Phe is a bright system with stars of similar brightness where the eclipses are total. This gives a direct measurement of the flux ratio for the binary from the depth of the eclipse where one star is completely occulted, and strong constraints on the geometry of the binary from the contact points of the eclipse. Limb darkening does add some uncertainty to the measurements of the radii. Maxted et al. (2020) accounted for this in their analysis by modelled the light curve using several different methods to parameterise

the limb darkening. Haberreiter et al. (2009) found that the radius of the apparent solar disc is 0.33 Mm larger than its Rosseland radius. Scaling this value according to the atmospheric pressure scale height we find that the Rosseland radii of the stars in AI Phe are approximately 0.1% smaller than the values given in Maxted et al. (2020). All radius values used in this paper refer to the Rosseland radius including this correction. AI Phe is an important system for testing stellar evolution models of single stars (e.g., Andersen et al., 1988; Pols et al., 1997; Ribas et al., 2000; Lastennet & Valls-Gabaud, 2002; Spada et al., 2013; Ghezzi & Johnson, 2015; Higl & Weiss, 2017) so we felt it would be valuable to have effective temperature estimates of comparable accuracy to the masses and radii measured by Maxted et al. (2020).

4.2   Data

4.2.1   *Gaia* parallax and stellar radii

The input data for our analysis of AI Phe are listed in Tables 4.1, 4.2 and 4.3. For the parallax, which we take to be 5.885 ± 0.019 mas, we used the average of the orbital parallax from Gallenne et al. (2019, 5.905 ± 0.024 mas) and the value from the *Gaia* DR2 catalogue (5.8336 ± 0.0262 mas; *Gaia* collaboration 2018) including the zero-point correction from Graczyk et al. (2019), -0.031 ± 0.011 mas. For the errors on the radii, we use the sum of the random and systematic errors quoted in Maxted et al. (2020). The radii used to calculate the angular diameters used in the T_{eff} calculation are given in Table 4.6.

4.2.2   Catalog photometry

The *Gaia* G, BP and RP magnitudes are also from the *Gaia* DR2 catalogue and include the correction from Casagrande & VandenBerg (2018) that is required to make these magnitudes consistent with the CALSPEC flux scale. WISE magnitudes are taken from the All-Sky Release Catalog (Cutri & et al., 2012) because we find that
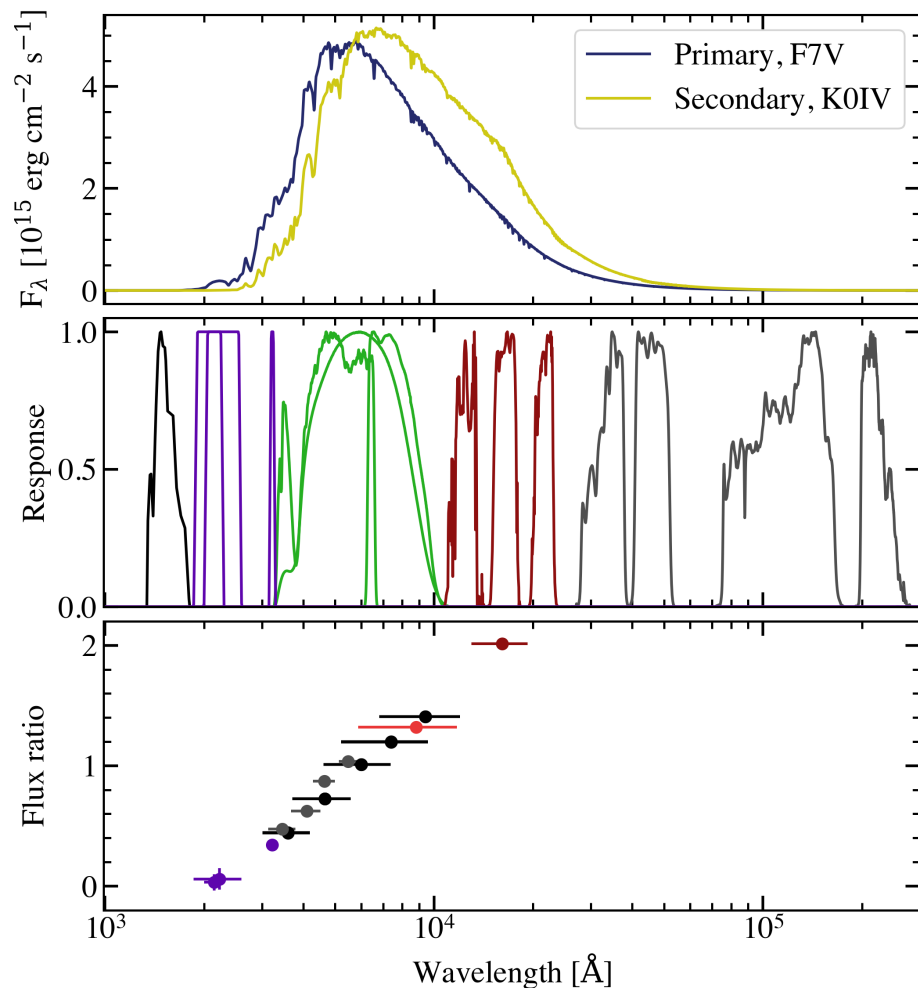
Figure 4.1: Multi-panel plot showing data we used in our analysis. *Top*: BT-Settl 1D model SEDs for the two stars: primary $T_{\mathrm{eff},1} = 6200\,\mathrm{K}$, $\log g = 3.5$, [Fe/H] $= -0.14$, [α/Fe] $= 0.06$; secondary $T_{\mathrm{eff},2} = 5100\,\mathrm{K}$, $\log g = 4.0$, [Fe/H] $= -0.14$, [α/Fe] $= 0.06$. These have been brought onto the same scale by multiplying by r_1^2 and r_2^2 respectively, where $r = R/a$. *Middle*: Filter response profiles for apparent magnitude data. In order of increasing wavelength: *GALEX FUV*, *IUE* (see Section 4.2.3), *Gaia BP*, *G* and *RP*, 2MASS *JHKs*, WISE *W*1-4. *Bottom*: Observed flux ratio values and standard errors from *IUE*, Strömgren *uvby*, Johnson *UBVRI*, *TESS*, and *H* plotted over the associated bandpass, centred on pivot wavelength.

Table 4.1: Angular diameters used in our analysis, along with predicted values and residuals for the best-fit model from Run A.

Quantity	Input	Output	Residual	Source
θ_1	0.0988 ± 0.0004	0.0989 ± 0.0004	$+0.0000 \pm 0.0006$	$2R_1\varpi$
θ_2	0.1606 ± 0.0005	0.1605 ± 0.0006	-0.0001 ± 0.0007	$2R_2\varpi$

the photometry is more reliable for bright stars in this catalogue than the ALLWISE catalogue. [1] The standard error estimates for the Strömgren photometric indices are taken from Olsen (1994).

Flux ratios from the analysis of the $UBVRI$ and $uvby$ light curves are taken from Andersen et al. (1988). These should be very reliable because the primary eclipse is total, i.e. the flux ratio is determined directly from the depth of the eclipse. For the flux ratio in the $TESS$ band we take the mean value with its standard deviation from the results presented in Maxted et al. (2020) using a variety of analysis methods. We also include the flux ratio value 2.012 measured in the H-band using the VLTI interferometer by Gallenne et al. (2019). The bandpass for this flux ratio measurement is not well defined so we assign a nominal error to this value of 0.01, and use the 2MASS H-band to calculate the flux ratio for the measurement.

4.2.3   Ultraviolet photometry and flux ratios

The near-UV band contains a significant portion of the total flux, therefore including photometry measurements in this region is useful for constraining the shape of the SED. AI Phe has archival $GALEX\ NUV$, FUV fluxes and IUE spectra. Recent

---

[1] `http://wise2.ipac.caltech.edu/docs/release/allwise/`

Table 4.2: Observed magnitudes and Strömgren photometry along with predicted values and residuals for the best-fit model from Run A.

Band	Observed	Synthetic	Residual	Source
FUV	20.473 ± 0.160	20.27 ± 0.13	$+0.20 \pm 0.21$	$GALEX$
$u320$	10.734 ± 0.035	10.750 ± 0.043	-0.016 ± 0.056	This work
$u220n$	13.932 ± 0.100	14.029 ± 0.043	$+0.037 \pm 0.126$	"
$u220w$	14.066 ± 0.199	14.000 ± 0.043	-0.068 ± 0.109	"
G	8.443 ± 0.0002	8.440 ± 0.001	$+0.003 \pm 0.001$	$Gaia$ DR2
BP	8.798 ± 0.001	8.809 ± 0.001	-0.011 ± 0.001	"
RP	7.914 ± 0.001	7.904 ± 0.004	$+0.009 \pm 0.004$	"
J	7.301 ± 0.023	7.293 ± 0.005	$+0.008 \pm 0.024$	2MASS
H	6.935 ± 0.034	6.910 ± 0.005	$+0.025 \pm 0.034$	"
Ks	6.819 ± 0.026	6.794 ± 0.005	$+0.025 \pm 0.026$	"
$W1$	6.747 ± 0.037	6.722 ± 0.002	$+0.025 \pm 0.037$	WISE
$W2$	6.830 ± 0.022	6.837 ± 0.002	-0.007 ± 0.0022	"
$W3$	6.811 ± 0.016	6.805 ± 0.002	$+0.006 \pm 0.016$	"
$W4$	6.768 ± 0.061	6.709 ± 0.002	$+0.059 \pm 0.061$	"
Strömgren photometry				
$(b-y)$	0.431 ± 0.0037	0.461 ± 0.004	-0.030 ± 0.006	Holmberg et al. (2009)
m_1	0.209 ± 0.0041	0.153 ± 0.006	$+0.056 \pm 0.007$	"
c_1	0.356 ± 0.0066	0.461 ± 0.008	-0.105 ± 0.011	"
$(b-y)$	0.424 ± 0.0037	0.461 ± 0.004	-0.037 ± 0.006	Reipurth (1978)
m_1	0.219 ± 0.0041	0.153 ± 0.006	$+0.066 \pm 0.007$	"
c_1	0.357 ± 0.0066	0.461 ± 0.008	-0.104 ± 0.011	"

Table 4.3: Observed flux ratios along with predicted values and residuals for the best-fit model from Run A.

Band	Observed	Synthetic	Residual	Source
$u320$	0.342 ± 0.042	0.414	0.342 ± 0.042	This work
$u220n$	0.030 ± 0.066	0.048	0.059 ± 0.090	"
$u220w$	0.059 ± 0.090	0.025	0.030 ± 0.066	"
U	0.442 ± 0.021	0.467	0.442 ± 0.021	Andersen et al. (1988)
U	0.446 ± 0.020	0.467	0.446 ± 0.020	"
B	0.725 ± 0.011	0.731	0.725 ± 0.011	"
B	0.727 ± 0.011	0.731	0.727 ± 0.011	"
V	1.011 ± 0.009	1.005	1.011 ± 0.009	"
V	1.011 ± 0.009	1.005	1.011 ± 0.009	"
R	1.197 ± 0.024	1.206	1.197 ± 0.024	"
R	1.198 ± 0.024	1.206	1.198 ± 0.024	"
I	1.406 ± 0.023	1.374	1.406 ± 0.023	"
I	1.406 ± 0.023	1.374	1.406 ± 0.023	"
u	0.475 ± 0.017	0.443	0.475 ± 0.017	"
v	0.624 ± 0.009	0.635	0.624 ± 0.009	"
b	0.870 ± 0.006	0.835	0.870 ± 0.006	"
y	1.036 ± 0.007	1.007	1.036 ± 0.007	"
$TESS$	1.319 ± 0.001	1.324	1.319 ± 0.001	Maxted et al. (2020)
H	2.012 ± 0.010	2.017	2.012 ± 0.010	Gallenne et al. (2019)
Priors on near-infrared flux ratios				
J	–	1.658	$+0.030 \pm 0.023$	This work
H	–	2.017	$+0.014 \pm 0.033$	"
Ks	–	2.076	$+0.059 \pm 0.030$	"
$W1$	–	2.103	$+0.053 \pm 0.044$	"
$W2$	–	2.134	$+0.047 \pm 0.073$	"
$W3$	–	2.198	$+0.003 \pm 0.042$	"
$W4$	–	2.143	$+0.059 \pm 0.078$	"

Table 4.4: Properties of our *IUE* trapezoidal band passes: pivot wavelength λ_{pivot}, minimum λ_{min} and maximum λ_{max} wavelengths at which the band pass is defined, and the wavelength range over which to taper, λ_{soft}.

Band	λ_{pivot} [Å]	λ_{min} [Å]	λ_{max} [Å]	$\Delta\lambda_{\mathrm{soft}}$ [Å]
$u320$	3224	3151	3298	50
$u220w$	2221	1860	2600	50
$u220n$	2149	2000	2300	50

studies into the absolute photometric calibrations of *GALEX* magnitudes find a nonlinear offset between archive and comparison fluxes, particularly for bright stars in the *NUV* (Camarota & Holberg, 2014; Wall et al., 2019). We compared the observed and calculated *NUV* magnitudes for a set of FGK dwarfs with corrected archive *GALEX* magnitudes and CALSPEC spectra (Bohlin et al., 2014). We found that the scatter was too large for us to confidently rely on the *GALEX NUV* magnitude for stars of comparable brightness to AI Phe so we decided to not include it in our dataset.

Milone et al. (1981) obtained a series of spectra of AI Phe during primary minimum with the International Ultraviolet Explorer (*IUE*) satellite. We downloaded the data from the *IUE* NEWSIPS archive[2] and applied the wavelength-dependent corrections suggested by Bohlin & Bianchi (2019) to put the flux on the CALSPEC scale. We created three trapezoidal filters with which to integrate the *IUE* spectra, the properties of which are given in Table 4.4. Quality flags on the data restricted the range of useful wavelengths we could use, so we placed one filter at 3200Å (*u320*) to capture the majority of flux, and two (narrow and wide) around the 2175Å absorption feature due to interstellar extinction (*u220n*, *u220w*) to investigate whether we could use this feature to constrain the reddening.

---

[2]`https://archive.stsci.edu/iue/newsips/newsips.html`
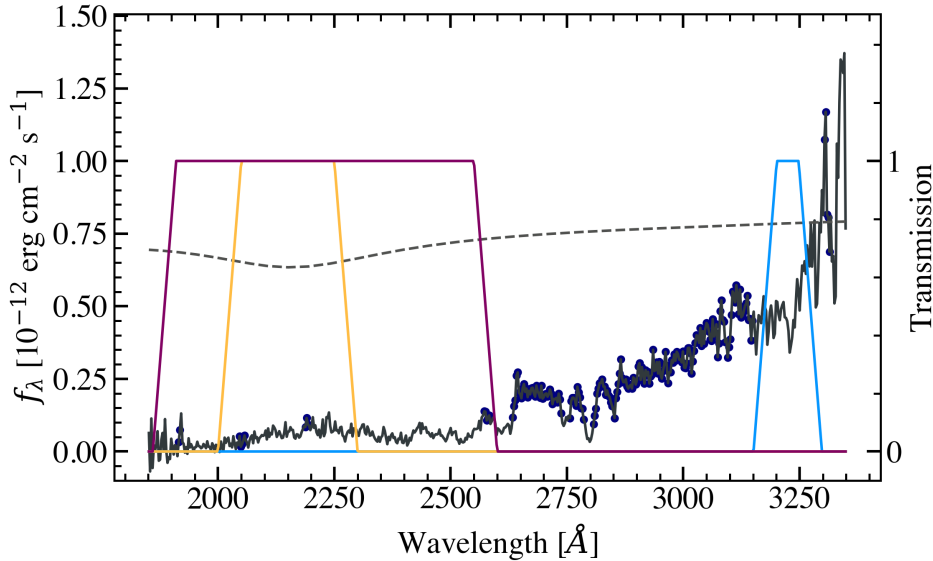
Figure 4.2: *IUE* spectrum of AI Phe outside of primary minimum, with poor quality data marked (circles). Also shown are transmission profiles of the three filters *u320* (purple), *u220w* (blue) and *u220n* (yellow) and an extinction profile for *E(B−V)*=0.05 (dotted line) to illustrate the location of the 2175Å absorption feature.

We integrated the mean flux in each filter using Equation A5 from Bessell & Murphy (2012),

$$\langle f_\nu \rangle = \frac{\int f_\nu(\nu) R_\nu(\nu) d\nu}{\int R_\nu d\nu},$$

and constructed light curves for each band. We fitted each with an ellc light curve model (Maxted, 2016), using a POWER2 limb darkening law with coefficients calculated from STAGGER 3D atmospheric models. The primary eclipse of AI Phe is total so the choice of limb darkening model is less important, and we obtained similar results with linear and POWER2 limb darkening models. We used emcee to sample the posterior distribution with the flux out of eclipse, flux ratio and log(f) as free parameters. The maximum likelihood values for flux out of eclipse were then converted to an AB magnitude included as input data in our analysis, along with values for the flux ratio between the two stars.

4.2.4   Synthetic photometry

Comparing synthetic magnitudes calculated from the SED of a star to observed magnitudes requires some care. We found appendix A of Bessell & Murphy (2012) to be a very helpful introduction to the subject of synthetic photometry.

For the *GALEX FUV* band we used the response function published on the *GALEX* web pages[3]. For the error on the zero-point of the *GALEX* AB magnitude scale we use the value 0.134 mag from Camarota & Holberg (2014). For the *Gaia* photometry we use the revised response functions and zero-points from Evans et al. (2018). The 2MASS response functions were obtained from the Explanatory Supplement to the 2MASS All Sky Data Release[4]. The zero-points with their standard errors are taken from Maíz Apellániz & Pantaleoni González (2018). For the WISE photometry we calculate synthetic magnitudes on the AB magnitude scale and then apply the corrections to Vega magnitudes from Jarrett et al. (2011) for which the estimated error is 1.45% (0.016 mag). For the *IUE* NEWSIPS spectra we adopted a zero point error of 4% from Nichols & Linsky (1996).

4.2.5   Interstellar reddening

Figure 4.3 shows a selection of HARPS spectra of AI Phe obtained from the ESO Science Archive Facility in the region of the Na I doublet. There are no detectable interstellar absorption lines in this region and so the reddening towards AI Phe must be very close to $E(B-V) = 0$ (Karataş & Schuster, 2010). Accordingly, we set a Gaussian prior on the reddening $E(B-V) = 0 \pm 0.005$ and set a lower limit $E(B-V) \geq 0$.

---

[3]https://asd.gsfc.nasa.gov/archive/galex/tools/Resolution_Response
[4]https://old.ipac.caltech.edu/2mass/releases/allsky/doc/explsup.html
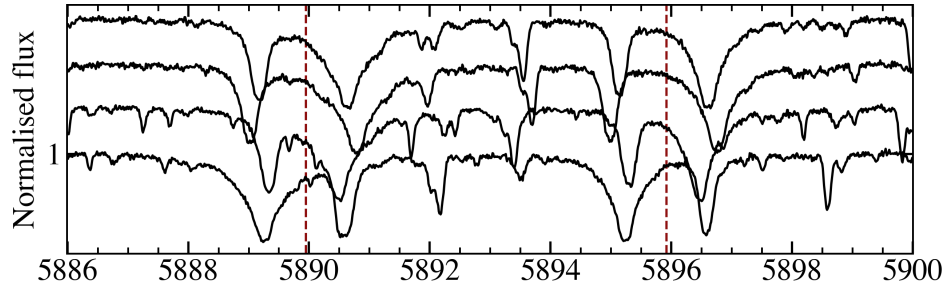
Figure 4.3: HARPS spectra of AI Phe in the region of the Na I doublet. The spectra have been normalized and vertically offset for clarity. The rest wavelengths of the Na I lines are indicated by vertical dashed lines.

4.2.6 Priors on infrared flux ratios

The near-infrared (NIR) flux from solar-type stars compared to the total flux or the flux at optical wavelengths shows a well-defined relationship with T_{eff} that is almost linear and that has little dependence on metallicity or surface gravity. This is the basis of the infrared flux method (Blackwell et al., 1979; Casagrande et al., 2010) or the use of colours such as $(V - K_{\mathrm{s}})$ to estimate effective temperatures for FGK-type stars (Boyajian et al., 2013). There is only one direct measurements of the flux ratio for AI Phe at wavelengths longer than $1\,\mu$m. We were concerned that not imposing any additional constraints on the flux ratio at these wavelengths could mean that the resulting models become unrealistic, e.g., the $(V - K_s)$ colours computed using samples from $P(M|D)$ might show a much large scatter than is observed in real stars. This could happen if the use of distortion coefficients allows for models where the flux from one star is unrealistically high at NIR wavelengths while the other is too low, unless some constraint in placed on the flux ratio at these wavelengths. We address this concern by making the assumption that the stars in AI Phe behave similarly to other dwarf and sub-giant FGK-type stars in the solar neighbourhood in order to put some constraint on the flux ratio in the 2MASS J, H and K_s bands, and the WISE $W1$, $W2$, $W3$ and $W4$ bands. We use stars from the Geneva-Copenhagen survey (Holmberg et al., 2009) to define relationships between T_{eff} and $(V - J)$, $(V - H)$, etc. The values

of $T_{\rm eff}$, $E(B-V)$, $\log g$ and [Fe/H] for each star are taken from Casagrande et al. (2011). We define separate relations for the F7 V star and the K0 IV star based on a different sub-sample of stars with similar properties to each. For the F7 V star the sub-sample is defined by the following limits:

- [Fe/H] > -0.5

- $E(B-V) < 0.05$

- $3.5 < \log g < 4.5$

- $6200\,{\rm K} < T_{\rm eff} < 6600\,{\rm K}$.

For the K0 IV star the limits on [Fe/H] and $E(B-V)$ are the same but for effective temperature and surface gravity we use the following limits:

- $3.0 < \log g < 4.5$

- $4900\,{\rm K} < T_{\rm eff} < 5500\,{\rm K}$.

Both sub-samples were cross-matched with the WISE All Sky Data release (Cutri & et al., 2012) using VO tools within TOPCAT (Taylor, 2017) and matching radius of 6 arcsec. Duplicate sources were removed from the sub-samples, leaving 4123 stars in the sub-sample for the F7 V star and 556 stars in the sub-sample for the K0 IV star. Linear relations for the colours of these stars corrected for extinction of the form

$$(V - X)_0 = c + m \times (T_{\rm eff} - T_{\rm ref})/1000\,{\rm K}$$

were established using the median value of the sample and the robust Theil-Sen estimator of the slope, as implemented in python function `scipy.stats.mstats.theilslopes`. The scatter around these relations was measured using the root-mean-square of the residuals within 5 times the median absolute deviation from the fit. The results are given in Table 4.5 and the fit to the data for $(V - K_s)$ is shown in Figure 4.4. The flux ratio in each band is calculated anew from the values of $T_{\rm eff,1}$, $T_{\rm eff,2}$ and the V-band flux

Table 4.5: Results for robust linear fits to extinction-corrected $(V - X)_0$ colours for selected stars in the solar neighbourhood.

X	$T_{ref} = 6400\,K$			$T_{ref} = 5200\,K$		
	c	m	rms	c	m	rms
J	0.919	−0.408	0.015	1.511	−0.605	0.018
H	1.118	−0.549	0.019	1.918	−0.821	0.027
K_s	1.181	−0.564	0.017	2.033	−0.872	0.025
$W1$	1.230	−0.568	0.027	2.094	−0.865	0.035
$W2$	1.234	−0.547	0.039	2.101	−0.928	0.062
$W3$	1.182	−0.554	0.021	2.062	−0.907	0.036
$W4$	1.225	−0.519	0.050	2.095	−0.951	0.060

ratio for each trail chain step, but otherwise are included in the calculation of the like-lihood in the same way as the directly measured flux ratios. The flux ratio in the $W1$ band as a function of the effective temperature ratio is shown in Figure 4.5 for every pairing of stars from the two sub-samples excluding stars more than 5-sigma from the appropriate linear T_{eff}–$(V - W1)$ relation. There is a well-defined correlation between the flux ratio and the effective temperature ratio relation which is accurately predicted by our linear relations, despite the fact that we have paired stars with disparate [Fe/H] and $\log g$ values.

4.3   Results

The results of 14 fits using different sets of input parameters are given in Table 4.7. By testing the effects of our inputs, we were able to characterise the method — see Section 4.4. We adopt the values from Run A as our final results for T_{eff}: $6193 \pm 24\,K$ for the F7 V component and $5090 \pm 17\,K$ for the K0 IV component. We give the
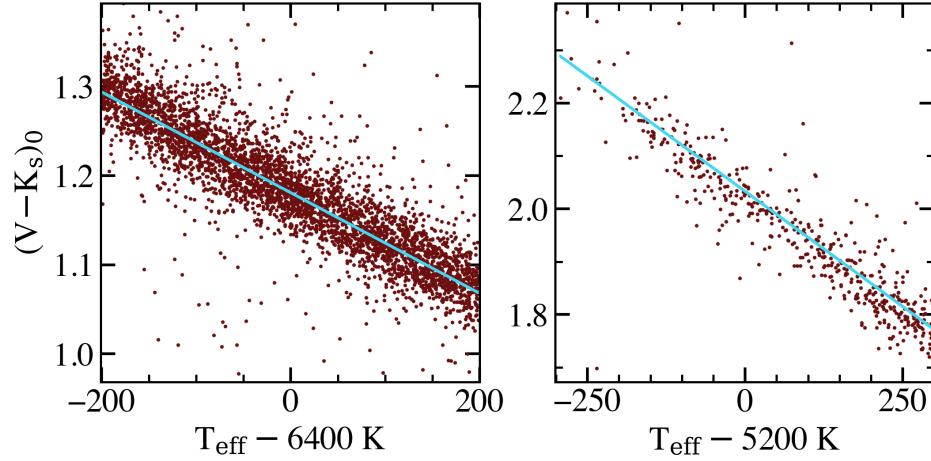
Figure 4.4: De-reddened $V - K$ colours of F-type dwarfs stars (left panel) and G/K-type sub-giants (right panel) in the solar neighbourhood. The turquoise lines show the linear fits to these data described in Section 4.2.6.
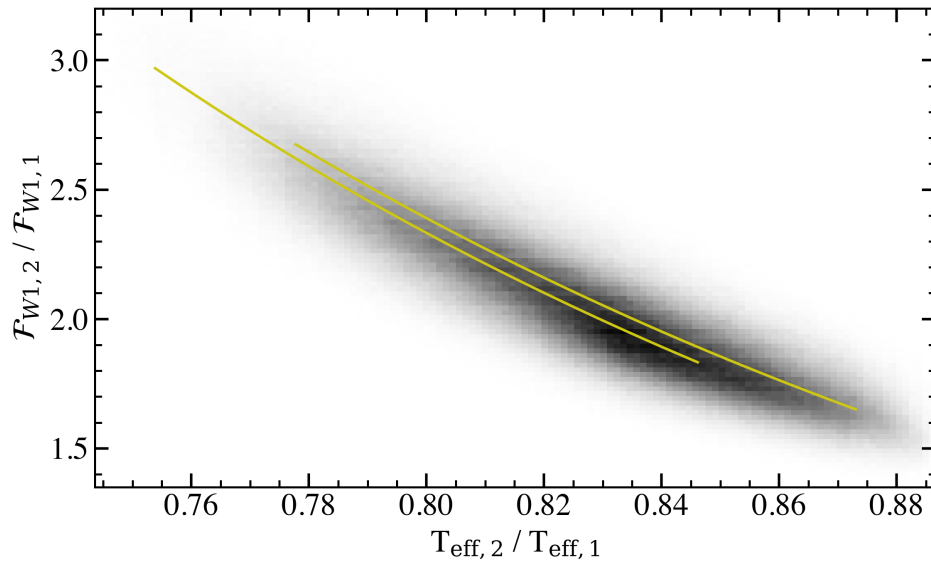
Figure 4.5: Flux ratios in the WISE W1 band for G/K-type sub-giants relative to F-type dwarfs stars in the solar neighbourhood. The fluxes have been scaled so that the flux ratio in the V-band is 1. The orange lines show the flux ratio predicted by our linear $T_{\mathrm{eff}} - (V{-}W1)$ relations assuming T_{eff} 6300 K or 6500 K.

Table 4.6: Fundamental parameters of AI Phe from this work and Maxted et al. (2020). The radii here are Rosseland radii, calculated by applying a small correction to the radii obtained from the analysis of the eclipses by Maxted et al. (2020) All quantities are given in nominal solar units (Prša et al., 2016)

Parameter	Value	Source
$M_1/\mathcal{M}_\odot^{\rm N}$	1.1938 ± 0.0008	Maxted et al. (2020)
$M_2/\mathcal{M}_\odot^{\rm N}$	1.2438 ± 0.0008	”
$R_1/\mathcal{R}_\odot^{\rm N}$	1.8036 ± 0.0022	”
$R_2/\mathcal{R}_\odot^{\rm N}$	2.9303 ± 0.0023	”
$T_1/\mathcal{T}_\odot^{\rm N}$	1.074 ± 0.004	This work
$T_2/\mathcal{T}_\odot^{\rm N}$	0.882 ± 0.003	”
$L_1/\mathcal{L}_\odot^{\rm N}$	4.329 ± 0.0627	”
$L_2/\mathcal{L}_\odot^{\rm N}$	5.207 ± 0.065	”

fundamental parameters of AI Phe from this work and Maxted et al. (2020) in Table 4.6 for reference. The output integrating function and distortion functions for this solution are shown in Figure 4.8. For our adopted run, we used 256 walkers randomly dispersed close to the Nelder-Mead best fit solution and ran the chain over 10000 steps with a burn-in of 4000. The resultant distributions of parameters (distortion coefficients excluded for clarity) can be seen in Figure 4.6.

Some care must be taken when using MCMC methods to explore a model parameter space with many dimensions because of the possibility that the likelihood function has more than one maximum, or that the PPD has a complex shape. Either of these possibilities makes it difficult to fully sample the PPD. This problem can be avoided by using model parameters that are closely related to features visible in the data. Legendre polynomials are orthogonal to one another, i.e.,

$$\int_0^1 \bar{P}_m(x)\bar{P}_n(x)dx = \frac{1}{2n+1}\delta_{mn}$$
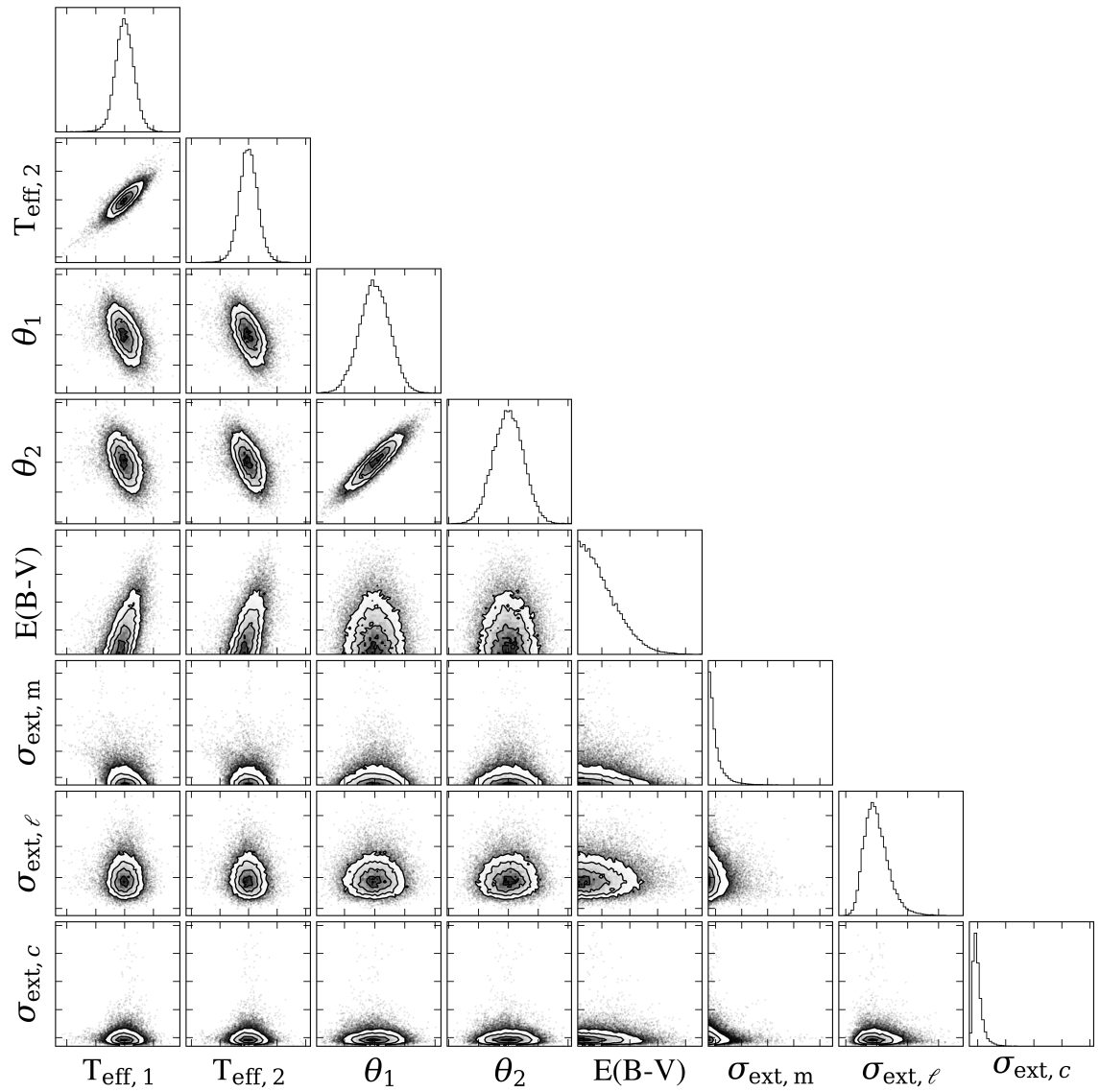
Figure 4.6: Contour plot of the eight main parameters used in our MCMC analysis, for our primary Run A in Table 4.7.
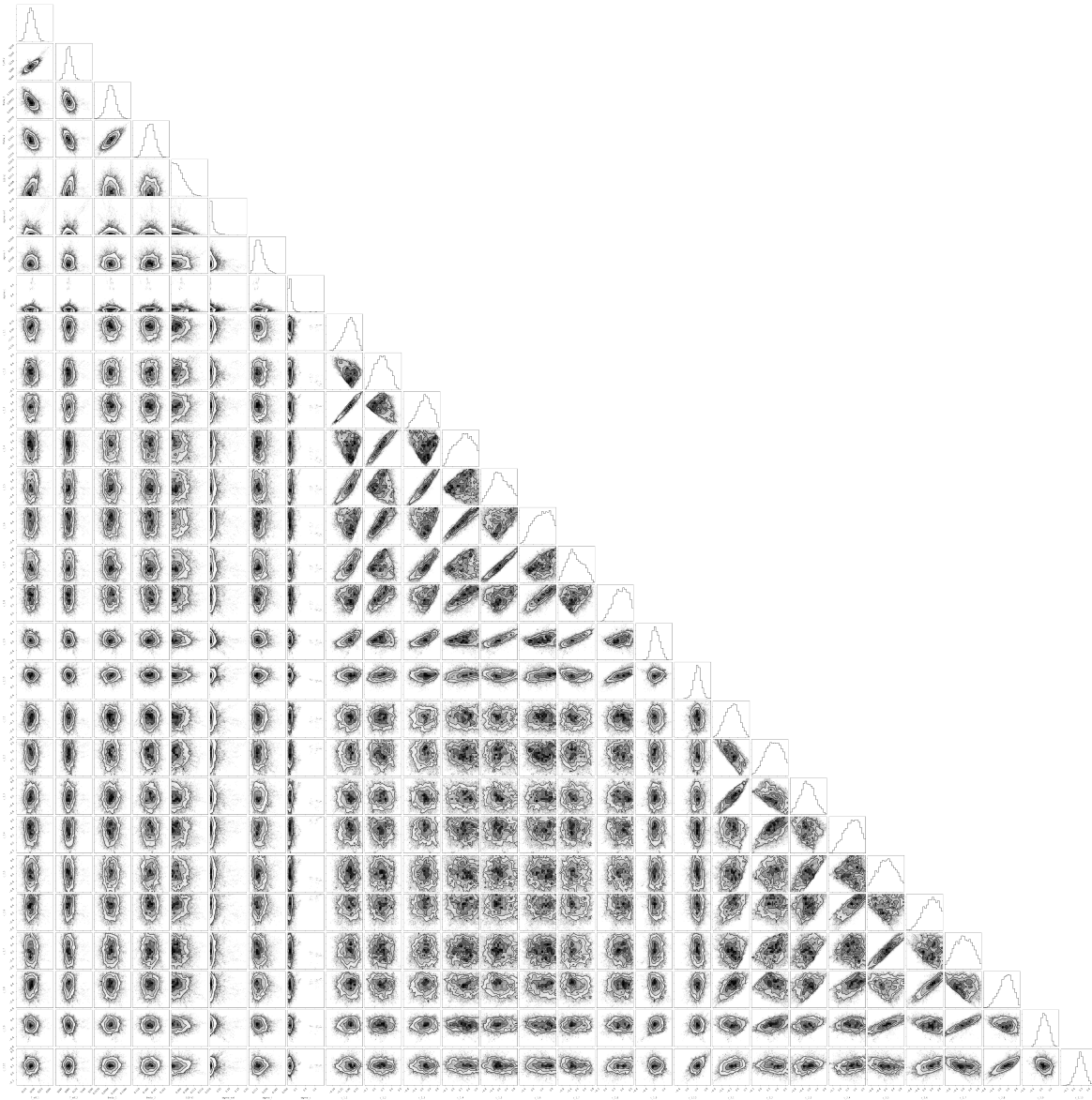
Figure 4.7: Contour plot for the complete set of parameters used in the MCMC analysis for our primary run A in Table 4.7. The first eight parameters are those shown in Figure 4.6, the next ten are the distortion coefficients for the primary star, and the final ten are those for the secondary star.

We therefore expect that any linear combination of these polynomials that can give a good fit to the data will have coefficients with similar values.

As expected, there is some correlation between the distortion coefficients, but the Legendre polynomials are well-behaved and the probability distributions are unimodal. Therefore the correlation is not an issue, since the affine-invariant MCMC algorithm is able to properly account for correlation in unimodal distributions. Our effective temperatures are correlated, with a Pearson correlation coefficient of 0.805. An irreducible error in our analysis is the uncertainty in the flux of Vega that sets the zero-points of the photometric systems we have used. We use the value 0.5% for the uncertainty in the flux of Vega at 5556Å from Bohlin et al. (2014) together with the wavelength-dependent error in the flux scale shown in their Figure 14 to estimate the systematic error in our T_{eff} values from this zero-point error. By adding both these errors to the best-fit SED of each star we find that the systematic error in the integrated flux is 0.8% for both stars, so the systematic errors in T_{eff} are 12 K for the F7 V star and 10 K for the K0 IV star. For most applications, the random and systematic errors can simply be added, but there are applications where the systematic error should be only added once, for example, light curve models which use the parameters $T_{\mathrm{eff},1}$ and $T_{\mathrm{eff},2}/T_{\mathrm{eff},1}$. We also calculated stellar luminosities by exploring the parameter space of T_{eff}, R and ϖ for each star with emcee. We find that $\log(L_1/L_\odot) = 0.636 \pm 0.007$ and $\log(L_2/L_\odot) = 0.717 \pm 0.005$, and correlations between the free parameters are shown in Figure 4.9.
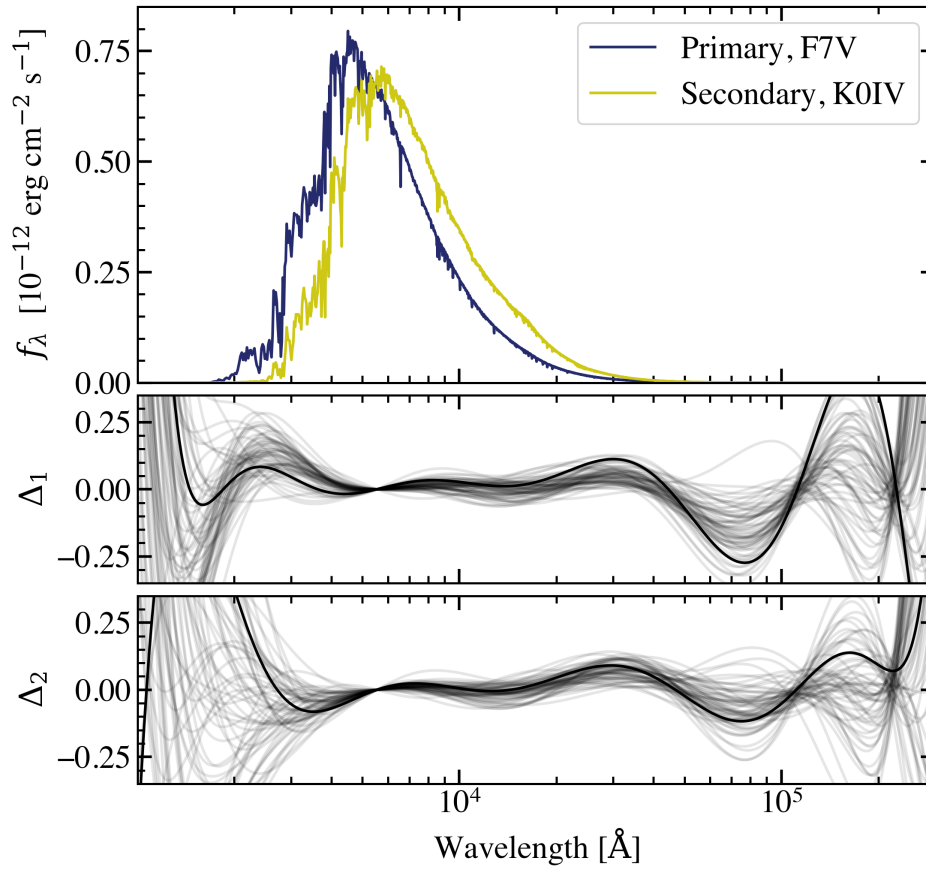
Figure 4.8: Integrating functions and distortion functions, as defined in Equation 2.14, for our best solution (Run A). *Top*: Maximum likelihood integrating functions of the two stars. *Middle*: The distortion functions applied to the model SED for the primary star, showing maximum likelihood fit (thick line) and all other solutions. *Lower*: Same, but for the secondary star.
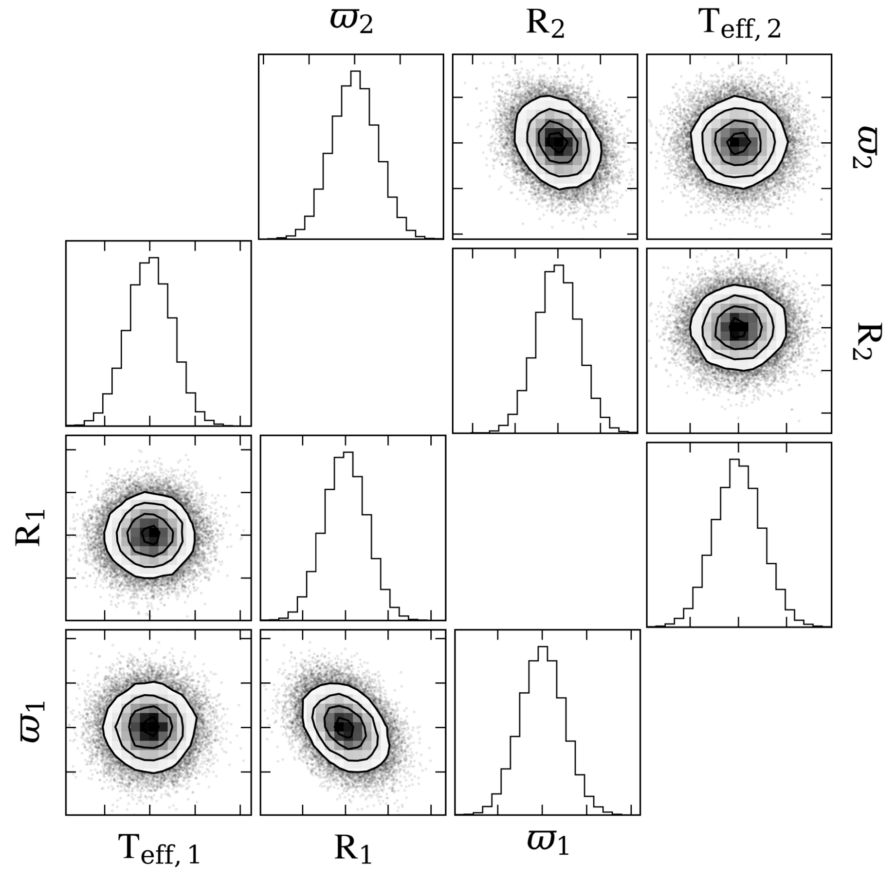
Figure 4.9: Contour plot of the parameters used to calculate stellar luminosities.

Table 4.7: Fit results from different sets of input parameters. Run A is our adopted output. Values in parentheses are 1-σ standard errors in the final digit(s) of the preceding value. N_Δ is the number of distortion coefficients included per star, $\Delta\lambda$ is the size of the integrating function wavelength bins in Å. *N.B. these parameters have a non-Gaussian probability distribution. $E(B{-}V)$ are given as 1-σ upper limits.

Run	N_Δ	$\Delta\lambda$ [Å]	$T_{\mathrm{mod},1}$ [K]	$T_{\mathrm{mod},2}$ [K]	[Fe/H] [dex]	[α/Fe] [dex]	$T_{\mathrm{eff},1}$ [K]	$T_{\mathrm{eff},2}$ [K]	$E(B{-}V)$* [mag]	$\sigma_{\mathrm{ext,m}}$* [mag]	$\sigma_{\mathrm{ext},\ell}$* [mag]	$\sigma_{\mathrm{ext,c}}$* [mag]	$\mathrm{rms}_{\Delta,1}$	$\mathrm{rms}_{\Delta,2}$
A	10	20	6200	5100	-0.14	0.06	6199 ± 22	5094 ± 16	< 0.004	0.01(2)	0.02(1)	0.09(4)	0.04(2)	0.04(2)
B	10	50	6200	5100	-0.14	0.06	6197 ± 22	5093 ± 17	< 0.004	0.01(2)	0.02(1)	0.09(4)	0.04(1)	0.04(1)
C	10	50	6250	5050	-0.14	0.06	6196 ± 40	5090 ± 29	< 0.005	0.02(4)	0.02(1)	0.09(3)	0.05(4)	0.06(4)
D	6	50	6200	5100	-0.14	0.06	6197 ± 20	5095 ± 15	< 0.004	0.01(1)	0.02(1)	0.10(5)	0.02(1)	0.02(1)
E	14	50	6200	5100	-0.14	0.06	6193 ± 32	5091 ± 24	< 0.005	0.03(3)	0.02(1)	0.08(3)	0.06(4)	0.058(4)
F	10	50	6200	5100	0	0	6192 ± 23	5089 ± 18	< 0.004	0.02(2)	0.02(1)	0.10(3)	0.06(2)	0.04(2)
G	10	50	6200	5100	-0.5	0.2	6198 ± 22	5092 ± 16	< 0.005	0.01(2)	0.02(1)	0.08(3)	0.05(1)	0.06(1)
H[1]	10	50	6200	5100	-0.14	0.06	6196 ± 20	5091 ± 15	< 0.004	0.01(1)	0.02(1)	0.10(4)	0.03(1)	0.03(1)
I[2]	10	50	6200	5100	-0.14	0.06	6287 ± 87	5146 ± 56	< 0.03	0.02(4)	0.02(1)	0.09(3)	0.07(4)	0.05(4)
J	0	50	6200	5100	-0.14	0.06	6196 ± 18	5098 ± 13	< 0.005	0.01(1)	0.03(1)	0.10(4)	−	−
K[3]	10	50	6200	5100	-0.14	0.06	6332 ± 120	5171 ± 76	< 0.04	0.01(2)	0.02(1)	0.08(3)	0.07(4)	0.06(3)
L[4]	10	50	6200	5100	-0.14	0.06	6194 ± 23	5091 ± 17	< 0.004	0.01(2)	0.02(1)	0.09(3)	0.03(2)	0.04(2)
M[5]	10	50	6200	5100	-0.14	0.06	6217 ± 86	5072 ± 65	< 0.005	0.02(3)	0.01(1)	0.09(4)	0.06(3)	0.08(5)
N[6]	10	50	6200	5100	-0.14	0.06	6196 ± 21	5092 ± 15	< 0.005	0.01(2)	0.02(1)	0.09(4)	0.04(2)	0.036(2)

[1] No NIR prior used. [2] No $E(B{-}V)$ prior used. [3] No $E(B{-}V)$ prior or u220n data used. [4] No u220n data used. [5] Only *TESS* band flux ratio used. [6] NIR prior model temperatures shifted up by 100 K.

4.4   Discussion

4.4.1   Distortion functions

We need to include enough distortion to avoid just performing an SED fit (see Run J in Table 4.7; uncertainties in parameters are underestimated), but not so much that the distortion of SEDs becomes non-physical. Therefore in order to better understand how much distortion is needed in our approach, we looked into the difference between one-dimensional and three-dimensional stellar models. Comparing BT-Settl and STAGGER-3D models of similar temperatures, we found that the rms difference between the two models for the primary was 0.027, and the secondary was 0.025 — i.e. the difference between 1-D and 3-D models is about 3%. Most of this difference lies in the UV and, if smoothed, looks like a moderately high order (6-12) polynomial in logarithmic space. Therefore we chose to use this type of distortion in our method.

In order to be sure that we used a reasonable number of distortion coefficients, we performed some extra tests on the code to characterise the effects of distortion. We looked into the range of $0 \leq N_\Delta \leq 20$; being sure that on the scale of absorption lines and features, the highest order of these Legendre polynomials are linear and have no unrealistic effects. We quantified the amount of distortion with the following:

$$\mathrm{rms} = \sqrt{\frac{\int F_1^m(\lambda)\Delta_1^2 d\lambda}{\int F_1^m(\lambda)d\lambda}}$$

We note a steady rise in the amount of distortion used with number of coefficients. A choice of $4 \leq N_{\Delta,i} \leq 10$ gives a balance between too little distortion and too much uncertainty in the amount of distortion needed, and $\mathrm{rms}_{\Delta,i}$ is approximately constant in this range. We cannot directly compare these rms differences with those between 1-D BT-Settl and 3-D STAGGER models: the latter are defined over a narrower range $(0.2 - 20\,\mu\mathrm{m})$ than the former (we use $0.1 - 30\,\mu\mathrm{m}$). Restricting the wavelength range we use to match STAGGER increases $\mathrm{rms}_{\Delta,i}$ at least twofold as we lose useful constraints in the UV.

Figure 4.11 shows the effect the number of distortion coefficients used has on the
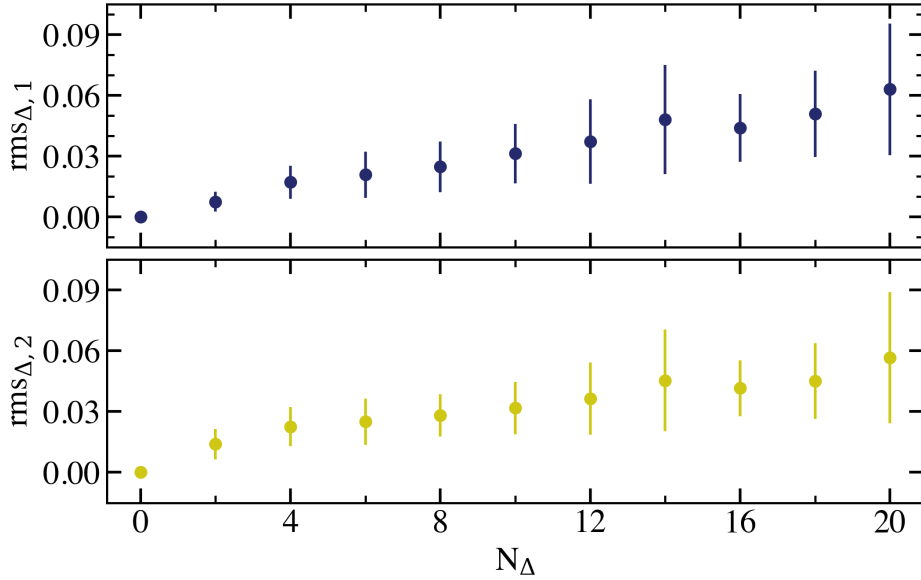
Figure 4.10: Amount of distortion (rms) needed by the polynomials in order to fit the data to the model SEDs as a function of the number of distortion coefficients Δ_i used in the fit.

uncertainties in fit parameters. The uncertainties in additional noise due to external sources of error, particularly $\sigma_{\mathrm{ext,c}}$, decrease with N_Δ while the uncertainties in physical parameters T_{eff}, θ and $E(B-V)$ increase. This could be explained by the hypothesis that for higher N_Δ, the distortions begin to take advantage of flux ratios being unconstrained between filters and begin to move flux in and out of gaps between filters to improve the fit, which is not physically justified. The largest gap between filters we use is in the infrared (see Figure 4.1), but models are generally reliable in the IR (see IRFM) so we do not expect this to be a major issue in our final results. Our choice of $N_\Delta = 10$ was made to balance the rising error in physical parameters with the high error in $\sigma_{\mathrm{ext,c}}$ at low orders.
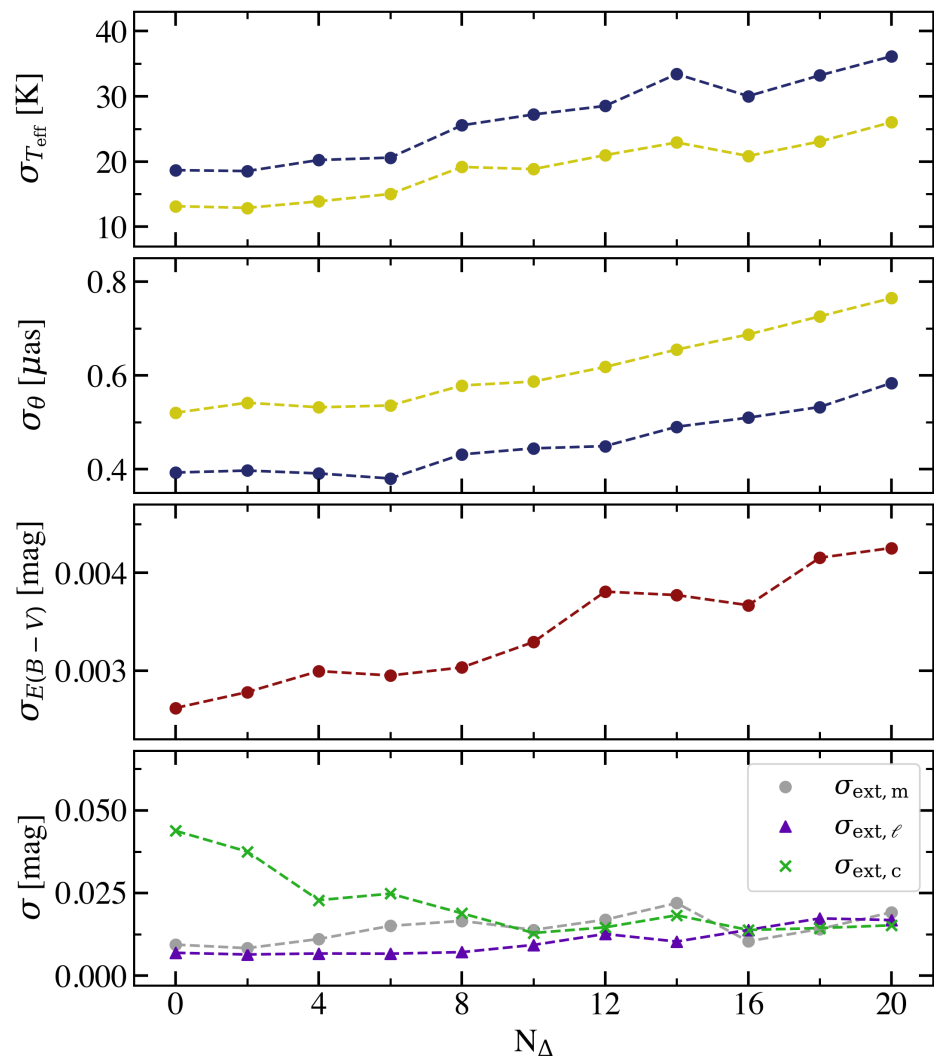
Figure 4.11: Standard error on each fit parameter for each number of distortion co-efficients Δ_i. *Top*: Errors on effective temperatures $T_{\text{eff},1}$ (blue) and $T_{\text{eff},2}$ (orange). *Second panel*: Errors on angular diameters θ_1 (blue) and θ_2 (orange). *Third panel*: Errors on interstellar reddening $E(B-V)$. *Lower panel*: Errors on external error sources $\sigma_{\text{ext,m}}$, $\sigma_{\text{ext},\ell}$ and $\sigma_{\text{ext,c}}$.

4.4.2 Different models

We tested the effect of using models with different input parameters — wavelength binning (Runs A and B), temperature (Run C) and metallicity (Runs F and G). There is no significant effect in the result when changing the input SEDs. This indicates that our method of distortion is working and not very dependent on the input model. In calculating our adopted values in Run A, we used temperatures and a metallicity appropriate for AI Phe (Andersen et al., 1988), and smaller wavelength binning. There was no significant difference in the output between 20 Å and 50 Å bins, so we chose to run all other tests with the larger bin size in order to save computational costs.

4.4.3 Constraining $E(B{-}V)$ in the ultraviolet

Constraints on interstellar reddening are vital in reducing the uncertainty on the derived values of effective temperature. In the case of AI Phe we were fortunate to be able to restrict the range of $E(B{-}V)$ explored in our Bayesian analysis using the absence of the NaI doublet in HARPS spectra, and the depth of the 2175 Å absorption feature using the u220n and u220w ultraviolet fluxes and flux ratios. However, we looked at the effect of removing these constraints. In Run I of Table 4.7 we see a significant increase in the uncertainties on $E(B{-}V)$ and T_{eff}. If we remove the additional constraint provided by placing a narrow bandpass ($u220n$) in the UV, the uncertainties increase even further (Run K).

Our results suggest that imposing a prior on $E(B{-}V)$ is the strongest constraint on reddening, so including prior knowledge of interstellar reddening from e.g. spectroscopy or Stromgren photometry is a powerful way to improve results. If this is not possible, having UV observations to pin down the shape of the UV end of the SED helps in determining the fit. By defining narrow bands in the *IUE* spectra, we were able to constrain the shape of the SED in the NUV more than if we used broad bands. These encompass more flux than narrow bands, but narrower bands are better at fixing the shape of the ultraviolet end of the SEDs.

4.4.4   NIR flux ratios

The T_{eff} values used in Section 4.2.6 to derive the NIR flux ratio priors are calculated using the InfraRed Flux Method (IFRM), so there may be some systematic offset between these values and the true T_{eff}. Therefore, we need to check what the impact of an offset T_{eff}-T_{IFRM} is on our results. We found that our NIR flux ratio priors showed a very weak dependence on the values of T_{IFRM} used: introducing an offset of $100\,\mathrm{K}$ changes the T_{eff} results by no more than $1-2\,\mathrm{K}$ (see Run N in Table 4.7). In general, applying NIR flux ratio priors to our data had little effect on our results for AI Phe.

4.5   Conclusions

For eclipsing binaries stars with well-defined eclipses it is possible to measure the radii of the two stars to much better than 1% using high quality data: over 70 DEBs in DEBCat (Southworth, 2015a) have masses and radii of both components measured to this accuracy. The end-of-mission accuracy of the parallaxes from the *Gaia* mission is expected to be at least $16\,\mu\mathrm{as}$ for bright stars, i.e. better than 0.5% for stars within $300\,\mathrm{pc}$. Therefore, precise and accurate angular diameters for many stars in eclipsing binaries are already available. There is potential to use these results to calculate precise and accurate fundamental effective temperatures for many stars, but this requires accurate measurements of the bolometric flux. The method that we present in this paper is a robust tool for deriving the bolometric flux for both stellar components in an DEB, provided there are enough photometric data. We show the potential of this method with the well-characterised DEB, AI Phoenicis. The fundamental effective temperatures we obtained for this system are very precise: $T_{\mathrm{eff},1} = 6199 \pm 22\,\mathrm{K}$, $T_{\mathrm{eff},2} = 5094 \pm 16\,\mathrm{K}$. This is due to the high quality of the R and ϖ measurements, a strong upper limit on interstellar reddening, and constraints from ultraviolet photometry. While the choice of input model SED has a small effect on the output effective temperatures, the tests we have done on the method show that uncertainties on the

interstellar reddening have a large effect the uncertainty on the derived values of effective temperature. From the results in Table 4.7, we see that a constraint on $E(B-V)$ of about $0.01\,\mathrm{mag}$ is needed to reduce T_{eff} errors to less than $50\,\mathrm{K}$. Uncertain reddening will tend to bias the T_{eff} estimates as $E(B-V)$ cannot be negative.

There are many bright eclipsing binaries of all types being discovered as a results of survey like WASP, KELT, *K2*, *TESS*, ASAS (Kirkby-Kent et al., 2018; Lubin et al., 2017; Maxted & Hutcheon, 2018; Lee et al., 2019; Hełminiak et al., 2019), many of which have both *Gaia* parallaxes and a wealth of archival photometry. We conclude that the prospects for measuring accurate and precise effective temperatures for a large number of stars in eclipsing binaries are excellent.

5 Fundamental effective temperature measurements for CPD-54 810

There is nothing like looking, if you want to find something ... You certainly usually find something, if you look, but it is not always quite the something you were after.

J. R. R. Tolkien, *The Hobbit, or There and Back Again* (1937)

Note: The following chapter is heavily based the paper "Fundamental effective temperature measurements for eclipsing binary stars – II. The detached F-type eclipsing binary CPD-54 810" (Miller et al., 2022; accepted for publication in MNRAS, October 2022). Contributions from co-authors consist of the independent light curve analysis and accompanying text by D. Graczyk (Section 5.3.3.2), observations of CPD-54 810 by T.G. Tan; independent light curve analysis (Section 5.3.3.3) and comparison of CPD-54 810 to stellar evolution tracks and accompanying text by P. Maxted (Section 5.4.2).

5.1 Introduction

CPD-54 810 (also known as ASAS J051753-5406.0 or TYC 8511-888-1) is a moderately bright (V= 10.5), totally-eclipsing detached eclipsing binary system first studied by Ratajczak et al. (2021), hereafter R21. They performed light curve and radial velocity fits to obtain masses and radii for both components, and obtained spectroscopic effective temperature estimates from disentangled optical spectra. Their analysis of the system suggests that the primary component is either an evolved main-sequence star or sub-giant of a late-F type ($M_1 = 1.311 \pm 0.035\,\mathrm{M_\odot}$, $R_1 = 1.935 \pm 0.020\,\mathrm{R_\odot}$, $T_{\mathrm{eff},1} = 5980 \pm 205\,\mathrm{K}$), while the secondary is a lower mass, early G-type main-sequence star ($M_2 = 1.093 \pm 0.029\,\mathrm{M_\odot}$, $R_2 = 1.181 \pm 0.014\,\mathrm{R_\odot}$, $T_{\mathrm{eff},2} = 5850 \pm 190\,\mathrm{K}$). These spectroscopic temperatures are $\sim$500 K cooler than what we would expect from a preliminary look at the *Gaia* photometric colours.

Here we present a re-analysis of all available observations of CPD-54 810, to obtain new values for the masses and radii. Since the publication of R21, the number of *TESS* sectors containing observations of CPD-54 810 have more than doubled so we have been able to improve the precision of the mass and radius measurements. In addition, we measure fundamental effective temperatures of both components, and draw conclusions about the evolutionary status of the system. In contrast to AI Phoenicis, there are no published high-quality multi-band light curves of CPD-54 810 apart from *TESS*; it is thus more representative of the vast number of eclipsing binaries in the process of being identified by *TESS* and other large-scale photometric surveys. This makes it an interesting system to test whether the method introduced in Miller et al. (2020) will produce meaningful results for a large sample of poorly-studied DEBs and what other data are required to reach the levels of accuracy in mass, radius and effective temperature required for a particular system to be suitable as a benchmark system.

5.2 Observations

5.2.1 *TESS* photometry

The *TESS* satellite observed CPD-54 810 in the 2-minute cadence mode between 24 September 2018 and 17 July 2019, covering seven sectors (3-7, 10, 13). *TESS* returned to observe CPD-54 810 in the 10-minute cadence mode between 05 July 2020 and 13 January 2021, covering another five sectors (27, 30-33).

5.2.2 Ground based photometry

CPD-54 810 was observed by the All-Sky Automated Survey (ASAS) from 20 November 2000 to 12 October 2009 in the *V* band, with 698 good quality data points available in the ASAS Catalog of Variable Stars (ACVS; Pojmanski, 2002). However, there were comparatively few good data points within the eclipses to obtain tight constraints on the orbital parameters or flux ratio of the binary. We used the times of primary minima

present in the ASAS data to check the linear ephemeris of the system with a longer time baseline than otherwise possible. These were consistent with the other data but the lack of precision from the light curve fits led us to not include these data in our results.

We obtained photometric observations of CPD-54 810 with the Perth Exoplanet Survey Telescope (PEST) during the secondary eclipse on 04 January 2021. The PEST is a 0.3 m telescope in Perth, Australia. At the time of these observations it was equipped with an SBIG ST-8XME camera and Astrodon B, V, Rc, Ic filters, giving an image scale of 1".2 and a 31' x 21' field of view. Individual exposure times for the B, V, Rc, Ic bands were 120s, 60s, 30s, 60s respectively. Differential photometry was done with reference to an ensemble of comparison stars in the field. These photometric observations were reduced using the custom PEST pipeline[1]. Magnitudes and errors for the PEST observations are given in Table 5.1.

In addition, CPD-54 810 was observed by the WASP-South instrument (Pollacco et al., 2006), from 24 September 2012 to 19 November 2014, yielding a total of 24398 good quality data points. For observations of CPD-54 810, the WASP-South instrument was operated using Canon 85-mm f/1.2 lenses, 2k×2k $e2V$ CCD detectors, and an r' filter. With these lenses the image scale was 33 arcsec/pixel. Fluxes were measured in an aperture with a radius of 132 arcsec and were processed with the SYSRem algorithm (Tamuz et al., 2005) to remove instrumental effects. Magnitudes and errors for WASP observations during and up to one day before and after eclipses are given in Table 5.1.

5.2.3   Catalog photometry

In our T_{eff} analysis, we require magnitude measurements throughout the entire optical range, converted to the AB magnitude scale to allow us to compare observed magnitudes with synthetic magnitudes generated by the synthetic spectra (see Chapter 2).

---

[1]http://pestobservatory.com/the-pest-pipeline/
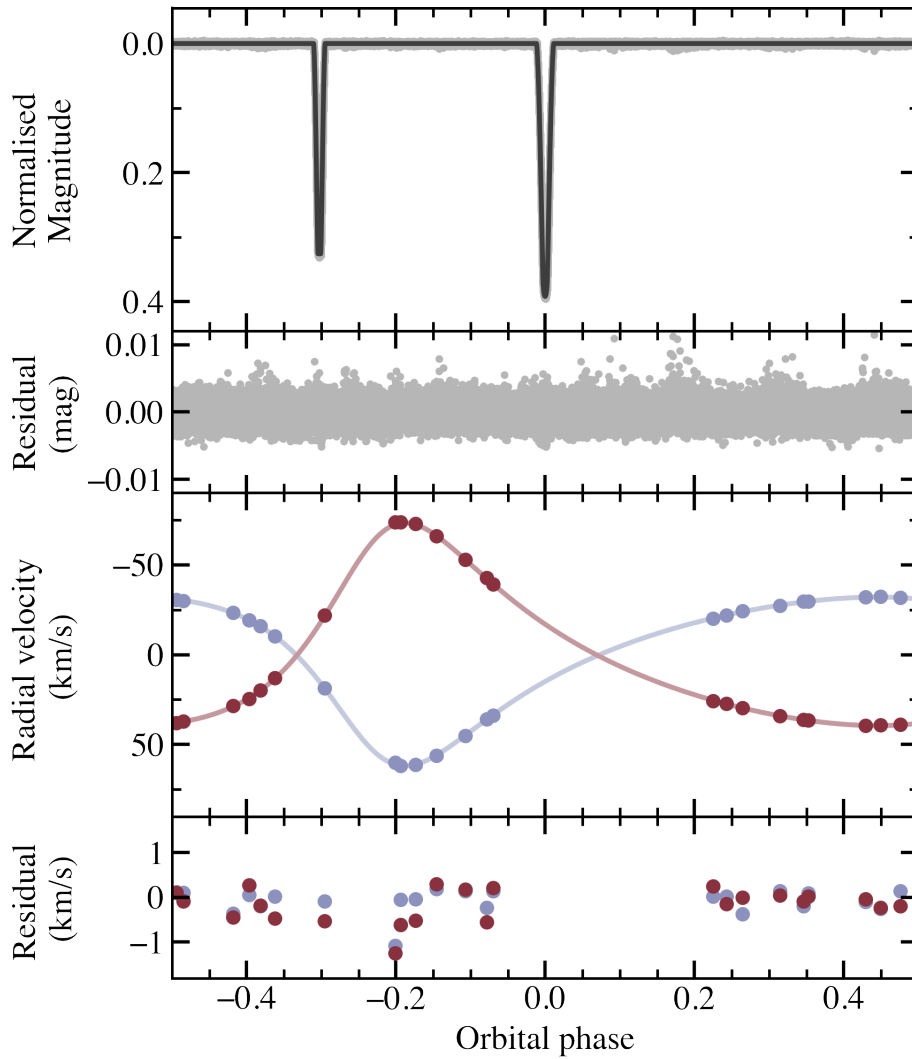
Figure 5.1: Top: *TESS* light curve consisting of all 2-minute cadence observations from Sectors 3-7, 10 and 13 with the JKTEBOP light curve solution and residual over the full orbital cycle. Bottom: Radial velocities extracted by R21, re-fitted using the radial velocity model in the ellc code, along with residuals from the best solution.

Table 5.1: Ground-based photometric observations for CPD-54 810 from PEST (B, V, R, I) and WASP (r') observatories. For brevity, only WASP photometry of and around the eclipses used in the ephemeris calculation are provided. The full version of this table will be made available in the online supplementary materials for the paper.

BJD	Filter	Magnitude	Error
2456195.4380815	r'	10.4497	0.0309
2456195.4384171	r'	10.4130	0.0292
2456195.4387528	r'	10.4207	0.0295
2456195.4427344	r'	10.4413	0.0288
2456195.4434172	r'	10.4338	0.0280
2456195.4474451	r'	10.4261	0.0270
2456195.4477808	r'	10.4150	0.0265
2456195.4481280	r'	10.4439	0.0264
2456195.4520517	r'	10.4251	0.0265
2456195.4523873	r'	10.4516	0.0264

For details on these transformations, see appendix A of Bessell & Murphy (2012).

GALEX (Martin et al., 2005) observed CPD-54 810 in the *FUV* and *NUV* bands. Photometric response functions were taken from the *GALEX* web pages[2] and the zero-point error from Camarota & Holberg (2014). Our previous work on AI Phoenicis (Miller et al., 2020) showed that more constraints on the ultraviolet and blue end of the optical range improve the reliability of the T_{eff} measurements obtained. Unlike AI Phoenicis, CPD-54 810 does not have any archival space-based ultraviolet light curves or flux ratio measurements. Therefore we chose to include u and v magnitudes from the SkyMapper survey (Keller et al., 2007). We calculated a zero-point for each of these bands by calculating synthetic magnitudes for a set of CALSPEC (Bohlin et al., 2014) stars in the magnitude range $8-15$ mag with SkyMapper u- and v- photometry. We include G, BP and RP magnitudes and photometric zero points from *Gaia* Early Data Release 3 (EDR3; Gaia Collaboration et al., 2021a) in our analysis. We included magnitudes in the J, H and Ks bands from 2MASS (Skrutskie et al., 2006),

---

[2]`https://asd.gsfc.nasa.gov/archive/galex/tools/Resolution_Response/`

with response functions obtained from the Explanatory Supplement to the 2MASS All Sky Data Release.[3] The zero-points with their standard errors are taken from Maíz Apellániz & Pantaleoni González (2018). WISE magnitudes are taken from the All-Sky Release Catalog (Cutri & et al., 2012), with corrections to Vega magnitudes made as recommended by Jarrett et al. (2011).

5.2.4 Spectroscopic observations

We used spectroscopic observations from the European Southern Observatory science archive facility[4] obtained with the 2.2-m MPG telescope equipped with the Fiberfed Extended Range Optical Spectrograph (FEROS; R~48000; Kaufer et al., 1999) to obtain measurements of the stars' metallicity and rotational velocity, and the equivalent widths of the Na I D lines used to obtain an estimate of the interstellar reddening. CPD-54 810 was observed by FEROS on three occasions between 21 September 2012 and 25 September 2012 (Run ID: 089.D-0097(A), PI: Hełminiak) and three occasions between 28 December 2012 and 31 December 2012 (Run ID: 090.D-0061(A), PI: Hełminiak).

5.2.5 Ground based radial velocity measurements

We reanalysed the radial velocity measurements of CPD-54 810 extracted by Ratajczak et al. (2021) to ensure that the parameters of the stars' spectroscopic orbits are consistent with the new results derived here from the light curves. The spectra from which these were measured were taken with FEROS (described in Section 5.2.4), the Swiss 1.2-m Leonhard Euler Telescope with CORALIE (R~60000; Queloz et al., 2001) and the 1.5-m SMARTS telescope (Subasavage et al., 2010) at Cerro Tololo Inter-American Observatory with the CHIRON spectrograph in fiber mode (R~25000) and slit mode (R~90000).

---

[3]https://old.ipac.caltech.edu/2mass/releases/allsky/doc/explsup.html
[4]http://archive.eso.org

5.3   Methods and analysis

5.3.1   Reduction of photometric data

The available *TESS* sectors were split into the 2-minute and 10-minute cadence modes. Sectors 4 and 32 were excluded from the analysis due to significant anomalous variation in the out-of-eclipse levels that appear to be due to instrumental effects. For the first set of *TESS* observations in the 2-minute cadence, we used target pixel files extracted by the Science Processing Operations Center (SPOC) pipeline (Jenkins et al., 2016). For the later set of sectors observed in the 10-minute cadence, we used target pixel files extracted from full frame image (FFI) files by the "TESS-SPOC" pipeline (Caldwell et al., 2020). All *TESS* products were accessed from the Mikulski Archive for Space Telescopes[5] (MAST) via the lightkurve package (Lightkurve Collaboration et al., 2018). Due to significant inconsistencies between the eclipse depths of the 2-minute and 10-minute cadence data sets for the pipeline-extracted light curves, we decided to perform our own simple aperture photometry. For this we used the pipeline-defined target aperture and a custom background aperture for each cadence, defined as the 20% of pixels with the lowest flux. We removed systematics for each sector using cotrending basis vectors (CBVs), and applied corrections for crowding and fraction of flux in the aperture. We then cleaned each sector by removing any data points with a poor quality flag, then normalised each sector by masking the eclipses, fitting a low-order polynomial to the out-of-eclipse continuum and dividing through the entire sector.

5.3.2   Updated linear ephemeris

We obtained a new measurement of the linear ephemeris using high quality observations of primary eclipses from WASP and *TESS*. For the *TESS* observations, we chose to only include eclipses for which the majority of the ingress and egress were observed. Despite some ASAS observations occurring further back in time than WASP observations, we

---

[5]https://archive.stsci.edu/

Table 5.2: Times of mid eclipse for CPD-54 810. The (O–C) residuals are from the linear ephemeris given in Section 5.3.2. Details for the source of each eclipse used in the calculation are given, including the cadence of the *TESS* observations.

BJD–2450000	(O–C) [s]	Source
6196.67563 ± 0.00062	37.4	WASP
6954.48397 ± 0.00092	23.8	WASP
8391.70667 ± 0.00003	−3.6	*TESS* Sector 3
8443.96944 ± 0.00004	6.2	*TESS* Sector 5
8470.10068 ± 0.00004	−1.2	*TESS* Sector 6
8496.23202 ± 0.00004	−0.8	*TESS* Sector 7
8574.62604 ± 0.00004	2.6	*TESS* Sector 10
8679.15128 ± 0.00004	−3.1	*TESS* Sector 13
9044.98993 ± 0.00004	1.8	*TESS* Sector 27
9123.38392 ± 0.00004	2.4	*TESS* Sector 30
9149.51519 ± 0.00004	−2.6	*TESS* Sector 31

chose not to include the ASAS light curves in our measurements due to its poor quality. Times of mid eclipse were measured for each eclipse with JKTEBOP, fixing all other fit parameters to adopted values. From these times, given in Table 5.2 we measured the following linear ephemeris for the system:

$$\text{BJD } T_{\mathrm{mid}} = 2458679.151318(12) + 26.13132764(11) \ E.$$

From performing the same analysis on secondary eclipses, we see no evidence of a third body or apsidal motion in the system. Fitting a quadratic ephemeris gives an upper limit on the rate of period change $|\dot{P}/P| < 5 \times 10^{-6}$.

Table 5.3: Comparison of results for the analysis of the *TESS* light curves of CPD-54 810 using 3 different methods. Figures in parentheses give the standard error in the final digit of the preceding value.

Parameter	JKTEBOP	WD	ellc	Adopted
r_1	0.03893(2)	0.03886(7)	0.03890(1)	0.03891(4)
r_2	0.02379(4)	0.02395(10)	0.02384(2)	0.02383(7)
i [°]	89.72(2)	89.83(3)	89.742(9)	89.76(5)
e	0.3686(1)	0.3691(1)	0.36859(6)	0.3688(4)
ω [°]	327.02(3)	327.01(2)	326.83(3)	329.96 (9)
L_2/L_1	0.350(2)	0.3596(42)	0.3535(9)	0.3534(44)
ℓ_3	0.002(4)	0.013(3)	0.009(2)	0.008(5)

5.3.3 Orbital and stellar parameters from *TESS* light curves

We decided to re-analyse the light curves and radial velocities of CPD-54 810 using the *TESS* data that has become available since the analysis by R21. As is advised in Maxted et al. (2020), it is good practice to carry out an independent analysis when performing light curve fitting at high precision. Therefore, we performed three independent analyses using different light curve fitting codes: JKTEBOP (Southworth, 2013), ellc (Maxted, 2016), and the Wilson-Devinney (WD) code (Wilson & Devinney, 1971). A full description of the approach taken by each of the analyses is given in Sections 5.3.3.1, 5.3.3.2, and 5.3.3.3 but we present a summary of the results of the light curve fits in Table 5.3.

The adopted values in Table 5.3 were calculated using the weighted mean and weighted sample standard deviation assuming that each of the three values from the JKTEBOP, WD and ellc analyses are affected by the same systematic error σ_{sys} added in quadrature to the standard errors quoted in the three input values. The value of σ_{sys} was adjusted such that the weighted mean value as a model for the three input

values has a reduced chi-square value $\chi_r^2 = 1$.

5.3.3.1 Analysis with JKTEBOP

For this analysis, we re-analysed the light curve of CPD-54 810 using all suitable *TESS* data that is currently available, including the newer 10-minute cadence observations. The two sets of observations (2-minute and 10-minute cadences) were split further into 5 and 4 sections respectively, containing at least one primary and one secondary eclipse, which were all analysed separately. We performed light curve fits for each section with JKTEBOP[6] (Southworth, 2013), which uses Levenberg-Marquardt minimisation (Press et al., 1992) to find the optimal solution for the EBOP light curve model (Popper & Etzel, 1981; Etzel, 1981). We used the quadratic limb darkening law for both components of CPD-54 810. The free parameters in each fit were: the surface brightness ratio in the *TESS* band $J = S_{\mathrm{T},2}/S_{\mathrm{T},1}$, sum of the fractional radii $r_{\mathrm{sum}} = r_1 + r_2 = R_1/a + R_2/a$, ratio of the fractional radii $k = r_2/r_1$, the quadratic limb darkening coefficients (where the coefficient for the secondary star was set as equal to those for the primary), orbital inclination i, $e\cos\omega$, $e\sin\omega$, third light ℓ_3, and the light scale factor. The values of orbital period P and time of primary minimum T_0 were fixed at the best values from the calculation of the linear ephemeris in Section 5.3.2. The mean and standard error for each free parameter was calculated from all nine sections of *TESS* observations and taken as the adopted solution. This approach is justified by Maxted et al. (2020), in which the authors demonstrate that the MC and RP errorbars in JKTEBOP are reliable, and in Southworth (2021), where the author shows that these MC and RP errorbars agreed with those obtained from fitting the data in subsets. The best values for each parameter fitted by JKTEBOP are shown in Table 5.4.

We performed a new fit of the radial velocities extracted by R21 using the radial velocity model in ellc (Maxted, 2016). We allowed the following parameters to be free: K_1, K_2, γ_1, γ_2, T_0, period P, $\sqrt{e}\cos\omega$, $\sqrt{e}\sin\omega$ and the excess noise in the radial

---

[6]Version 40. The code is available at `https://www.astro.keele.ac.uk/jkt/codes/jktebop.html`

Table 5.4: Orbital elements of CPD-54 810 from the JKTEBOP fits to the *TESS* light curves and ellc radial velocity fits. The quadratic limb darkening coefficients c_1, c_2 are the same for both stars.

Parameter	Light curves	Radial velocities
J	0.9372 ± 0.0020	–
r_{sum}	0.06272 ± 0.00003	–
k	0.6110 ± 0.0013	–
c_1	0.32 ± 0.03	–
c_2	0.09 ± 0.05	–
i (°)	89.72 ± 0.021	–
ℓ_3	0.002 ± 0.004	–
e	0.3686 ± 0.0001	0.3683 ± 0.0006
ω (°)	327.02 ± 0.03	327.18 ± 0.17
K_1 $(\mathrm{km\,s^{-1}})$	–	46.93 ± 0.06
K_2 $(\mathrm{km\,s^{-1}})$	–	56.40 ± 0.10
γ_1 $(\mathrm{km\,s^{-1}})$	–	0.38 ± 0.05
γ_2 $(\mathrm{km\,s^{-1}})$	–	0.56 ± 0.07
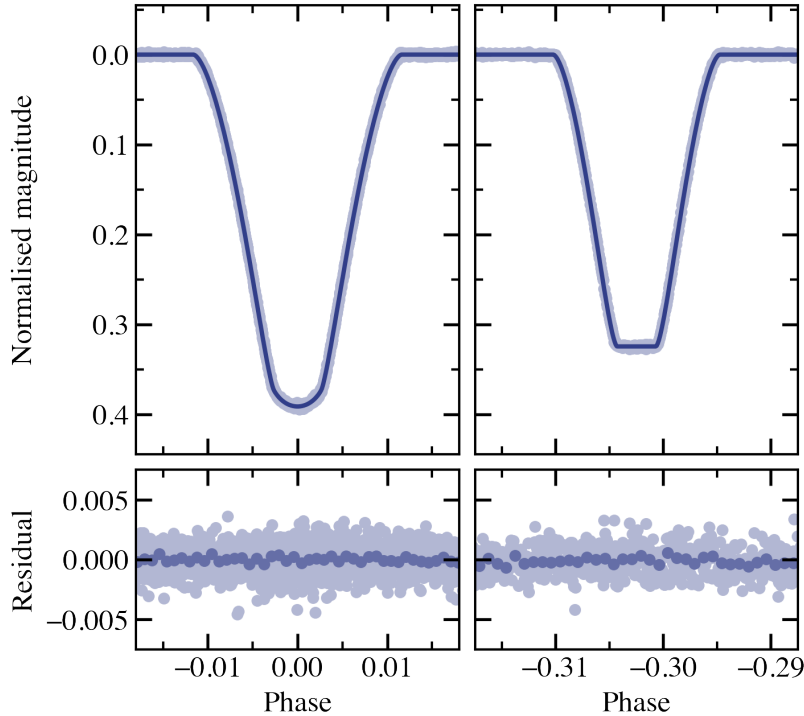
Figure 5.2: Primary and secondary eclipses of CPD-54 810 in Sectors 6 and 7, as observed by *TESS* in the 2-minute cadence. The best model from JKTEBOP for this section of the 2-minute data set and the residual of the fit are shown alongside the raw photometry data.

velocities σ_{rv}. We placed Gaussian priors on T_0 and P from the ephemeris derived in Section 5.3.2. The posterior probability distribution of the model parameters was sampled using the emcee implementation of the affine-invariant ensemble sampler for Markov chain Monte Carlo (Foreman-Mackey et al., 2013), using 512 walkers over a chain of 600 steps and burn-in of 400 steps. The model parameters derived are given in Table 5.4. We also did a least-squares fit to the radial velocity data including priors on e and ω from the analysis of the light curves. The results were almost identical to those presented in Table 5.4 so we do not report them here. This insensitivity to the exact choice of e and ω is because the radial velocity curves for both stars are well sampled around their minima and maxima.

5.3.3.2   Analysis with the WD code

For the analysis we used 2-minute cadence data from 5th, 6th and 10th *TESS* sectors. The data contain three primary and three secondary eclipses. We retained all points within eclipses and just around them and each 40th point in out-of-eclipse parts of the light curve. The light curve was detrended from a long-term small light variations. Its out-of-eclipse parts are practically flat. In total 3834 data points were used. For radial velocities we adopted RVs published by R21. We used all their RVs with an exception of one measurement taken at HJD 2456400.485 (at the orbital phase 0.20), which deviates significantly from the model. Our naming of components is reversed to that used by R21 as we call the primary a more massive, larger and brighter component which is eclipsed during a deeper minimum.

Simultaneous analysis of light and radial velocity curves was performed with the Wilson-Devinney (WD) code version 2015 (Wilson & Devinney, 1971; Wilson, 1979, 1990; Van Hamme & Wilson, 2007; Wilson & Van Hamme, 2014) equipped with the Python GUI written by Güzel & Özdarcan (2020). The latest WD version allows for a direct modeling of photometry obtained in the *TESS* filter (number 95 in the WD) and a high numerical precision. The orbital period was set to the value derived from analysis of minima times (see Section 5.3.2), the surface grid parameters (the numerical precision) was set to `N1=N2=80`. The limb darkening coefficients were fixed to values from updated tables originally published by van Hamme (1993) according to actual values of surface gravity and temperature at fixed metallicity of [Fe/H]=0 (see Section 5.3.5). During analysis both the logarithmic (Klinglesmith & Sobieski, 1970) and square root (Diaz-Cordoves & Gimenez, 1992) limb-darkening (LD hereafter in this section) laws were tested. The albedo parameters were set to 0.5 and the gravity brightening parameters were set to 0.32 for both components as their atmospheres are expected to be fully convective. The atmosphere approximation was used `IFAT1=IFAT2=1` and the radial velocity corrections were applied `ICOR1=ICOR2=1`. While modeling the following parameters were allowed to vary: the orbital phase shift, the luminosity of the primary L_1, the eccentricity e, the longitude of periastron ω, the mass ratio q, the semi-major

Table 5.5: Photometric and orbital parameters of CPD-54 810 from the WD fits to the *TESS* light curves and the radial velocities. [1]T_0 is measured in BJD-2450000.

Parameter	Value	Comments
Period (d)	26.13132764	fixed
T_0 (d)[1]	8470.10157 ± 0.00024	
Ω_1	27.054 ± 0.043	
Ω_2	36.397 ± 0.145	
$T2$ (K)	6359 ± 3	
i (°)	89.825 ± 0.030	
e	0.3691 ± 0.0001	
ω (°)	326.86 ± 0.03	
a ($R_\odot$)	49.718 ± 0.090	
q	0.8317 ± 0.0028	
γ_1 (km s^{-1})	0.40 ± 0.04	
γ_2 (km s^{-1})	0.39 ± 0.05	
ℓ_3 (TESS)	0.0130 ± 0.0025	
Derived parameters		
K_1 (km s^{-1})	47.03 ± 0.09	
K_2 (km s^{-1})	56.54 ± 0.14	
r_1	0.03886 ± 0.00007	
r_2	0.02395 ± 0.00010	
r_{sum}	0.06281 ± 0.00005	
k	0.6164 ± 0.0033	
L_2/L_1 (TESS)	0.3596 ± 0.0042	direct
L_2/L_1 (V)	0.3519	extrapolated
L_2/L_1 (K$_{2\mathrm{MASS}}$)	0.3735	extrapolated

axis a, the orbital inclination i, the dimensionless Roche potentials Ω, the temperature of the secondary T_2, the systemic velocities γ and also the third light ℓ_3. After few iteration the phase shift was fixed at 0.1136 and then the epoch of the primary minimum T_0 was adjusted during later analysis.
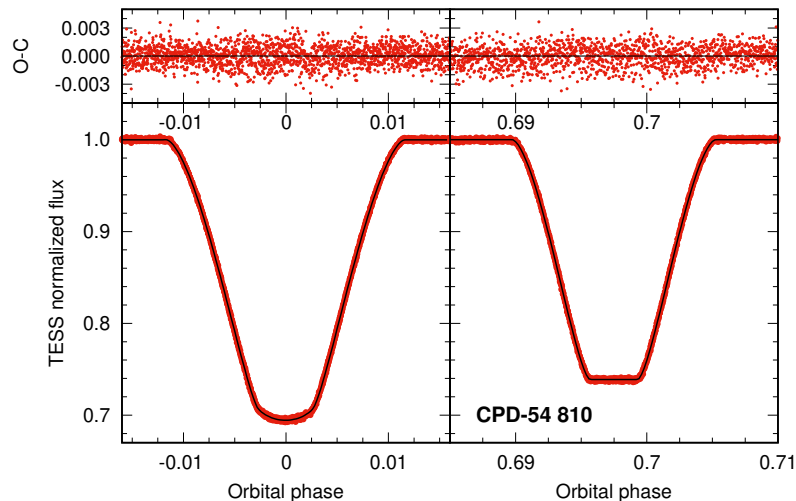
Figure 5.3: The WD fit to *TESS* light curve from 5th, 6th and 10th sectors.

We started the analysis by adopting as an input the model parameters reported by R21. In the beginning the logarithmic LD law was used and no third light was assumed. The resulted solution produced small but systematic residuals in both eclipses. A use of the square root LD law improved the *rms* of *TESS* light curve solution but the systematics were still present. Finally, adjusting ℓ_3 produced acceptable fit to both eclipses without any noticeable systematics in residuals. The detected third light in *TESS* is small, at 1.3%. It is not clear if that detection is real or results from using the LD law which is not fully adequate in case of both components.

Mean errors on the radial velocity determination are 145 m s^{-1} and 330 m s^{-1} (R21), while the obtained solution for radial velocities has the *rms* 175 m s^{-1} and 273 m s^{-1} for the primary and the secondary, respectively. The primary shows the slightly larger *rms* then expected which might be attributed to an influence of a putative third body in the system. The systemic velocities of both components are very similar and they differ no more than 40 m s^{-1}.

In Table 5.5 we summarised parameters of the best fit model. Errors quoted are formal errors returned by the Differential Corrections procedure but multiplied by a factor of three. For some parameters like fractional radii r_1 and r_2 they are much larger than those reported from the analysis with JKTEBOP or ellc. The difference comes from very conservative errors adopted in case of the WD analysis but also from correlations between model parameters especially between the sum of the radii r_{sum}, the orbital inclination i and ℓ_3.

5.3.3.3   Analysis with ellc

We used the binary star model ellc (Maxted, 2016) to analyse every sector of *TESS* data containing both a complete primary and complete secondary eclipse, viz. sectors 4 to 7, 10 and 13 at 2-minute cadence, and sectors 27, 31 and 32 and 10-minute cadence. Only data within one eclipse width of the phase of mid-eclipse were included in the analysis. The data for each eclipse were divided by a straight line fit to the data either side of eclipse to remove instrumental trends prior to analysis. We used the power-2 limb darkening law for both stars assuming that same values of h_1 and h_2 (as defined in Maxted 2018) for both stars. We used the "fine" grid for the numerical integration of the fluxes through the eclipses so that the numerical noise is well below 20 ppm at all phases. The mutual gravitational distortion of the stars has a negligible impact on the light curve so we assumed spherical stars for the calculation of the model light curves. For the 10-minute cadence data we used numerical integration to account for the finite integration time. The orbital period was fixed at the value $P = 26.131328\,\text{d}$. The free parameters in the fit were: $J = S_{\text{T},2}/S_{\text{T},1}$, $r_{\text{sum}} = r_1 + r_2$, $k = r_2/r_1$, i, $f_c = \sqrt{e}\cos\omega$, $f_s = \sqrt{e}\sin\omega$, T_0, h_1, h_2, third light ℓ_3, and a scaling factor. We used emcee (Foreman-Mackey et al., 2013) to find the mean and standard error of these parameters in the posterior probability distribution (PPD) assuming Gaussian white noise for the data. The standard deviation per point was included as a hyperparameter when sampling the PPD. Broad uniform priors were applied to all parameters. For ℓ_3, negative values were permitted to allow for systematic errors in background subtraction

and/or star spots. The PPD was sampled using 100 walkers running for 500 steps after discarding a "burn-in" phase of 1500 steps. Convergence of the chains was verified by visual inspections of parameter values as a function of step number. No trends or excess noise during the eclipses was apparent from a visual inspection of the residuals from the best fit for all sectors. The weighted mean and standard error of the weighted mean for the main parameters of interest are given in Table 5.3. The mean values of the limb-darkening parameters are $h_1 = 0.820 \pm 0.001$, $h_2 = 0.44 \pm 0.02$. These values agree well with the values expected based on STAGGER-grid 3-D atmosphere models (Magic et al., 2015) given the effective temperature, surface gravity and metalicity of the two stars (Star 1: $h_1 = 0.826$, $h_2 = 0.409$; Star 2: $h_1 = 0.813$, $h_2 = 0.429$; Maxted 2016).

5.3.4   Flux ratios from *TESS* and PEST light curves

The *TESS* flux ratios used in the $T_{\rm eff}$ analysis were taken from the adopted light curve fit using JKTEBOP, as described in Section 5.3.3.1. The adopted value and error, from the standard deviation of the eight subsets, are given in Table 5.6. The PEST flux ratios were calculated by fitting each light curve in JKTEBOP. Due to the limited phase coverage of the observations, we only allowed the surface brightness ratio J and light scale factor to vary. We fixed the quadratic limb darkening coefficients for each filter to those described in Claret (2000) and fixed all other parameters to the adopted values from the *TESS* fits. We used the MC methods in JKTEBOP to perform a fit for each light curve over 1000 simulations perturbing each observation randomly by its standard error to estimate the uncertainty on the flux ratio due to noise in the light curve. We also performed fits to the light curve with each of the parameters $r_{\rm sum}$, k, i, ℓ_3 perturbed by their standard errors in order to quantify the uncertainty on the flux ratio due to errors on these parameters. Similarly, we also performed fits with the linear limb darkening coefficients for each star perturbed by a somewhat arbitrary error estimate of 0.1. The best values for the flux ratio (calculated from the surface brightness ratio) are given in Table 5.6 with all the contributions to the uncertainty
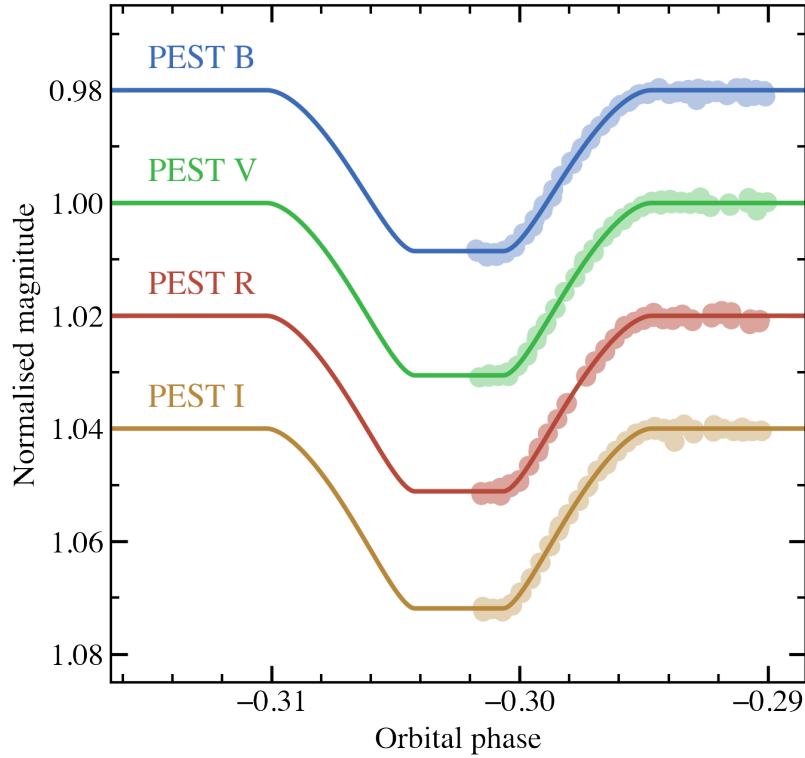
Figure 5.4: Photometric observations taken by the PEST observatory in $BVRI$ bands along with the best JKTEBOP fit.

added in quadrature. The light curve fits can be seen in Figure 5.4.

5.3.5 Estimate of the interstellar extinction

An accurate measurement of a star's effective temperature based on photometry requires a robust estimate of the interstellar reddening. The importance of having a suitable prior on the interstellar reddening was demonstrated in Miller et al. (2020), where placing no prior increased the uncertainty on the derived effective temperatures by 400%. Relationships have previously been established between the equivalent widths of selected interstellar absorption lines such as the Na I doublet and K I line. The empirical relations established in Poznanski et al. (2012) are calibrated using spectra of

quasars and galaxies, and hence are not well-constrained in the regime of $E(B-V)$ < 0.01, which is where we would expect our relatively local ($\sim$380 pc) system to lie. However, the approach taken by Munari & Zwitter (1997) uses a sample of O- and early B-type stars with a range of $E(B-V)$ values from $0.0 - 1.6$ (Sūdžius & Bobinas, 1994). In general, equivalent width W of an interstellar absorption line is related to $E(B-V)$ by

$$W = \alpha \sum_{n=1}^{\infty} (-1)^{n-1} \frac{(\beta E_{B-V})^n}{n!\sqrt{n}},$$

where the constants $\alpha = 0.354 \pm 0.01$ Å and $\beta = 11.0 \pm 1.0$ for the Na I D$_1$ line. FEROS spectra of CPD-54 810 were obtained from the ESO Science Archive Facility and the regions around the Na I doublet are shown in Figure 5.5. We fitted the Na I D$_1$ line in each spectrum with grids of Gaussian models centred on the rest wavelength and spanning the ± 25 km/s velocity range of local clouds in the ISM (Frisch et al., 2011). Taking a mean equivalent width of 0.0074 ± 0.0006 Å, we used a Bayesian approach to find a best fit and hence $E(B-V)$ estimate for the system, exploring the posterior distribution of the model with MCMC methods to obtain a robust error. For CPD-54 810 we obtain a reddening estimate of $E(B-V) = 0.002 \pm 0.012$, which includes an additional error of 0.011 from the scatter of the Munari & Zwitter (1997) relation.

5.3.6 Metallicity estimate

It was necessary to obtain an estimate of the metallicity [Fe/H] for CPD-54 810 in order to select a reasonable model SED to use in the T_{eff} calculation. We generated a grid of synthetic spectra for both stars over the metallicity range [Fe/H] = $(-0.6, -0.4, -0.2, 0.0, 0.2)$ using the ISPEC (Blanco-Cuaresma et al., 2014b; Blanco-Cuaresma, 2019) implementation of the TURBOSPECTRUM code (Plez, 2012). We used the MARCS grid (Gustafsson et al., 2008) and solar abundances from Grevesse et al. (2007). We fixed the surface gravity to the values given in Table 5.9 and fixed the effective temperatures to the values 6500 K and 6350 K, consistent with the values we derive below. Following
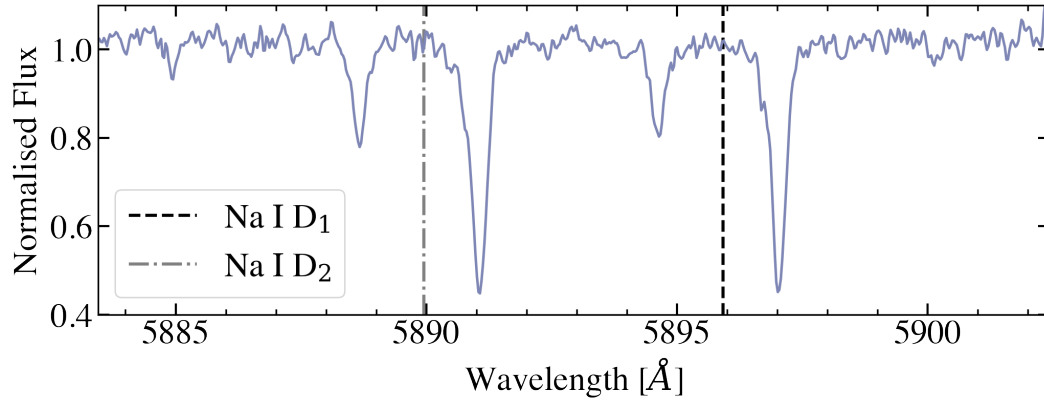
Figure 5.5: The FEROS spectrum with the largest wavelength spacing between stellar lines about the rest wavelength of the Na I D$_1$ and D$_2$ lines. The rest wavelengths of the two lines are marked with vertical lines.

Valenti & Fischer (2005) we assumed a value of $v_{\mathrm{mic}} = 0.85\,\mathrm{km/s}$ for both stars, and used their Equation (1) to obtain estimates for the macroturbulence velocities from our T_{eff} estimates: $v_{\mathrm{mac},1} = 2.84\,\mathrm{km/s}$, $v_{\mathrm{mac},2} = 3.05\,\mathrm{km/s}$. We synthesised a grid of synthetic combined spectra, by shifting the template spectrum of each component from rest wavelength to match its observed radial velocity, and co-adding the primary and secondary spectra. This allowed us to directly compare the observed FEROS spectra and synthetic spectra. We iterated over the list of unblended Fe I and Fe II lines presented in Doyle et al. (2017) and noted which of the synthetic grid best matched the depth of the Fe line. Any lines that were not present or blended were not included in the analysis. We took an average of the measured metallicities and obtained an estimate of $[\mathrm{Fe/H}] = 0.0 \pm 0.2$.

5.3.7 Effective temperatures

We use an approach based on the Stefan-Boltzmann law to obtain independent, fundamental effective temperatures for both components of an eclipsing binary system. For a detached, non-interacting binary star system at distance d, i.e. with parallax

Table 5.6: Observational data for CPD-54 810 used in our T_{eff} analysis. The quoted parallax is including correction from Flynn et al. (2022), and radii include a correction from apparent disc radius to Rosseland radius.

Quantity	Value	Source
Parallax, ϖ	$2.631 \pm 0.020\,\mathrm{mas}$	*Gaia* EDR3
Radius, R_1	$1.9288 \pm 0.0030\,\mathrm{R}_\odot$	This work
Radius, R_2	$1.1815 \pm 0.0037\,\mathrm{R}_\odot$	”
Apparent magnitude		
FUV	19.527 ± 0.206	*GALEX*
NUV	14.187 ± 0.009	”
u	11.770 ± 0.009	SkyMapper
v	11.312 ± 0.011	”
G	10.343 ± 0.003	*Gaia* EDR3
BP	10.576 ± 0.003	”
RP	9.958 ± 0.004	”
J	9.554 ± 0.027	2MASS
H	9.380 ± 0.026	”
Ks	9.283 ± 0.023	”
$W1$	9.218 ± 0.023	WISE
$W2$	9.240 ± 0.020	”
$W3$	9.241 ± 0.021	”
$W4$	8.973 ± 0.254	”
Flux ratios		
B	0.3299 ± 0.0012	This work
V	0.3413 ± 0.0008	”
R	0.3475 ± 0.0009	”
I	0.3517 ± 0.0008	”
$TESS$	0.3517 ± 0.0009	”
Derived quantities		
θ_1	$0.04720 \pm 0.00040\,\mathrm{mas}$	$2R_1\varpi$
θ_2	$0.02891 \pm 0.00024\,\mathrm{mas}$	$2R_2\varpi$
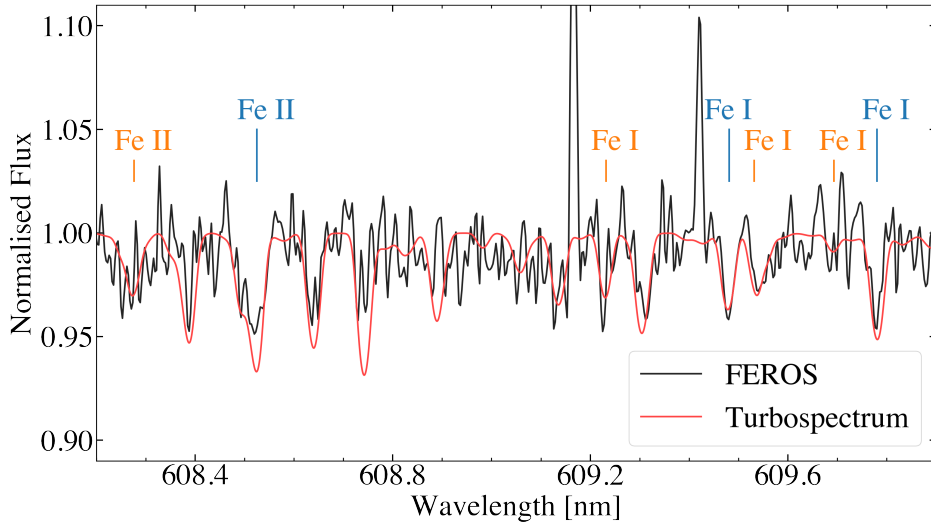
Figure 5.6: Observed FEROS spectrum of CPD-54 810 compared to the synthetic TURBOSPECTRUM generated from the best $T_{\rm eff}$, $\log g$ and [M/H] estimates from our analysis. Prominent iron lines from Doyle et al. (2017) used to estimate the metallicity of the system are noted above the continuum, shifted to the velocities of the primary (blue) and secondary (orange) components.

$\varpi = 1/d$, where each star has angular diameter $\theta = 2R\varpi$, the total flux of the binary corrected for extinction at the top of the Earth's atmosphere is

$$f_{0,b} = f_{0,1} + f_{0,2} = \frac{\sigma_{\rm SB}}{4} \left[\theta_1^2 T_{\rm eff,1}^4 + \theta_2^2 T_{\rm eff,2}^4 \right],$$

where $\sigma_{\rm SB}$ is the Stefan-Boltzmann constant. The radius R used in the calculation of θ is the Rosseland radius, which is obtained by applying a correction to the photometric radius by noting the difference between the two radii for the Sun found by Haberreiter et al. (2009) and scaling it to the appropriate $T_{\rm eff}$ for the stars in CPD-54 810 using values measured by Morello et al. (2017). This correction is on the order of the atmospheric scale height, so is only significant for stars with very precise radii measured from the light curves. The parallax for CPD-54 810 is taken from *Gaia* EDR3 with zero-point corrections from Flynn et al. (2022). All of these quantities are known or can be measured for CPD-54 810 if we can independently and accurately obtain the integrated fluxes $f_{0,1}$, $f_{0,2}$ for both stars. This can be done by using observations of

apparent magnitudes at ultraviolet, visible and infrared wavelengths, and since the light curve of CPD-54 810 shows total eclipses, it is possible to obtain a reliable estimate of the flux ratio in several photometric bands. To obtain reliable integrated fluxes for CPD-54 810, we use the method first described in Miller et al. (2020), which aims to avoid the caveats of simple SED fitting by balancing the observational constraints from photometry with the small-scale spectral features provided by the model SED. The method uses Legendre polynomials to distort the model SEDs based on the photometry, such that the large-scale shape of the flux integrating functions are determined by the data rather than the choice of model. The method uses emcee to sample the posterior distribution of $P(M|D) \propto P(D|M)P(M)$ for the model parameters M with prior $P(M)$ given the data, D (observed magnitudes and flux ratios). The model parameters are

$$M = (T_{\mathrm{eff},1}, T_{\mathrm{eff},2}, \theta_1, \theta_2, E(B-V), \sigma_{\mathrm{ext}}, \sigma_\ell, d_{1,1}, \ldots, d_{2,1}, \ldots).$$

The prior $P(M)$ is calculated as a combination of the priors on the near-infrared flux ratios (Section 5.3.7.1), ratio of the stellar radii (Section 5.3.7.2) and a Gaussian prior on the interstellar extinction. The hyper-parameters σ_{ext} and σ_ℓ take into account additional uncertainties in the synthetic magnitudes and flux ratios, respectively, due to errors in the zero-points and response functions of the photometric passbands, errors in the SED models, or stellar variability. The distortion function Δ_i for each star applied to a given model SED (to calculate synthetic photometry for a given T_{eff}) is a linear superposition of Legendre polynomials in wavelength with coefficients for star 1 $d_{1,1}, d_{1,2}, \ldots$, and similarly for star 2. The number of coefficients N_Δ can be varied, such that the optimal number can be found. The distorted model SED for each star is then normalised and can be integrated to calculate the total bolometric flux and synthetic photometry for each star. The effective temperatures derived using this method are based on the angular diameter and integrated stellar flux calculated using distortion to include the realistic stellar absorption features from the models but to allow the overall shape to be determined by the observed magnitudes, and thus much of the dependence on models that SED fitting suffers from is alleviated.

5.3.7.1   Priors on infrared flux ratios

We do not have any direct measurements of the binary flux ratio at wavelengths longer than $1\,\mu$m for CPD-54 810. If there is no constraint placed on the flux for both stars in the near-infrared (NIR), the distortion functions could allow for models where the flux is unrealistically high or low. Following from Miller et al. (2020), we note that for solar-type stars, there is a well-defined relationship between T_{eff} and the NIR flux compared to total optical flux that shows little dependence on $\log g$ or [M/H]. Therefore, assuming that the stars in CPD-54 810 behave like other dwarf and subgiant FGK-type stars in the solar neighbourhood, we can put some constraints on the flux ratio in the 2MASS J, H, Ks and WISE $W1$, $W2$, $W3$, $W4$ bands. Using stars from the Geneva-Copenhagen survey (Holmberg et al., 2009; Casagrande et al., 2011) that are present in both 2MASS (Skrutskie et al., 2006) and WISE (Cutri & et al., 2012) catalogs, we defined relations between T_{eff} and $(V-X)$ colours for each NIR bandpass. We defined separate relations for the two stars, based on two subsets of stars with similar properties to each component of CPD-54 810. We restricted both subsets to an interstellar reddening range of $E(B-V) < 0.01$, with the primary sample further restricted to $5800 < T_{\text{eff}} < 6800\,$K and $3.5 < \log g < 4.5$, and the secondary sample restricted to $5500 < T_{\text{eff}} < 6600\,$K and $3.8 < \log g < 4.8$. These relations are given in Table 5.7.

5.3.7.2   Priors on ratio of the stellar radii

CPD-54 810 is a totally-eclipsing system, which means that we have a very good estimate of the ratio of the fractional stellar radii k from the *TESS* light curves. We apply an additional prior to the T_{eff} fitting method to constrain the parameter space to a realistic solution.

Table 5.7: Quadratic colour–T_{eff} relations used to place Gaussian priors on the near-infrared flux ratio for CPD-54 810, and the uncertainty on the colour for each.

Colour	Primary	Error	Secondary	Error
$V - J$	$0.000X_1^2 - 0.417X_1 + 0.965$	0.042	$0.000X_2^2 - 0.435X_2 + 1.073$	0.042
$V - H$	$0.050X_1^2 - 0.555X_1 + 1.173$	0.044	$0.064X_2^2 - 0.585X_2 + 1.315$	0.044
$V - Ks$	$0.066X_1^2 - 0.576X_1 + 1.238$	0.039	$0.085X_2^2 - 0.616X_2 + 1.387$	0.039
$V - W1$	$0.046X_1^2 - 0.582X_1 + 1.286$	0.061	$0.095X_2^2 - 0.623X_2 + 1.434$	0.061
$V - W2$	$0.060X_1^2 - 0.576X_1 + 1.277$	0.097	$0.050X_2^2 - 0.599X_2 + 1.424$	0.097
$V - W3$	$0.074X_1^2 - 0.575X_1 + 1.235$	0.053	$0.112X_2^2 - 0.624X_2 + 1.383$	0.053
$V - W4$	$0.098X_1^2 - 0.560X_1 + 1.281$	0.092	$0.106X_2^2 - 0.613X_2 + 1.426$	0.092

5.3.7.3 Application of the method to CPD-54 810

For CPD-54 810, we use BT-Settl model atmospheres (Allard et al., 2013) accessed via the Spanish Virtual Observatory[7] to calculate SEDs for both stars, using linear interpolation to obtain a model for each star with the parameters: $T_{\text{mod},1} = 6450\,\text{K}$, $\log g_{\text{mod},1} = 3.98$, $T_{\text{mod},2} = 6300\,\text{K}$, $\log g_{\text{mod},2} = 4.33$, and the same composition [Fe/H] $= 0.0$, [α/Fe] $= 0.0$ for both components. The model SEDs, along with the observed magnitudes and flux ratios used in the analysis of CPD-54 810, are shown in Figure 5.7. The predicted apparent magnitudes and flux ratios along with their photometric zero-point errors for our adopted values of T_{eff} fit are given in Table 5.8, and are compared with the observed photometry.

We ran 16 different versions of the T_{eff} analysis with 256 walkers over 1000 steps, with a burn-in of 1000 steps, to experiment with different input models, different numbers of distortion coefficients, and removing priors and observational data. Convergence

---

[7]http://svo2.cab.inta-csic.es/theory/newov2/index.php?models=bt-settl

of the fits were checked by a visual inspection of the trail plots. The details of each of these are discussed in detail in Section 5.4.3. The spectral energy distribution for the adopted fit is shown in Figure 5.8 and our best estimates for the stars' effective temperatures are given in Table 5.9. The errors quoted in Table 5.10 do not account for the systematic error present due to uncertainties in the calibration of the CALSPEC flux scale (Bohlin et al., 2014). For CPD-54 810, this error is an additional $13\,\mathrm{K}$ for both components.
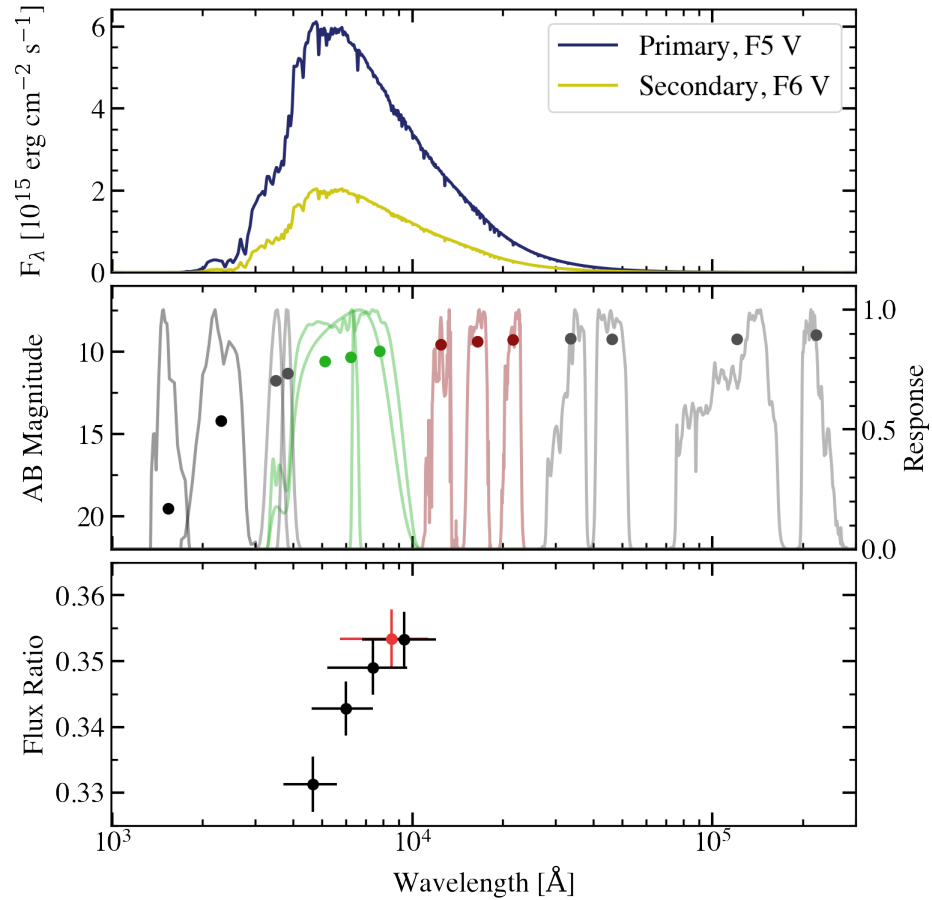
Figure 5.7: Summary of the photometric information used to derive T_{eff}. Top: BT-Settl spectral energy distributions for the two component stars of CPD-54 810 with solar abundances from Asplund et al. (2009), where $T_{\mathrm{eff},1}$= 6450 K, $\log g_1 = 3.98$ dex, $[\mathrm{Fe/H}]_1 = 0.0$, and $T_{\mathrm{eff},2}$= 6300 K, $\log g_2 = 4.33$ dex. $[\mathrm{Fe/H}]_2 = 0.0$. Each SED is scaled by the fractional radii of the two stars. Middle: Observed AB magnitudes used to constrain the overall shape of the bolometric flux integrating functions in the T_{eff} fit, and their photometric response functions. Lower: Flux ratios obtained from light curve fits of the PEST (black) and *TESS* (red) data, where the x-error is the wavelength span of the filter bandpass.

Table 5.8: Predicted data values and residuals for the best-fit model from Run A. The predicted apparent magnitudes are quoted together with the error on the zero-point.

Parameter	Value	Residual
Apparent magnitude		
FUV	19.762 ± 0.374	-0.235 ± 0.427
NUV	14.142 ± 0.883	$+0.045 \pm 0.883$
u	12.288 ± 0.219	-0.518 ± 0.219
v	11.442 ± 0.102	-0.130 ± 0.103
G	10.340 ± 0.003	$+0.003 \pm 0.004$
BP	10.573 ± 0.003	$+0.003 \pm 0.004$
RP	9.960 ± 0.004	-0.003 ± 0.005
J	9.533 ± 0.005	$+0.021 \pm 0.027$
H	9.339 ± 0.005	$+0.041 \pm 0.026$
Ks	9.283 ± 0.005	$+0.000 \pm 0.024$
$W1$	9.245 ± 0.002	-0.027 ± 0.023
$W2$	9.239 ± 0.002	$+0.001 \pm 0.020$
$W3$	9.224 ± 0.002	$+0.017 \pm 0.021$
$W4$	9.284 ± 0.002	-0.311 ± 0.254
Observed flux ratios		
B	0.332	-0.001 ± 0.004
V	0.343	$+0.000 \pm 0.004$
R	0.351	-0.002 ± 0.004
I	0.355	-0.002 ± 0.004
$TESS$	0.353	$+0.000 \pm 0.004$
Predicted flux ratios		
J	0.361	-0.001 ± 0.020
H	0.369	-0.004 ± 0.021
Ks	0.369	-0.003 ± 0.019
$W1$	0.370	-0.004 ± 0.029
$W2$	0.368	-0.001 ± 0.046
$W3$	0.360	$+0.006 \pm 0.025$
$W4$	0.339	$+0.026 \pm 0.044$
Angular diameters (mas)		
θ_1	0.04721 ± 0.00036	-0.0000 ± 0.0005
θ_2	0.02892 ± 0.00022	-0.0000 ± 0.0003

Table 5.9: Fundamental parameters of CPD-54 810 from the adopted light curve, radial velocity and T_{eff} fits. For comparison we also quote the values from Ratajczak et al. (2021). Quantities are given in nominal solar units (Prša et al., 2016).

Parameter	Value (This work)	Value (R21)
M_1 ($\text{M}_\odot$)	1.3094 ± 0.0051	1.311 ± 0.035
M_2 ($\text{M}_\odot$)	1.0896 ± 0.0034	1.093 ± 0.029
R_1 ($\text{R}_\odot$)	1.9288 ± 0.0030	1.935 ± 0.020
R_2 ($\text{R}_\odot$)	1.1815 ± 0.0037	1.181 ± 0.014
$M_1 + M_2$	2.3990 ± 0.0082	—
M_2/M_1	0.8321 ± 0.0018	—
$\log g_1$ (cm/s)	3.9836 ± 0.0012	3.982 ± 0.006
$\log g_2$ (cm/s)	4.3297 ± 0.0026	4.332 ± 0.008
ρ_1 ($\rho_\odot$)	0.18207 ± 0.00059	—
ρ_2 ($\rho_\odot$)	0.6595 ± 0.0059	—
$T_{\text{eff},1}$ (K)	6462 ± 43	5980 ± 205
$T_{\text{eff},2}$ (K)	6331 ± 43	5850 ± 190
$T_{\text{eff},2}/T_{\text{eff},1}$	0.9799 ± 0.0023	—
$\log L_1$ ($\text{L}_\odot$)	0.766 ± 0.011	0.635 ± 0.059
$\log L_2$ ($\text{L}_\odot$)	0.305 ± 0.012	0.168 ± 0.060

Table 5.10: Fit results from different sets of input parameters. Values in parentheses are 1-σ standard errors in the final digit(s) of the preceding value. N_Δ is the number of distortion coefficients included per star, $\Delta\lambda$ is the size of the integrating function wavelength bins in Å, and $\log \mathcal{L}$ is the log-likelihood. *N.B. these parameters have a non-Gaussian probability distribution. E(B$-$V) are given as 1-σ upper limits.

Run	$T_{mod,1}$ [K]	$T_{mod,2}$ [K]	[Fe/H] [dex]	N_Δ	$\Delta\lambda$ [Å]	$T_{eff,1}$ [K]	$T_{eff,2}$ [K]	E(B$-$V)* [mag]	$\sigma_{ext,m}$* [mag]	$\sigma_{ext,\ell}$* [mag]	$\log \mathcal{L}$	Notes
A	6450	6300	0.0	3	50	6462 ± 43	6331 ± 43	0.0096 (72)	0.015 (16)	0.0029 (29)	89.0	Adopted values
B	6650	6500	0.0	3	50	6463 ± 42	6334 ± 42	0.0094 (72)	0.011 (11)	0.0028 (28)	89.3	Varying T_{mod}
C	6250	6100	0.0	3	50	6460 ± 47	6326 ± 46	0.0092 (70)	0.021 (23)	0.0031 (31)	86.0	"
D	6650	6100	0.0	3	50	6458 ± 41	6321 ± 40	0.0092 (70)	0.010 (12)	0.0036 (36)	88.3	"
E	6375	6375	0.0	3	50	6461 ± 42	6333 ± 43	0.0094 (70)	0.014 (15)	0.0031 (30)	88.7	"
F	6450	6300	-0.2	3	50	6476 ± 41	6343 ± 41	0.0098 (73)	0.010 (11)	0.0032 (33)	89.9	Varying [Fe/H]
G	6450	6300	0.2	3	50	6448 ± 44	6316 ± 44	0.0095 (71)	0.016 (19)	0.0029 (29)	87.4	"
H	6450	6300	0.0	3	50	6461 ± 40	6335 ± 41	0.0090 (69)	0.013 (12)	0.0028 (29)	89.5	BT-Settl-CIFIST
I	6450	6300	0.0	3	50	6467 ± 54	6312 ± 101	0.0094 (72)	0.014 (14)	0.0150 (140)	66.9	No PEST data
J	6450	6300	0.0	3	50	6459 ± 45	6333 ± 59	0.0095 (71)	0.014 (15)	0.0051 (66)	64.2	No NIR flux ratios
K	6450	6300	0.0	3	50	6592 ± 139	6456 ± 133	0.0400 (320)	0.014 (15)	0.0029 (28)	89.1	No $E(B-V)$ prior
L	6450	6300	0.0	3	50	6462 ± 43	6331 ± 44	0.0095 (73)	0.015 (15)	0.0028 (27)	89.4	No k prior
M	6450	6300	0.0	0	50	6428 ± 29	6298 ± 30	0.0039 (31)	0.013 (11)	0.0026 (24)	84.2	SED fitting
N	6450	6300	0.0	6	50	6463 ± 45	6330 ± 44	0.0090 (68)	0.018 (16)	0.0041 (45)	89.7	Varying N_Δ
O	6450	6300	0.0	9	50	6472 ± 49	6329 ± 53	0.0094 (72)	0.020 (18)	0.0080 (100)	88.7	"
P	6450	6300	0.0	3	20	6465 ± 43	6334 ± 43	0.0101 (75)	0.013 (14)	0.0028 (27)	89.2	Varying $\Delta\lambda$
Q	6450	6300	0.0	3	80	6463 ± 42	6331 ± 43	0.0096 (72)	0.016 (16)	0.0031 (34)	88.9	"
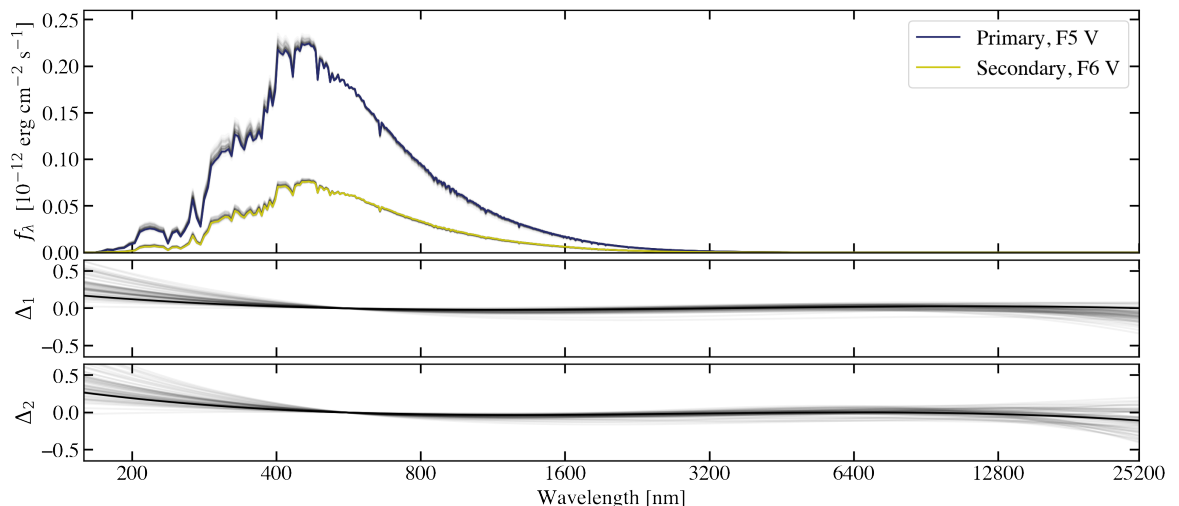
Figure 5.8: Integrating functions and distortion polynomials for our adopted T_{eff} solution. Top: Best log-likelihood integrating functions of the two stars used to obtain the best values for $T_{\text{eff},1}$ and $T_{\text{eff},2}$. Middle: The distortion functions applied BT-Settl input model SEDs for the primary star, showing best log-likelihood fit (dark line) and all other solutions (faint grey lines). Lower: Same, but for the secondary star.

5.4 Discussion

5.4.1 Impact of third light

We are not confident that the value of $\ell_3 \approx 1$ per cent found from the analysis of the *TESS* light curve represents a genuine detection of flux from a third body in the system. We suspect that this value is more likely due to systematic errors in the values of the background flux level in the *TESS* images and/or an underestimated contamination of the photometric aperture by other stars in the image. Nevertheless, we should consider the possibility that this flux is due to a low-mass tertiary star in the system and estimate the impact on our effective temperature measurements. The absolute magnitude of CPD-54 810 in the *Gaia RP* band is $M_{RP} = 2.071$. The *Gaia RP* band is similar to the *TESS* bandpass so we can estimate that the absolute magnitude of the putative third body is $M_{RP} \approx 7.1$. Assuming that the third body is a main-sequence

star, this corresponds to a K9V star with a luminosity of $0.066\,\mathrm{L_\odot}$, i.e. 0.8 per cent of the total luminosity.[8] Assuming that the extra luminosity is assigned equally between the two stars by our method if it is not accounted for, the effective temperatures we have measured will be over-estimated by $9\,\mathrm{K}$ for the primary star and $25\,\mathrm{K}$ for the secondary star. This is a negligible effect when compared to the standard errors on the values.

5.4.2   Comparison to stellar evolution models

We have compared the properties of CPD-54 810 to stellar evolution tracks computed with the Garching Stellar Evolution Code (GARSTEC; Weiss & Schlattl 2008). The microphysics used in these models is described in Serenelli et al. (2013) and Weiss & Schlattl (2008), but we provide a very brief summary here. The convection is described by the standard mixing length theory of Kippenhahn & Weigert (1990), where the solar mixing length is $\alpha_{\mathrm{ml},\odot} = 1.801$ using the Grevesse & Noels (1993) solar composition. The models include convective mixing and convective overshooting described in terms of diffusive processes. Due to the effects of diffusion, the initial solar composition is found to be $[\mathrm{Fe/H}]_{\mathrm{i}} = +0.06$.

Several grids of models were computed varying either the initial helium abundances or the assumed mixing length. Each grid covers stellar masses in the range 0.7-$2.0\,\mathrm{M_\odot}$ in steps of $0.02\,\mathrm{M_\odot}$ and ages from the zero-age main sequence up to $\tau =17.5\,\mathrm{Gyr}$. For each grid of models we used a Markov-chain Monte Carlo method to sample the posterior probability distribution of the model parameters $P(\tau,\ M_1,\ M_2,\ [\mathrm{Fe/H}]_{\mathrm{i}}|D)$, where the data D are the fundamental parameters of the stars given in Table 5.9. Further details of the stellar evolution models and MCMC methods used are provided in Kirkby-Kent et al. (2018).

We found the best fit to the observed parameters of CPD-54 810 for the grid of models with an initial helium abundance 0.03 dex higher than our assumed solar

---

[8] http://www.pas.rochester.edu/~emamajek/EEM_dwarf_UBVIJHK_colors_Teff.txt

initial helium abundance and a mixing length $\alpha_{\mathrm{ml}} = 1.78$ at an age $\tau = 2.83$ Gyr. The best-fit stellar evolution tracks are shown in the Hertzsprung-Russell diagram in Fig. 5.9. For the best fit we obtain $\chi^2 = 8.2$ for 7 observed quantities and 4 free parameters, i.e. 3 degrees of freedom. Models of solar initial helium abundance give a significantly worse fits to the observations ($\chi^2 > 50$). However, we note that the primary star is near the end of its main-sequence evolution where the evolution models are sensitive to assumptions about the nature and extent of mixing processes near the core, so there may be other models that fit the observations equally well assuming an initial helium abundance closer to the solar value. A full exploration of the parameter space for stellar models is beyond the scope of this study, but is certainly worthwhile given the high precision and accuracy of the fundamental parameters for these stars that are now available.

This analysis shows that the parameters we have obtained are consistent with stellar evolution models for a normal pair of main-sequence stars slightly younger than the Sun with the primary close to the end of its main-sequence lifetime. It also suggests that the high-precision and accuracy of the stars' fundamental parameters we have derived, particularly the effective temperatures, provide useful constraints on model parameters such as the mixing length and initial helium abundance. A full exploration of the model parameter space is needed to quantify the precision of the model parameters that can be derived from such a comparison and the correlations between them, but is beyond the scope of this study.

5.4.3 Requirements for precise & accurate T_{eff} estimates

5.4.3.1 Handling of 'incorrect' choice of model with distortion

To verify the ability of our method to handle a range of reasonable starting values without the result changing significantly, we ran the method with different starting temperatures (runs B–E) and metallicities (runs F–G) for the BT-Settl model SEDs than those used to derive the values given in Table 5.9. Increasing the model tem-
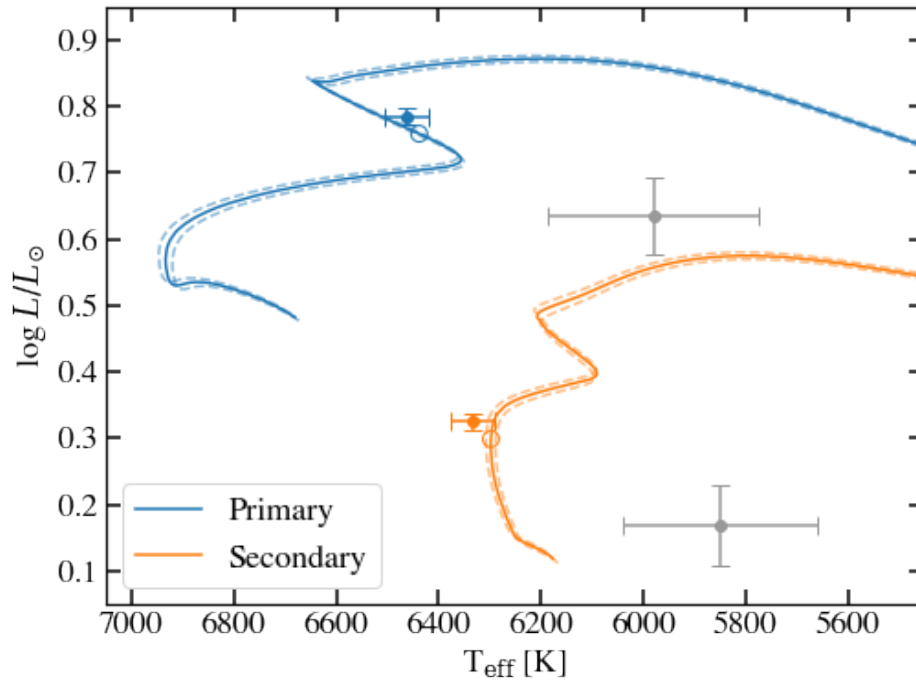
Figure 5.9: CPD-54 810 in the Hertzsprung-Russell diagram compared to GARSTEC stellar evolution models. Error bars in grey are the parameters from Ratajczak et al. (2021). GARSTEC stellar evolution tracks are shown for masses $M_1 = 1.308 \pm 0.005\,M_\odot$ and $M_2 = 1.085 \pm 0.003\,M_\odot$, initial metallicity $[\text{Fe/H}]_\text{i} = -0.05$, initial helium abundance $Y_\text{i} = Y_{\text{i},\odot} + 0.03$ and a mixing length $\alpha_\text{MLT} = 1.78$. The open circles on the evolutionary tracks correspond to the best-fit age of 2.83 Gyr.

peratures for both stars by 200 K (run B) gives a near-indistinguishable result, but decreasing both model temperatures by the same amount (run C) slightly increases the errors in derived temperatures and increases the amount of additional noise given to the observed magnitudes. Increasing and decreasing the ratio between the model temperatures for the two stars (runs D and E respectively) again shows no significant difference to the adopted values, although in run D we can see that the code tries to compensate for the increased temperature ratio by boosting the additional noise for the flux ratios and reducing the estimate for interstellar reddening, which in turn results in a derived secondary star temperature 10 K cooler than our adopted value. Varying the ratio of the input temperatures is a useful test to check whether the distortion is behaving correctly, and given the agreement of runs D and E with our adopted values from run A, we do see that the method of distortion works. Since our estimate for the metallicity of CPD-54 810 has an uncertainty of ± 0.2 dex, we tested whether an input [Fe/H] value at either end of this range (runs F and G) would have a significant impact on the derived effective temperatures. We see a slight increase of 10-15 K in the derived T_{eff} for both components when [Fe/H] $= -0.2$, and a similar decrease for both components when [Fe/H] $= 0.2$. At a lower metallicity, the amount of line-blanketing in the near-ultraviolet region increases in the model SEDs. To compensate for this, the distortion functions must boost the amount of flux in the ultraviolet, and hence increasing the derived effective temperatures. This highlights how important it is to not only have a reliable estimate for [Fe/H], but also photometry in the near-ultraviolet region to provide a reasonable constraint on the fit. Finally, we also tested whether using a different set of model SEDs (BT-Settl-CIFIST rather than BT-Settl, run H) with different abundances would have an impact on the derived effective temperatures. We see no significant change in the derived temperatures or goodness-of-fit metrics, which suggests that there is no significant dependence on the choice of model SED. From these tests, we have shown that the temperature method is robust to different input model SEDs generated using a reasonable range of temperatures and metallicities. The distortion handles "incorrect" temperature ratios that a simple SED fit would be unable to, and these results show that the distortion breaks any strong dependence on model

choice, i.e. the effective temperatures we have derived are not strongly dependent on the details of how the analysis has been done.

5.4.3.2 Value of multi-band light curves

CPD-54 810, like many eclipsing binary systems in the literature, does not have light curves in passbands beyond the broad-band visible or NIR of large photometric surveys such as ASAS, WASP, *Kepler* and *TESS*. While it is possible to obtain an estimate of T_{eff} with only one binary flux ratio, the distortion functions are less well constrained throughout the optical range and the results are therefore less precise. Obtaining light curves of CPD-54 810 during the total secondary eclipse made it possible to add an additional four constraints on the binary flux ratio throughout the visible range, and tightened up the uncertainties on T_{eff}: when running the T_{eff} fit with the same parameters as the adopted run but excluding PEST flux ratios (Run I), the uncertainties on T_{eff} increase from $6462 \pm 43\,\text{K}$ to $6467 \pm 54\,\text{K}$ for the primary and $6331 \pm 43\,\text{K}$ to $6311 \pm 101\,\text{K}$ for the secondary. Given the importance of obtaining robust and precise direct measurements for the T_{eff}, this comparative test of the method with and without the PEST flux ratios highlights the importance of including as much multi-band photometric data as possible.

5.4.3.3 Priors on parameters

We tested the impact of each of the additional priors we placed on model parameters for the temperature fit: near infrared flux ratios (run J), interstellar reddening (run K), and ratio of the fractional stellar radii (run L). As with AI Phoenicis (Miller et al., 2020), placing a prior on the relative flux of the two component stars in the near-infrared was a useful addition to the code that prevented any potential distributions of flux about the wavelength range that was non-physical. Removing this prior in run J gives no significant change in the value of T_{eff} for either component, but the effect can be seen in the increased amount of additional noise used to fit the observed flux

ratios, and slightly increased uncertainty in the effective temperature for the secondary component ($\sim 16\,\mathrm{K}$). These results are encouraging and support the use of this prior on the near-infrared flux ratio for systems like CPD-54 810 as part of the standard procedure for the temperature method in future work.

To derive precise and accurate effective temperatures with our method, it is essential to have a reliable, direct estimate for $E(B-V)$. This is demonstrated in run K, for which we relaxed the prior we placed on $E(B-V)$ from the Na I D_1 line equivalent width. Both the values and uncertainties for the derived temperatures of both components in CPD-54 810 have significantly increased from the adopted run A to this run, K. The code climbs to a much higher yet more uncertain value for $E(B-V)$ without the constraint from the prior, which in turn makes it necessary to increase the derived temperatures. In contrast, the prior on the radius ratio has very little impact on the results or quality of fit for CPD-54 810 (run L).

5.4.3.4 Number of distortion coefficients

The measurements of the flux ratios are least affected by systematic errors because they are directly related to the eclipse depth, and the SED for both stars are very similar, so errors in zero-points and instrumental response functions affect both stars equally. We can therefore inspect how well the code treats the flux ratio measurements and use this to select the optimal number of distortion coefficients; i.e. the fit with the lowest $\sigma_{\mathrm{ext},\ell}$. An inflated value for $\sigma_{\mathrm{ext},\ell}$ can be due to over-fitting – the wavelength space is poorly sampled due to very few measurements of flux ratio – or due to SED fitting, where there is little else the code can vary to optimise the overall fit. The results for the temperature fit, using the method with no distortion to illustrate a standard SED fitting procedure, is shown as run M. While the errors on derived T_{eff} for both components are lower than all other runs in Table 5.10, we argue that these are underestimates of the true errors. The additional noise required to fit the observed flux ratios is double that which was required for the adopted run A, and the log-likelihood is much lower, which indicates a worse fit. We thoroughly tested which number of distortion coefficients was

optimal for CPD-54 810. The results for $N_\Delta = 3$ (adopted values, run A), 6 (run N) and 9 (run O) are shown in Table 5.10. The uncertainties on derived temperatures increase with an increasing number of coefficients, to the point of potential over-fitting with run O. We settled on 3 sets of coefficients for CPD-54 810, balancing the need for distortion whilst avoiding over-fitting due to the sparse photometric data available. For stars with more photometric data throughout the log-wavelength space, such as AI Phoenicis, it is more reasonable to use a larger number of coefficients to ensure the models can be distorted on a small enough scale to accurately fit the observational data. With spectrophotometry across the optical range from the upcoming *Gaia* DR3 and beyond, it may be possible to employ a greater number of distortion coefficients for the $T_{\rm eff}$ fitting method.

5.4.3.5 Effects of model SED binning

We tested whether the model SED being binned into smaller or larger wavelength bins would have an effect on the results of the $T_{\rm eff}$ fit. Run P has the most fine grid at $20\,\text{Å}$, Run Q has the largest bin size of $80\,\text{Å}$ and these can both be compared to the adopted Run A with a bin size of $50\,\text{Å}$. The output of the $T_{\rm eff}$ fit in all three scenarios is largely the same, with the log-likelihood growing slightly with smaller wavelength bins. The main difference between these three fits is the run time. For 2000 steps with 256 walkers on a standard desktop computer with 4 Intel Core i5-7500 CPUs at $3.40\,\text{GHz}$, the most fine wavelength grid of $20\,\text{Å}$ (run P) takes 2 hours 13 minutes, the adopted run with a $50\,\text{Å}$ grid takes 1 hour 16 minutes, and the most coarse grid we tested (run Q at $80\,\text{Å}$) takes 1 hour 04 minutes. We therefore conclude that the choice in wavelength bin size is ultimately a balance between minimising run time and maximising the quality of the fit. For the adopted and other runs we settled for $50\,\text{Å}$ as a compromise between these factors.

5.4.4 Effective temperature estimates from disentangled spectra

When compared to the spectroscopic temperature estimates derived in R21, the fundamental effective temperatures measured in this work are significantly hotter for both components (see Table 4.6). Despite the difference in $T_{\rm eff}$ estimates between the two analyses, we can still obtain a synthetic spectrum fit of a similar quality with the higher temperatures (see Figure 5.6 versus Figure 1 in R21). This highlights the difficulties of obtaining reliable $T_{\rm eff}$ estimates from low to moderate signal-to-noise spectra, and stresses the importance of not only developing a catalog of stars with accurate fundamental effective temperature measurements, but of independently checking spectroscopic effective temperature estimates with other methods where possible.

5.5   Conclusions

We have measured precise and accurate masses, radii and effective temperatures for both stars in the detached eclipsing binary CPD-54 810 using a wealth of new *TESS* light curves, radial velocities measured by R21, observations of the total secondary eclipse in *BVRI* bands, photometry from the ultraviolet to near-infrared, and parallax from *Gaia* EDR3. Using the method first described in Miller et al. (2020), we have significantly improved the measured values for effective temperature. We find that the stars in CPD-54 810 are slightly younger than the Sun, with the primary F5 V component appearing to be close to the end of its main-sequence lifetime. CPD-54 810 is a detached, well-behaved and isolated system which makes it ideal for testing calibrating data-driven stellar parameter pipelines from spectroscopic surveys, along with testing stellar evolution models. There are many more moderately-bright systems like CPD-54 810 being discovered by large scale surveys such as *TESS* which are suitable candidate benchmark stars for future work building on this method for deriving direct, accurate effective temperatures for stars in detached eclipsing binaries.

6 Fundamental effective temperature measurements for EBLM J0113+31

But that sunset! I've never seen anything like it in my wildest dreams ... the two suns! It was like mountains of fire boiling into space ... We only ever had the one Sun at home.

Douglas Adams, *Hitchhiker's Guide to the Galaxy* (1979)

Note: The following chapter is a reproduction of the paper "Fundamental effective temperature measurements for eclipsing binary stars – III. SPIRou near-infrared spectroscopy and *CHEOPS* photometry of the benchmark G0V star EBLM J0113+31" (Maxted, Miller et al., 2022; accepted in MNRAS, April 2022). My contribution to the work was providing the code and guidance for the direct measurement of the stellar effective temperature (Section 6.3.7) and in discussions about EBLM systems as benchmark stars (Section 6.4.3). The rest of the paper was contributed by P. Maxted and collaborators. The full paper has been included in this chapter to provide context for my contributions.

6.1 Introduction

Benchmark stars have properties that have been directly and accurately measured to good precision. They play a fundamental role in stellar astrophysics because we can only ascertain the accuracy and reliability of stellar models by comparing their predictions to the observed properties of real stars. Benchmark stars can also be used to establish empirical relations between stellar properties, e.g. colour – effective temperature ($T_{\rm eff}$) relations (Boyajian et al., 2013; van Belle et al., 2021; Huang et al., 2015), or equations to estimate the mass or radius of a main-sequence star from $T_{\rm eff}$, $\log g$ and [Fe/H] (Torres et al., 2010). Empirical relations are particularly useful in cases where stellar structure models are known to be unreliable, e.g. for low-mass stars, where

stellar models tend to under-predict the radius and over-predict T_{eff} (Spada et al., 2013; Cassisi & Salaris, 2019; Zhou et al., 2014; Berger et al., 2006).

Considerable effort has put into calibrating the T_{eff} scale for FGK-type dwarf stars. In recent years, this effort has been partly driven by the need for accurate T_{eff} estimates for planet host stars in order to estimate their masses and radii using stellar models (Boyajian et al., 2015; Baines et al., 2009). Much of the progress in characterising exoplanets in recent years has been due to the improved precision in measuring stellar masses and radii (Jontof-Hutter, 2019).

Benchmark FGK-type stars are also essential to calibrate the level of systematic and random uncertainties in massive spectroscopic surveys such as RAVE (Steinmetz et al., 2020), the *Gaia*-ESO survey (Gilmore et al., 2012), LAMOST (Deng et al., 2012), GALAH (Buder et al., 2018), etc. (Blanco-Cuaresma et al., 2014a; Heiter et al., 2015; Jofré et al., 2018). These surveys aim to reconstruct the formation history of the Galaxy by studying the pattern of elemental abundances in stars as a function of their mass, age and kinematics. Jofré et al. (2019) in their recent comprehensive review of "industrial scale" stellar abundance measurements suggest that it is today not possible to know the temperature of a star better than an accuracy of 50 K. This uncertainty has a direct impact on reliability of trends observed in stellar abundance patterns between different stellar populations. Errors in T_{eff} are the dominant source of uncertainty when estimating the mass, radius, composition and age of a star (Valle et al., 2018; Jofré et al., 2019).

Validation and calibration of T_{eff} estimates for FGK-type dwarf stars currently rely on angular diameter measurements for a small sample of very bright stars such as Procyon, τ Cet, 18 Sco, α Cen A, etc. (Karovicova et al., 2022; Heiter et al., 2015; Boyajian et al., 2013). Repeated measurements of the angular diameter for the same star often show differences much larger than the quoted uncertainties, with systematic errors of 5 per cent or more being quite common. For example, the 15 repeated measurements provided in Table 9 of Karovicova et al. (2022) for 7 G-type dwarf stars require an additional "external error" of about 0.04 mas to be added to the quoted uncertainties to achieve $\chi_r^2 = 1$ for a fit of a constant offset to these difference.

Tayar et al. (2022) show that current uncertainties on measured interferometric angular diameters and bolometric fluxes set a systematic uncertainty floor of ≈ 2 per cent in T_{eff} for solar-type exoplanet host stars, i.e. $\pm 120\,\mathrm{K}$ at $T_{\mathrm{eff}} = 6000\,\mathrm{K}$.

Very low-mass stars (VLMSs, $\lesssim 0.2 M_{\odot}$) are attractive targets for exoplanet studies because of the possibility to detect and characterise the atmospheres of terrestrial planets in the habitable zones of these stars (Sebastian et al., 2021). There are very few well-characterised VLMSs because they are intrinsically very faint and small. For example, the recent empirical colour$-T_{\mathrm{eff}}$, colour$-$luminosity and colour$-$radius relations published by Boyajian et al. (2012) are based on a sample that contains only one star with a spectral type later than M4V ($M \approx 0.2 M_{\odot}$, Mann et al., 2019).

The EBLM project (Triaud et al., 2013) aims to improve our understanding of VLMSs by studying eclipsing binaries with low-mass companions that have been found by the WASP survey (Pollacco et al., 2006). These eclipsing binaries typically have a late-F- to mid-G-type primary star with an M-dwarf that contributes $\ll 1$ per cent of the flux at optical wavelengths. The light curves of these EBLM systems look very similar to those of transiting hot Jupiters, which are the main targets for the WASP survey. As a result, dozens of these EBLM systems have been identified in the WASP survey. The analysis of the light curve combined with a spectroscopic orbit for the primary star and an estimate for its mass provides a direct estimate for the mass and radius of the M-dwarf companion (von Boetticher et al., 2019; Gill et al., 2019). With very high quality photometry it is possible to detect the eclipse of the M-dwarf and, hence, its surface brightness relative to the primary star. This surface brightness ratio can then be used to infer T_{eff} for the M-dwarf given an estimate of T_{eff} for the primary star and a surface brightness $-$ T_{eff} relation for the stars, either empirical (Graczyk et al., 2021) or based on stellar model atmospheres. The first results from an on-going programme to measure mass, radius and T_{eff} for the M-dwarf in a sample of EBLM systems using ultrahigh-precision photometry obtained as part of the guaranteed time observations (GTO) with the *CHEOPS* mission (Benz et al., 2021) have been published by Swayne et al. (2021). Most of the targets for this programme were selected from a sample of over 100 EBLM systems with spectroscopic orbits published by Triaud et al.

(2017).

The first study of EBLM J0113+31, the target for this study, was published by Gómez Maqueo Chew et al. (2014, GMC+2014 hereafter). They used ground-based photometry of the eclipse in the J-band to infer $T_{\mathrm{eff}} \approx 3900\,\mathrm{K}$ for the very low-mass companion, much higher than expected given their estimate for its mass ($M_2 = 0.186 \pm 0.010 M_{\odot}$). Subsequent analysis of the *TESS* light curve for this binary system by Swayne et al. (2020) found no evidence for a very hot companion. Their value of $T_{\mathrm{eff},2} = 3208 \pm 43\,\mathrm{K}$ is similar to that for other VLMSs. They conclude that the anomalous result from GMC+2014 was due to systematic errors in the J-band photometry, illustrating the need for very high-quality space-based photometry to make reliable measurements of $T_{\mathrm{eff},2}$ in EBLM systems.

Here we present new photometry of the transit and eclipse in EBLM J0113+31 obtained with *CHEOPS*, and high-resolution, phase-resolved spectroscopy obtained with the near-infrared échelle spectrograph SPIRou on the Canada-France-Hawaii telescope. We have used the SPIRou spectroscopy to directly measure the semi-amplitude of the M-dwarf's spectroscopic orbit. We have used this measurement combined with the analysis of the new light curves and other published data to directly and accurately measure the mass, radius and T_{eff} of both stars in this binary system. We discuss the use of the techniques developed here to determine fundamental stellar properties for stars in EBLM systems, and conclude that it is now feasible to establish a network of well-studied EBLM systems that will be an ideal set of benchmark stars for future surveys.

6.2 Observations

6.2.1 *CHEOPS* photometry

CHEOPS is a telescope with an effective aperture of $30\,\mathrm{cm}$ in low Earth orbit that is designed to obtain ultrahigh precision broadband photometry of bright stars (Benz

et al., 2021). To achieve this, the instrument has been purposely defocused to produce a point-spread function (PSF) with a diameter of approximately $32''$. We observed two transits and one eclipse of EBLM J0113+31 with *CHEOPS* (Table 6.1). There are gaps in the observations due to occultation of the target by the Earth and passages of the satellite though the South Atlantic Anomaly.

The raw data were processed using version 13.1.0 of the *CHEOPS* data reduction pipeline (DRP, Hoyer et al., 2020). The DRP corrects the images for environmental and instrumental effects before performing aperture photometry of the target. The contamination of the photometric aperture during the exposure by nearby stars is estimated using simulations of the field of view based on the *Gaia* DR2 catalogue (Gaia Collaboration et al., 2018). The instrument response function for *CHEOPS* is very similar to the *Gaia G* band. The detector used on the *CHEOPS* instrument is a frame-transfer charge-coupled device (CCD), so the DRP must also account for the "smear" trails from bright stars produced during the frame transfer. Both of these effects (contamination and smear) vary from image to image because the satellite rotates continuously during its 99-minute orbit.

Aperture photometry is extracted by the DRP using three different fixed aperture sizes labelled "RINF", "DEFAULT" and "RSUP" (at radii of 22.5, 25.0 and 30.0 pixels, respectively) and a further "OPTIMAL" aperture whose size is determined for each visit dependent upon the amount of contamination. The observed and processed data are made available on the Data Analysis Center for Exoplanets (DACE) web platform[1]. We downloaded our data from DACE using `pycheops`[2], a PYTHON module developed for the analysis of data from the *CHEOPS* mission (Maxted et al., 2022b).

There are three stars that are 5–6 magnitudes fainter than EBLM J0113+31 within $1'$ of the target (Fig. 6.1). As a result, the OPTIMAL aperture is set to its maximum allowed value by the DRP (40 pixels = $40''$). Although this maximises the contamination of the aperture by these nearby stars, it minimises the noise due to the

---

[1]The DACE platform is available at `http://dace.unige.ch`
[2]`https://pypi.org/project/pycheops/`

Table 6.1: Log of *CHEOPS* observations. Effic. is the fraction of the observing interval covered by valid observations of the target. The variables in final column are spacecraft roll angle, ϕ, and aperture contamination, contam.

Event	Start date [UTC]	Duration [s]	N_{obs}	Effic. [%]	Decorrelation. params
Transit	2020-11-24T15:41:07	48 682	429	52.8	contam, $\sin\phi$, $\cos 3\phi$
Transit	2021-10-19T00:20:09	48 983	519	63.5	contam, $\sin\phi$, $\cos\phi$,$\sin 2\phi$
Eclipse	2021-09-28T03:09:09	34 936	338	57.9	contam, $\sin\phi$, $\cos 2\phi$,$\sin 3\phi$

variations in this contamination due to changes in the fraction of the stars' PSFs inside the photometric aperture as the field of view rotates.

6.2.2 CFHT SPIRou spectroscopy

SPIRou is a fibre-fed, cross-dispersed échelle spectrograph mounted on the Canada-France-Hawaii telescope (CFHT) on Maunakea, Hawaii. The spectrograph provides spectra covering the entire wavelength range from 0.95 to 2.35 microns at a spectral resolving power $R \approx 75,000$ (Donati et al., 2020). 22 spectra of EBLM J0113+31 with a signal-to-noise per pixel between 77 and 103 near 1 micron were obtained on separate nights between 2020-02-05 and 2020-08-01.

We used spectra extracted from the raw data provided by the observatory using data reduction system (DRS) version 0.6.131. We dealt with the data order-by-order, selecting only those orders with little contamination due to telluric features. The selected wavelength regions are listed in Table 6.2. The corrections for the échelle blaze function and telluric absorption provided by the DRS were applied.

6.2.3 *TESS* photometry

One transit and two secondary eclipses of EBLM J0113+31 were observed at 120 s cadence by the Transiting Exoplanet Survey Satellite (TESS, Ricker et al., 2015) in
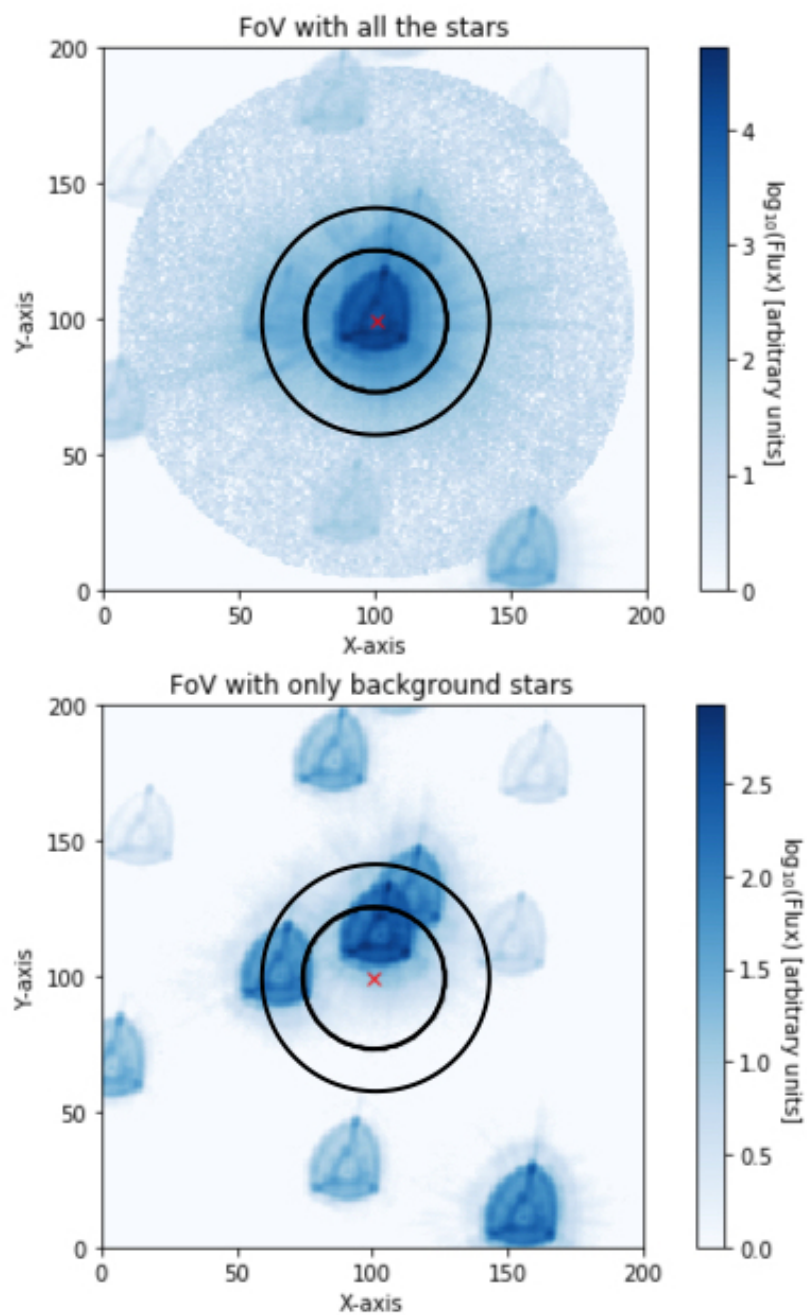
Figure 6.1: Simulated images of the *CHEOPS* field of view. Upper panel: all the stars in the field of view including the target. Lower panel: The target has been removed to show only the background stars in the field of view. Black circles show the DEFAULT (25 pixel) and OPTIMAL (40 pixel) apertures and the red cross shows the location of the target star.

Table 6.2: SPIRou échelle orders used in this analysis. Features typically visible in the spectra of M dwarfs from Jones et al. (1994) are listed with wavelengths in nm in the final column.

Order	$\lambda_{\min}$ [nm]	$\lambda_{\max}$ [nm]	Notes
32	2363	2437	
33	2291	2363	
34	2224	2294	
35	2160	2228	Na I 2206, 2209
36	2100	2166	
37	2043	2108	
44	1718	1772	
45	1680	1733	
46	1643	1695	Al 1676, 1677
47	1608	1659	
48	1575	1624	
58	1303	1344	
59	1281	1321	Ca I 1313
62	1219	1257	K I 1243, 1252
63	1199	1237	
64	1181	1218	VO 1200
65	1162	1199	K I 1169, 1177, 1178
66	1145	1181	
72	1049	1082	
73	1035	1067	
74	1021	1053	
75	1007	1039	
78	968	999	FeH 990
79	956	986	
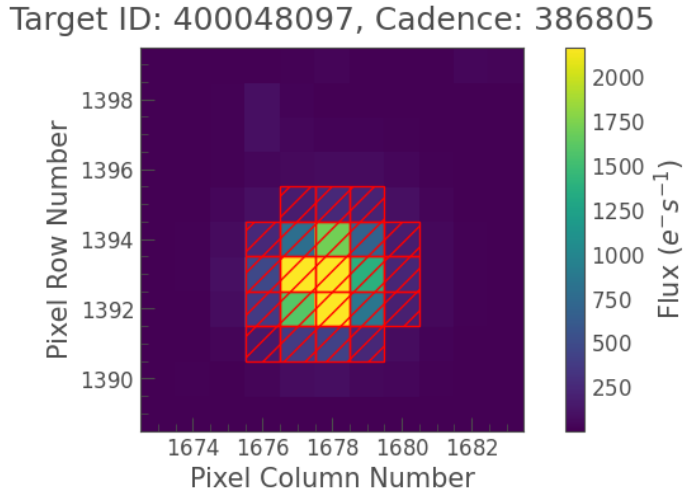
Figure 6.2: A typical image of EBLM J0113+31 from the *TESS* target pixel file showing the pixels used to extract the light curve (red hatching).

Sector 17 of the primary mission. The *TESS* target pixel files were downloaded from the Mikulski Archive for Space Telescopes[3] (MAST) and processed to produce a light curve using the package LIGHTKURVE 2.0 (Lightkurve Collaboration et al., 2018).[4] The pixels used to extract the photometry from the target pixel file are shown in Fig. 6.2. Instrumental noise was removed using the cotrending basis vectors (CBVs) provided by the *TESS* Science Processing Operations Center (SPOC) (Jenkins et al., 2016). We used 16 "Single-Scale" and 7 "Spike" CBVs to model trends present in all targets on the same CCD as EBLM J0113+31. The amplitude of each CBV was determined using only data outside the eclipses and transit. We set the L2-norm penalty to $\alpha = 0.1$ to achieve a balance between over-fitting the data and effectively removing instrumental trends.

---

[3]https://archive.stsci.edu/
[4]https://docs.lightkurve.org/

6.3   Analysis

6.3.1   Radial velocity measurements from the SPIRou data

We use synthetic spectra taken from Husser et al. (2013)[5] to produce a template for the spectrum of the G0V primary star, using linear interpolation to create a spectrum appropriate for $T_{\mathrm{eff}} = 6150\,\mathrm{K}$, $[\mathrm{Fe/H}] = -0.4$, $\log g = 4.15$ and $[\alpha/\mathrm{Fe}] = 0.0$. We then measure the position of the peak in the cross-correlation against this template for the observed spectra order-by-order. Low-frequency noise in the data for each order was removed prior to cross-correlation using a 5-th order high-pass Butterworth filter with a critical frequency of $16/4096$ pixels^{-1}. We then reject measurements more than $5\,\mathrm{km\,s}^{-1}$ from the median before calculating the mean and standard error in the mean given in Table 6.3.

6.3.2   Pre-processing of the SPIRou data

The M dwarf contributes less than $2\,$per cent of the flux at $1\,\mu$m so we removed the spectral features in the SPIRou data due to the G0V primary star prior to our attempt to detect the faint companion in these spectra. We use the spectroscopic orbit from GMC+2014 to shift the template spectrum for the primary star to the radial velocity corresponding to the time of mid-exposure for each SPIRou spectrum and then divide the observed spectrum by the shifted model spectrum.

The correction for telluric absorption in the observed spectra will be imperfect so we mask pixels where the telluric absorption is greater than $50\,$per cent. We also mask all pixels in order 47 at wavelengths $> 1616\,$nm because there is a strong telluric absorption band at these wavelengths. The removal of spectral features from the primary star will also be imperfect so we mask pixels where absorption lines in the template spectrum are deeper than $50\,$per cent. We then flatten the spectrum by

---

[5]`http://phoenix.astro.physik.uni-goettingen.de/`

Table 6.3: Radial velocity measurements for EBLM J0113+31 A measured from the SPIRou spectra of EBLM J0113+31. The number of orders used to calculate the mean and standard error on the mean is given in the final column.

Exposure number	BJD$_{\mathrm{TDB}}$	V_r [km/s]	N
2503696	2459063.1144	16.72 ± 0.14	24
2502923	2459059.1322	27.01 ± 0.14	24
2469680	2458896.7054	-1.79 ± 0.18	24
2499300	2459038.1105	3.12 ± 0.16	24
2498079	2459033.1244	22.56 ± 0.11	24
2493617	2459011.1184	-1.84 ± 0.13	24
2498553	2459035.1050	14.54 ± 0.13	23
2499489	2459039.0948	-0.06 ± 0.08	24
2468747	2458885.7312	5.73 ± 0.15	22
2502578	2459056.1340	-1.91 ± 0.13	24
2469510	2458895.7054	2.27 ± 0.16	23
2497677	2459031.1037	27.73 ± 0.12	24
2498357	2459034.1213	18.36 ± 0.16	23
2499115	2459037.1309	6.50 ± 0.17	24
2499760	2459040.1279	-2.89 ± 0.16	23
2498783	2459036.1298	10.66 ± 0.15	23
2468572	2458884.7115	-2.25 ± 0.18	24
2497879	2459032.1204	25.75 ± 0.14	24
2499953	2459041.1116	-3.52 ± 0.13	23
2503110	2459060.0927	27.40 ± 0.15	23
2469883	2458897.7056	-3.43 ± 0.14	23
2470074	2458898.7057	-3.21 ± 0.12	24

dividing the data by a 16th-order polynomial fit by least-squares to the unmasked data in each order.

Outliers due to cosmic ray hits on the detector and other image anomalies were then identified and removed by flagging pixels more than 4 times the inter-quartile range from the mean in 10 blocks of data per order.

The signal-to-noise is similar for each spectrum but varies quite strongly with wavelength so we use $1.25\times$ the mean absolute deviation of the data across the observed spectra to assign a standard error to the pixels at each wavelength.

6.3.3   Detection of the M dwarf in the SPIRou spectra

The signal from the M dwarf is too weak to be detected in the individual SPIRou spectra, but it is possible to measure the semi-amplitude of M dwarf's spectroscopic orbit, K_2, by calculating the average cross-correlation function against a suitable template spectrum after shifting these CCFs to the rest frame of the M dwarf assuming a range of K_2 values. The barycentric radial velocity of the M dwarf at the time of mid-exposure for each spectrum is

$$V_{r,2} = K_2 \left[\cos(\nu + \omega_2) + e \cos(\omega_2) \right] \tag{6.1}$$

The value of the eccentricity e and the longitude of periastron $\omega_2 = \omega_1 + \pi$ are known accurately from the spectroscopic orbit of the primary star with longitude of periastron ω_1, taken from GMC+2014. Similarly, the true anomaly at the time of mid-exposure, ν, can be accurately predicted from the values of T_0 (time of mid-transit), P (orbital period), e and ω_1, also taken from GMC+2014.

We use synthetic spectra taken from Husser et al. (2013) as a template for the spectra of the M dwarf, using linear interpolation to create a spectrum appropriate for $T_{\mathrm{eff}} = 3300\,\mathrm{K}$, $[\mathrm{Fe/H}] = -0.4$, $\log g = 5.0$ and $[\alpha/\mathrm{Fe}] = 0.0$. The cross-correlation function is calculated order-by-order. Low-frequency noise in the data for each order was removed prior to cross-correlation using a 5-th order high-pass Butterworth filter with a critical frequency of $32/4096$ pixels^{-1}. The data are apodized using a Gaussian

filter with a standard deviation of 64 pixels applied to the data at each end of the order. The correlation coefficient for each order is calculated after shifting the template according to radial velocity computed with equation (6.1) includes the weights calculated from the estimated standard errors on each pixel. This is repeated for a uniform grid of K_2 values. The average CCF over all orders and all exposures as a function of K_2 ("stacked CCF") is shown in Fig. 6.3. Gómez Maqueo Chew et al. (2014) estimate that $K_2 = 80.3 \pm 1.5 \, \mathrm{km\,s^{-1}}$. There is indeed a peak in the stacked CCF near this value of K_2. To measure the position of this peak we model the stacked CCF as a Gaussian process (GP) plus a Gaussian profile. We use the CELERITE package (Foreman-Mackey et al., 2017) to compute the likelihood for a GP with a kernel of the form $k(\tau) = a_j \, e^{-c_j \tau}$ and the affine-invariant Markov chain Monte Carlo sampler EMCEE (Foreman-Mackey et al., 2013) to sample the posterior probability distribution for the model parameters. Based on this analysis, the peak in the stacked CCF occurs at $K_2 = 82.9 \pm 0.7 \, \mathrm{km\,s^{-1}}$ and has a width of $5.7 \pm 0.6 \, \mathrm{km\,s^{-1}}$.

The broad peak in the stacked CCF around $K_2 = 0$ is due to imperfect removal of telluric features and spectral features from the G0V primary star. We compared the stacked CCF to the average CCF computed with negative values of K_2 plotted against $|K_2|$, i.e. the mirror image of the stacked CCF. As can be seen in Fig. 6.3, there is no corresponding peak at $K_2 \approx -83 \, \mathrm{km\,s^{-1}}$. This reassures us that the peak at $K_2 \approx +83 \, \mathrm{km\,s^{-1}}$ is unlikely to be due to imperfect removal of telluric features or spectral features from the G0V primary star. We used a fit to the stacked CCF done in the same way as above but excluding data around the peak at $K_2 = 83 \, \mathrm{km\,s^{-1}}$ to estimate the statistical significance of this feature. Based on the GP prediction of the correlated noise in this region shown in Fig. 6.3, we estimate that the peak height corresponds to a detection with a significance ≈ 4-σ. We also verified that the height of the peak in the stacked CCF is very close to the height expected for an M-dwarf companion given the flux ratio $\ell_T \approx 0.00155$ inferred from the depth of the secondary eclipse in the *TESS* light curve. We subtracted a scaled version of the template M-dwarf spectrum from the spectra used to compute the stacked CCF based on this flux ratio in the *TESS* band and re-computed the stacked CCF. As can be seen in Fig. 6.3, the
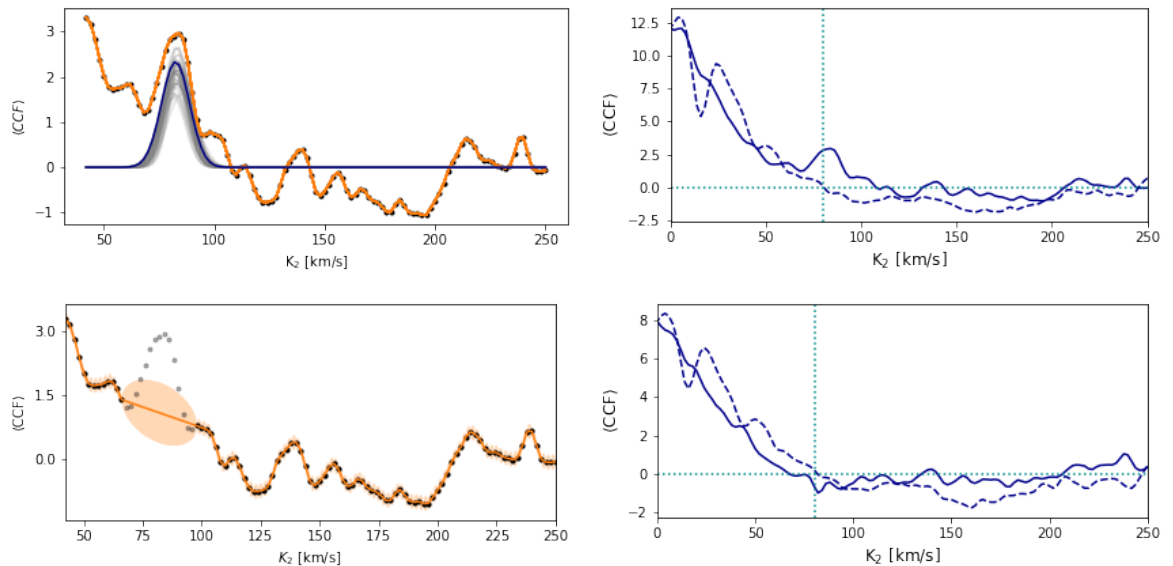
Figure 6.3: Mean cross-correlation function of EBLM J0113+31 after shifting to the rest frame of EBLM J0113+31 B assuming a range of K_2 values. *Upper-left panel:* Gaussian process fit (orange) of a Gaussian profile to the peak near $K_2 = 83$ km/s in the stacked CCF (black points). The maximum-likelihood Gaussian profile is plotted in dark blue and 50 samples from the posterior probability distribution are plotted in light grey. *Upper-right panel:* the stacked CCF (solid line) and its reflection about $K_2 = 0$ (dashed line). The estimated value of $K_2 = 80.3$ km/s from GMC+2014 is indicated by a vertical dotted line. *Lower-left panel:* Gaussian process fit to the stacked CCF excluding the peak near $K_2 = 83$ km/s. The orange shaded region shows $2\times$ the standard error range on the predicted values of the Gaussian process. *Lower-right panel:* the stacked CCF (solid line) and its reflection about $K_2 = 0$ (dashed line) computed for spectra with the signature of the M dwarf removed using a model spectrum with $T_{\rm eff} = 3300$ K.

resulting stacked CCF has no peak near $K_2 = 83 \, \rm km \, s^{-1}$. Based on these three tests, we are confident that our detection of the M-dwarf is robust and that the measurement of K_2 is reliable.

6.3.4 Initial assessment of the *CHEOPS* data

We used the software package PYCHEOPS (Maxted et al., 2022b) to make an initial assessment of the light curve data from each of the three *CHEOPS* visits to the target listed in Table 6.1. We excluded data from the analysis where the background level in the images due to scattered light is more than 20 per cent larger than the median value during the visit. The data file provided by the data reduction pipeline (DRP, Hoyer et al., 2020) includes a quantity LC_CONTAM that is an estimate of the contamination of the photometric aperture by nearby stars. This quantity varies during the orbit because of the rotation of the spacecraft and the strongly asymmetric point spread function of the instrument. This calculation of LC_CONTAM is based on a simulation of the field of view using the mean G-band magnitudes of the target and nearby stars from *Gaia* DR2. Fig. 6.1 shows the results of this simulation for one image. This contamination estimate does not account for variability of target itself, so we added a new function to PYCHEOPS version 1.0.2 that corrects the measured flux (FLUX) by subtracting the value LC_CONTAM $\times 10^{-0.4(G-G_0)}$ from FLUX. The zero-point G_0 is calculated from the average value of

$$-2.5 \log[(\texttt{LC\_CONTAM} + 1) \times 10^{-0.4G} \times f_{\text{frac}}/\texttt{FLUX}],$$

where f_{frac} is the fraction of the total flux from the target in the photometric aperture, G is the mean G-band magnitude of the target, and the average is taken over data points outside of transit and eclipse.

Based on the simulated image of the field of view shown in Fig. 6.1, we decided to use the OPTIMAL aperture with a radius of 40 pixels for our analysis. This maximises the contamination of the photometric aperture but minimises the uncertainty in this quantity due to errors in measuring the positions of the stars in the image and, hence, the fraction of the flux from each star that is contained in the aperture. We repeated our analysis using the DEFAULT aperture with a radius of 25 pixels and found that the results are entirely consistent with those presented here. For each visit we calculate a best-fit for a transit or eclipse model to the light curve including linear decorrelation
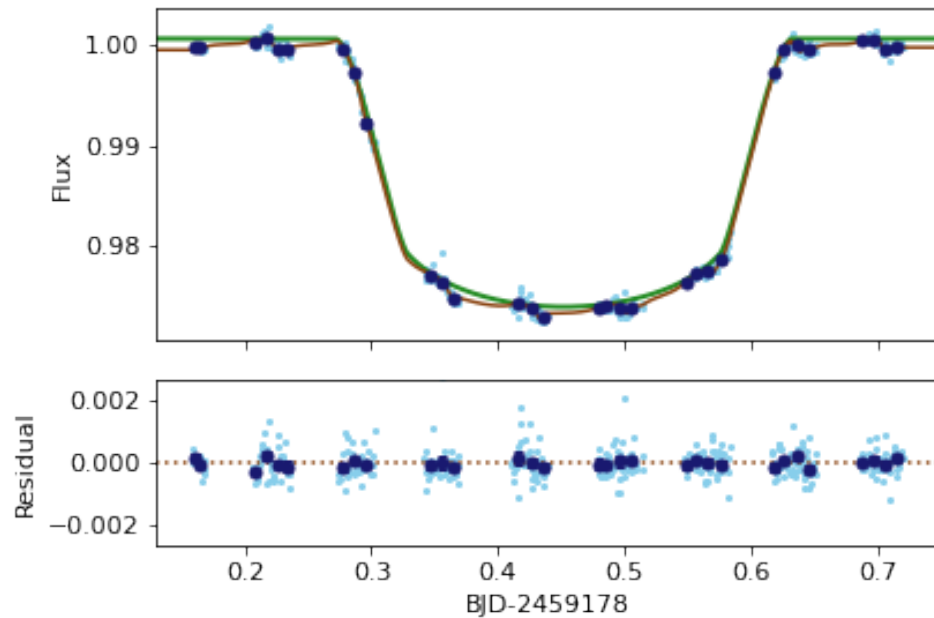
Figure 6.4: *CHEOPS* light curve from one visit to observe the transit of EBLM J0113+31. *Upper panel:* The observed light curve is displayed in cyan. The dark blue points are the data points binned over 0.01 phase units. The full model including instrumental trends is shown in brown and the transit model without trends is shown in green. *Lower panel*: Residuals obtained after subtraction of the best-fit model.

against `LC_CONTAM` to account for small errors in estimating the amplitude of the variations in this quantity. We then calculate the best-fit light curves including each of the other available decorrelation parameters and add them one-by-one if the Bayes factor for the parameter exceeds 1. The decorrelation parameters selected by this method are listed in Table 6.1. The fit to the data from a typical visit including these detrending parameters in shown in Fig. 6.4.

Table 6.4: Times of mid-transit for EBLM J0113+31. Residuals from the linear ephemeris given in Section 6.3.5 are given in the second column.

BJD$-$2450000	(O $-$ C) [s]	Source
6023.27063 ± 0.00036	3.9	GMC+2014
8778.70047 ± 0.00042	-22.3	*TESS*
9178.45224 ± 0.00017	-1.0	*CHEOPS*
9506.81960 ± 0.00013	2.2	*CHEOPS*

6.3.5   Updated transit time ephemeris

The two times of mid-transit measured from the *CHEOPS* data during the initial assessment of the data described above are listed in Table 6.4 together with the time of mid-transit from GMC+2014 and one new time of mid-transit from a least-squares fit to the *TESS* light curve using the transit model from PYCHEOPS. From a least-squares fit to these data we obtain the following updated ephemeris for the times of mid-transit in EBLM J0113+31:

$$\text{BJD } T_{\mathrm{mid}} = 2459107.068051(45) + 14.27684012(73)\,\text{E} \tag{6.2}$$

There is no evidence for any change in orbital period greater than $|\dot{P}/P| \approx 1 \times 10^{-5}$ from these times of mid-transit.

6.3.6   Combined analysis of light curve and radial velocity data

We used the light curve model `ellc` (Maxted, 2016) to calculate synthetic light curves in the *TESS* and *CHEOPS* bands, and the spectroscopic orbit of the primary star. This model gives us more flexibility in choosing the level of numerical noise in these synthetic light curves than is possible with the qpower2 algorithm used in PYCHEOPS (Maxted & Gill, 2019). For the analysis presented here we used the "default" grid size for the primary star and the "very_sparse" grid size for the companion, which gives numerical noise of only a few ppm at most orbital phases and everywhere less than

10 ppm. We also tested for the impact of the gravitational distortion of the stars by their mutual gravity on the light curve. This is less than 1.5 ppm through the transit so we assumed spherical stars for our analysis in order to speed-up the calculation.

The parameters of the binary star model are: the radii of the stars in units of the semi-major axis (fractional radii), $r_1 = R_1/a$ and $r_2 = R_2/a$; the surface brightness ratios in the *TESS* and *CHEOPS* bands, S_T and S_C, respectively; the orbital inclination, i; the time of mid-transit, T_0; the orbital period, P; $f_s = \sqrt{e}\sin(\omega)$ and $f_c = \sqrt{e}\cos(\omega)$, where e is the orbital eccentricity and ω is the longitude of periastron for the primary star; the semi-amplitude of the primary star's spectroscopic orbit, K_1; the limb-darkening parameters assuming a power-2 limb-darkening law, $h_{1,T}$ and $h_{2,T}$ in the *TESS* band, and $h_{1,C}$ and $h_{2,C}$ in the *CHEOPS* band. The ephemeris for the time of mid-transit derived in Section 6.3.5 is very accurate so we fix T_0 and P at these values in our analysis. The curvature of the light curve between the second and third contact points is very clearly seen in the *CHEOPS* and *TESS* light curves, and is almost directly related to the parameters $h_{1,C}$ and $h_{1,T}$, respectively, so we leave this as a free parameter in the analysis. The parameters $h_{2,C}$ and $h_{2,T}$ will have a much more subtle influence on the light curve that is almost entirely confined to the ingress and egress phases so we impose priors on these parameters based on the tabulated values of h_2 in the *TESS* and *CHEOPS* bands from Maxted (2018). The width of the priors is based on the comparison of these tabulated values to the observed values of this parameter from an analysis of the *Kepler* light curves of transiting exoplanet systems in the same study.

Prior to the analysis of the *CHEOPS* data combined with the other data sets, we applied a correction for hot pixels in the photometric aperture. Quantitatively, we define hot pixels as pixels with dark current above $3~e^-\,s^{-1}$. Since the beginning of the mission, hot pixels have appeared regularly in the *CHEOPS* CCD at a rate of $\sim$100 new hot pixels per day. The *CHEOPS* Instrument Team monitors closely the number and location of hot pixels. Approximately once per week, "dark images" are acquired for that purpose (10 full frame images obtained observing a region of the sky void of stars). These images are used to produce the reference files that track the

location and dark current of hot pixels. These reference file are available from the *CHEOPS* data archive.[6] We used hot pixel maps generated about 2 days after each visit to EBLM J0113+31 to calculate the contribution of these hot pixels to the count rate in the photometric aperture. The hot-pixel contamination is ≈ 0.6 per cent in the OPTIMAL aperture for the visit in 2020 and ≈ 1.2 per cent for the visits in 2021. The hot-pixel contamination in the DEFAULT aperture is ≈ 0.3 per cent for all visits. The hot pixel contamination is calculated for every image but the variation in this quantity is small ($\lesssim 10$ per cent of its value) so we apply the correction by subtracting the mean value of the contamination during the visit from the count rate.

Our model includes the parameter $\ell_{3,\mathrm{C}}$ that is a constant added to the synthetic *CHEOPS* light curve to account for contamination of the photometric aperture. We applied a correction to the light curves for contamination prior to the combined analysis so, to account for uncertainties in these corrections, we assign a Gaussian prior to $\ell_{3,\mathrm{C}}$ with a mean value of 0 and a standard error equal to 50 per cent of the total contamination estimate. Similarly, the parameter $\ell_{3,\mathrm{T}}$ accounts for the contamination of the photometric aperture shown in Fig. 6.2 used to extract the *TESS* light curve. We noticed that the entry TIC 400048098 in the *TESS* input catalogue (TIC, Stassun et al., 2019) has no counterpart in *Gaia* EDR3 (Gaia Collaboration et al., 2016, 2021a) so we assume that this is a spurious entry and do not include it in our calculation of the contamination. The star TIC 400048094 appears near the edge of the default photometric aperture provided with the target pixel file. We added one pixel to this aperture so that there is no ambiguity over whether this star should be included in the calculation of the contamination or not. From the T magnitudes listed the TIC we estimate $\ell_{3,\mathrm{T}} = 0.0030$. We allow this parameter to vary in the fit but assign a Gaussian prior to it, assuming an arbitrary uncertainty of 50 per cent.

The light curves produced by *CHEOPS* are known to have very low levels of instrumental noise after decorrelation. Similarly, the *TESS* light curve following correction for instrumental trends that we calculated with LIGHTKURVE shows little sign

---

[6]`https://cheops-archive.astro.unige.ch/archive_browser/`

of residual instrumental noise or stellar variability. We therefore adopt a white noise model for our analysis and assume that the standard deviation per point in the *TESS* and *CHEOPS* light curves – σ_T and σ_C, respectively – are the same for all data points from the same instrument. The logarithm of these standard errors are included as hyperparameters in our analysis by correctly normalising the calculation of the posterior probability distribution. We only include data from the *TESS* light curves at orbital phases near the transit and eclipses in this analysis. For both the *CHEOPS* and *TESS* data, each section of data around a transit or eclipse is divided by a straight line fit to the data either side of the transit or eclipse prior to analysis.

We use all the radial velocities published by GMC+2014 plus the new radial velocities from Table 6.3 in our analysis. We see no evidence for excess noise in the radial velocities so we use their standard errors as quoted for the calculation of the posterior probability distribution.

In total, we are using nine sets of data, each of which has an uncertain zero-point that should be included in the analysis. Additionally, there are eleven basis functions that are used for the removal of instrumental noise from the *CHEOPS* data, each with its own coefficient that should be varied independently during the fit to the data. To avoid explicitly calculating these nuisance parameters we use the procedure described by Luger et al. (2017), in which the likelihood for any proposed set of model parameters marginalised over a set of nuisance parameters for a linear model can be calculated by modifying the covariance matrix.

We used EMCEE (Foreman-Mackey et al., 2013), a PYTHON implementation of an affine invariant Markov chain Monte Carlo (MCMC) ensemble sampler, to calculate the posterior probability distribution of the model parameters. The maximum-likelihood model fit to the data is shown in Fig. 6.5. The mean and standard error of the posterior probability distributions for each of the model parameters and various derived parameters are given in Table 6.5.

The parameters in Table 6.5 can be combined with our measured value of K_2 from the analysis of the SPIRou spectra to determine the masses and radii of both stars with no additional model input. To account for the correlations between parameters, we do

Table 6.5: Fit to RV and LC data. $\mathcal{N}(\mu, \sigma)$ denotes a Gaussian prior applied to a parameter with mean μ and standard deviation σ.

Parameter	Value	Notes
R_1/a	0.05348 ± 0.00031	
R_2/a	0.008111 ± 0.000063	
$i\,[^\circ]$	89.110 ± 0.041	
f_s	-0.54885 ± 0.00043	
f_c	0.08693 ± 0.00026	
S_{T}	0.0675 ± 0.0033	
S_{C}	0.0384 ± 0.0023	
$K_1\,[\mathrm{km/s}]$	15.861 ± 0.010	
$h_{1,\mathrm{C}}$	0.7683 ± 0.0038	
$h_{2,\mathrm{C}}$	0.720 ± 0.036	$\mathcal{N}(0.409, 0.045)$
$h_{1,\mathrm{T}}$	0.8008 ± 0.0074	
$h_{2,\mathrm{T}}$	0.779 ± 0.022	$\mathcal{N}(0.379, 0.045)$
$\ell_{3,\mathrm{C}}$	0.007 ± 0.009	$\mathcal{N}(0.000, 0.012)$, 1
$\ell_{3,\mathrm{T}}$	0.019 ± 0.010	$\mathcal{N}(0.030, 0.015)$, 2
$\ln \sigma_{\mathrm{C}}$	-7.80 ± 0.02	
$\ln \sigma_{\mathrm{T}}$	-7.04 ± 0.02	
Derived parameters		
e	0.30879 ± 0.00045	
$\omega\,[^\circ]$	279.000 ± 0.031	
$\sin i$	0.99988 ± 0.00001	
R_2/R_1	0.15164 ± 0.00073	
ℓ_{T}	0.00155 ± 0.00008	Flux ratio, *TESS*
ℓ_{C}	0.00088 ± 0.00005	Flux ratio, *CHEOPS*
$\sigma_{\mathrm{T}}\,[\mathrm{ppm}]$	874 ± 18	
$\sigma_{\mathrm{C}}\,[\mathrm{ppm}]$	410 ± 8	

1: After correction for contamination of the photometric aperture by nearby stars and hot pixels. 2: Including flux from other stars in the photometric aperture.

this using the sampled posterior probability distribution for the relevant parameters generated by EMCEE together with a sample of K_2 values assuming a Gaussian distribution for this parameter. The masses and radii derived are given in Table 6.6.
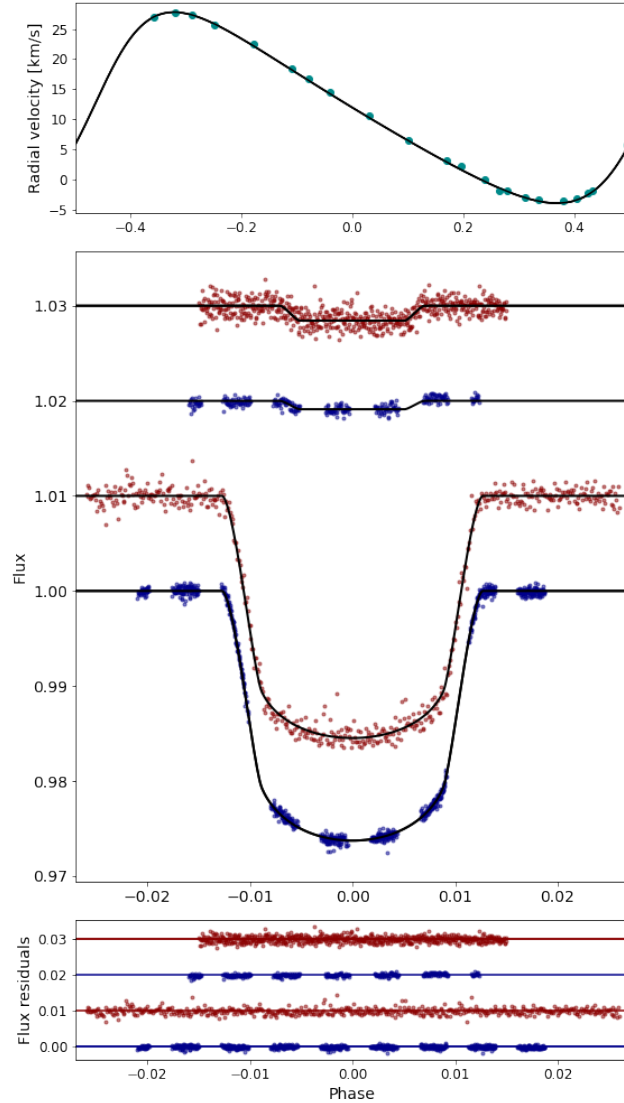
Figure 6.5: *Top panel:* radial velocity measurements for EBLM J0113+31 (points) and our maximum-likelihood model (line) based on a fit to the combined radial-velocity and light-curve data. Middle panel: *TESS* (red points) and *CHEOPS* (blue points) photometry of the transit and eclipse in EBLM J0113+31. The maximum-likelihood models based on a fit to the combined radial-velocity and light-curve data is also shown (lines). Data obtained during around the eclipses are plotted as function of orbital phase −0.5323. Data and models have been offset vertically for clarity. The *CHEOPS* data have been corrected for instrumental noise calculated as part of the analysis. *Lower panel:* Residuals from the maximum likelihood models plotted in the middle panel.

Table 6.6: Mass, radius, effective temperature and derived parameters for the stars in EBLM J0113+31. The metallicity [M/H] is estimated from our analysis of the spectrum of EBLM J0113+31 A. N.B. $T_{\mathrm{eff},1}$ and $T_{\mathrm{eff},2}$ are subject to additional systematic uncertainty of $10\,\mathrm{K}$ and $7\,\mathrm{K}$, respectively.

Parameter	Value	Error	
$M_1/\mathcal{M}_\odot^{\mathrm{N}}$	1.029	$\pm\ 0.0025$	[2.4%]
$M_2/\mathcal{M}_\odot^{\mathrm{N}}$	0.197	$\pm\ 0.003$	[1.5%]
$R_1/\mathcal{R}_\odot^{\mathrm{N}}$	1.417	$\pm\ 0.014$	[1.0%]
$R_2/\mathcal{R}_\odot^{\mathrm{N}}$	0.215	$\pm\ 0.002$	[1.1%]
$T_{\mathrm{eff},1}$ [K]	6124	$\pm\ 40$	[0.6%]
$T_{\mathrm{eff},2}$ [K]	3375	$\pm\ 40$	[1.3%]
$\rho_1/\rho_\odot^{\mathrm{N}}$	0.362	$\pm\ 0.006$	[1.7%]
$\rho_2/\rho_\odot^{\mathrm{N}}$	19.9	$\pm\ 0.5$	[2.4%]
$\log g_1$ [cgs]	4.148	$\pm\ 0.006$	[1.5%]
$\log g_2$ [cgs]	5.068	$\pm\ 0.006$	[1.5%]
$\log L_1/\mathcal{L}_\odot^{\mathrm{N}}$	0.406	$\pm\ 0.014$	[3.2%]
$\log L_2/\mathcal{L}_\odot^{\mathrm{N}}$	-2.267	$\pm\ 0.024$	[5.5%]
[M/H]	-0.3	$\pm\ 0.1$	

6.3.7 Direct measurement of the stellar effective temperature

The effective temperature for a star with Rosseland radius R and total luminosity L is defined by the equation

$$L = 4\pi R^2 \sigma_{\mathrm{SB}} \mathrm{T}_{\mathrm{eff}}^4,$$

where σ_{SB} is the Stefan-Boltzmann constant. For a binary star at distance d, i.e. with parallax $\varpi = 1/d$, the flux corrected for extinction observed at the top of Earth's atmosphere is

$$f_{0,b} = f_{0,1} + f_{0,2} = \frac{\sigma_{\mathrm{SB}}}{4} \left[\theta_1^2 \mathrm{T}_{\mathrm{eff},1}^4 + \theta_2^2 \mathrm{T}_{\mathrm{eff},2}^4 \right],$$

where $\theta_1 = 2R_1\varpi$ is the angular diameter of star 1, and similarly for star 2. All the quantities are known or can be measured for EBLM J0113+31 provided we can accurately integrate the observed flux distributions for the two stars independently. This is possible because photometry of the combined flux from both stars is available from ultraviolet to mid-infrared wavelengths, and the flux ratio at wavelengths where the majority of the flux is emitted by the primary star has been measured from the *TESS* and *CHEOPS* light curves. Although we have no direct measurement of the flux ratio at infrared wavelengths, we can make a reasonable estimate for the small contribution of the M-dwarf to the measured total infrared flux using empirical colour – T_{eff} relations. The M-dwarf contributes less than 0.2 per cent to the total flux so it is not necessary to make a very accurate estimate of the M-dwarf flux distribution in order to derive an accurate value of T_{eff} for the G0-type primary star.

The photometry used in this analysis is given in Table 6.7. The *NUV* and *FUV* magnitudes are taken from *GALEX* data release GR7 (Bianchi et al., 2014) with a correction to the *IUE* flux scale based on the results from Camarota & Holberg (2014). We assume that the flux from the M-dwarf at ultraviolet wavelengths is negligible. The *Gaia* photometry is from *Gaia* data release EDR3. *J*, *H* and *Ks* magnitudes are from the 2MASS survey (Skrutskie et al., 2006). WISE magnitudes are from the All-Sky Release Catalog (Cutri & et al., 2012) with corrections to Vega magnitudes made as recommended by Jarrett et al. (2011). Photometry in the PanSTARRS-1 photometry system is taken from Tonry et al. (2018). Details of the zero-points and

response functions used to calculate synthetic photometry from an assumed spectral energy distribution are given in Miller et al. (2020).

To estimate the reddening towards EBLM J0113+31 we use the calibration of $E(B-V)$ versus the equivalent width of the interstellar Na I D_1 line by Munari & Zwitter (1997). To measure EW(Na I D_1) we used 11 spectra obtain with the FIES spectrograph on the Nordic Optical Telescope used in medium resolution mode ($R = 46,000$). We first shifted these spectra into the rest frame of the primary star and then took the median value at each wavelength to obtain a high signal-to-noise spectrum of the G0V primary star. We then divided each observed spectrum by this spectrum of the G0V primary star after shifting it back to the barycentric rest frame. We then took the median of these residual spectra to obtain a high signal-to-noise spectrum of the interstellar features. The equivalent width of the Na I D_1 line measured by numerical integration is EW(Na I D_1) $= 77.1 \pm 6.0$ mÅ. This value is less than the values of EW(Na I D_1) for all the stars in the calibration sample of Munari & Zwitter (1997). To estimate the uncertainty on the value of $E(B-V)$ for EBLM J0113+31 we take the sample standard deviation for the 5 stars in the calibration sample with the lowest values of EW(Na I D_1)≈ 250 mÅ. Based on this analysis we obtain the estimate $E(B-V) = 0.002 \pm 0.012$. We use this as a Gaussian prior in our analysis but exclude negative values of $E(B-V)$.

To establish colour$-T_{\rm eff}$ relations suitable for dwarf stars with $3100\,{\rm K} < T_{\rm eff} < 3500\,{\rm K}$ we use a robust linear fit to the stars listed in Table 6 of Fouqué et al. (2018) within this $T_{\rm eff}$ range. Photometry for these stars is taken from the *TESS* input catalogue. To estimate a suitable standard error for a Gaussian prior based on this fit we use $1.25\times$ the mean absolute deviation of the residuals from the fit. Colour$-T_{\rm eff}$ relations suitable for the primary G0V star were calculated in similar way based on stars selected from the Geneva-Copenhagen survey (Holmberg et al., 2009; Casagrande et al., 2011) with $5950\,{\rm K} < T_{\rm eff} < 6250\,{\rm K}$, $E(B-V) < 0.01$ and $3.5 < \log g < 4.5$. The results are given in Table 6.8.

The method we have developed to measure $T_{\rm eff}$ for eclipsing binary stars is described fully in Miller et al. (2020). Briefly, we use EMCEE (Foreman-Mackey et al.,

Table 6.7: Observed apparent magnitudes for EBLM J0113+31 and predicted values based on our synthetic photometry. The predicted magnitudes are shown with error estimates from the uncertainty on the zero-points for each photometric system. The pivot wavelength for each band pass is shown in the column headed λ_{pivot}. The magnitudes of the primary G0V star alone corrected for the contribution to the total flux from the M-dwarf are shown in the column headed m_1. The flux ratio in each band is shown in the final column.

Band	λ_{pivot} [nm]	Observed	Computed	$O - C$	m_1	ℓ [%]
FUV	154	20.01 ± 0.54	20.74 ± 0.13	-0.73 ± 0.55	20.01 ± 0.54	0.00
NUV	230	14.28 ± 0.71	14.41 ± 0.15	-0.13 ± 0.73	14.28 ± 0.71	0.00
G	622	9.920 ± 0.003	9.919 ± 0.003	$+0.002 \pm 0.004$	9.922 ± 0.003	0.09
BP	511	10.197 ± 0.003	10.202 ± 0.003	-0.005 ± 0.004	10.197 ± 0.003	0.04
RP	777	9.477 ± 0.004	9.475 ± 0.004	$+0.002 \pm 0.005$	9.479 ± 0.004	0.17
g_{P1}	485	10.249 ± 0.020	10.234 ± 0.005	$+0.015 \pm 0.021$	10.249 ± 0.020	0.03
r_{P1}	620	9.961 ± 0.024	9.911 ± 0.005	$+0.050 \pm 0.025$	9.962 ± 0.024	0.07
i_{P1}	754	9.868 ± 0.021	9.820 ± 0.005	$+0.048 \pm 0.022$	9.870 ± 0.021	0.16
J	1241	8.982 ± 0.024	8.973 ± 0.005	$+0.009 \pm 0.025$	8.987 ± 0.024	0.45
H	1650	8.692 ± 0.029	8.713 ± 0.005	-0.021 ± 0.029	8.699 ± 0.029	0.60
K_{s}	2164	8.620 ± 0.024	8.652 ± 0.005	-0.032 ± 0.025	8.628 ± 0.024	0.73
$W1$	3368	8.590 ± 0.023	8.613 ± 0.002	-0.023 ± 0.023	8.600 ± 0.023	0.91
$W2$	4618	8.629 ± 0.020	8.619 ± 0.002	$+0.010 \pm 0.020$	8.642 ± 0.020	1.18
$W3$	12073	8.633 ± 0.021	8.617 ± 0.002	$+0.016 \pm 0.021$	8.651 ± 0.021	1.64
$W4$	22194	8.38 ± 0.22	8.674 ± 0.002	-0.29 ± 0.22	8.40 ± 0.22	1.64

Table 6.8: Colour-T_{eff} relations used to establish Gaussian priors on the flux ratio at infrared wavelengths for EBLM J0113+31. The dependent variables are $X_1 = T_{\mathrm{eff},1} - 6.1\,\mathrm{kK}$ and $X_2 = T_{\mathrm{eff},2} - 3.3\,\mathrm{kK}$.

Colour	Primary	Secondary
$V - J$	$1.048 - 0.4257\,X_1 \pm 0.015$	$4.187 - 2.762\,X_2 \pm 0.11$
$V - H$	$1.288 - 0.5568\,X_1 \pm 0.019$	$4.776 - 2.552\,X_2 \pm 0.15$
$V - K_{\mathrm{s}}$	$1.357 - 0.5926\,X_1 \pm 0.016$	$5.049 - 2.776\,X_2 \pm 0.12$
$V - W1$	$1.405 - 0.5829\,X_1 \pm 0.027$	$5.207 - 2.720\,X_2 \pm 0.12$
$V - W2$	$1.411 - 0.5753\,X_1 \pm 0.045$	$5.365 - 2.957\,X_2 \pm 0.11$
$V - W3$	$1.355 - 0.5919\,X_1 \pm 0.022$	$5.477 - 3.091\,X_2 \pm 0.13$
$V - W4$	$1.397 - 0.5812\,X_1 \pm 0.045$	$5.620 - 3.248\,X_2 \pm 0.23$

2013) to sample the posterior probability distribution $P(\Theta|D) \propto P(D|\Theta)P(\Theta)$ for the model parameters Θ with prior $P(\Theta)$ given the data, D (observed apparent magnitudes and flux ratios). The model parameters are

$$\Theta = (\mathrm{T}_{\mathrm{eff},1}, \mathrm{T}_{\mathrm{eff},2}, \theta_1, \theta_2, \mathrm{E(B-V)}, \sigma_{\mathrm{ext}}, \sigma_\ell, c_{1,1}, \ldots, c_{2,1}, \ldots).$$

The prior $P(\Theta)$ is calculated using the angular diameters θ_1 and θ_2 derived from the radii R_1 and R_2 and the parallax ϖ, the priors on the flux ratio at infrared wavelengths based on the colour – Teff relations in Table 6.8, and the Gaussian prior on the reddening described above. The hyperparameters σ_{ext} and σ_ℓ account for additional uncertainties in the synthetic magnitudes and flux ratio, respectively, due to errors in zero-points, inaccurate response functions, stellar variability, etc. The parallax is taken from *Gaia* EDR3 with corrections to the zero-point from Flynn et al. (2022).

To calculate the synthetic photometry for a given value of T_{eff} we used a model spectral energy distribution (SED) multiplied by a distortion function, $\Delta(\lambda)$. The distortion function is a linear superposition of Legendre polynomials in log wavelength. The coefficients of the distortion function for star 1 are $c_{1,1}, c_{1,2}, \ldots$, and similarly for star 2. The distorted SED for each star is normalized so that the total apparent flux prior to applying reddening is $\sigma_{\mathrm{SB}}\theta^2\mathrm{T}_{\mathrm{eff}}^4/4$. These distorted SEDs provide a convenient function that we can integrate to calculate synthetic photometry that has realistic stellar absorption features, and where the overall shape can be adjusted to match the observed magnitudes from ultraviolet to infrared wavelengths, i.e. *the effective temperatures we derive are based on the integrated stellar flux and the star's angular diameter, not SED fitting.*

For this analysis we use model SEDs computed from BT-Settl model atmospheres (Allard et al., 2013) obtained from the Spanish Virtual Observatory.[7] We use linear interpolation to obtain a reference SED for the G0V star appropriate for $T_{\mathrm{eff},1} = 6130\,\mathrm{K}$, $\log g_1 = 4.15$, $[\mathrm{Fe/H}] = -0.3$ and $[\alpha/\mathrm{Fe}] = 0.0$. For the reference SED for the M dwarf companion we assume $T_{\mathrm{eff},1} = 3380\,\mathrm{K}$, $\log g_1 = 5.0$, and the same composition. We

---

[7]`http://svo2.cab.inta-csic.es/theory/newov2/index.php?models=bt-settl`

Table 6.9: Results from our analysis to obtain the effective temperatures for both stars in EBLM J0113+31. N.B. $T_{\text{eff,1}}$ and $T_{\text{eff,2}}$ are subject to additional systematic uncertainty of 10 K and 7 K, respectively.

Parameter	Value	Error	Units
$T_{\text{eff,1}}$	6124	± 40	K
$T_{\text{eff,2}}$	3375	± 40	K
θ_1	0.0745	± 0.0007	mas
θ_2	0.0113	± 0.0001	mas
$E(B-V)$	0.010	± 0.007	
σ_{ext}	0.014	± 0.011	
σ_ℓ	0.0002	± 0.0001	
$c_{1,1}$	0.06	± 0.03	
$c_{1,2}$	-0.08	± 0.05	
$c_{2,1}$	0.3	± 0.2	
$c_{2,2}$	-0.3	± 0.2	

experimented with distortion functions with 1, 2, 3, 4 coefficients per star and found the results to be very similar in all cases. The results presented here use two distortion coefficients per star because there is no improvement in the quality of the fit if we use a larger number of coefficients. The predicted apparent magnitudes including their uncertainties from errors in the zero-points for each photometric system are compared to the observed apparent magnitudes in Table 6.7. The posterior probability distribution for the model parameters is summarised in Table 6.9 and the spectral energy distribution is plotted in Fig. 6.6.

The random errors quoted in Table 6.9 do not allow for the systematic error due to the uncertainty in the absolute calibration of the CALSPEC flux scale (Bohlin et al., 2014). This additional systematic error is 10 K for the G0V primary star and 7 K for the M-dwarf companion.
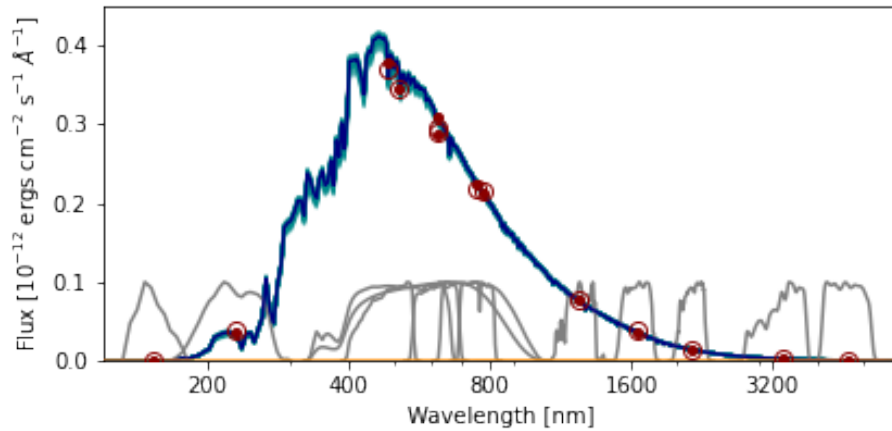
Figure 6.6: The spectral energy distribution (SED) of EBLM J0113+31. The observed fluxes are plotted with open circles and the predicted fluxes for the mean of the posterior probability distribution (PPD) integrated over the response functions shown in grey are plotted with filled symbols. The SED predicted by the mean of the PPD is plotted in dark blue and light blue shows the SEDs produced from 100 random samples from the PPD. The contribution to the total SED from the M dwarf (barely visible) is shown in orange. The $W3$ and $W4$ mid-infrared bands also used in the analysis are not shown here.

6.3.8 Abundance analysis

We have used the H-band spectrum of EBLM J0113+31 A to estimate this star's metallicity. For this abundance analysis we used the observed SPIRou spectra merged into 1-dimensional spectra provided by the observatory. We first subtracted the model spectrum for the M-dwarf companion described in Section 6.3.3 from each of these 1-dimensional spectra, scaled such that the flux ratio in the *TESS* band matched the value measured from the depth of the secondary eclipse in the light curve. We then co-added the spectra in the rest frame of the primary star to produce a high signal-to-noise spectrum of the G0V star with negligible contamination from the M-dwarf.

For the analysis of this spectrum we used iSpec (Blanco-Cuaresma et al., 2014b; Blanco-Cuaresma, 2019) with the APOGEE line list for atomic and molecular data in the wavelength range $1500-1700$ nm (Shetrone et al., 2015). We followed Sarmento et al. (2020) in selecting Turbospectrum (Alvarez & Plez, 1998; Plez, 2012) for the spectrum synthesis assuming a micro-turbulent velocity $v_{\mathrm{mic}} = 1.06\,\mathrm{km\,s^{-1}}$ with model atmospheres from the MARCS grid (Gustafsson et al., 2008) and solar abundances from Grevesse et al. (2007). We excluded from the fit ± 4 nm around the two Brackett series lines at 1681.11 nm and 1641.17 nm, and also some instrumental features that occur near the ends of the échelle orders at $1657-1659$ nm and 1622-1624 nm. We fixed the value of $T_{\mathrm{eff}} = 6124\,\mathrm{K}$ and $\log g = 4.15$. For the macro-turbulent velocity we used the calibration by Valenti & Fischer (2005) to estimate $v_{\mathrm{mac}} = 4.67\,\mathrm{km\,s^{-1}}$. We included the rotational broadening parameter $v \sin i$ as a free parameter in the least-squares fit with a linear limb-darkening coefficient of 0.5 in the H-band based on the results from Claret (2018). We attempted a least-squares fit including the α-element abundance as a free parameter but found that the value obtain is not accurate enough to be useful so we fixed $[\alpha/\mathrm{Fe}] = 0$ in the least-squares fit. From this least-squares fit we obtained $[\mathrm{M/H}] = -0.33 \pm 0.01$ and $v \sin i = 6.6 \pm 0.3\,\mathrm{km\,s^{-1}}$. There are several additional sources of uncertainty in this analysis, e.g. inaccurate normalisation, errors in atomic data, approximations in the stellar atmosphere models, etc., so the accuracy of our metallicity estimate will be much worse than the precision estimated from the

least-squares fitting algorithm (Blanco-Cuaresma, 2019; Jofré et al., 2019). Based on the results from independent analyses of APOGEE spectra by Jönsson et al. (2018), we assume an accuracy of 0.15 dex, i.e. $[\text{M/H}] = -0.33 \pm 0.15$. The fit to the spectrum is shown in Fig. 6.7.

We used the co-added FIES spectra of the star to determine the stellar atmospheric parameters (T_{eff}, $\log g$, micro-turbulence, and [Fe/H]) and chemical abundances following the methodology described in our previous works (Sousa, 2014; Santos et al., 2013; Adibekyan et al., 2012, 2015). In brief, we make use of the equivalent widths (EW) of spectral lines, as measured using the ARES v2 code[8] (Sousa et al., 2015), and we assume ionization and excitation equilibrium. The process makes use of a grid of Kurucz model atmospheres (Kurucz, 1993) and the radiative transfer code MOOG (Sneden, 1973).

For the stellar spectroscopic parameters we obtained $T_{\text{eff}} = 6025 \pm 50 \, \text{K}$, $\log g = 4.10 \pm 0.05$, $V_{\text{tur}} = 1.07 \pm 0.06 \, \text{km s}^{-1}$ and $[\text{Fe/H}] = -0.31 \pm 0.04$. Within the uncertainties, these values are in agreement with those presented in Table—6.9. In order to be consistent, and because of higher accuracy, we fixed the values of effective temperature and surface gravity to $T_{\text{eff}} = 6124 \pm 40 \, \text{K}$ and $\log g = 4.148 \pm 0.006$ when determining the abundances of individual elements. Our derivation of three α-elements ($[\text{Mg/H}] = -0.18 \pm 0.09$, $[\text{Si/H}] = -0.26 \pm 0.04$, $[\text{Ti/H}] = -0.22 \pm 0.07$) indicates that EBLM J0113+31 is not an α-enhanced star ($[\alpha/\text{Fe}] = 0.09 \pm 0.08$) which is typical for stars in the Galactic thin-disk population (Adibekyan et al., 2011).

Using the astrometric data from *Gaia* EDR3 and the radial velocity of the system ($11.179 \pm 0.004 \, \text{km s}^{-1}$, GMC+2014) we calculated the Galactic space velocity components $(U, V, W) = (-17, 16, 21) \, \text{km s}^{-1}$ with respect to the local standard of rest (Schönrich et al., 2010). Based on these velocities, adopting the characteristics parameters of Galactic stellar populations of Reddy et al. (2006), and following Adibekyan et al. (2012) we estimated a probability of 99% that the star belongs to the Galactic

---

[8]The last version of ARES code (ARES v2) can be downloaded at `http://www.astro.up.pt/ sousasag/ares`
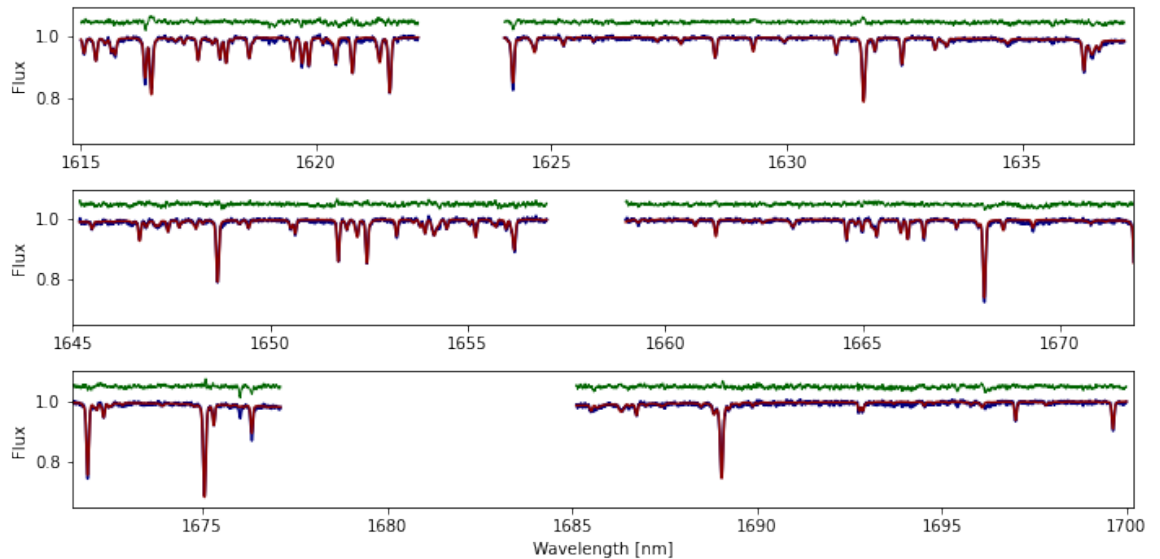
Figure 6.7: The *H*-band spectrum of EBLM J0113+31 A (blue) and a synthetic spectrum fit by least-squares using iSpec (red). Residuals from the synthetic spectrum fit are shown in green offset vertically by 1.05 units.

thin disk, which is in agreement with our conclusion based on the composition of the star.

Based on the results from the analysis of the SPIRou and FIES spectra we adopt the value [M/H] = -0.3 ± 0.1 for the metallicity of EBLM J0113+31. The co-added SPIRou spectra corrected for the contribution from the M-dwarf and the co-added FIES spectrum are available from the supplementary online information that accompanies this article.

6.4 Discussion

6.4.1 Astrometric noise due to binary orbital motion

The projected semi-major axis of the G0V star's orbit is $\alpha_1 = a_1/d = 0.11$ mas, so we expect excess noise in the *Gaia* astrometry ≈ 0.1 mas due to the orbital motion of

the primary star. Indeed, the astrometric excess noise in the *Gaia* EDR3 catalogue for EBLM J0113+31 is 0.163 mas. This is higher than expected for a good fit to the data for a single star with G ≈ 10, and consistent with the noise expected from the orbital motion of the G0V star. This will only lead to a systematic error in the parallax if the position angle of the binary at the times of observation are not randomly distributed around the binary star orbit. This can be checked using the parameter `ipd_gof_harmonic_amplitude` provided in the EDR3 catalogue (Lindegren et al., 2021a). For EBLM J0113+31, this parameter takes the value 0.014, which is less than the median value of this statistic for stars with 6-parameter solutions in the magnitude range G=9-12 (0.020). Although the detection of the astrometric noise is statistically significant, it is a small contribution to the uncertainties on the parallax. The renormalised unit weight error for EBLM J0113+31 is RUWE=1.154, which is only slightly higher than the median value for stars with 6-parameter solutions in the magnitude range G=9-12 (RUWE=1.127), and is close to the expected value ≈ 1 for "well behaved sources".

We can therefore be confident that the orbital motion of the G0V star does not produce a systematic error in the measured *Gaia* parallax.

6.4.2   Comparison to stellar evolution models

The mass, radius and effective temperature for both stars in EBLM J0113+31 are given in Table 6.6, together with the derived surface gravity, mean stellar density and luminosity for both stars.

We used the software package BAGEMASS (Maxted et al., 2015) to compare the parameters of the primary star, EBLM J0113+31 A, to a grid of stellar models computed with the GARSTEC stellar evolution code (Weiss & Schlattl, 2008). The methods used to calculate the stellar model grid are described in Serenelli et al. (2013). BAGEMASS uses a Markov-chain Monte-Carlo method to explore the posterior probability distribution (PPD) for the mass and age of a star based on its observed T_{eff}, luminosity, mean stellar density and surface metal abundance [Fe/H]. We find a very good fit to the

observed parameters of EBLM J0113+31 A for an age of 6.7 ± 0.5 Gyr, as can be seen in Fig. 6.8. More the 99 per cent of samples from the PPD correspond to models where EBLM J0113+31 A is a post main-sequence star that has exhausted all the hydrogen in its core. The GARSTEC model grid accounts for diffusion so the initial metal abundance for this star is inferred to be [Fe/H] $= -0.2 \pm 0.1$. Isochrones for the same age and initial metal abundance from the Dartmouth stellar evolution database (Dotter et al., 2008) and the MESA Isochrones & Stellar Tracks (MIST, Choi et al., 2016) are also shown in Fig. 6.8. There is very good agreement between these different stellar evolution codes, as might be expected given that the properties of EBLM J0113+31 A are similar to the Sun and all three grids of stellar models are calibrated to match the observed properties of the Sun.

The same isochrones from the Dartmouth and MIST stellar model grids are compared to the properties of EBLM J0113+31 B in Fig. 6.9. Our grid of GARSTEC models does not extend to these very low masses. The agreement between the models and observations is reasonably good, which is somewhat surprising given the long-standing observation that stellar models tend to under-predict the radius and over-predict T_{eff} for low-mass stars (Spada et al., 2013; Cassisi & Salaris, 2019; Zhou et al., 2014; Berger et al., 2006; Hoxie, 1973; Lacy, 1977). This can be seen from the mass, radius and T_{eff} measurements for six other very low-mass stars in the same figure. These six stars are members of three eclipsing binaries with orbital periods less than 2 days. This complicates the interpretation of their properties in the light of the so-called "radius inflation" problem because these stars will be forced to rotate much faster than most single M-dwarf stars by tidal forces in these short-period binaries. EBLM J0113+31 B is a valuable addition to the small sample of well-characterised VLMSs because we have an independent estimate of its age and initial metal abundance based on observations of the G0V primary star to add to the accurate mass, radius and T_{eff} measurements.
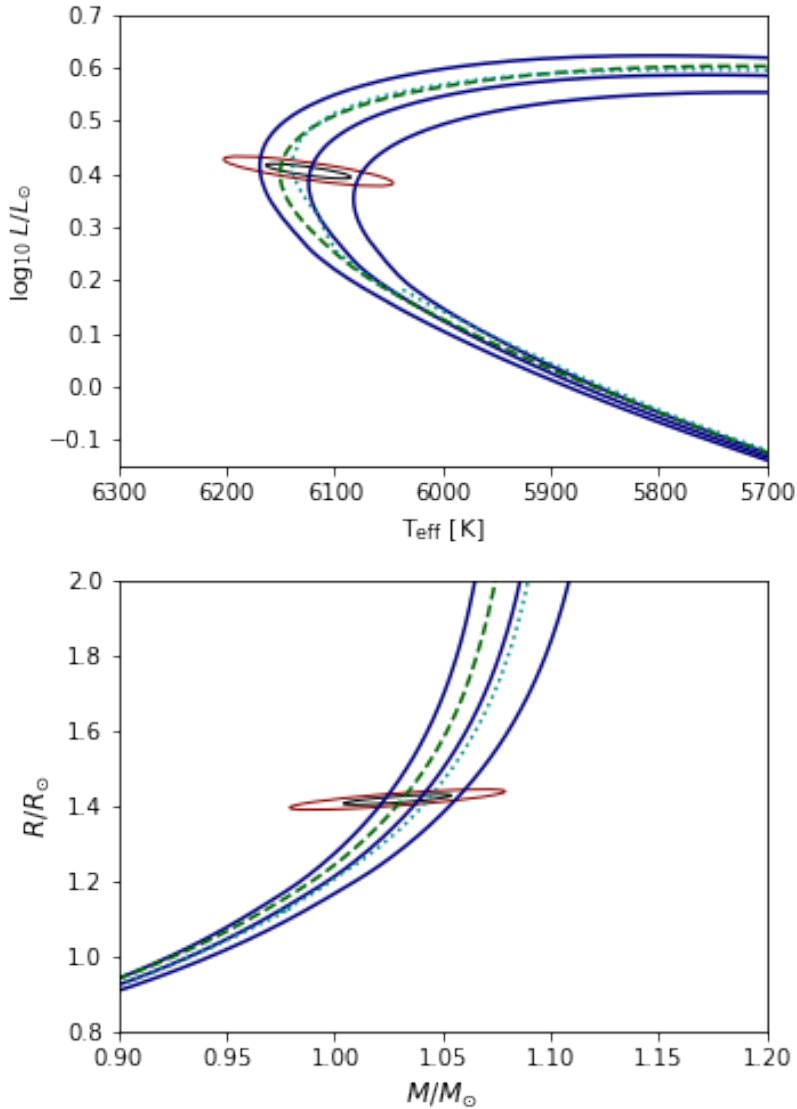
Figure 6.8: EBLM J0113+31 A in the mass-radius and Hertzsprung-Russell diagrams compared to isochrones for an age of 6.7 ± 0.7 Gyr assuming an initial metal abundance [Fe/H] $= -0.2$ interpolated from a grid of GARSTEC stellar models. The ellipses show 1-σ and 2-σ confidence regions on the parameters of EBLM J0113+31 A. Also shown are isochrones for the same age and initial metal abundance from the Dartmouth stellar evolution database (cyan dotted line) and MIST (green dashed line).
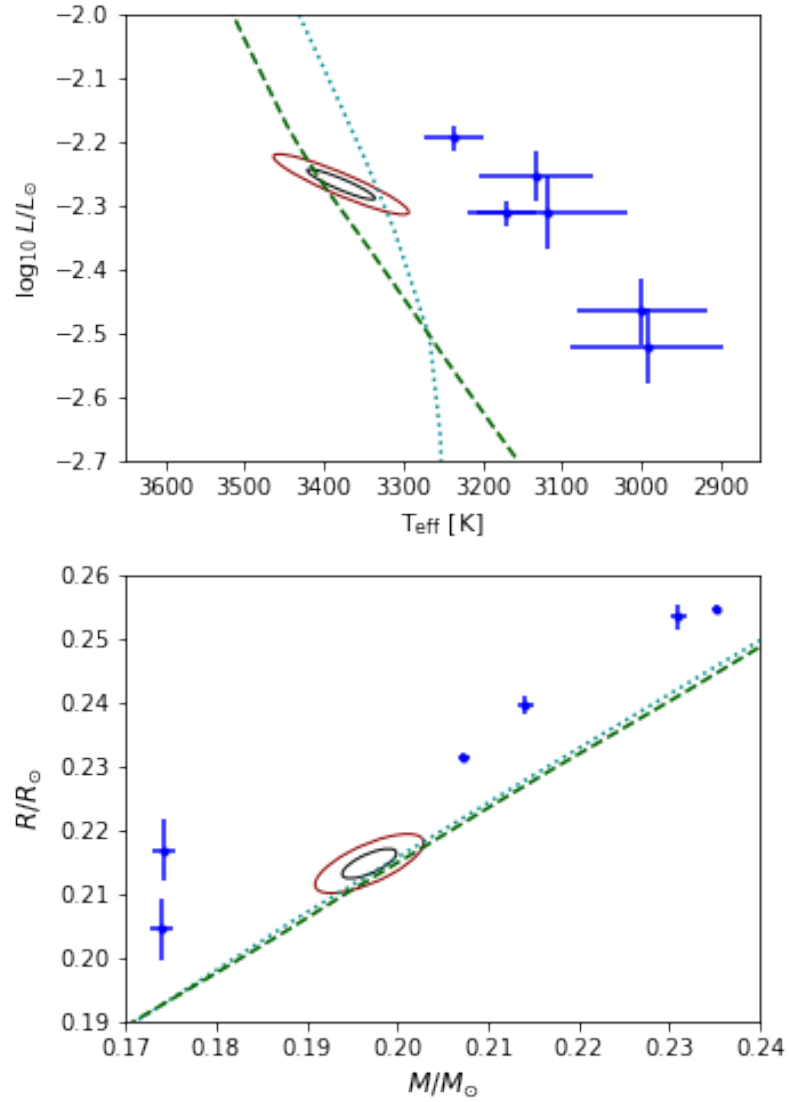
Figure 6.9: EBLM J0113+31 B in the mass-radius and Hertzsprung-Russell diagrams compared to isochrones for ages of 6.8 Gyr assuming [Fe/H] = −0.2 from the Dartmouth stellar evolution database (cyan dotted line) and MIST (green dashed line). The ellipses show 1-σ and 2-σ confidence regions on the parameters of EBLM J0113+31 B. Parameters for very low mass stars shown as error bars in blue are taken from DEBCat (Southworth, 2015a).

6.4.3   EBLM systems as benchmark stars

Benchmark FGK dwarf stars with direct T_{eff} measurements based on angular diameters measured by interferometry typically have apparent magnitudes $V = 1-6$ (Jofré et al., 2014). This is $5-10$ magnitudes brighter than the magnitude limits for large-scale spectroscopic surveys, so special observing modes must be employed to obtain spectra of these benchmark stars. These bright benchmark stars also tend to be single stars, so there are often no direct measurements of their mass or surface gravity. It is difficult to extend this sample because new candidates for benchmark stars will necessarily be more distant than the existing sample, i.e. they will have smaller angular diameters than the existing benchmark stars. For example, a nominal Sun-like star at distance of $10\,\mathrm{pc}$ will have an angular diameter $\theta = 0.465\,\mathrm{mas}$, so a systematic error of only $0.04\,\mathrm{mas}$, which is typical for existing measurements (Karovicova et al., 2022), implies a systematic error of $250\,\mathrm{K}$ in the measured value of T_{eff} for such a star.

In contrast, EBLM J0113+31 is within the magnitude range of recent large-scale spectroscopic surveys, e.g. the *TESS*-HERMES survey ($10 < V < 13.1$, Sharma et al., 2018), LAMOST "VB mode" observations ($9.0 \leq J \leq 12.5$, Luo et al., 2015), and stars in open clusters observed as part of the *Gaia*-ESO survey ($9 < V < 16.5$, Bragaglia et al., 2022). This makes it feasible to observe EBLM J0113+31 and other EBLM binaries in exactly the same way as other stars observed by these survey instruments as part of their routine operations. The contribution of the M-dwarf to the total flux at optical wavelengths is $\lesssim 0.2$ per cent for EBLM binaries, so the M-dwarf will have a completely negligible effect on the atmospheric parameters derived from the analysis of the optical spectrum. This makes it possible to make an "end-to-end" test of the accuracy of parameters derived by the combination of these survey instruments plus their data processing and analysis pipelines. Even at near-infrared wavelengths used by surveys such as APOGEE (Jönsson et al., 2018) the contribution from the M-dwarf is $\lesssim 1$ per cent, so the results of any analysis that includes a correction for this small contribution to the total flux will be insensitive to the details of how this correction is done.

Many EBLM binaries in the magnitude range $10 \lesssim V \lesssim 12$ have been identified and have well-determined spectroscopic orbits that have been published (Triaud et al., 2017) or that are in preparation thanks to the EBLM project and BEBOP survey (Standing et al., 2022). High-quality space-based photometry is already available for many of these stars from the *TESS* survey and/or from our on-going *CHEOPS* GTO programme. Several échelle spectrographs that can provide high-resolution spectroscopy at near-infrared wavelengths are currently operational on $4-10\,\mathrm{m}$ telescopes, e.g. CARMENES on the Calar Alto Observatory 3.5-m telescope (Quirrenbach et al., 2016), NIRPS on the ESO 3.6-m telescope (Grieves et al., 2021), CRIRES+ on the ESO 8.2-m VLT (Kaeufl et al., 2004), and IRD on the 8.2-m Subaru telescope (Kotani et al., 2014). We can also look forward to high-quality spectrophotometry and improved parallax measurements for these EBLM systems in future data releases from the *Gaia* mission.[9] In summary, the instrumentation, data and targets needed to create a network of moderately-bright FGK dwarf stars covering both hemispheres that are ideal benchmark stars for on-going large-scale spectroscopic surveys are all now available.

Apart from their utility as benchmarks stars for large-scale spectroscopic surveys, follow-up observations of additional EBLM systems will also provide valuable data on the properties of very low-mass stars. With observations similar to those presented here we can create a sample of VLMSs with precise and accurate T_{eff}, mass and radius measurements. These EBLM binaries will have independent estimates for their age and initial metallicity based on the observed properties of the primary stars in these systems. It is not feasible to obtain a direct spectrum for these very faint companion stars, but it should be possible given sufficiently high-quality data to estimate the projected rotational velocity of the star from the width of the peak in the stacked-CCF. Data of this quality will be very useful for testing and calibrating models of very low mass stars that include additional physics to account for the radius inflation problem (Mullan et al., 2018; Feiden & Chaboyer, 2014).

---

[9]https://www.cosmos.esa.int/web/gaia/release

Many of these EBLM binary systems will also be ideal benchmark stars for the upcoming *PLATO* mission (Rauer et al., 2014) if we can measure model-independent masses for the primary star using the techniques presented in this study. The *PLATO* mission will focus on bright stars (4−11 mag) with the aim to detect and characterize planets down to Earth-size by photometric transits. Asteroseismology will be performed for these bright stars to obtain stellar parameters, including masses and ages. The *PLATO* Definition Study Report[10] ("red book") specifies that *PLATO* must be capable of delivering accurate stellar ages with a precision of 10 per cent. Some corrections for systematic errors in the current generation of stellar models will be needed to reach this accuracy in stellar ages (Goupil, 2017). The planned observing strategy includes a step-and-stare phase that will cover about 50 per-cent of the sky. EBLM binaries can be used to perform "end-to-end" tests of the *PLATO* data analysis to ensure that the mass estimates delivered for these stars are accurate, and to calibrate the next generation of stellar models using direct mass, radius, and T_{eff} measurements combined with asteroseismology.

6.5   Conclusions

We have derived precise and accurate masses, radii and effective temperatures for both stars in the eclipsing binary system EBLM J0113+31. These data can be used to validate and calibrate stellar models, empirical relations for stellar properties, and to test data analysis techniques. With the techniques established here, it is feasible to create a network of moderately-bright FGK dwarf stars covering both hemispheres that are ideal benchmarks for on-going large-scale spectroscopic surveys and for the upcoming *PLATO* mission.

---

[10]https://sci.esa.int/science-e/www/object/doc.cfm?fobjectid=59251

7 Conclusions and Future Direction

Never give up. Never surrender.

Commander Peter Quincy Taggart, *Galaxy Quest* (1999)

In this thesis I have presented a new method for measuring the fundamental effective temperatures for stars in detached eclipsing binaries, and applied it to five FGK-type stars across three binaries: AI Phe, CPD-54 810, EBLM J0113+31. I have also designed and implemented a dispatch scheduler for the Xamidimura instrument, which will observe eclipsing binaries during eclipse in multiple optical bands.

7.1 Summary of results

In Chapter 3, I discuss the design choices of the scheduler for Xamidimura, describe the feasibility and priority scoring models in detail and present results of the simulation of the scheduler over a five-year period using historical weather logs for the site. Using a database of suitable detached eclipsing binary targets, I optimised the scheduler scoring model parameter weightings to maximise the number of targets that would have 'complete' light curves. The scheduler is ready to be used on the Xamidimura instrument, and has been used during the commissioning phase to select two eclipsing binaries that were then successfully observed during eclipse.

In Chapter 4, we measure the effective temperatures of both components of AI Phe to very high accuracy: $T_{\mathrm{eff},1} = 6199 \pm 22\,\mathrm{K}$, and $T_{\mathrm{eff},2} = 5094 \pm 16\,\mathrm{K}$. The very accurate measurements for T_{eff} were made possible by the high precision measurements of the radii and parallax, along with a wealth of photometric data available on the system. The radii, which were measured to better than 0.2 per cent accuracy by Maxted et al. (2020), are due to the detailed analyses of the *TESS* light curve using multiple approaches and codes. The parallax measurements for AI Phe were accurate due to

not only a *Gaia* parallax measurement, but an independent measurement using interferometry by Gallenne et al. (2019). While *Gaia* DR2 parallaxes do not account for binarity, the lack of photocentre motion and agreement with the measurement from Gallenne et al. (2019) show that it was appropriate to use in this case. AI Phe, unlike most other eclipsing binaries, has multi-band photometry providing strong constraints on the flux ratio of the binary across the ultraviolet, visible and infrared range. In particular, the *IUE* spectroscopy taken during and outside of an eclipse proved a most valuable constraint on the flux in the ultraviolet. Only one other detached, FGK-type eclipsing binary has such data: the G5 III+F7 III binary TZ Fornacis. The accuracy of the bolometric flux, and ultimately T_{eff}, depends on having a reliable estimate of $E(B-V)$. AI Phe is a star with very low reddening, as evidenced by the lack of Na D lines in its high resolution spectra. If AI Phe was more distant, or had more significant reddening, it may not have been possible to reach the accuracy on T_{eff} that we did. The analysis of AI Phe was also a useful initial testing ground for teb – we were able to gain an understanding of how the code works in practice, and adjust the parameters of the model such as number of distortion coefficients. We found that the T_{eff} for both components is robust to choice of input spectral energy distributions, which suggests that our method and results are sufficiently model-independent for the stars to be used as calibration stars.

In Chapter 5, we measure T_{eff} for both components of CPD-54 810 to a much improved accuracy, obtaining $T_{\mathrm{eff,1}}= 6462 \pm 43\,\mathrm{K}$, and $T_{\mathrm{eff,2}}= 6331 \pm 43\,\mathrm{K}$. We also performed a complete re-analysis of the radial velocities extracted by Ratajczak et al. (2021) along with the *TESS* light curves to improve their masses and radii. Unlike AI Phe, CPD-54 810 has significantly fewer photometric data, which required us to acquire additional *BVRI* observations during totality and egress of the total secondary eclipse to complement the *TESS* observations. The most notable result from the analysis of CPD-54 810 was the significant difference in our fundamental T_{eff} measurements, and the spectroscopic T_{eff} estimates presented by Ratajczak et al. (2021): our T_{eff} values are almost $500\,\mathrm{K}$ hotter (cf. $T_{\mathrm{eff,1}}= 5980 \pm 205\,\mathrm{K}$, and $T_{\mathrm{eff,2}}= 5850 \pm 190\,\mathrm{K}$). This is likely due to the quality of the spectroscopy used in the T_{eff} estimates; in our analysis

it was difficult to find a good fit to all of the spectral lines, and our fit with much hotter T_{eff} shows a similar fit quality to the one presented by Ratajczak et al. (2021). The analysis of CPD-54 810 was particularly informative in how best to approach the analysis of DEBs with few data: more than one flux ratio is required for meaningful results, fewer flux ratios translates to fewer distortion coefficients (to avoid over-fitting), and as with AI Phe, a reliable estimate for $E(B-V)$. CPD-54 810 also does not show significant evidence for reddening in its spectra, but this time we chose to measure the equivalent width of the Na DI line and employ the relation from Munari & Zwitter (1997) to obtain an estimate for $E(B-V)$ that is somewhat lower than from reddening maps. This is something to investigate in future work, as described in Section 7.3.4. Our results improve the previously published physical parameters for CPD-54 810, and with the improvements in the accuracy of T_{eff} make it a suitable candidate benchmark star for use in the testing and calibration of stellar models and pipelines.

Finally, in Chapter 6, I present my contributions to Maxted et al. (2022a). In this paper, we measured the fundamental T_{eff} for the primary component of EBLM J0113+31 using teb, finding $T_{\text{eff},1} = 6124 \pm 40\,\text{K}$, along with $T_{\text{eff},2} = 3375 \pm 40\,\text{K}$ for the M-dwarf companion. This was the first time using teb on an eclipsing binary with a low-mass component, and it successfully handled the extreme flux ratios. As with CPD-54 810, the available photometry was more limited than the ideal case, but with a smaller number of distortion coefficients, we obtained T_{eff} results that are robust to the choice of input SED. EBLM systems such as EBLM J0113+31 have the potential to be ideal end-to-end tests of spectroscopic surveys. With high quality *CHEOPS* light curves and high resolution near-infrared spectroscopy, we have shown that it is possible to obtain accurate masses and radii for this kind of system, despite the primary component significantly dominating the flux in the visible range.

7.2   This work in context

A comparable sample of FGK main sequence and subgiant stars with direct T_{eff} measurements that I have discussed throughout this thesis is the *Gaia* FGK benchmark stars, a set of bright stars with angular diameters that have been measured using interferometry. These stars are shown along with our results in Figure 7.1. The density of nearby stars in the Geneva-Copenhagen Survey III (Casagrande et al., 2011) is shown, as are Dartmouth stellar tracks for 0.9–1.5 $\mathrm{M}_\odot$ (Dotter et al., 2008). Our sample of DEB benchmarks is already filling parameter space missed by the *Gaia* benchmark sample; notably our four F-type stars are hotter than any *Gaia* benchmarks with T_{eff} measured to 50 K or better. The stars in the GCS III catalog with age estimates with uncertainties less than 15% are also shown in Figure 7.1 to highlight the need to fill the $\log g$–T_{eff} parameter space around the main-sequence turn-off (MSTO). Stars near the MSTO are key for measuring the age of a stellar population, such as stellar streams identified via kinematics, or stars with the same chemical abundance pattern that are thought to have been born together (chemical tagging; Hogg et al. 2016). Similarly, in Figure 7.2 I also include the *Kepler* LEGACY sample of stars with detailed asteroseismology (Silva Aguirre et al., 2017) to highlight where benchmark stars are particularly useful for calibrating asteroseismic scaling relations.

There is still a long way to go until the FGK IV-V $\log g$–T_{eff} parameter space is fully populated by benchmark stars. There is already a number of eclipsing binaries with detailed mass and radius measurements in DEBCat (Southworth, 2015a), which would need re-visiting with teb to measure homogeneous fundamental temperatures. The current set of stars in DEBCat is shown in context with our results in Figure 7.3.

Our work on developing a new method to measure T_{eff} for DEBs and work towards building a homogeneous benchmark sample of stars with accurate and consistent physical properties has been successful, contributing analyses of five such FGK-type stars to the literature. Our work provides new benchmark stars in parameter space not currently occupied by T_{eff} benchmark samples and there is potential to apply our method to many more EBs from DEBCat and/or discovered by *TESS*, *K2* and *Kepler*.
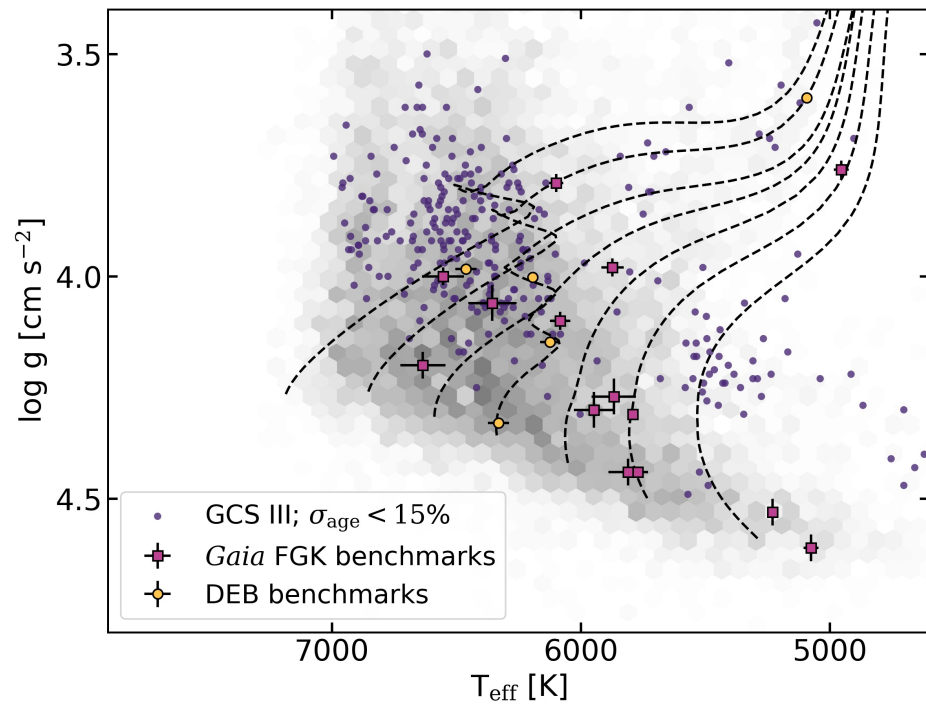
Figure 7.1: Surface gravity against effective temperature for FGK-type stars. Density of stars from the Geneva-Copenhagen survey III is shown as grey hexagons, overlaid by Dartmouth stellar tracks for 0.9–$1.5\,\mathrm{M_\odot}$ and the GCS III stars with ages determined to better than 15%. Benchmark stars from the *Gaia* FGK sample (pink squares) and from DEBs (yellow circles) are plotted in front.
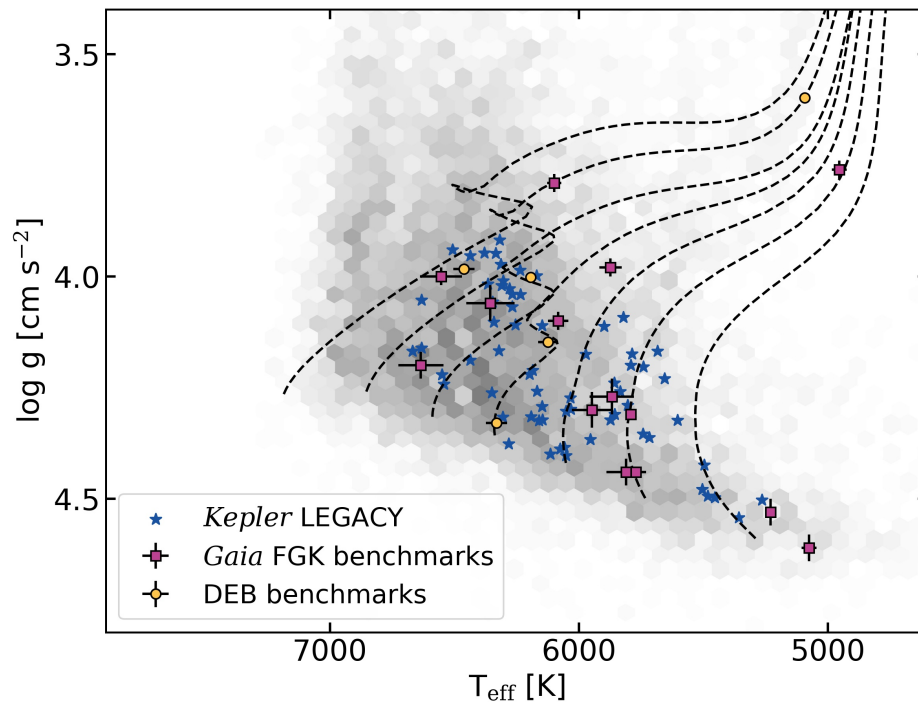
Figure 7.2: Surface gravity against effective temperature for FGK-type stars. Density of stars from the Geneva-Copenhagen survey III is shown as grey hexagons, overlaid by Dartmouth stellar tracks for 0.9–$1.5\,M_\odot$ and the *Kepler* LEGACY sample of stars with detailed asteroseismology (dark blue). Benchmark stars from the *Gaia* FGK sample (pink squares) and from DEBs (yellow circles) are plotted in front.

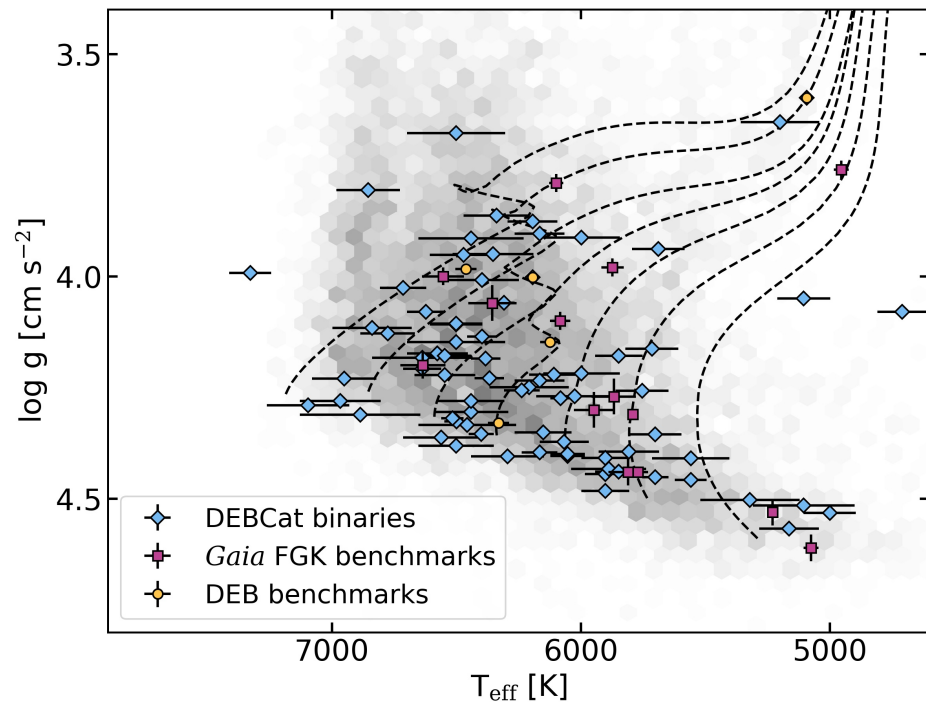Figure 7.3: Surface gravity against effective temperature for FGK-type stars, similar to Figure 7.1. The benchmark stars from the *Gaia* FGK sample (pink squares) and from DEBs (yellow circles) are accompanied by the systems in DEBCat that have not been analysed with teb (light blue diamonds).

7.3 Future direction

7.3.1 Building a catalog of T_{eff} benchmark DEBs

The work I have presented in this thesis is work towards the goal of creating a catalog of well-characterised benchmark DEBs with reliable and accurate direct measurements of T_{eff}. A natural next step would be to continue analysing more DEBs. Not only are there the previously well-characterised systems present in the DEBCat sample, but numerous ground-based and space-based surveys and telescopes have discovered and continue to discover hundreds of thousands of DEBs. The *TESS*, *Kepler* and *K2* missions have observed vast numbers of DEBs during their lifetimes, providing very precise and high cadence light curves suitable for making detailed characterisations of these systems. For example, 4584 eclipsing binaries were recently observed in short cadence mode by *TESS* (Prša et al., 2022). The detached systems from this new catalogue are ideal for radial velocity follow-up, with which a full solution of the system can be obtained, giving precise and accurate masses and radii. As we showed with CPD-54 810, it is possible to measure a useful T_{eff} for DEBs with only a handful of multi-band light curves, so it would realistically be possible to apply teb to many of these systems with only some additional work required: obtaining, extracting and fitting radial velocities, obtaining and fitting multi-band light curves, and calculating a reliable interstellar extinction estimate. This work would culminate in the creation of a large catalogue of well-characterised DEBs that can be used as a benchmark sample for surveys and calibration of stellar models, similarly to the *Gaia* interferometric benchmark sample (Heiter et al., 2015).

7.3.2 Developing and improving teb

There is still a lot that can be done with the teb code. Not only can it be improved in terms of usability, flexibility and speed, but its limits are still to be fully tested. For example, how distant of a DEB or large of an interstellar extinction value can it handle?

For EBLM J0113+31, we measured T_{eff} for the primary component of an EBLM, but could we expand `teb` to also handle M-dwarfs? What about stars hotter than an F5 spectral type – at what point does the ultraviolet flux become too dominant? – or stars more evolved than a subgiant? How well can it handle the degeneracies involved when analysing systems without total eclipses? Can `teb` handle triple systems, single stars, or stars with planets?

7.3.3 Additional data

7.3.3.1 Multi-band light curves from Xamidimura

As we showed in Chapter 5, flux ratios in multiple optical bands is critical for constraining the derived T_{eff}. While most eclipsing binaries have wide-band catalog light curves from e.g. *TESS*, and catalog photometry, there is no real equivalent all-sky catalog for multi-band light curves in several optical bands such as B,V,R,I. As a dedicated instrument for observing the eclipses of DEBs in several bands, Xamidimura will be a very useful tool for increasing the number of feasible systems for analysis with `teb`. The first light curves from Xamidimura for systems selected with the scheduler I presented in Chapter 3, are shown in Figures 3.11 and 3.12. The exact number of eclipsing binaries Xamidimura will observe and complete the light curves for will be determined by the choice of how 'completeness' is defined.

7.3.3.2 *Swift* ultraviolet photometry

I applied for and was successfully awarded observing time on the UVOT instrument of the Neils Gehrels Swift Observatory (*Swift*, Roming et al. 2005) to obtain ultraviolet photometry of seven eclipsing binary stars that have limited to no catalog ultraviolet *GALEX* photometry, along with twelve calibration stars. Details of these targets are given in Tables 7.1 and 7.2. Figure 7.4 shows these targets with their current catalog results taken from DEBCat. We expect the eventual T_{eff} results to improve to carry uncertainties close to those found in our analyses of CPD-54 810 and EBLM J0113+31.
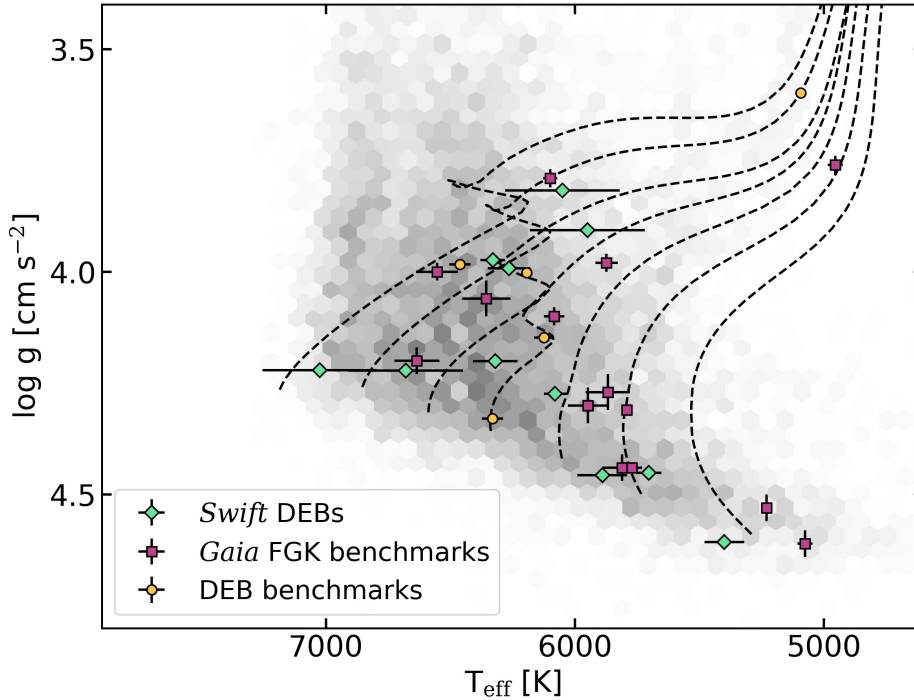
Figure 7.4: Surface gravity against effective temperature for FGK-type stars, similar to Figure 7.1. The benchmark stars from the *Gaia* FGK sample (pink squares) and from DEBs (yellow circles) are accompanied by the EBs that *Swift* will observe (green diamonds).

The stars will be observed during *Swift* Cycle 18, from April 2022-23, so too late to be included in work for my thesis. However, these observations will provide valuable constraints on future analyses for these systems using `teb`.

7.3.3.3 *Gaia* **DR3 low-resolution spectroscopy**

The *Gaia* satellite published its third major data release on 13th June 2022. This release, amongst numerous other results and data products, includes low-resolution spectra for 219 million sources across the wavelength range of its BP and RP bands. This high quality, space-based spectro-photometry will compliment the existing catalog photometry and provide significantly improved constraints on the total flux, especially

Table 7.1: Proposed *Swift* EB targets in order of priority. Count rates in $UVW1$, $UVM2$, $UVW2$ filters were estimated with the UVOT Signal-to-Noise calculator. T_{min} is the minimum exposure time for each target will yield S/N>50 in each UVOT filter. The exact exposure times will be determined by the UVOT configuration.

Target name	Priority	SpTy	m_V	T_{min} (s)	$UVW1$ (s^{-1})	$UVM2$ (s^{-1})	$UVW2$ (s^{-1})
TYC 7091-888-1	1	F6 + G9	10.66	300	132.17	30.25	40.54
V530 Ori	1	G1 + M1	9.96	300	152.21	15.77	33.08
LL Aqr	2	F9 + G3	9.32	300	274.44	28.43	59.65
V501 Her	2	G3 + G3	11.15	900	46.96	4.85	10.28
TYC 6511-1799-1	2	F9 + G0	11.43	900	47.75	6.96	11.56
BK Peg	3	F8 + F7	10.04	300	171.76	25.04	41.6
TYC 8590-374-1	3	F1 + F3.5	10.63	300	201.42	73.82	100.16

Table 7.2: Proposed *Swift* CALSPEC flux standard stars we will use for calibration. Estimated count rates and minimum exposure times calculated as in Table 7.1. *These stars have previously been used in UVOT calibrations.

Target Name	Priority	SpTy	m_V	T_{min} (s)	$UVW1$ (s^{-1})	$UVM2$ (s^{-1})	$UVW2$ (s^{-1})
BD+29 2091	3	F5	10.22	240	198.21	45.37	60.79
HD074000	3	sdF6	9.66	120	332	75.99	101.82
HD115169	3	G3V	9.2	120	282.96	29.2	61.93
HD200654	3	G	9.11	120	307.41	31.72	67.28
P041C*	3	G0V	12.16	600	20.07	2.08	4.36
P177D*	3	G0V	13.49	600	5.89	0.61	1.28
P330E*	3	G2V	12.92	600	9.2	0.95	2.01
TYC 4424-1286-1	3	A4V	12.53	120	88.58	50.21	79.93
TYC 4212-455-1	3	A3V	12.01	120	142.99	81.05	129.04
TYC 4209-1396-1	3	A4V	12.28	120	111.51	63.21	100.22
TYC 4433-1800-1	3	A3V	11.69	120	192.01	108.83	173.27
TYC 4205-1677-1	3	A3V	12.01	120	142.99	81.05	129.04

towards the blue end of the spectrum. An initial look at the *Gaia* BP/RP spectra for CPD-54 810 and EBLM J0113+31, when compared to the best fit combined flux

Figure 7.5: Sum of the flux integrating functions for CPD-54 810 compared to the *Gaia* DR3 spectro-photometic data, with residuals given in the lower panel.

integrating function for both components shows that our approach with `teb` pre-*Gaia* DR3 has yielded results that agree very well with the *Gaia* data. These comparisons can be seen in Figures 7.5 and 7.6. The majority of the discrepancy between the *Gaia* and `teb` spectra is blueward of 450 nm for CPD-54 810 and blueward of 500 nm for EBLM J0113+31. This is suspected to be due to the fewer, poorer quality photometric constraints available in this wavelength range, but could be partly due to the *Gaia* flux calibration blueward of 400 nm (Montegriffo et al., 2022). A detailed inspection, perhaps informed by a re-analysis of all systems studied in this thesis with synthetic photometry using the new *Gaia* data may reveal some answers and perhaps improve our already impressive T_{eff} results.
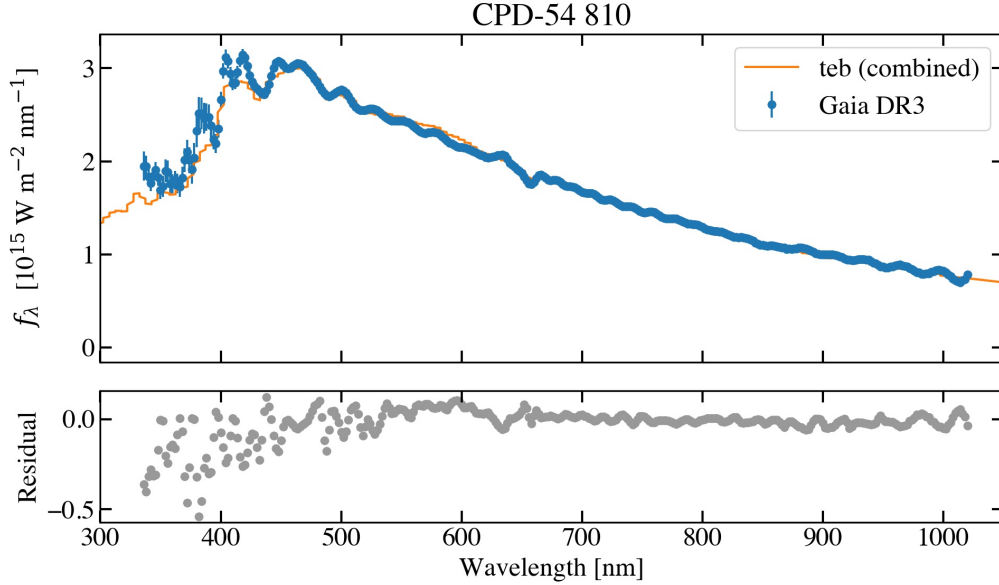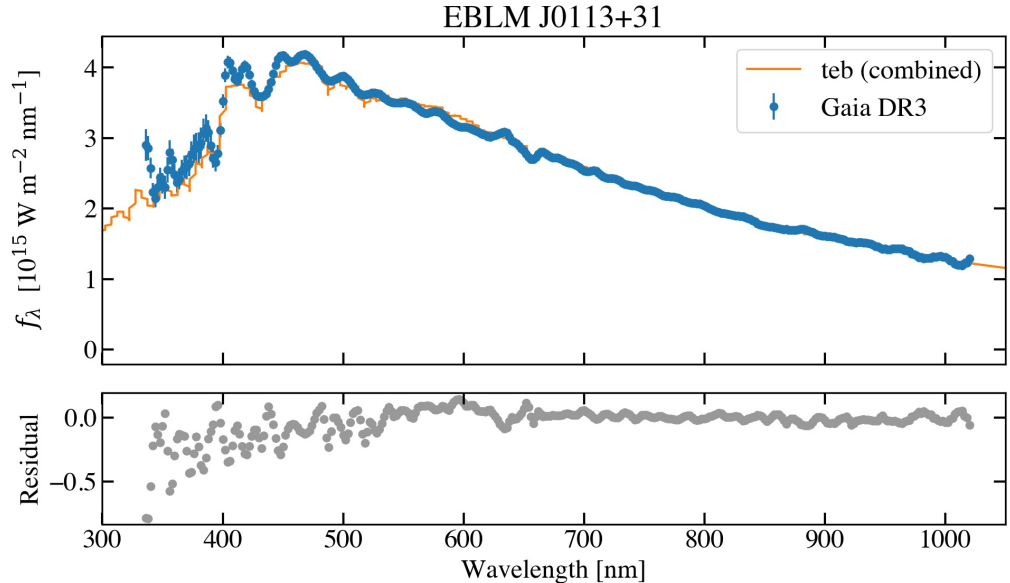
Figure 7.6: Sum of the flux integrating functions for EBLM J0113+31 compared to the *Gaia* DR3 spectro-photometic data, with residuals given in the lower panel.

7.3.4 Improving interstellar extinction estimates

A major factor to consider when analysing the spectral energy distributions of eclipsing binary stars with teb is the interstellar extinction. Work in Chapters 4 and 5 on AI Phe and CPD-54 810 have shown that a robust estimate of this, ideally through a direct measurement of spectral features due to the interstellar medium rather than from a reddening map, is vital in constraining the estimate for the effective temperatures. Through our work, we noticed that the sample of stars used by Munari & Zwitter (1997) to calibrate their relation between the equivalent width of the Na DI line and interstellar extinction is very limited, especially at the low $E(B-V)$ end. Effort towards establishing new relations between observed features in spectra (Na DI lines, diffuse interstellar bands, etc.) and extinction, would be beneficial to any work that relies on robust estimates of interstellar extinction.

Publications

This is a list of refereed publications that I produced or contributed to during my PhD.

- **Miller N. J.**, Maxted P. F. L., Graczyk D., Tan T. G., Southworth J., MN-RAS, submitted June 2022

- Maxted P. F. L., **Miller N. J.** et al., 2022, MNRAS, in press

- King G. W., Wheatley P. J., Fawcett V. A., **Miller N. J**., Corrales L. R., Agüeros M. A., 2022, MNRAS, 512, 41

- Triaud A. H. M. J., Standing M. R., Heidari N., Martin D. V., Boisse I., Santerne A., Correia A. C. M., **et al.**, 2022, MNRAS, 511, 3561

- Martin D. V., El-Badry K., Hodžić V. K., Triaud A. H. M. J., Angus R., Birky J., Foreman-Mackey D., **et al**., 2021, MNRAS, 507,

- Swayne M. I., Maxted P. F. L., Triaud A. H. M. J., Sousa S. G., Broeg C., Florén H.-G., Guterman P., **et al.**, 2021, MNRAS, 506, 306

- **Miller N. J.**, Maxted P. F. L., Smalley B., 2020, MNRAS, 497, 2899

Bibliography

Abdurro'uf et al., 2022, ApJS, 259, 35

Adibekyan V. Z., Santos N. C., Sousa S. G., Israelian G., 2011, A&A, 535, L11

Adibekyan V. Z., Sousa S. G., Santos N. C., Delgado Mena E., González Hernández
    J. I., Israelian G., Mayor M., Khachatryan G., 2012, A&A, 545, A32

Adibekyan V., et al., 2015, A&A, 583, A94

Allard F., Homeier D., Freytag B., Schaffenberger W., Rajpurohit A. S., 2013, Memorie
    della Societa Astronomica Italiana Supplementi, 24, 128

Allen C. W., 1973, Astrophysical quantities. The Athlone Press, University of London

Alvarez R., Plez B., 1998, A&A, 330, 1109

Andersen J., 1991, A&A Rv, 3, 91

Andersen J., Clausen J. V., Nordstrom B., Gustafsson B., Vandenberg D. A., 1988,
    A&A, 196, 128

Antia H. M., Basu S., 2005, ApJL, 620, L129

Asplund M., Grevesse N., Sauval A. J., Scott P., 2009, ARA&A, 47, 481

Astropy Collaboration et al., 2013, A&A, 558, A33

Astropy Collaboration et al., 2018, AJ, 156, 123

Baines E. K., McAlister H. A., ten Brummelaar T. A., Sturmann J., Sturmann L.,
    Turner N. H., Ridgway S. T., 2009, ApJ, 701, 154

Baschek B., Scholz M., Wehrse R., 1991, A&A, 246, 374

Bensby T., Feltzing S., Oey M. S., 2014, A&A, 562, A71

Benz W., et al., 2021, Experimental Astronomy, 51, 109

Berger D. H., et al., 2006, ApJ, 644, 475

Berger T. A., Huber D., van Saders J. L., Gaidos E., Tayar J., Kraus A. L., 2020, AJ, 159, 280

Bessell M. S., 2005, ARA&A, 43, 293

Bessell M., Murphy S., 2012, PASP, 124, 140

Bessell M., Bloxham G., Schmidt B., Keller S., Tisserand P., Francis P., 2011, PASP, 123, 789

Bianchi L., Conti A., Shiao B., 2014, VizieR Online Data Catalog, p. II/335

Blackwell D. E., Shallis M. J., 1977, MNRAS, 180, 177

Blackwell D. E., Shallis M. J., Selby M. J., 1979, MNRAS, 188, 847

Blanco-Cuaresma S., 2019, MNRAS, 486, 2075

Blanco-Cuaresma S., Soubiran C., Jofré P., Heiter U., 2014a, A&A, 566, A98

Blanco-Cuaresma S., Soubiran C., Heiter U., Jofré P., 2014b, A&A, 569, A111

Bohlin R. C., Bianchi L., 2019, AJ, 157, 107

Bohlin R. C., Dickinson M. E., Calzetti D., 2001, AJ, 122, 2118

Bohlin R. C., Gordon K. D., Tremblay P. E., 2014, PASP, 126, 711

Borucki W. J., et al., 2010, Science, 327, 977

Boyajian T. S., et al., 2012, ApJ, 757, 112

Boyajian T. S., et al., 2013, ApJ, 771, 40

Boyajian T., et al., 2015, MNRAS, 447, 846

Bragaglia A., et al., 2022, A&A, 659, A200

Bressan A., Marigo P., Girardi L., Salasnich B., Dal Cero C., Rubele S., Nanni A., 2012, MNRAS, 427, 127

Buder S., et al., 2018, MNRAS, 478, 4513

Caldwell D. A., et al., 2020, Research Notes of the American Astronomical Society, 4, 201

Camarota L., Holberg J. B., 2014, MNRAS, 438, 3111

Cannon A. J., Pickering E. C., 1901, Annals of Harvard College Observatory, 28, 129

Cardelli J. A., Clayton G. C., Mathis J. S., 1989, ApJ, 345, 245

Casagrande L., VandenBerg D. A., 2018, MNRAS, 479, L102

Casagrande L., Ramírez I., Meléndez J., Bessell M., Asplund M., 2010, A&A, 512, A54

Casagrande L., Schönrich R., Asplund M., Cassisi S., Ramírez I., Meléndez J., Bensby T., Feltzing S., 2011, A&A, 530, A138

Cassisi S., Salaris M., 2019, A&A, 626, A32

Chi W., Agrawal J., Chien S., Fosse E., Guduri U., 2021, Proceedings of the International Conference on Automated Planning and Scheduling, 29, 501

Choi J., Dotter A., Conroy C., Cantiello M., Paxton B., Johnson B. D., 2016, ApJ, 823, 102

Claret A., 2000, A&A, 363, 1081

Claret A., 2007, A&A, 475, 1019

Claret A., 2018, A&A, 618, A20

Claret A., Torres G., 2016, A&A, 592, A15

Claret A., Torres G., 2018, ApJ, 859, 100

Claret A., Torres G., 2019, ApJ, 876, 134

Cohen M., Wheaton W. A., Megeath S. T., 2003, AJ, 126, 1090

Colomé J., Casteels K., Ribas I., Francisco X., 2010, in Radziwill N. M., Bridger A., eds, Society of Photo-Optical Instrumentation Engineers (SPIE) Conference Series Vol. 7740, Software and Cyberinfrastructure for Astronomy. p. 77403K, doi:10.1117/12.857672

Colome J., et al., 2012, in Peck A. B., Seaman R. L., Comeron F., eds, Society of Photo-Optical Instrumentation Engineers (SPIE) Conference Series Vol. 8448, Observatory Operations: Strategies, Processes, and Systems IV. p. 84481L, doi:10.1117/12.926899

Constantino T., Baraffe I., 2018, A&A, 618, A177

Cousins A. W. J., 1976, MmRAS, 81, 25

Crawford D. L., 1958, ApJ, 128, 185

Cutri R. M., et al. 2012, VizieR Online Data Catalog, p. II/311

Deng L.-C., et al., 2012, Research in Astronomy and Astrophysics, 12, 735

Diaz-Cordoves J., Gimenez A., 1992, A&A, 259, 227

Donati J. F., et al., 2020, MNRAS, 498, 5684

Dotter A., 2016, ApJS, 222, 8

Dotter A., Chaboyer B., Jevremović D., Kostov V., Baron E., Ferguson J. W., 2008, ApJS, 178, 89

Doyle A. P., Smalley B., Faedi F., Pollacco D., Gómez Maqueo Chew Y., 2017, MNRAS, 469, 4850

Etzel P. B., 1981, in Carling E. B., Kopal Z., eds, NATO Advanced Study Institute (ASI) Series C Vol. 69, Photometric and Spectroscopic Binary Systems. p. 111

Evans D. W., et al., 2018, A&A, 616, A4

Feiden G. A., Chaboyer B., 2014, A&A, 571, A70

Flynn C., Sekhri R., Venville T., Dixon M., Duffy A., Mould J., Taylor E. N., 2022, MNRAS, 509, 4276

Foreman-Mackey D., Hogg D. W., Lang D., Goodman J., 2013, PASP, 125, 306

Foreman-Mackey D., Agol E., Ambikasaran S., Angus R., 2017, celerite: Scalable 1D Gaussian Processes in C++, Python, and Julia, Astrophysics Source Code Library, record ascl:1709.008 (ascl:1709.008)

Fouqué P., et al., 2018, MNRAS, 475, 1960

Frank J., Kürklü E., 2005, in Proceedings of the Second International Conference on Integration of AI and OR Techniques in Constraint Programming for Combinatorial Optimization Problems. CPAIOR'05. Springer-Verlag, Berlin, Heidelberg, p. 183–200

Fraser S. N., 2012, PhD thesis, Liverpool John Moores University

Fraser S., Steele I. A., 2004, in Quinn P. J., Bridger A., eds, Society of Photo-Optical Instrumentation Engineers (SPIE) Conference Series Vol. 5493, Optimizing Scientific Return for Astronomy through Information Technologies. pp 331–340, doi:10.1117/12.551380

Frisch P. C., Redfield S., Slavin J. D., 2011, ARA&A, 49, 237

Gaia Collaboration et al., 2016, A&A, 595, A1

Gaia Collaboration et al., 2018, A&A, 616, A1

Gaia Collaboration et al., 2021a, A&A, 649, A1

Gaia Collaboration et al., 2021b, A&A, 649, A6

Gallenne A., et al., 2019, A&A, 632, A31

Garcia-Piquer A., et al., 2017, A&A, 604, A87

Garstang R. H., 1986, PASP, 98, 364

Gent M. R., et al., 2022, A&A, 658, A147

Ghezzi L., Johnson J. A., 2015, ApJ, 812, 96

Gill S., et al., 2019, A&A, 626, A119

Gilmore G., et al., 2012, The Messenger, 147, 25

Glass I. S., 1973, MNRAS, 164, 155

Gómez Maqueo Chew Y., et al., 2014, A&A, 572, A50

Goupil M., 2017, in European Physical Journal Web of Conferences. p. 01003, doi:10.1051/epjconf/201716001003

Graczyk D., et al., 2019, ApJ, 872, 85

Graczyk D., et al., 2021, A&A, 649, A109

Grevesse N., Noels A., 1993, in Prantzos N., Vangioni-Flam E., Casse M., eds, Origin and Evolution of the Elements. pp 15–25

Grevesse N., Asplund M., Sauval A. J., 2007, SSRv, 130, 105

Grieves N., et al., 2021, in European Planetary Science Congress. pp EPSC2021–555, doi:10.5194/espc2021-555

Gustafsson B., Edvardsson B., Eriksson K., Jørgensen U. G., Nordlund Å., Plez B., 2008, A&A, 486, 951

Güzel O., Özdarcan O., 2020, Contributions of the Astronomical Observatory Skalnate Pleso, 50, 535

Haberreiter M., Kosovichev A. G., Schmutz W., 2009, in EGU General Assembly Conference Abstracts. EGU General Assembly Conference Abstracts. p. 3961

Harris C. R., et al., 2020, Nature, 585, 357

Hastings W. K., 1970, Biometrika, 57, 97

Hawkins K., et al., 2016, A&A, 592, A70

Heiter U., et al., 2002, A&A, 392, 619

Heiter U., Jofré P., Gustafsson B., Korn A. J., Soubiran C., Thévenin F., 2015, A&A, 582, A49

Hełminiak K. G., et al., 2019, A&A, 622, A114

Higl J., Weiss A., 2017, A&A, 608, A62

Hilditch R. W., 2001, An Introduction to Close Binary Stars. Cambridge University Press

Hogg D. W., et al., 2016, ApJ, 833, 262

Holmberg J., Nordström B., Andersen J., 2007, A&A, 475, 519

Holmberg J., Nordström B., Andersen J., 2009, A&A, 501, 941

Hoxie D. T., 1973, A&A, 26, 437

Hoyer S., Guterman P., Demangeon O., Sousa S. G., Deleuil M., Meunier J. C., Benz W., 2020, A&A, 635, A24

Huang Y., Liu X. W., Yuan H. B., Xiang M. S., Chen B. Q., Zhang H. W., 2015, MNRAS, 454, 2863

Hunter J. D., 2007, Computing in Science & Engineering, 9, 90

Husser T. O., Wende-von Berg S., Dreizler S., Homeier D., Reiners A., Barman T., Hauschildt P. H., 2013, A&A, 553, A6

International Organization for Standardization 1972, Technical report, Standard Atmosphere. International Standard ISO 2533

Jarrett T. H., et al., 2011, ApJ, 735, 112

Jenkins J. M., et al., 2016, in Chiozzi G., Guzman J. C., eds, Society of Photo-Optical Instrumentation Engineers (SPIE) Conference Series Vol. 9913, Software and Cyberinfrastructure for Astronomy IV. p. 99133E, doi:10.1117/12.2233418

Jofré P., et al., 2014, A&A, 564, A133

Jofré P., Heiter U., Tucci Maia M., Soubiran C., Worley C. C., Hawkins K., Blanco-Cuaresma S., Rodrigo C., 2018, Research Notes of the American Astronomical Society, 2, 152

Jofré P., Heiter U., Soubiran C., 2019, ARA&A, 57, 571

Johnson H. L., 1966, ApJ, 143, 187

Johnson H. L., Morgan W. W., 1953, ApJ, 117, 313

Johnston M. D., 1988, in Very Large Telescopes and their Instrumentation, Vol. 2. p. 1273

Johnston M. D., Miller G. E., 1994, in Mark Fox Monty Zweben eds, , Intelligent Scheduling. Morgan-Kaufmann, San Francisco, pp 391–422

Jones H. R. A., Longmore A. J., Jameson R. F., Mountain C. M., 1994, MNRAS, 267, 413

Jones A., Noll S., Kausch W., Szyszka C., Kimeswenger S., 2013, A&A, 560, A91

Jones A., Noll S., Kausch W., Unterguggenberger S., Szyszka C., Kimeswenger S., 2019, A&A, 624, A39

Jönsson H., et al., 2018, AJ, 156, 126

Jontof-Hutter D., 2019, Annual Review of Earth and Planetary Sciences, 47, 141

Joslin D. E., Clements D. P., 1999, Journal of Artificial Intelligence Research, 10, 353

Justesen A. B., Albrecht S., 2021, ApJ, 912, 123

Kaeufl H.-U., et al., 2004, in Moorwood A. F. M., Iye M., eds, Society of Photo-Optical Instrumentation Engineers (SPIE) Conference Series Vol. 5492, Ground-based Instrumentation for Astronomy. pp 1218–1227, doi:10.1117/12.551480

Karataş Y., Schuster W. J., 2010, NewA, 15, 444

Karovicova I., White T. R., Nordlander T., Casagrande L., Ireland M., Huber D., 2022, A&A, 658, A47

Kasten F., 1965, Archives for Meteorology Geophysics and Bioclimatology Series B Theoretical and Applied Climatology, 14, 206

Kasten F., Young A. T., 1989, ApOpt, 28, 4735

Kaufer A., Stahl O., Tubbesing S., Nørregaard P., Avila G., Francois P., Pasquini L., Pizzella A., 1999, The Messenger, 95, 8

Keller S. C., et al., 2007, PASA, 24, 1

Kippenhahn R., Weigert A., 1990, Stellar Structure and Evolution. Springer-Verlag

Kirk B., et al., 2016, Astron. J, 151, 21pp

Kirkby-Kent J. A., Maxted P. F. L., Serenelli A. M., Anderson D. R., Hellier C., West R. G., 2018, A&A, 615, A135

Kjurkchieva D., Vasileva D., Atanasova T., 2017, AJ, 154, 105

Klinglesmith D. A., Sobieski S., 1970, AJ, 75, 175

Kopal Z., 1955, Annales d'Astrophysique, 18, 379

Kotani T., et al., 2014, in Ramsay S. K., McLean I. S., Takami H., eds, Society of Photo-Optical Instrumentation Engineers (SPIE) Conference Series Vol. 9147, Ground-based and Airborne Instrumentation for Astronomy V. p. 914714, doi:10.1117/12.2055075

Krisciunas K., Schaefer B. E., 1991, Publ. Astron. Soc. Pac, 103, 1033

Kurucz R. L., 1970, SAO Special Report, 309

Kurucz R. L., 1993, SYNTHE spectrum synthesis programs and line data

Lacy C. H., 1977, ApJS, 34, 479

Lallement R., Vergely J. L., Valette B., Puspitarini L., Eyer L., Casagrande L., 2014, A&A, 561, A91

Lastennet E., Valls-Gabaud D., 2002, A&A, 396, 551

Lee J. W., Kristiansen M. H., Hong K., 2019, AJ, 157, 223

Lightkurve Collaboration et al., 2018, Lightkurve: Kepler and TESS time series analysis in Python, Astrophysics Source Code Library, record ascl:1812.013 (ascl:1812.013)

Lindegren L., et al., 2018, A&A, 616, A2

Lindegren L., et al., 2021a, A&A, 649, A2

Lindegren L., et al., 2021b, A&A, 649, A4

Liu Q., Wei P., Shang Z.-H., Ma B., Hu Y., 2018, Research in Astronomy and Astrophysics, 18, 005

Lubin J. B., et al., 2017, ApJ, 844, 134

Luger R., Foreman-Mackey D., Hogg D. W., 2017, Research Notes of the American Astronomical Society, 1, 7

Luo A. L., et al., 2015, Research in Astronomy and Astrophysics, 15, 1095

Magg E., et al., 2022, A&A, 661, A140

Magic Z., Collet R., Asplund M., Trampedach R., Hayek W., Chiavassa A., Stein R. F., Nordlund Å., 2013, A&A, 557, A26

Magic Z., Chiavassa A., Collet R., Asplund M., 2015, A&A, 573, A90

Magrin D., et al., 2018, in Lystrup M., MacEwen H. A., Fazio G. G., Batalha N., Siegler N., Tong E. C., eds, Society of Photo-Optical Instrumentation Engineers (SPIE) Conference Series Vol. 10698, Space Telescopes and Instrumentation 2018: Optical, Infrared, and Millimeter Wave. p. 106984X, doi:10.1117/12.2313538

Maíz Apellániz J., Pantaleoni González M., 2018, A&A, 616, L7

Majewski S. R., et al., 2017, AJ, 154, 94

Mann A. W., et al., 2019, ApJ, 871, 63

Martin D. C., et al., 2005, ApJL, 619, L1

Maxted P. F. L., 2010, PHY-30024 'Binary stars and exoplanets' lecture notes

Maxted P. F. L., 2016, A&A, 591, A111

Maxted P. F. L., 2018, A&A, 616, A39

Maxted P. F. L., Gill S., 2019, A&A, 622, A33

Maxted P. F. L., Hutcheon R. J., 2018, A&A, 616, A38

Maxted P. F. L., Serenelli A. M., Southworth J., 2015, A&A, 575, A36

Maxted P. F. L., et al., 2020, MNRAS, 498, 332

Maxted P. F. L., et al., 2022a, MNRAS, 513, 6042

Maxted P. F. L., et al., 2022b, MNRAS, 514, 77

Mayor M., Mermilliod J. C., 1984, in Maeder A., Renzini A., eds, International Astronomical Union Symposium Vol. 105, Observational Tests of the Stellar Evolution Theory. p. 411

Metropolis N., Rosenbluth A. W., Rosenbluth M. N., Teller A. H., Teller E., 1953, JChPh, 21, 1087

Miller N. J., Maxted P. F. L., Smalley B., 2020, MNRAS, 497, 2899

Milone E. F., Hrivnak B. J., Clark T. A., Kjeldseth Moe O., Blades J. C., Shelton I., 1981, Information Bulletin on Variable Stars, 2060, 1

Montegriffo P., et al., 2022, arXiv e-prints, p. arXiv:2206.06205

Morello G., Tsiaras A., Howarth I. D., Homeier D., 2017, AJ, 154, 111

Mullan D. J., MacDonald J., Dieterich S., Fausey H., 2018, ApJ, 869, 149

Munari U., Zwitter T., 1997, A&A, 318, 269

Nelson B., Davis W. D., 1972, ApJ, 174, 617

Nichols J. S., Linsky J. L., 1996, AJ, 111, 517

Noll S., Kausch W., Barden M., Jones A. M., Szyszka C., Kimeswenger S., Vinther J., 2012, Astron. Astrophys, 543

Ogilvie G. I., 2014, ARA&A, 52, 171

Oke J. B., 1965, ARA&A, 3, 23

Oke J. B., Gunn J. E., 1983, ApJ, 266, 713

Olsen E. H., 1994, A&AS, 106, 257

Onken C. A., et al., 2019, PASA, 36, e033

Padmanabhan N., et al., 2007, MNRAS, 378, 852

Parviainen H., 2018, in Deeg H. J., Belmonte J. A., eds, , Handbook of Exoplanets. Springer, p. 149, doi:10.1007/978-3-319-55333-7_149

Paxton B., Bildsten L., Dotter A., Herwig F., Lesaffre P., Timmes F., 2011, ApJS, 192, 3

Pecaut M. J., Mamajek E. E., 2013, ApJS, 208, 9

Pilecki B., et al., 2017, ApJ, 842, 110

Plez B., 2012, Turbospectrum: Code for spectral synthesis, Astrophysics Source Code Library, record ascl:1205.004 (ascl:1205.004)

Pojmanski G., 2002, AcA, 52, 397

Pollacco D. L., et al., 2006, PASP, 118, 1407

Pols O. R., Tout C. A., Schroder K.-P., Eggleton P. P., Manners J., 1997, MNRAS, 289, 869

Popper D. M., 1980, ARA&A, 18, 115

Popper D. M., Etzel P. B., 1981, AJ, 86, 102

Poznanski D., Prochaska J. X., Bloom J. S., 2012, MNRAS, 426, 1465

Press W. H., Teukolsky S. A., Vetterling W. T., Flannery B. P., 1992, Numerical recipes in FORTRAN. The art of scientific computing. Cambridge University Press

Price-Whelan A. M., Goodman J., 2018, ApJ, 867, 5

Prša A., et al., 2016, AJ, 152, 41

Prša A., et al., 2022, ApJS, 258, 16

Queloz D., et al., 2001, The Messenger, 105, 1

Quirrenbach A., et al., 2016, in Evans C. J., Simard L., Takami H., eds, Society of Photo-Optical Instrumentation Engineers (SPIE) Conference Series Vol. 9908, Ground-based and Airborne Instrumentation for Astronomy VI. p. 990812, doi:10.1117/12.2231880

Ratajczak M., et al., 2021, MNRAS, 500, 4972

Rauer H., et al., 2014, Experimental Astronomy, 38, 249

Reddy B. E., Lambert D. L., Allende Prieto C., 2006, MNRAS, 367, 1329

Reipurth B., 1978, Information Bulletin on Variable Stars, 1419, 1

Ribas I., Gimenez A., Torra J., Jordi C., Oblak E., 1998, A&A, 330, 600

Ribas I., Jordi C., Giménez Á., 2000, MNRAS, 318, L55

Ricker G. R., et al., 2014a, Proceedings of the SPIE, 9143, 15pp

Ricker G. R., et al., 2014b, in Oschmann Jacobus M. J., Clampin M., Fazio G. G., MacEwen H. A., eds, Society of Photo-Optical Instrumentation Engineers (SPIE) Conference Series Vol. 9143, Space Telescopes and Instrumentation 2014: Optical, Infrared, and Millimeter Wave. p. 914320 (arXiv:1406.0151), doi:10.1117/12.2063489

Ricker G. R., et al., 2015, Journal of Astronomical Telescopes, Instruments, and Systems, 1, 014003

Riess A. G., et al., 2018, ApJ, 861, 126

Riess A. G., Casertano S., Yuan W., Bowers J. B., Macri L., Zinn J. C., Scolnic D., 2021, ApJL, 908, L6

Rodrigo C., Solano E., 2020, in XIV.0 Scientific Meeting (virtual) of the Spanish Astronomical Society. p. 182

Roming P. W. A., et al., 2005, SSRv, 120, 95

Rozenberg G. V., 1966, in , Twilight. Springer US, Boston, MA, pp 59–124, doi:10.1007/978-1-4899-6353-6˙3

Russell H. N., 1948, in , Vol. 7, Harvard Observatory Monographs. p. 181

Santos N. C., et al., 2013, A&A, 556, A150

Sarmento P., Delgado Mena E., Rojas-Ayala B., Blanco-Cuaresma S., 2020, A&A, 636, A85

Sasaki T., Kosugi G., Hawkins R., Kawai J. A., Kusumoto T., 2004, in Quinn P. J., Bridger A., eds, Society of Photo-Optical Instrumentation Engineers (SPIE) Conference Series Vol. 5493, Optimizing Scientific Return for Astronomy through Information Technologies. pp 367–372, doi:10.1117/12.550756

Schlafly E. F., Finkbeiner D. P., 2011, ApJ, 737, 103

Schlegel D. J., Finkbeiner D. P., Davis M., 1998, ApJ, 500, 525

Schönrich R., Binney J., Dehnen W., 2010, MNRAS, 403, 1829

Schrijver C. J., Zwaan C., 1991, Astron. Astrophys, 251, 183

Sebastian D., et al., 2021, A&A, 645, A100

Serenelli A. M., Bergemann M., Ruchti G., Casagrande L., 2013, MNRAS, 429, 3645

Sharma S., 2017, ARA&A, 55, 213

Sharma S., et al., 2018, MNRAS, 473, 2004

Shetrone M., et al., 2015, ApJS, 221, 24

Silva Aguirre V., et al., 2017, ApJ, 835, 173

Simons D. A., Tokunaga A., 2002, PASP, 114, 169

Skrutskie M. F., et al., 2006, AJ, 131, 1163

Smalley B., 2014, in , Determination of Atmospheric Parameters of B. Springer, pp
    85–95, doi:10.1007/978-3-319-06956-2_8

Sneden C. A., 1973, PhD thesis, The University of Texas at Austin.

Snell C. M., Heiser A. M., 1968, Publ. Astron. Soc. Pac, 80, 336

Sousa S. G., 2014, [arXiv:1407.5817],

Sousa S. G., Santos N. C., Adibekyan V., Delgado-Mena E., Israelian G., 2015, A&A,
    577, A67

Southworth J., 2013, A&A, 557, A119

Southworth J., 2015a, in Rucinski S. M., Torres G., Zejda M., eds, Astronomical Society
    of the Pacific Conference Series Vol. 496, Living Together: Planets, Host Stars and
    Binaries. p. 164 (`arXiv:1411.1219`)

Southworth J., 2015b, in Living Together: Planets, Host Stars and Binaries. pp 164–165

Southworth J., 2021, The Observatory, 141, 190

Spada F., Demarque P., Kim Y. C., Sills A., 2013, ApJ, 776, 87

Standing M. R., et al., 2022, MNRAS, 511, 3571

Stassun K. G., Torres G., 2018, ApJ, 862, 61

Stassun K. G., et al., 2019, AJ, 158, 138

Steinmetz M., et al., 2020, AJ, 160, 83

Strömgren B., 1951, AJ, 56, 142

Strömgren B., 1966, ARA&A, 4, 433

Subasavage J. P., Bailyn C. D., Smith R. C., Henry T. J., Walter F. M., Buxton M. M., 2010, in Silva D. R., Peck A. B., Soifer B. T., eds, Society of Photo-Optical Instrumentation Engineers (SPIE) Conference Series Vol. 7737, Observatory Operations: Strategies, Processes, and Systems III. p. 77371C, doi:10.1117/12.859145

Sūdžius J., Bobinas V., 1994, Baltic Astronomy, 3, 158

Swayne M. I., Maxted P. F. L., Hodžić V. K., Triaud A. H. M. J., 2020, MNRAS, 498, L15

Swayne M. I., et al., 2021, MNRAS, 506, 306

Tamuz O., Mazeh T., Zucker S., 2005, MNRAS, 356, 1466

Tayar J., Claytor Z. R., Huber D., van Saders J., 2022, ApJ, 927, 31

Taylor M., 2017, arXiv e-prints, p. arXiv:1707.02160

Tokunaga A. T., Simons D. A., Vacca W. D., 2002, PASP, 114, 180

Tonry J. L., et al., 2018, ApJ, 867, 105

Torres G., Andersen J., Giménez A., 2010, A&A Rv, 18, 67

Triaud A. H. M. J., et al., 2013, A&A, 549, A18

Triaud A. H. M. J., et al., 2017, A&A, 608, A129

Valenti J. A., Fischer D. A., 2005, ApJS, 159, 141

Valenti J. A., Piskunov N., 1996, A&AS, 118, 595

Valle G., Dell'Omodarme M., Prada Moroni P. G., Degl'Innocenti S., 2016, A&A, 587, A16

Valle G., Dell'Omodarme M., Prada Moroni P. G., Degl'Innocenti S., 2018, A&A, 620, A168

Van Hamme W., Wilson R. E., 2007, ApJ, 661, 1129

VandenBerg D. A., Bond H. E., Nelan E. P., Nissen P. E., Schaefer G. H., Harmer D., 2014, ApJ, 792, 110

Viani L. S., Basu S., 2020, ApJ, 904, 22

Wall R. E., Kilic M., Bergeron P., Rolland B., Genest-Beaulieu C., Gianninas A., 2019, MNRAS, 489, 5046

Wang R., et al., 2020, ApJ, 891, 23

Weiss A., Schlattl H., 2008, Ap&SS, 316, 99

Wenger M., et al., 2000, A&AS, 143, 9

Wilson R. E., 1979, ApJ, 234, 1054

Wilson R. E., 1990, ApJ, 356, 613

Wilson R. E., Devinney E. J., 1971, ApJ, 166, 605

Wilson R. E., Van Hamme W., 2014, ApJ, 780, 151

Wright E. L., et al., 2010, AJ, 140, 1868

Xiang M. S., et al., 2015, MNRAS, 448, 822

Xu S., Zhang B., Reid M. J., Zheng X., Wang G., 2019, ApJ, 875, 114

Zahn J. P., 1977, A&A, 57, 383

Zhou G., et al., 2014, MNRAS, 437, 2831

Zinn J. C., 2021, AJ, 161, 214

Zucker S., Mazeh T., 1994, ApJ, 420, 806

van Belle G. T., et al., 2021, ApJ, 922, 163

van Hamme W., 1993, AJ, 106, 2096

von Boetticher A., et al., 2019, A&A, 625, A150